

CRANFIELD UNIVERSITY

Lawrence Tinsley

Pulse Thermography-based Ageing Assessment of Thin Thermal
Barrier Coatings

School of Aerospace Transport and Manufacturing

PhD

Academic Year: 2012 - 2019

Supervisor: Dr Yifan Zhao, Prof. Rajkumar Roy

Associate Supervisor: Dr Jörn Mehnert

June 2019

ABSTRACT

With the motivation to drive gas turbines at increasing power and efficiency, the increase of combustion temperatures is highly desirable, while turbine temperatures are met by material limitations where the temperatures readily exceed the melting point of the metals used to make the components. In response to this, engine manufacturers implement thermal control systems, from air cooling of the component, to Thermal Barrier Coatings (TBCs) applied on the component surfaces, reflecting radiant heat energy and providing an insulating layer. These materials reduce the temperature experienced by the component materials, enabling higher operational temperatures; while the metallic bond coat in between also protects against oxidation and corrosion attack. With TBCs playing such a crucial role in the standard operation of gas turbines at the edge of its performance capability, standing between materials performing one of the most stringent engineering roles ever designed, and the hot gases capable of melting them; the durability of the TBC to resist its own degradation and their ensuing material life are vital. The assessment of TBC health and its Remaining Useful Life (RUL) are of key interest in the maintenance of aero engine components.

This thesis presents a review of Non-Destructive Testing (NDT) methods utilised in the inspection of TBCs, proceeding to evaluate the use of pulsed-active flash thermography NDT for ageing assessment of thin TBCs undergoing cyclic oxidation ageing, selected for study to adapt the method to the more challenging context at the cutting edge of gas turbine performance. The coatings were inspected with and without emissivity-improving soot coating to evaluate a realistic inspection scenario – where contamination may not be justifiable – with ideal inspections performed in parallel. In order to address the challenge of capturing a fast thermal event through a thin TBC, an inspection framework was developed to optimise the data capture and analysis parameters. Through-depth diffusivity has been measured during oxidation ageing of six 150µm thick TBCs deposited via Electron Beam Physical Vapour Deposition (EB-PVD), showing a repeatable trend with distinct features, which can be exploited for ageing characterisation, with automation of thermographic NDT of TBC parts

demonstrating the potential for rapid implementation of the technique. The research provides through-life captures of each of the TBC samples uniquely coupled with parallel captures in the non-ideal inspection condition without application of an emissivity improving soot coating, simulating a real-world inspection scenario in which a wide area un-treated surface inspection is desired. Additionally, a novel inspection framework has been developed for establishing the multiple coupled parameters required to tackle the complexities introduced when applying optical flash for thermography of thin EB-PVD TBCs.

Keywords: Non-Destructive Testing, Degradation Lifting Assessment, Thermographic Inspection, Remaining Useful Life, Thermal Barrier Coatings

ACKNOWLEDGEMENTS

I would very much like to thank everyone who has been involved in my work and personal development over the course of my thesis. My deepest gratitude goes first towards my supervisors, Professors Rajkumar Roy, Jörn Mehnert and Dr Yifan Zhao for their continuous guidance, friendship and patient encouragement.

I would like to thank our industrial partners for sharing their real world expertise, and helping to guide the focus of my research.

For their expert knowledge of Thermal Barrier Coatings, I would like to express my sincerest gratitude to Professor John Nicholls, and Dr. Christine Chalk.

I also want to thank Luke Oakey and Pavan Addepalli, Teresa Bandee, John Erkoyuncu, Matthew Caffrey, Sam Court and Rian Connell for their friendship and support, and to everyone on the outside of my work life; my parents, my sister Claudette, to Nikki and Andrew and my extended family, and to Dilara, my fiancé.

A very special thank you goes to Mr Liaqat Chowoo, consultant surgeon of Bedford hospital, and Linda Bavister and the fantastic team at Addenbrooke's hospital Cambridge for saving my life. My gratitude in this is further extended to the NHS and all her staff, for all you have done for me and so many special people, day after day.

The work in this thesis was undertaken at the Through-life Engineering Services Centre, founded in 2011 as a joint collaboration between Cranfield and Durham Universities, and was led by Prof. Rajkumar Roy. The aim of the TES centre is for the research and development to improve the design, manufacture and service life of high value manufacturing (HVM) components. With a focus on the whole life aspect of a component, the centre aims to improve upon all aspects of an HVM component's life, from improvements in their design and manufacturing to ensure a longer lasting component with extended availability and lower overall cost.

This work has been funded by the Engineering and Physical Sciences Research Council, under grant number EP/I033246/1. The variety of work it has fostered continues to grow, and further thanks will continue to be extended in thanks for the support of the EPSRC and the centre's partners, for years to come.

TABLE OF CONTENTS

ABSTRACT	ii
ACKNOWLEDGEMENTS	iv
LIST OF FIGURES	ix
LIST OF TABLES	xvii
LIST OF EQUATIONS	xix
LIST OF ABBREVIATIONS	xx
1 Introduction.....	1
1.1 Maintenance, Repair and Overhaul (MRO).....	1
1.2 Scale of Maintenance in Aerospace	2
1.3 Degradation of gas turbine components	3
1.4 Role of MRO operations	6
1.5 The need for Thermal Barrier Coatings	6
1.5.1 The Importance of TBCs.....	11
1.5.2 Types of TBCs	13
1.6 Thesis Structure	17
1.7 Summary	18
2 Literature Review	19
2.1 Literature Selection Criteria.....	19
2.2 Introduction to Non-destructive Testing	21
2.2.1 Visual Inspection	22
2.2.2 Dye penetrant inspection	23
2.2.3 Magnetic particle inspection.....	23
2.2.4 Ultrasonic inspection	24
2.2.5 Eddy current inspection	25
2.2.6 Industrial Radiography.....	26
2.2.7 Fluorescence Spectroscopy.....	27
2.2.8 Thermography.....	28
2.3 NDT comparison chart.....	36
2.4 TBCs & thermal properties.....	38
2.5 TBC ageing: causal factors in changes of thermal properties in TBCs... 40	
2.5.1 Increase in thermal conductivity & diffusivity: Sintering, changes in microstructure surface features	41
2.5.2 Increase in thermal conductivity: changes in porosity	43
2.5.3 Changes in the thermally grown oxide interface associated with TGO thickening and possible interface separations.....	46
2.5.4 Other changes in coating properties.....	49
2.6 Prediction and Assessment of TBC life.....	51
2.6.1 Turbine Engine Hot Section Technology (HOST) Project.....	52
2.6.2 Statistical life modelling	54
2.6.3 Later developments in TBC lifing	54

2.6.4 Other approaches of TBC life (mechanistic, NDT & data driven)	56
2.7 NDT of TBCs	58
2.7.1 Acoustic emissions	59
2.7.2 Microwave NDT	60
2.7.3 Micro-indentation loading method	60
2.7.4 Ultrasonic inspection	61
2.7.5 Eddy Current testing + electrical resonance-based testing	62
2.7.6 Emission spectroscopy	62
2.7.7 Impedance spectroscopy (IS)	63
2.7.8 X-ray diffraction (XRD)	64
2.7.9 Photo-luminescent piezospectroscopy (PLPS)	64
2.7.10 Thermography: thermal cycle monitoring of TBC	65
2.7.11 Active thermography: laser flash method	66
2.7.12 Active thermography: Induction thermographic inspection	67
2.7.13 Active Thermography: Infrared reflectance technique	67
2.7.14 Active Thermography: oscillating heat application	68
2.7.15 Active Thermography: Pulsed inspection (front surface)	68
2.8 Definition of “non-destructive” and “in-situ” in service / MRO contexts ...	71
2.9 Classification scheme: Non-destructive testing	73
2.9.1 Non-destructive (true) testing (NDT-A i)	73
2.9.2 Non-destructive (true) testing (NDT-X ii)	73
2.9.3 Non-destructive (true) testing (NDT-X iii)	73
2.9.4 Non-destructive (applied) testing (NDT-B)	73
2.9.5 Non-destructive (practical) testing (NDT-C)	74
2.9.6 Non-destructive (practical) testing (NDT-D)	74
2.9.7 Non-destructive (practical) testing (NDT-E)	74
2.10 Classification scheme: situational context	75
2.10.1 In-situ (on-line, hot) (S-A)	75
2.10.2 In-situ (on-line, cool) (S-B)	75
2.10.3 In-situ (on-line, cool) (S-C)	75
2.10.4 Ex-situ (S-D)	76
2.10.5 Ex-situ (S-E)	76
2.11 Classification scheme: Estimation of RUL	76
2.11.1 Remaining Useful Life: applied (RUL-A)	76
2.11.2 Remaining Useful Life: entailed (RUL-B)	77
2.11.3 Remaining Useful Life: plausible (RUL-C)	77
2.12 Non Destructive Testing & Remaining Useful Life of TBCs	77
2.13 Gaps in knowledge / state of the art	83
2.14 Summary: predictions of TBC cyclic ageing experiment	84
3 Research Aims, Objectives, Methodology	85
3.1 Scope & Aims	85
3.2 Objectives	85

3.2.1 Objective One: Identify industry requirements, current practice.....	85
3.2.2 Objective Two: Conduct TBC lifing experiment to capture degradation of TBCs.....	86
3.2.3 Objective Three: Development of a framework for thermographic NDT for through-life degradation assessment of thin EB-PVD TBCs	86
3.2.4 Objective Four: Development of an automation process to support thermographic NDT for through-life assessment	86
3.3 Methodology.....	87
4 Current industrial practice	91
4.1 Questionnaire design: the key questions	91
4.1.1 People involved: background, years of experience	92
4.1.2 Summary of results	94
4.1.3 Interview analysis.....	95
4.1.4 Key degradation mechanisms.....	98
4.1.5 Summary and gap analysis	100
5 Thermographic NDT & parametric study	102
5.1 Setup and samples.....	103
5.1.1 Equipment	105
5.1.2 Data processing: Two-layer thermal pulse model	106
5.1.3 Data calibration: digital level to temperature.....	107
5.2 Data capture parameters	112
5.2.1 Parametric Study.....	114
5.2.2 Step one: background parameters	119
5.2.3 Step two: data window.....	124
5.2.4 Step three: Integration time	129
5.2.5 Step four: flash power intensity.....	131
5.2.6 Step five: Soot coating influence.....	133
5.3 Final parameter selection.....	134
5.3.1 Summary	135
6 TBC lifing experiment.....	136
6.1 Inspection-exposure methodology.....	136
6.1.1 Initial experment run.....	137
6.1.2 Limitations	140
6.1.3 Inspection process layout	141
6.2 Furnace cycle runs.....	142
6.3 Trend identification	145
6.4 Results.....	146
6.4.1 Sample lifetime	146
6.4.2 Results: tabulated	147
6.4.3 Results: plotted	151
6.5 Summary	153
7 Diffusivity Analysis and pattern seeking	154

7.1 Anomaly resolution.....	154
7.2 Analysis of results.....	156
7.3 Pattern seeking.....	158
7.4 Pattern detail summary.....	168
7.5 Comparison with pre-aged coatings of unknown age.....	175
7.6 Summary.....	176
8 Automation of data capture and feature detection.....	178
8.1 Industry requirements.....	178
8.2 Experimental method.....	179
8.3 Automated inspection cell for damage detection.....	180
8.4 Pulsed thermography: delamination detection.....	181
8.5 Automated analysis: image processing.....	181
8.6 Segmentation of features of interest from structure.....	183
8.7 Automated sizing.....	184
8.8 Results and discussion.....	185
8.9 Summary.....	189
9 Discussion.....	190
9.1 Causal factors in changes of thermal properties in TBCs.....	191
9.1.1 Feature 2: Growth of TGO with ageing?.....	192
9.1.2 Increase in thermal conductivity and diffusivity: Sintering, changes in microstructure surface features.....	193
9.1.3 Increase in thermal conductivity and diffusivity: changes in porosity	195
9.1.4 TC – TGO interface changes from with TGO growth, with possible interface separations.....	196
9.1.5 Changes in porosity: phonon scattering relation.....	201
9.2 Reflection on pre-aged coating samples.....	201
9.3 Discussion: TBC lifing experiment.....	202
9.4 Limitations of research.....	207
10 Conclusions.....	210
10.1 Further research.....	211
REFERENCES.....	213
APPENDICES.....	235
Appendix A Industry Interviews.....	235
Appendix B – Report on flash bulb intensity.....	243
Appendix C – Data tables.....	248
Appendix D – full range of experiments for parametric study.....	249

LIST OF FIGURES

Figure 1 – A representative overview of typical operating costs for a commercial aircraft operator (left) [11], with a breakdown of average maintenance costs (right) [12].	3
Figure 2 – Illustration of a typical gas turbine engine; from left to right: intake fan / low pressure compressor; intermediate pressure compressor, the combustion chamber, and a high, intermediate and low pressure (power) turbine for extracting power.	4
Figure 3 – An ideal Brayton cycle, denoting the associated pressure-volume and temperature-entropy changes at different parts of the cycle.....	7
Figure 4 - Relationship between gas turbine specific output with operating temperature	9
Figure 5 - Temperature distribution in a typical aero engine, inspired by numerous similar depictions in books and literature [26] [27].....	10
Figure 6 - NASA/USAF experimental research aircraft X-15 (left) [32], where TBCs saw one of their first applications in the rocket nozzle (right) [33]....	11
Figure 7 - Development of turbine blade maximum operating temperature over the history of aerospace technologies, inspired by a diagram by Prof Tony Evans, represented in numerous publications: [35] [36] [37]	12
Figure 8 – Structure of a typical APS TBC, based on diagrams reproduced in various literatures [42]	14
Figure 9 – microstructure of a typical EB-PVD TBC, illustrating the columnar grains bound to the bond coat by the oxide layer, which in turn is bound directly to the metallic substrate; inspired by diagrams reproduced in various literatures [42]	15
Figure 10 – A cross-section of an SEM micrograph displaying an EB-PVD TBC in-situ on a turbine blade. The temperature variation is illustrated (solid line); along with its decrease upon encountering the TBC, and the resulting temperature gradient over each of the layers, from ceramic top coat (right), bond coat (mid) and the component itself (left). From Padture, Gell & Jordan, 2002 [43] - Reprinted with permission from AAAS.	16
Figure 11 - application of visual inspection via borescope on an aero engine, courtesy of NDT Education Resource Center, Iowa State University, USA [51]	22
Figure 12 – illustration of dye penetrant inspection principles (left), with image of a cracked part under UV-light inspection (right) [51] courtesy of the NDT Education Resource Center, Iowa State University, USA.	23

Figure 13 - Magnetic particle inspection, working principles (left), with example of inspection on a crane hook, [51], courtesy of the NDT Education Resource Center, Iowa State University, USA.....	24
Figure 14 - Illustration of ultrasonic inspection a-scan, with three inspection scenarios, (a) for no defect, showing only the reflected signal of the rear wall, (b) with small defect, showing both the reflected defect signal and the rear wall; and (c) a large defect, where the rear wall echo is obscured.	25
Figure 15 - illustration of eddy current inspection on a pipe (left), and photo of EC inspection on a component (right), courtesy of Ether NDE ltd.	25
Figure 16 - An x-ray inspection, with illustration (left) [51], and diagram of operating principles (right). Visual and X-ray courtesy image of the NDT Education Resource Center, Iowa State University, USA.	26
Figure 17 – spectral emission of an ideal Blackbody object at various temperatures, plotted using (2-1) in Matlab [56].....	30
Figure 18 – Typical time-temperature $T(t)$ plot of a thermographic inspection of component and defect area (inset), plotted in logarithmic domain, yielding the time of change of log-linear cooling (t^*) of a damage / feature (t_a^*) and sound (t_s^*) region.....	33
Figure 19 – propagation of incident light on a typical semi-transparent EB-PVD TBC and its structure, illustration by the author, inspired from Li and Clarke (2008) [66]	39
Figure 20 – The thermal conductivity change induced by heat treatment of PS TBCs at different temperatures (left), and over increasing treatment times at 1000°C. (right), adapted from (Dinwiddie et al., 1996) [72], courtesy of ASME.	41
Figure 21 – changes in an EB-PVD's surface morphology & internal porosity. Shown are the surface structure (#1), cross-section of internal structure (#2), showing the deposited condition (left; a), after dwell at 1100°C in air for 200 hours (mid, b); and 900 hours (right, c). Reproduced from (Rätzer-Scheibe & Schulz, 2007), courtesy of Elsevier [74]	43
Figure 22 - changes to thermal conductivity of EB-PVD TBCs, measured under steady-state heat flux at const. temperature (left), or cyclic testing (right) (Zhu et al., 2001) [70], courtesy of Elsevier.	44
Figure 23 – SEM of EB-PVDs undergoing high temperature oxidation ageing, showing the break-up of the feathery structure giving way to spherical pores from as soon as 1 hour, and developing further by 100 hour (bottom) Reproduced from Renteria & Saruhan (2006) [76], courtesy of Elsevier. ..	45
Figure 24 – cyclic behaviour of thermal conductivity of EB-PVD TBC subjected to cyclic testing (2h), reproduced from (Zhu et al., 2000, 2001) [70] [77], courtesy of Elsevier.	47

Figure 25 – EB-PVD TBC exposed to 40h of thermal cycling showing inter-columnar cracks (left), and propagation of a delamination crack at the interface (right); figure reproduced from (Zhu et al., 2001) [70], courtesy of Elsevier.....	47
Figure 26 – Mid-IR (rear heated) emission images of a TBC showing smaller delaminations leading to coalescing of cracks and spallation. Reproduced from (Kakuda et al., 2009) [73], courtesy of Elsevier.....	48
Figure 27 – changes to density with TBC thermal cycling, reproduced from (Kakuda et al., 2009) [73], courtesy of Elsevier.....	49
Figure 28 – optical penetration depth of a thermally cycled TBC, showing a large initial change, followed by a steady linear increase over cycle life. Reproduced from (Kakuda et al., 2009) [73], courtesy of Elsevier.	49
Figure 29 – thermal diffusivity change of a thermally cycled TBC, exhibiting a decaying exponential early increase, followed by a steady increase over cycle life, decreasing near end of life, reproduced from (Kakuda et al., 2009) [73], courtesy of Elsevier.	50
Figure 30 – changes in reflectance spectra of EB-PVD TBC when subjected to thermal cycling at 1150°C as studied by Kakuda et al., (2009) [73], courtesy of Elsevier.....	51
Figure 31 – expected TBC life via Weibull distribution over test temperatures, showing predicted life against temperature (left) containing populations of probability of failure of each sample set (right) in the sample life data, inspired by TBC life estimations in literature [87] [88].....	54
Figure 32 – illustration of the adopted research methodology.....	88
Figure 33 – drawing of TBC coupons manufactured for preliminary experiment	104
Figure 34 – Image of round coupon samples.....	104
Figure 35 – Thermographic data capture experimental setup.....	105
Figure 36 – Experimental setup of flash thermography equipment, showing the sample fixture (left), flash hood with xenon flash lamps (center), and radiometer (right).....	106
Figure 37 – Integration time adjustment for FLIR SC7600 with calibration curves for integration time vs temperature range as produced by the manufacturer’s software.....	108
Figure 38 – displaying and fitting to camera temperature calibration curves and the problem encountered attempting to calibrate pixels captured beyond the data range.....	109

Figure 39 – final calibration curve: fitting a hybrid of low and high range data points, extending beyond the range to follow calibration curve; then re-fitting to full range.....	110
Figure 40 – plotting error of each calibration fit against the calibration curve data, for low temperature range, high temperature range, and the hybrid fit (lowest error)	110
Figure 41 – plotting hybrid calibration curve error over temperature range, compared to 20mK, given as the camera’s NETD	111
Figure 42 – estimation of flash temperature to predict data range, and duration of flash for estimation of afterglow effects for preliminary trial settings.	120
Figure 43 – investigation of flash afterglow (marked), demonstrating a number of frames after the flash, introducing problems to inspection without soot condition	121
Figure 44 – comparison of different flash intensities on sample cool-down. Effect of ambient light leaking into inspection cell via removal of protective cover also indicated by the mid-recording ‘step’ in the data capture for 50%....	122
Figure 45 – emissivity estimation of TBC using manufacturer’s software to match emissivity estimate to yield the same temperature (2, left) as the electrical tape (3, right)	123
Figure 46 - Illustration of the data output showing different regions within the data, from pre-flash (a), flash duration and post-flash heating effects (b), coating data window (c) and heat pulse diffusion into the substrate material (d).	124
Figure 47 – plot of diffusivity results of a single data capture varied with analysis parameters (x-axis) taken with an integration time (2271us) and flash power (50%), cycling through data capture parameters in series from left to right: data offset (0), window length 10, 12, 14, 18, 20; data offset (1), window length (10, 12,..); (2), (10, 12..)	127
Figure 48 – estimated diffusivity values, for a range of data window parameters (offset 0, left, 4, right; and within each offset a variation of data window length 12, left, to 40, right); IT 2271 μs.	128
Figure 49 - estimated diffusivity values, for a range of data window parameters (offset 0, left, 4, right; and within each offset a variation of data window length 12, left, to 40, right); IT 4000 μs.	129
Figure 50 – Searching for stable settings using R ² indicating accuracy of fit of the two-layer model to the data under the given experimental conditions, showing R ² values for 5 experiments over different integration times at 50% flash power. Reproduced from Tinsley et al., (2017) [185], courtesy of Elsevier.....	131

Figure 51 – maintaining a constant IT of 2271 μs , the result of different levels of flash power are tested for their R^2 stability over different fitting parameters., figure reproduced from Tinsley et al., (2017) [185]., courtesy of Elsevier. 132

Figure 52 - Sensitivity analysis: flash power – result value with 4 parametric combinations for each flash power, identifying closest subset (50%, combinations 1, 2), where each data series is a quartet of parameter observations integration time (2271, left, Q1-2; and 4000, Q3-4, right), without soot condition (Q1, Q3) and with soot condition (Q2, Q4); refer to Table 12..... 132

Figure 53 – R^2 difference achieved without soot, compared to with soot, and with soot at the integration time of 4000 μs . This shows that offset of 0 and 1 frame (x-axis 1-14) are particularly erroneous and unstable, resulting in poor fits of the model to the data, while the uncoated condition (top row) is similarly stable as the coated condition (mid row). Plot reproduced from Tinsley et al.,(2017) [185], courtesy of Elsevier. 133

Figure 54 – Micrograph (10x zoom) of post-wash sample S11 in different locations, before (left) and after (right) soot coating contamination, at $t = 0$; contamination residue (right) survived ultrasonic path stage, step v. 138

Figure 55 – Micrograph (10x zoom) of post-wash sample S05 in different locations, before (left) and after (right) soot coating contamination, at $t = 0$; contamination residue (right) survived ultrasonic path stage, step v. 139

Figure 56 – Micrograph (10x zoom) of post-furnace sample S05 at $t = 16$, showing the coating free from soot. 139

Figure 57 – Flowchart illustrating the process stages of the oxidation ageing cycle, showing the different stages; from preliminary trials (i), through to inspections without (ii) and with the soot coating condition (iii). The process cycles through stages (ii)-(iii) until visible spallation in either of the last two stages..... 141

Figure 58 – Extraction of samples in-between oxidation cycles at $t = 0$ 16 hours, before the sample is allowed to cool in their holder on a ceramic brick... 142

Figure 59 – layout of furnace cycle planning (orange highlight), with inspection cycles (blue highlight), permitting four ageing runs and inspections per week. 143

Figure 60 – Chart of furnace cycles displaying time at temperature for each furnace run..... 144

Figure 61 – Sketch of expected experimental results. 145

Figure 62 – Sample life duration over time at temperature until coating failure (expected lifetime ~100-140 hours, (vertical lines))..... 147

Figure 63 – Plot of as-new sample diffusivity versus furnace cycle hours, without soot coating 152

Figure 64 - Plot of as-new sample diffusivity versus furnace cycle hours, with soot coating..... 153

Figure 65 – Identifying anomalies and outliers in the results, S01 at t=64 (lower middle), and S11 t=128 (right) are regarded as anomalous..... 154

Figure 66 – histogram showing number of sample data captures per time slot, indicating a failure to record data capture for S05 (with soot) at t = 0 hrs, and a reduction of data samples for later time periods, where all available samples were captured, reducing below the minimum requirement of 3 for reliable pattern inspection at t = 128 hrs. Data captures for as-new samples, only; pre-aged samples expired at 16-32 hours..... 156

Figure 67 - Plotting all results in the raw as-calculated value, without soot coating (above), and with soot coating (below), excluding the anomaly at t = 64 hrs for the without soot condition. 157

Figure 68 – A plot of thermal diffusivity (normalised) box plot of all as-deposited samples plotted against cycle time (hours). Data shown in the without soot condition (left) and with soot condition (right), showing a pattern between the samples over ageing (illustrated). Plot adapted from Tinsley et al., (2017) [185], courtesy of Elsevier. 159

Figure 69 – highlight of S07 in ‘without soot’ series, (left) versus average, and S11 in ‘with soot’ data series versus average (right); demonstrating similar pattern to the average, with an offset in x-axis from t=48 (left), offset in y-axis from the average (right); where the red and blue lines refer to the average of the dataset, while the green plots show the plots for individual samples S07 (left), and S11 (right), highlighting some of the variance in the sets between the samples, in both soot conditions. 160

Figure 70 – raw plots of all samples in the ‘without soot’ condition, displaying each sample’s pattern (green) against the average (red). 162

Figure 71 - raw plots of all samples in the ‘with soot’ condition, displaying each sample’s pattern (green) against the average (blue). 163

Figure 72 – adjusted plots of all samples, showing sample’s pattern (green) against the average (blue); modified: normalised for initial reading at, 0 hours. 164

Figure 73 – adjusted plots of all samples, showing sample pattern (green) against the average (blue); modified: normalised for first cycle, at 16 hours. 164

Figure 74 – polynomial fit of data, adjusted to t = 0, coeff = 4, full time series 166

Figure 75 – polynomial fit of data, adjusted to t = 16, coeff = 4, between t=16 – 112. 166

Figure 76 – pattern features of diffusivity behaviour over coating life, approximately detailing how each of the regions vary, and over their

respective timeframes. If feature (4) exists, it is not fixed to regions indicated, and the regions are variable for each sample and coating condition.....	170
Figure 77 – replotting individual results, with pattern features overlaid, shown here for samples without the soot condition, with each sample’s pattern (green line) plotted against average values: without soot (red line).	171
Figure 78 – replotting individual results, with pattern features overlaid, shown here for samples without the soot condition with each sample’s pattern (green line) plotted against average values: with soot condition (blue line).....	172
Figure 79 – replotting results, showing distribution of pattern features over life cycle (without soot condition), feature 1 (top left), 2 (top right), 3 (bottom left), 4 (bottom right), emphasising the presence of each feature to be shown in their full expression.	173
Figure 80 – replotting results, showing distribution of pattern features over life cycle (with soot condition), feature 1 (top left), 2 (top right), 3 (bottom left), 4 (bottom right), emphasising the presence of each feature to be shown in their full expression.	174
Figure 81 - Plot sample diffusivity versus furnace cycle hours, with soot coating condition: pre-aged coatings; with pre-aged samples over-plotted from t=128, in reverse.	175
Figure 82 - Plot of pre-aged sample diffusivity versus furnace cycle hours, with soot coating, with pre-aged samples over-plotted from t=128, in reverse.	176
Figure 83 – Automated NDT inspection system with use of the Fanuc M-20iA robotic arm, showing presentation of one type of component to the inspection system (left), and the collection of another type of component for inspection, (right); image reproduced from (Mehnen, Tinsley & Roy, 2014) [178], courtesy of Elsevier.	180
Figure 84 – Raw output image of component under inspection (greyscale); image reproduced from (Mehnen, Tinsley & Roy, 2014) [178], courtesy of Elsevier.	181
Figure 85 – example of binary image (left), respective filter mask (mid), resulting binary map (right); reproduced from (Mehnen, Tinsley & Roy, 2014) [178], courtesy of Elsevier.	183
Figure 86 – application of boundary trace algorithm to binary map, regions of interest plotted in rotating colour palette (left), filtered results plotted on original image (right); image reproduced from (Mehnen, Tinsley & Roy, 2014) [178], courtesy of Elsevier.	184
Figure 87 – A process flowchart showing the automated detection & sizing stages; image reproduced from (Mehnen, Tinsley & Roy, 2014) [178], courtesy of Elsevier.	185

Figure 88 – Automated damage detection and segmentation process; image reproduced from (Mehnen, Tinsley & Roy, 2014) [178], courtesy of Elsevier. 186

Figure 89 – Three damage types auto-segmented for Gaussian fitting, with fit results plotted over the damages. The fitting process is shown. Image reproduced from (Mehnen, Tinsley & Roy, 2014) [178], courtesy of Elsevier. 187

Figure 90 – Example of thermography inspection of TBC delamination (situated next to spallation regions), top-left (a), red, & top right (b), green, showing log-log (T,t) plot (b) containing thermal contrast of the delam regions from the “sound” in-tact TBC (a), (blue, mid), with 2nd differential plot giving different time of peak contrast change (c). Image reproduced from (Mehnen, Tinsley & Roy, 2014) [178], courtesy of Elsevier. 188

Figure 91 – model of TGO growth as a function of temperature & time at t ... 192

LIST OF TABLES

Table 1 - Comparison of NDT techniques, highlighting their suitability strengths from 1 (strong) to 4 (weak) against a range of inspection tasks, adapted and expanded from an NDT trainer’s online materials, [65]. Rankings are based on the ability of the technique to develop a response signal, and does not inherently imply a measurement is useful; many of the classifications are based on the author’s assumptions with limited experience with all the methods.	37
Table 2 – classification scheme of NDT categories	78
Table 3 – classification scheme of NDT situational (“situ”) categories	78
Table 4 – classification scheme of NDT situational (“situ”) categories	78
Table 5 – summary of literature on application of NDT methods to the estimation of RUL of TBCs	79
Table 6 - A summary of typical degradations in aerospace components which were identified as being potentially accessible to thermography NDT (reproduced from Mehnen, Tinsley & Roy 2014), [178], courtesy of Elsevier.	99
Table 7 – initial setup parameters options.....	115
Table 8 – Quantum well saturation of the detector for a set of integration times	117
Table 9 – High (+) and Low (-1) settings for parametric study.....	118
Table 10 – 2 ³ Three Factor, 2(2), 1(4) mixed-mode design of experiments tabulation, with runs in ‘standard order’ (left), and full factorial design of experiments, with factor levels used (right).....	118
Table 11 – estimation of manufactured TBC coupon properties.....	119
Table 12 – Full Factorial study results, based upon offset = 2, window length = 20	134
Table 13 – Final experiment setup, reproduced from Tinsley et al.,(2017) [185], courtesy of Elsevier.	135
Table 14 – Sample lifetime until failure (samples labeled to enable repeats).	146
Table 15 – Data table for Sample S01.....	148
Table 16 – Data table for Sample S03.....	148
Table 17 – Data table for Sample S05.....	149
Table 18 – Data table for Sample S07.....	149
Table 19 – Data table for Sample S09.....	150

Table 20 – Data table for Sample S11.....	150
Table 21 – Data table for Sample S21.....	151
Table 22 – Data table for Sample S23.....	151
Table 23 – Data table for Sample S25.....	151
Table 24 – standard deviation of datasets, in the original and adjusted conditions.	165
Table 25 – Summary of observed features from each dataset, where ‘–’ is used to indicate absence of the feature for that sample, in the specified soot coating condition.....	169
Table 26 – Examples of detected features output by the algorithm.....	188
Table 27 – reproduction of table Table 25, feature 4, filtering to show only co- expressed instances of feature 4;.....	198

LIST OF EQUATIONS

(1-1)	7
(1-2)	8
(1-3)	8
(1-4)	8
(1-5)	8
(2-1)	30
(2-2)	31
(2-3)	55
(2-4)	66
(2-5)	69
(5-1)	107
(5-2)	119
(5-3)	119
(5-4)	123
(7-1)	158

LIST OF ABBREVIATIONS

MRO	Maintenance, Repair and Overhaul
OEM	Original Equipment Manufacturer
HVC	High Value Component
RUL	Remaining Useful Life
TES	Through-life Engineering Services
TIT	Turbine Inlet Temperature
HP	High Pressure
NGV	Nozzle Guide Vane
TBC	Thermal Barrier Coating
APS / PS	Air Plasma Spray / Plasma Spray
CVD	Chemical Vapour Deposition
EB-PVD	Electron Beam Physical Vapour Deposition
TC	Top Coat
BC	Bond Coat
TGO	Thermally Grown Oxide
NDT	Non-Destructive Testing
X-CT	X-ray Computed Tomography
XRD	X-ray Diffractometry
IS	Impedance Spectroscopy
IR	InfraRed
SWIR	Short-wave Infrared
MWIR	Mid-wave Infrared
LWIR	Long-wave Infrared
PT	Pulsed Thermography
NASA	National Aeronautical and Space Administration
HOST	Turbine Engine Hot Section Technology project
SEM	Scanning Electron Microscopy
DL	Digital Level
IT	Integration Time
FWHM	Full Width at Half Maximum

1 Introduction

1.1 Maintenance, Repair and Overhaul (MRO)

Gas turbines are among the most high-value engineering assets employed across all industry sectors from aerospace, defence, marine and industrial power generation. High value products such as gas turbines are required to perform over long product lifetimes, which require application of continuous, on-going maintenance throughout their service life to ensure high use & performance [1].

Over the last decade, various industries in these sectors have undergone a transformation wherein they have shifted from the classic business model of the manufacture and sale of equipment and associated spare parts, to offering the inclusion of essential services as an integrated package in accompaniment with the product. This means the customer now purchases purely the use of the product, instead of ownership of the product itself along with the responsibility for arranging the high level of required maintenance. In manufacturing, this ownership-service structure is known as 'servitisation', where packages are defined as 'Industrial Product-Service Systems', encompassing a variety of associated definitions [2] [3]. In the aero-engine market, these contracts are known as 'Power-by-the-Hour' [4].

In the aerospace sector these services include maintenance, repair, replacement and retirement services, having been grouped together, known as 'Maintenance, Repair and Overhaul (MRO)', which has been defined as "the maintenance functions required to sustain an active aircraft fleet" [5]. The maintenance and associated services of components consumes a large proportion of the total cost

of running the aircraft, with the value of MRO services estimated at over 135bn USD in the year 2015, equivalent to 75% of the value of aircraft production for that year [6]. Since the introduction of 'servitization' to the aerospace industry, the MRO market has been a major focus for growth within the sector. This in turn has presented strong competition from countries with lower running costs associated with providing the services, according to the 2018 IBISWorld market report [7]; resulting in many MRO activities becoming outsourced, in order to pool inventories, staff and resources, reducing wastage, and in turn, cost [8]. Beyond the expected weight and fuel efficiency considerations, when the aerospace industry drives to reduce costs, their focus is predominantly on MRO costs [9]; thus creating a market where service costs are of key importance.

As such, the pressure for innovation now rests on the physical assets, their length of life, and the costs associated with their maintenance and replacement; the monitoring of component health, the rates at which they degrade, the application of repairs, and confidence in the integrity of those repairs and the associated extension to remaining component life are of key priority within the sector, which drives interest in research and development of degradation analysis techniques to maximise component life within safe confidence boundaries.

1.2 Scale of Maintenance in Aerospace

Among operators of industrial gas turbines, while essential, the provision of maintenance is one of the leading cost burdens, even comparable to the cost contribution of emissions taxes, placing its cost optimisation high among operational priorities [10]. Similarly, within the aerospace sector, maintenance represents approximately 13% [11] of operating costs, shown in Figure 1, below.

Of these, the engine represents approximately 40% of maintenance costs [12]. While this is a small percentage of the total operating costs, it is an area where minor adjustments can have the greatest impact, and where NDT technologies can be deployed to facilitate these improvements.

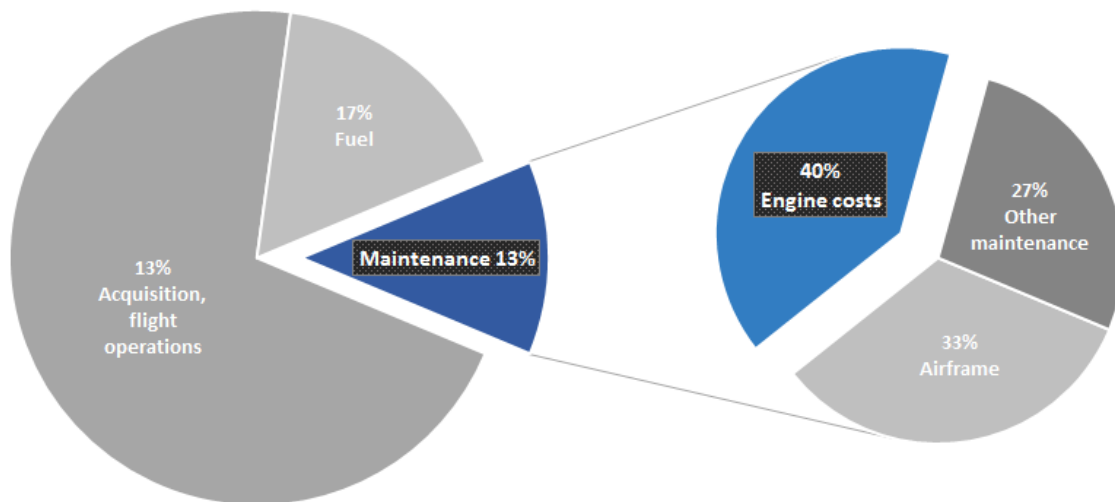


Figure 1 – A representative overview of typical operating costs for a commercial aircraft operator (left) [11], with a breakdown of average maintenance costs (right) [12].

1.3 Degradation of gas turbine components

Consisting of three main components, a gas turbine is made from (moving from intake to the exhaust) a compressor, a combustor, and a turbine. Downstream from the combustor are in the 'hot section', including the combustor apparatus, the turbine blades, and vanes. Depending on the application, the rotation output of the turbine is fed through a gear system to then drive the purposed output, whether it is a dynamo, propeller, or fan. An example of an aero engine gas turbine is shown in Figure 2. A gas turbine in operation relies upon the collective function of many components combined in a complex system, subjecting its components to some of the most extreme operating environments produced in any type of engineering.

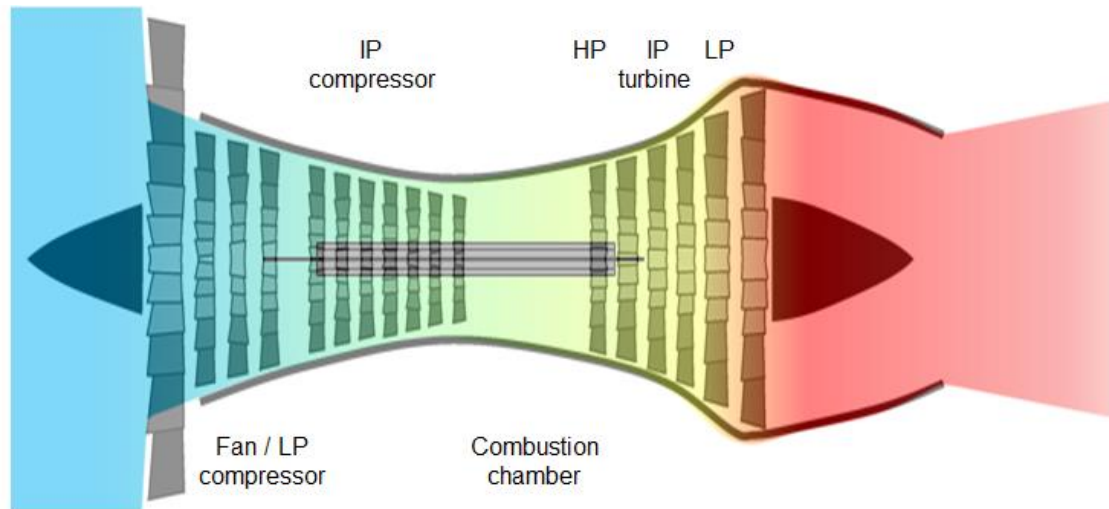


Figure 2 – Illustration of a typical gas turbine engine; from left to right: intake fan / low pressure compressor; intermediate pressure compressor, the combustion chamber, and a high, intermediate and low pressure (power) turbine for extracting power.

As a result, any component of a gas turbine typically exhibit wear and eventually degrade via a variety of mechanisms over the system's operational life; these include fouling, erosion, creep, wear, warping, and cracking [13]. Particularly due to the high temperature of the 'hot section' components, this list also includes high temperature oxidation and 'hot corrosion' [14]:

- **Erosion** involves physical material loss from mechanical contact or chemical interaction.
- **Fouling** caused by steady particulate build-up on material surfaces over time, increasing surface roughness.
- **Oxidation** – metals react with oxygen in the hot turbine temperatures, and are usually coated with a protective oxide scale that obstructs and resists further oxidation, although this too eventually grows, erodes, cracks and spalls, leaving the substrate exposed to oxidation attack.
- **Corrosion** – as the engine ingests dust and particulates – including chemicals released via fuel combustion – these contaminants react with

the metallic components in the high temperatures of the hot path components. Broadly, hot corrosion occurs in two temperature bands: “low temperature” hot corrosion, at 600-800°C; and “high temperature” hot corrosion, between ~800-950 °C [14].

It is worth noting some differences between the various gas turbine applications, which result in environmental differences and operational parameters. For example, while land-based turbines can benefit from filtration of air intakes to offset particulate ingestion, they also use different, lower cost fuels; both of which affects the type and volume of contaminant ingestion. In comparison, marine engines will be able to afford filtration, but will still ingest a high volume of salt contamination. Different chemical species attack at different temperatures, which the turbines undergo according to their service context. Aero engines will frequently experience a higher temperature thermal cycling, with shorter cycle length.

Some degradations exhibit changes in vibrations and turbine operational parameters, for which simulations of the effects of degradation exist [15]. Degradations such as fouling can be modelled [16] [17], and their effect on “engine health” and operational parameters can be used to detect their presence and progress [18] [19] [20], giving rise to diagnostics, or health-based maintenance. Approaches like this contribute to the reliable use and sustainment of intended operational parameters. However, for high cost, safety-critical components such as those in the hot gas path, vibration and operational parameters are a reflection of the part performance, but do not readily provide the physical health and integrity of the part itself, and this is where inspection and

material testing becomes a necessary aspect of the running of high value complex engineering systems, such as gas turbines.

1.4 Role of MRO operations

During a major overhaul, parts are removed, inspected and repaired; the objective is to restore function and material integrity to the turbine and its parts, to as close to the original design & manufactured condition as possible, both to maintain the safe operation of the turbine, and to sustain its performance parameters [21].

In the context of gas turbine MRO, a series of traditional methods are typically applied in frequent use, as will be discussed in more detail in the next chapter, these include; visual inspection, dye / fluorescent penetrant testing, ultrasonic tomography, x-ray inspection (2D scan and X-ray Computed Tomography, aka “X-CT”), and eddy current testing [22]. Other inspection methods in frequent use include tap testing, acoustic emission, thermography, and magnetic particle inspection [23].

1.5 The need for Thermal Barrier Coatings

In the on-going drive to improve the fuel efficiency and available power for generation of required speed and acceleration per unit of weight, the aviation industry is in continuous search for improvement of gas turbines turbines and their respective efficiencies.

Gas turbines follow the Brayton cycle, illustrated as:

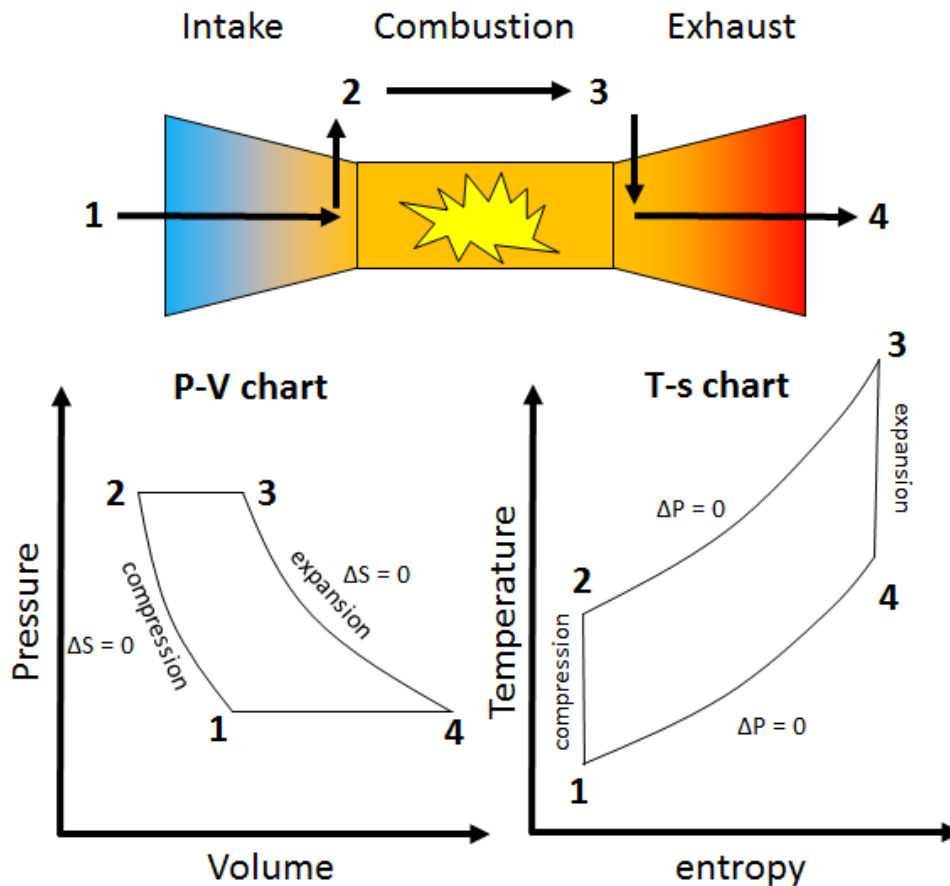


Figure 3 – An ideal Brayton cycle, denoting the associated pressure-volume and temperature-entropy changes at different parts of the cycle

The Brayton cycle describes a constant-pressure heat engine, which can be described by a steady state energy flow as [24]:

$$Q = -(h_2 - h_1) + \frac{1}{2}(C_2^2 - C_1^2) + W \quad (1-1)$$

where Q are heat and W work ‘transfers’ per unit mass flow of air through the gas turbine; h confers the stage at each respective part on the Brayton cycle: 1 (intake), 2 (compression), 3 (combustion) and 4 (expulsion).

Assuming no mass or kinetic energy loss, constant flow rate, and applying to the respective work required (for compression stage, 1-2), heat generated (combustion stage, 2-3) and work out (3-4), respectively, yields:

$$Work_{(compression\ required):\ 1-2} = -(h_2 - h_1) = -c_p(T_2 - T_1) \quad (1-2)$$

$$Heat_{(combustion:\ generated):\ 2-3} = -(h_3 - h_2) = -c_p(T_3 - T_2) \quad (1-3)$$

$$Work_{(turbine\ output):\ 3-4} = -(h_3 - h_4) = -c_p(T_3 - T_4) \quad (1-4)$$

where c_p is thermal capacity of the working fluid, and T_{\square} the temperature of the working fluid (gas) at each respective part of the cycle. The efficiency of the cycle is given by:

$$efficiency(\eta) = \frac{work\ output\ (w)}{heat\ supplied\ (combustion)\ (q)} \quad (1-5)$$

which in turn is reduced by the work required to drive the compressor. Further deriving the thermodynamic descriptions of the compressor, combustor and turbine, which cannot accurately represent the resulting true efficiency of the engine and has already been covered in the literature representing the ideal operation of a Brayton cycle [24] [25]; the work output of a gas turbine can be seen to improve with increased turbine inlet temperature, as shown in Figure 4. The work output or 'specific thrust' increases with both turbine inlet temperature and pressure ratio, with a similar, but smaller trend exhibited in improvements in ideal cycle efficiency in terms of the amount of work accessible per unit mass of intake air. Meanwhile, specific fuel consumption follows a trend of strong increase with increase in turbine inlet temperature, and decrease over increasing compression ratios; as more fuel can be burnt in a greater volume of air per second.

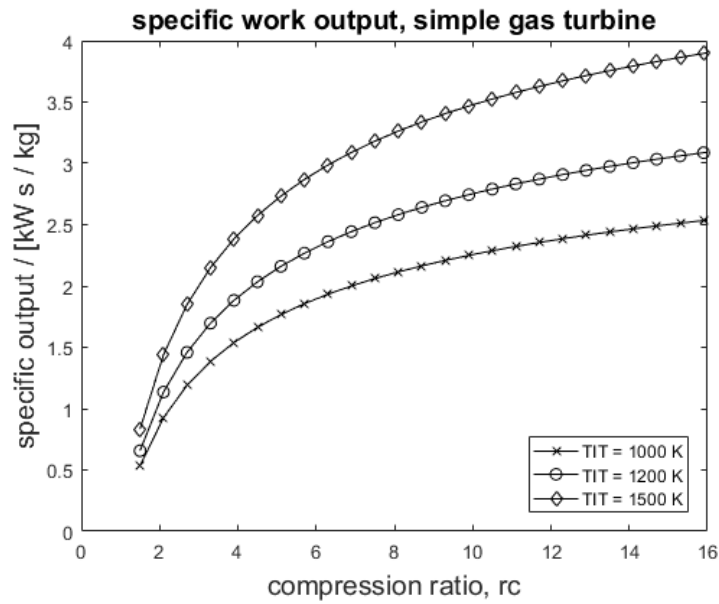


Figure 4 - Relationship between gas turbine specific output with operating temperature. Additionally, a higher fuel-to-air ratio is required to achieve the desired greater combustion temperature rise, while the preceding pressure / temperature rise from the compression stage draws parasitically from the turbine work output. Increase temperatures and the step increase in work output allow access also to the higher gas pressure compression ratios (which improve both thrust and specific fuel consumption), which in turn deliver a hotter gas temperature to the combustion chamber, contributing to the post-combustion gas temperature.

While operating the gas turbine at higher temperatures may improve the output power from the turbine, enabling heavier loads to be lifted for the same engine mass, it does however incur a cost on the materials that make up the turbine parts, situated at the most demanding “hot path” section of the engine, illustrated in Figure 5. Increased temperatures bring an overall increase in the environmental attack and associated degradation of the material of the hot path components, shortening their life.

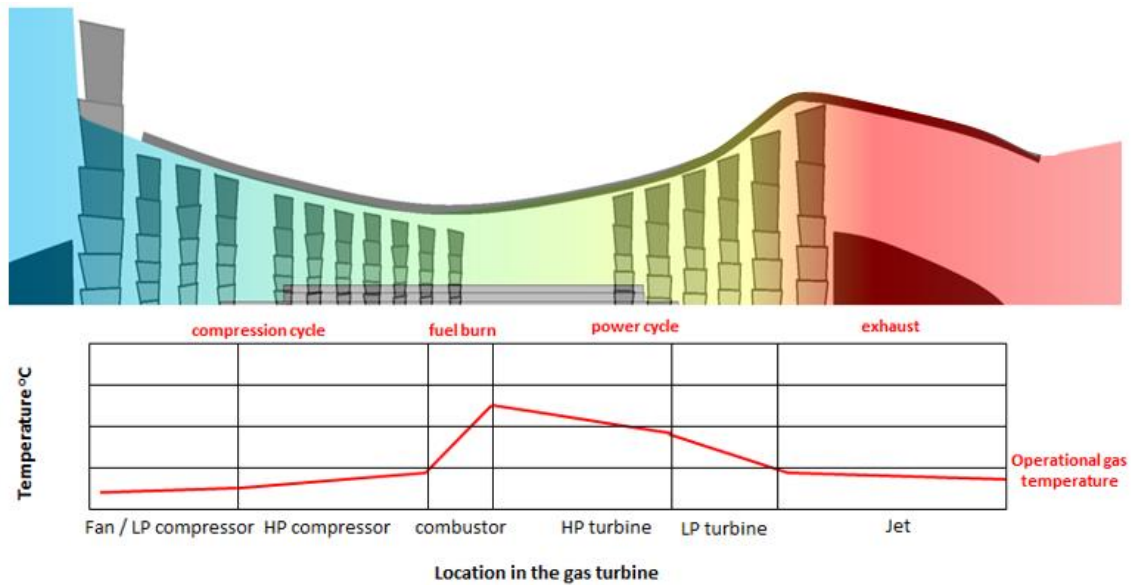


Figure 5 - Temperature distribution in a typical aero engine, inspired by numerous similar depictions in books and literature [26] [27]

In order to operate at higher temperatures, new material developments are continuously sought in the gas turbine and aero engine sectors are directly connected to the drive for increase engine performance, and the life of the components that make them up. With progress in the on-going development of new metal alloys for the components themselves, additional technological developments in the system have been made in order to push the envelope further than material developments alone can encompass. Initially, the first method to push engine operation to higher temperatures involved the cooling of the components via air channels to extract heat from the material. While this enabled a large jump in accessible gas temperatures, the outer material is still exposed directly to the high temperature, with a large temperature gradient expressed on the material surface and through the material, adding to oxidation attack, creep, and thermal fatigue; shortening its life, and this degradation itself limits the maximum gas temperature that is available, if the parts are not to be frequently repaired and renewed.

1.5.1 The Importance of TBCs

Thermal Barrier Coatings (TBCs) are surface coatings of insulating materials possessing a low value of thermal conductivity. These are typically applied to metallic components exposed to high temperatures, and are typically in use in gas turbines, aero engines and rocket engines. Their function is to reduce the temperature the components experience, permitting their use at higher temperatures, even above their melting point; and to prolong their life at those temperatures, where their lifetimes would not be commercially viable otherwise. One of the earliest appearances of TBCs in aerospace was reported in 1947 [28], developed over the following decades with tests for the US Air Force [29], [30], culminating in the application of TBCs in the rocket engine nozzle of the X-15 experimental aircraft [31], shown below.



Figure 6 - NASA/USAF experimental research aircraft X-15 (left) [32], where TBCs saw one of their first applications in the rocket nozzle (right) [33]

Later research focused on the development of TBCs for reducing strain experienced by rocket chambers in the 1980s [34], while two main developments were introduced in the same decade into the commercial gas turbine, from the extension of the turbine active cooling system to the exterior of the component, where cooler high pressure air from the compressor is forced out of cooling

channels over the component surface, forming a protective “air film” over the surface which obstructs the hot gas, and the first active use of TBCs in commercial aviation.

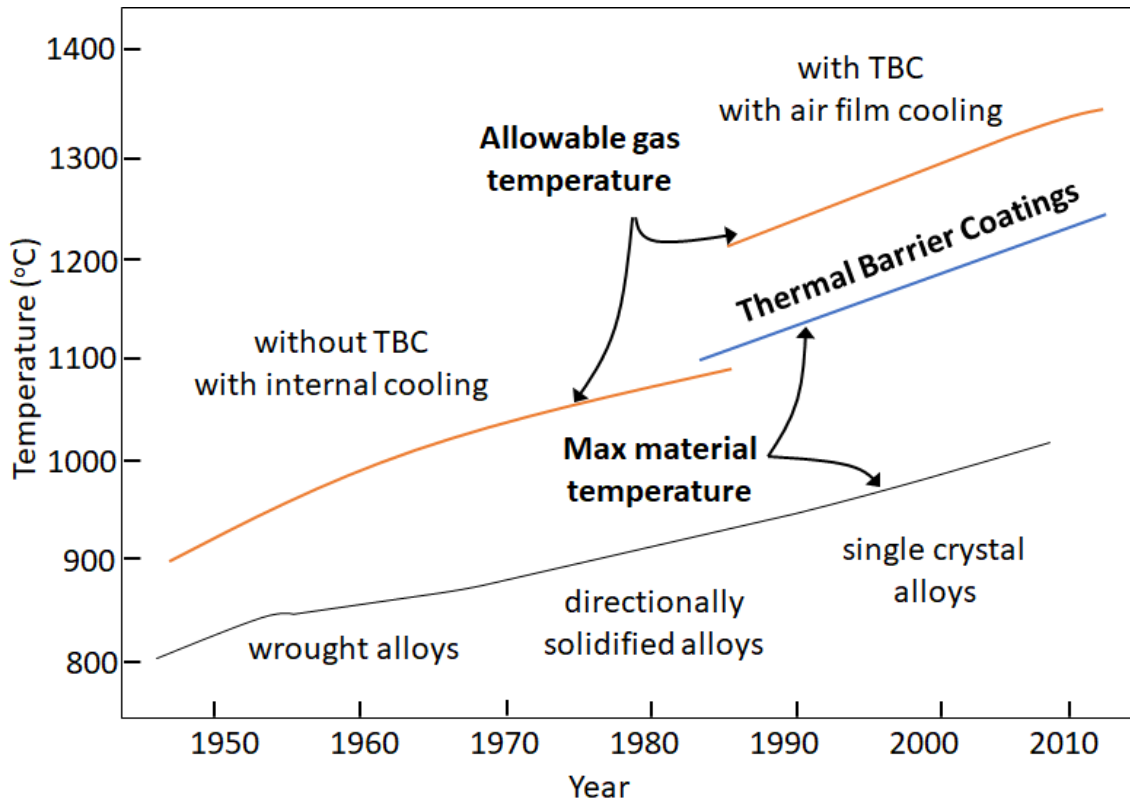


Figure 7 - Development of turbine blade maximum operating temperature over the history of aerospace technologies, inspired by a diagram by Prof Tony Evans, represented in numerous publications: [35] [36] [37]

The effect of air film cooling and the spread of TBCs into commercial aviation market can be seen in Figure 7, where the technologies progressively improved upon the maximum permissible operating temperature of the engine. For example, it has been shown that TBCs can exhibit a temperature gradient of up to 150 [38] - 180°C [39], while the coating structure, substrate material [40], and manufacturing conditions can have different effects on TBC properties and their material life [41].

1.5.2 Types of TBCs

The primary purpose of TBCs are to protect components from the high temperature oxidation and corrosion from the hot gas and its contents; the common core of research developments in the 1970s & 80s resulted in a structure of three layers: the ceramic topcoat (TC) to provide the heat insulation, a metallic coat for providing the actual adherence of the ceramic to the substrate; and an oxide layer between the bond coat (BC) and ceramic topcoat. Since the ceramic is permeable to oxygen, the oxide layer also provides an oxidation resistance to the metallic substrate, its thickness increasing gradually over exposure to high temperatures; also referred to as “Thermally Grown Oxide” (TGO). Two main TBC deposition methods are in frequent use:

Plasma Spray

The more widespread method of depositing a TBC use an implementation of “thermal spray”; deposition of the material in a high temperature molten or semi-molten state, which is then “sprayed” onto the surface of a part. When applied to thermal barrier coatings, where a very high temperature is required to melt the ceramic, this is typically applied with a plasma torch capable of achieving the high temperature, and is performed in the presence of an inert gas, such as Argon, Helium or Nitrogen; at atmospheric pressures. This gives it its name “Plasma Spraying” (PS) or more commonly “Air Plasma Spraying” (APS) (as this process could be applied under vacuum), and the application at atmospheric pressures reduces the overall time and financial cost of applying the process.

The ceramic, in a powdered form is fed into a plasma ‘flame’, melting the ceramic and shooting it at the target surface. As the molten ceramic particles impact, they

deform from their spherical shape and form “splats” on the surface, with a porous, laminate structure, shown below:

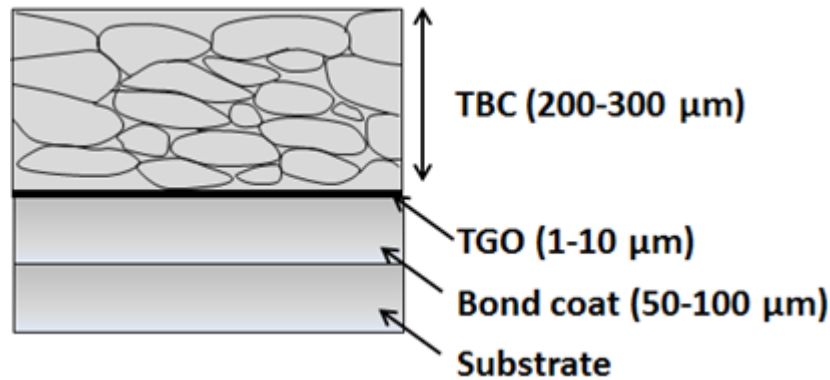


Figure 8 – Structure of a typical APS TBC, based on diagrams reproduced in various literatures [42]

While considerably cheaper than its counterpart, the adherence of the splats to each other is dependent on the contact that forms between them upon impact and cooling; meanwhile the particle size, their full deformation and the presence of intersplat voids, are all subject to random variation, introducing inherent randomisation in coating’s strain tolerance.

Electron Beam Physical Vapour Deposition

Another method for depositing TBCs is to evaporate the ceramic into a vapour, which then rises and condenses on the target surface, situated above the evaporation site. The vapour material then loses its heat and solidifies, forming a structure on the surface. The target material may be heated so that the ceramic does not cool too rapidly, solidifying on impact, allowing it to bond with the substrate and with the ceramic deposit, forming its microstructure. The ceramic is evaporated from a solid ingot using an electron beam directed under partial vacuum, giving the method its name; Electron Beam Physical Vapour Deposition (EB-PVD). In comparison to PS methods, the production of a vapour gives access

to a much finer resolution of the resulting structure, which can be further fine-tuned by control of the deposition parameters.

This process results in the formation of a coating that is “grown” on the surface. Unlike APS TBCs, which form “splats” from the spraying process, the deposition process forms structures that grow vertically from the component surface as individual columnar grains, or “trees”, with inter-columnar gaps which gives the TBC an appearance referred to as a “ceramic rug”; shown in Figure 9, below:

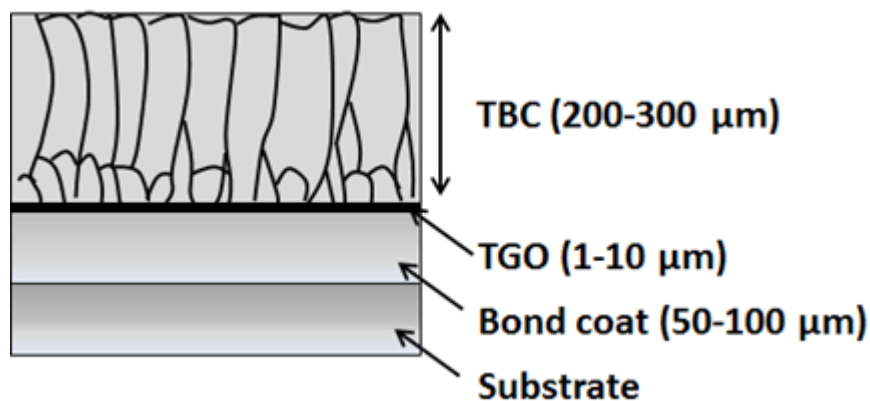


Figure 9 – microstructure of a typical EB-PVD TBC, illustrating the columnar grains bound to the bond coat by the oxide layer, which in turn is bound directly to the metallic substrate; inspired by diagrams reproduced in various literatures [42]

This unique structure is more costly and time consuming to manufacture, however the lack of bond between the columnar grains allows the coating to “stretch”, which yields greater strain compliance; while the small variation between the height of columnar tips gives the coating a lower roughness than APS TBCs. This makes the TBC more suitable to high temperature environment and thermal gradients, while the lower roughness of the surface has aerodynamic advantages for the high performance components, such as turbine blades, making the coating more advantageous for the more demanding components

despite its increased cost. An illustration of an EB-PVD in-situ on a component and its insulating effects on temperature are shown in Figure 10, below:

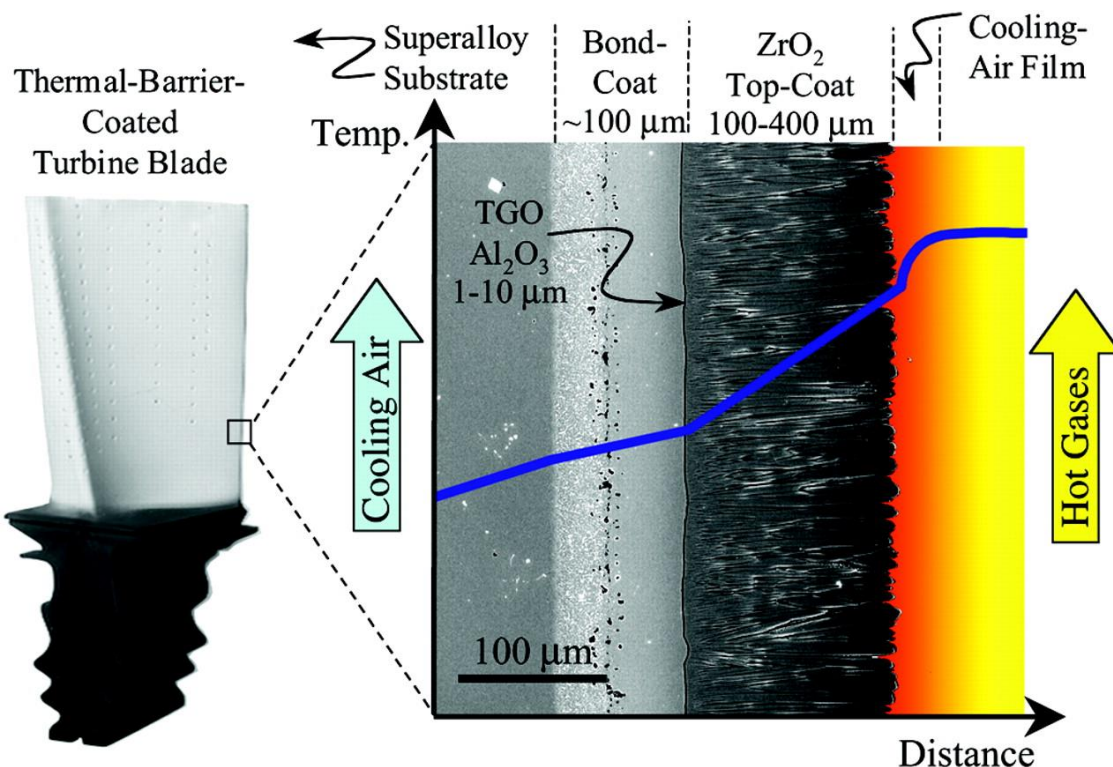


Figure 10 – A cross-section of an SEM micrograph displaying an EB-PVD TBC in-situ on a turbine blade. The temperature variation is illustrated (solid line); along with its decrease upon encountering the TBC, and the resulting temperature gradient over each of the layers, from ceramic top coat (right), bond coat (mid) and the component itself (left). From Padture, Gell & Jordan, 2002 [43] - Reprinted with permission from AAAS.

As TBCs are paramount for protecting the critical components from the harshest mechanical and operating environments in engineering, situated at the core function of gas turbines, the health and component life of TBCs are of critical importance and a leading research interest in the maintenance of aero engines; from contexts including on-wing inspections during regular use, to the MRO servicing between overhauls. It is in attempt to address this need in such a critical context that is the focus of this thesis is given.

1.6 Thesis Structure

The work in this thesis encompassed multiple aspects, their outcomes informing the requirement of the next. Sometimes this process was not in linear flow, with many performed in parallel to each other, however, they have been laid out so as to describe a story in their respective chapters.

In chapter one, the background of maintenance demand in the aerospace sector has been identified, and the main cost driver for improvement in maintenance discussed. The high value components and their demanding operational environment have been described, including how the life of the thermal barrier coating on these parts present a major opportunity for extension of product life, and reduction of overall engine running costs.

In chapter two, a survey of literature is performed to highlight current state of the art in NDT, with focus on TBCs, and to identify knowledge gaps that can be explored for the extension of TBC life, and/or reduction in maintenance cost.

In chapter three, the knowledge gap, research aims, objectives and methodology are laid out, which informs how and why each section of work in chapters 2, and 4-8 were conducted.

In chapter four, a series of industrial interviews were conducted to raise the challenges faced when trying to introduce new NDT technologies, capture existing NDT practice in industry, and to inform how experiments can be used to exploit the literature gap with a realistic approach.

Chapters five through seven covers the main experiment in assessment of TBC ageing via pulsed thermographic inspection and contains all details from

experiment design in chapter five, analysis method in chapter six, and the actual performance of the experiment and the results, in chapter seven.

Chapter eight contains work on automation of pulsed thermographic NDT with real components, developing a novel approach to component inspection, through which the technique used for the main experiment could be adapted for rapid deployment in industry.

Lastly, the final two chapters reflect on the entire thesis with discussion through the results and their suitability to the problems raised in industrial engagement, and whether the identified trends are exploitable; with concluding remarks on future work, and recommendations for further implementation.

1.7 Summary

This introduction has provided the background of costs in the aerospace sector and the importance of TBCs within the MRO sector as a key life-limited component and their role as a major cost driver and the role of NDT in MRO operations has provided the context for the research. The layout of the thesis structure has been discussed, explaining how the research draws upon the initial context to result in application of NDT for the assessment of TBCs.

2 Literature Review

2.1 Literature Selection Criteria

In order to fully comprehend the landscape of literature on TBC, the factors behind their ageing and respective life cycle, along with the various NDT methods available and tested against the challenge of maintenance and life assessment of TBCs, an approach was taken to survey the literature. The broad scope of the survey of literature sought to detail NDT applications for TBC degradation assessment and life assessment. It is expected that, owing to the thermal properties of TBCs being their core purpose, methods that record shifts in thermal material properties will dominate the results.

Search criteria

Key words: thermal barrier coatings, TBC, TBCs, thermal property, thermal properties, diffusivity, conductivity, oxidation, ageing, life cycle, lifing, assessment, measurement, characterisation, characterization, non-destructive testing, NDT.

Assessment Criteria

- Changes of material properties of thermal barrier coatings over ageing
- NDT Methodology applies to (or could be useful to apply to) APS or EB-PVD TBC life estimation
- Provides life estimation either as-manufactured or in-service state

Exclusion Criteria

- For life prediction methods older than 1985, and have not seen applications in industry

- Study covers damage mechanisms that are not applicable to APS / EB-PVD TBCs
- Study was published in a language other than English
- Publication is a conference or journal paper that does not add sufficient content to its twin, whichever is superior

Database

For the literature review, the database SCOPUS by Elsevier was selected. This was owing to the SCOPUS database containing all the publishers contained in the author's initial broad reading list on the topics of thermography and thermal barrier coatings. Additionally, it was critically important that the database used should contain some key papers in thermography and TBC life modelling:

- The basis of the laser flash method (Parker et al., 1961) [44]
- TBC Life prediction model development (Cruse Stewart, Ortiz 1988) [45]
- Life modelling of TBCs for aircraft gas turbine engines (Miller, 1989) [46]
- Thermographic Signal Reconstruction (Shepard et al., 2002) [47]

Additional search

When conducting a literature survey, it is often found that many insightful and seminal papers in any given field will cite texts and literatures that may not exist in the most frequently used databases; in which case, a responsive use of other databases, library catalogues and general internet searches will be useful for finding key sources, such as textbooks, historical literature, conference papers, and various NASA technical papers.

2.2 Introduction to Non-destructive Testing

“The simplest way to find out about a component’s structural or material properties is to quite literally push it to breaking point.”

- ‘The Engineer magazine, 31st January 2011 [48]

When a manufacturer produces a component that is required to perform to a set of specifications, the first type of testing the finished product might undergo is to consume a sample batch for establishment of product life under simulated service conditions. Today, tests such as this are standard even in regular low cost domestic products, such as furniture [49]. Through destructive tests, the component’s life and structural / material properties when stressed under simulated service conditions is obtained. This is vital to assert the component’s expected life, however, it also only provides the expected life cycle under standard or simulated conditions, simulating a variety of service conditions can add significantly to the cost, and only provides expected life (prognostics). If the part encounters a unique event or a combination of environmental factors not adequately accounted for, its true state of health may vary from its prognosis and the actual remaining life may differ. It is the actual remaining life, or Remaining Useful Life (RUL), that is the real subject of interest.

Non-Destructive Testing (NDT) applies to inspection of a part without causing any interference or damage, measuring its condition or material response against set criteria that are created to detect and interrogate known conditions that signal reduced life. This is translated into acceptance / rejection criteria specific to the component, and with some techniques the measurement may be useful for

quantifying the current state of health of the component. The following sections detail the major NDT techniques, known as the “big five” with the most historical developments, which are the most popular across all engineering sectors and the most developed, with a variety of established industrial standards.

“You don’t have to test everything to destruction just to see if you made it right!”

- Terry Pratchett & Neil Gaimann [50]

2.2.1 Visual Inspection

This is one of the most intuitive and accessible forms of NDT, which entails direct observation of the component in the visible spectrum. Typically performed by a technician using natural intuition coupled with their training and experience concerning which characteristic features for identification. Visual inspection can also be used to categorise the scanning of the component surface with a laser or the projection of fringe patterns for 3D surface profile measurement. These can be used to determine if a component is misshapen or otherwise outside specifications, to a finer resolution than may be possible by naked eye.



Figure 11 - application of visual inspection via borescope on an aero engine, courtesy of NDT Education Resource Center, Iowa State University, USA [51]

A visual inspection can also be performed by extension, using a periscope or optical borescope - an eyepiece and lens, with a flexible optical carrier or fiber-optic cable connecting the two - to allow the inspection of components in inaccessible areas, such as the inside of a gas turbine, as shown in Figure 11.

2.2.2 Dye penetrant inspection

This method of NDT is very similar to visual inspection, with the added application of a contrasting dye. First the component surface is cleaned, the dye is applied, which penetrates into surface-breaking cracks. The dye is then washed and removed from the surface, leaving the cracks - still containing dye - visible to the technician. For added contrast, a fluorescent dye can be used and placed under an ultra-violet light, allowing for finer cracks to be observed.

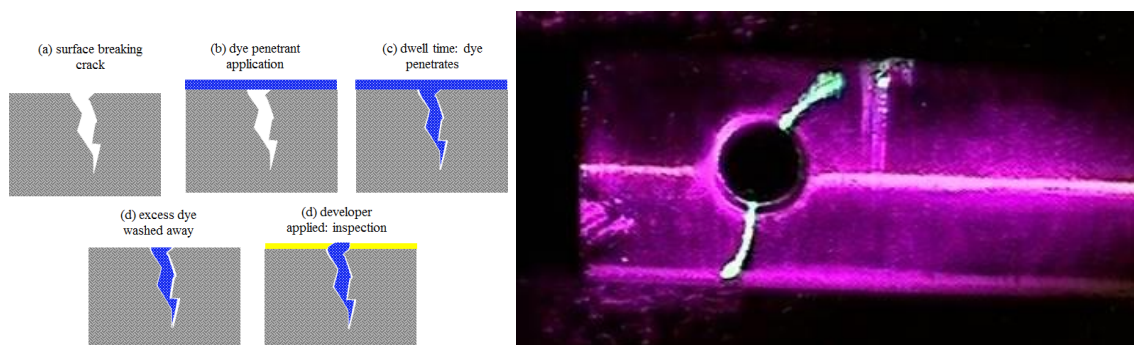


Figure 12 – illustration of dye penetrant inspection principles (left), with image of a cracked part under UV-light inspection (right) [51] courtesy of the NDT Education Resource Center, Iowa State University, USA.

2.2.3 Magnetic particle inspection

This is also a visual-type inspection, which involves creating a magnetic field in a component; discontinuities occurring in the surface or just below the surface via cracks and voids, if they are orientated normal to the induced magnetic field they disrupt the magnetic flux flowing through the material, resulting in “leakage” of the

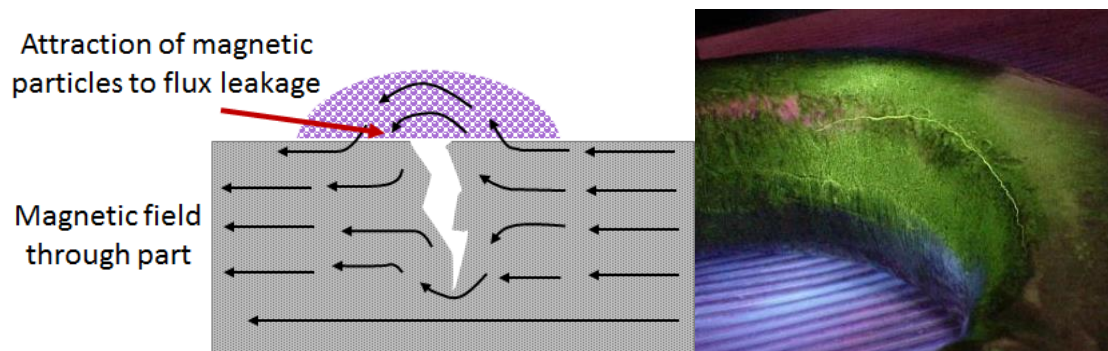


Figure 13 - Magnetic particle inspection, working principles (left), with example of inspection on a crane hook, [51], courtesy of the NDT Education Resource Center, Iowa State University, USA.

magnetic flux from the component over the surface of the part. This flux leakage essentially forms a magnetic trap for attracting ferrous (containing iron) particles applied to the surface. The magnetic particles can take the form of a dry powder or in a wet suspension; if a fluorescent dye carrier is used for the wet suspension, then the visual inspection of cracks can be aided with use of UV light. This is illustrated alongside a photographic example in Figure 13, where arrows indicate magnetic flux interrupted by a crack feature, forming a dipole on the material discontinuity which in turn exhibits flux leakage on the surface. This leakage of flux attracts the ferrous particles in a liquid suspension, providing a visibly-observable contrast.

2.2.4 Ultrasonic inspection

Ultrasound inspection involves the induction of sound waves in the component via a transducer placed directly in contact with the surface of the material. The sound waves propagate into the component and interact with features inside the material such as inclusions, structure, or the far surface, shown in Figure 14.

Most ultrasound inspections rely on “pulse-echo” method where the signal is reflected by features in the material and are measured at the surface.

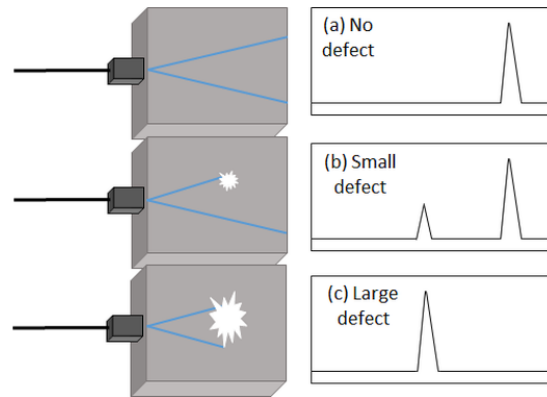


Figure 14 - Illustration of ultrasonic inspection a-scan, with three inspection scenarios, (a) for no defect, showing only the reflected signal of the rear wall, (b) with small defect, showing both the reflected defect signal and the rear wall; and (c) a large defect, where the rear wall echo is obscured.

Measurement can take place in a different location from the transmission; while more advanced methods than pulse-echo are also available.

2.2.5 Eddy current inspection

An induction coil carrying an alternating current induces a magnetic field that penetrates the surface of the part, creating eddy currents in the material; which in turn generate their own magnetic field, opposing the inducing field. Interruptions in material properties from the presence of cracks or damage cause a detectable impedance change in the inductor coil that can be measured as the coil is passed over the component surface [52].

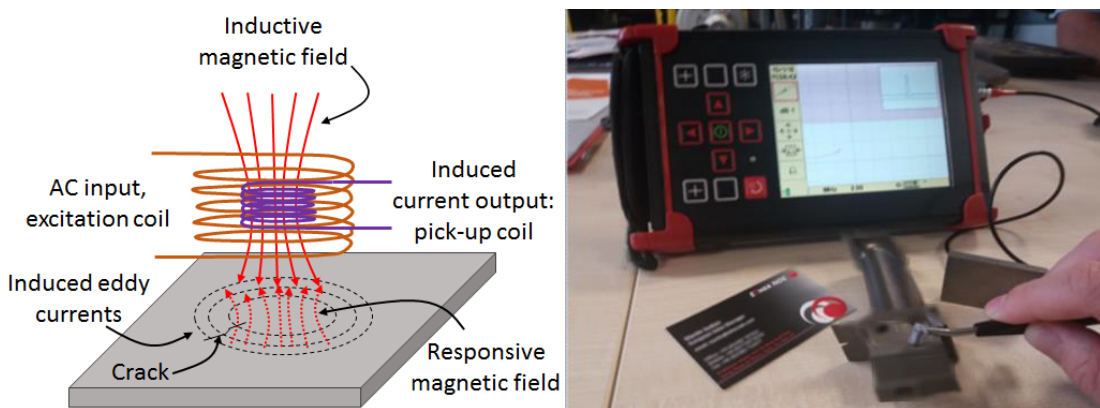


Figure 15 - illustration of eddy current inspection on a pipe (left), and photo of EC inspection on a component (right), courtesy of Ether NDE Ltd.

As the induced (primary) magnetic field is oscillating, so do the eddy currents and their respective (secondary) magnetic field, and the voltage induced in the receiver. For most materials, the phase and amplitude of the alternating current, and its voltage in the receiver coil is dependent on the test material's electric conductivity. The method is therefore highly responsive to interruptions of material electrical property, i.e. introduced via a crack in the material, but it can also be used to measure coating thickness on metallic surfaces.

2.2.6 Industrial Radiography

In radiographic inspection, a component may be inspected through highly-penetrating radiation, including x-rays or neutrons. The radiation is transmitted through the material, which is partly absorbed. Measurement of the transmitted signal is captured from the opposite side of the target part, giving the resulting image as essentially a 2D map of the attenuation coefficient; a measure of how much the volume of material between the source and detector weakens the incident signal. The method is used for detection of deep features such as cracks, inclusions and voids.

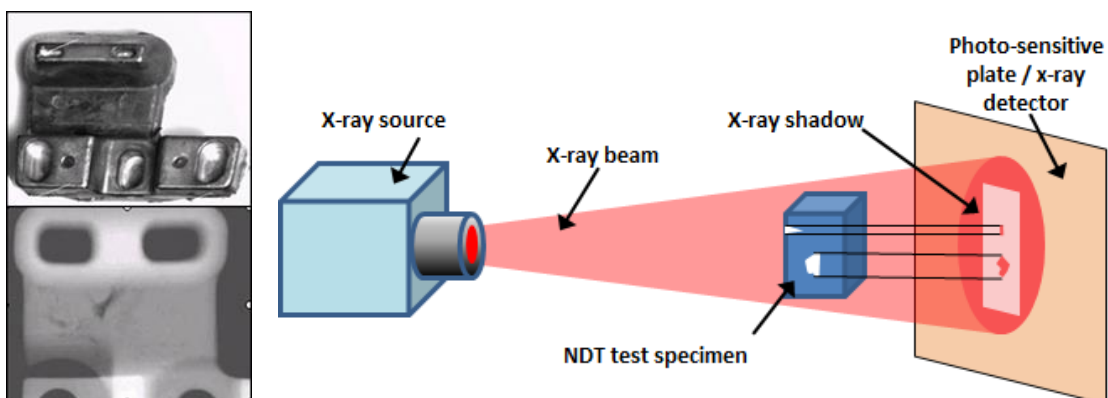


Figure 16 - An x-ray inspection, with illustration (left) [51], and diagram of operating principles (right). Visual and X-ray courtesy image of the NDT Education Resource Center, Iowa State University, USA.

If the method is applied in rotation around the component, or the component is rotated in the inspection field of view, the attenuation coefficient of individual pixels in 3D space (voxels) can be computed with the full scan data, known as Computed Tomography (CT, or X-CT), capable of producing cross-sectional images of the material structure, through any direction desired.

Inspection via CT scans require more expensive equipment and can be more time-consuming and costly for the amount of energy required to generate the scans, including the additional costs of providing the lab environment with radiation shielding the method requires, and so are more often used in research context, special cases, or in medical diagnosis scans.

2.2.7 Fluorescence Spectroscopy

A relatively recent diagnostic method that does not feature as one of the “big five” but is worthwhile discussion is the use of the fluorescence of a sample material; its propensity to absorb incident radiation - typically ultra-violet - and re-emit it at longer wavelengths, as the electrons excited by the incident laser relax back into lower energy states, emitting light at wavelengths characteristic of their orbital drops. The frequencies and intensity of re-emitted light provides signatures from the chemical composition on the surface via the presence and abundance of detectable permitted electron energy bands, and may be used to spectrographically analyse material composition. Degradation mechanisms that exhibit a change in surface material chemistry can be monitored in this way.

2.2.8 Thermography

Thermography involves the observation of a target specimen with an infrared camera or 'radiometer', and recording an image of radiant intensity. As thermography is the method that was selected for application in this thesis, more information is provided.

The radiometer captures images of radiant heat incident upon the lens of the detector, also known as a 'heat map' or a 'thermogram', described by British Standards as a "thermal map or image of a target where the grey tones or colour hues represent the distribution of infrared thermal radiant energy over the surface of the target" [53]. A thermogram of a test specimen is captured in order to detect differences in temperature radiating from the sample, or transmitted through it from the other side. These changes relate to a temperature change, or a change in the material's thermo-physical properties; emissivity, transmissivity, reflectivity, conductivity / diffusivity, and heat capacity. The first three refer to the material's ability to absorb, transmit and reflect incident radiant heat (transmissivity being similar to the attenuation coefficient for radiographic inspection), while the other properties refer to the material's ability to conduct, dissipate and store heat.

The thermographic technique can be broadly laid out into two categories: the first is the passive mode of thermography, where the material's latent emission of heat, where the material's emissive, reflective / transmissive properties are investigated – or the real temperature of the system under a given activity; the second is the active mode, where the material's reaction with applied heat is studied, with numerous sub-categories of implementations available. When accurate measurement is required, one of the atmospheric "transmission

windows” should be used, of which many are identified for various purposes by Yates & Taylor, USNRL, 1960 [54], but the most common banding scheme is given as:

- | | | |
|----|----------------------------|---------------------|
| 1) | Short-wave infrared (SWIR) | 1.4-3 μm |
| 2) | Mid-wave infrared (MWIR) | 3-8 μm |
| 3) | Long-wave infrared (LWIR) | 8-14 μm |

The selection of IR band influences which sensor and filter may be used; or the available hardware determines the band to be used, based on the material sensitivity of its detector material.

i Passive Thermography

In passive thermography the naturally apparent temperature emission or transmission of a target where it emits infrared radiation from its surface according to its surface temperature and properties, or permits the transmission of heat radiation through it, according to its thermal properties, in its environment or during operation of the system its part of, providing the heat captured by an infrared camera to display a temperature contrast image or video signal. Changes in radiant heat intensity can indicate either emissivity, through transmission or direct temperature changes. Emissivity is a measure of a material’s ability absorb and re-emit incident radiation on its surface, given as a ratio of the material’s surface radiance to that of a blackbody at the same temperature. A blackbody is a perfect body material with the characteristic of perfectly absorbing all radiation incident upon it, independently of wavelength, which is referred to as having an emissivity ratio equal to 1, or ‘100%’. In turn, the material emits this heat at a

radiant power that follows the wavelength-dependent emission profile described by Planck's law, given in (2-1), which describes the exit radiance (or "emittance") of a blackbody of a given temperature, as a function of wavelength [55]:

$$I(\lambda, T) = \frac{2 h c_0^2 \lambda^{-5}}{\exp\left(\frac{h c_0}{\lambda K_B T}\right) - 1} \quad (2-1)$$

where I is radiated intensity, h is Planck's constant $\sim 6.63 \times 10^{-34}$ J s, c_0 is the speed of light in a vacuum (2.998×10^8 m/s), λ is wavelength (m), and K_B Boltzmann's constant ($\sim 1.38 \times 10^{-23}$ J / Kelvin; K), and T is the temperature of the ideal blackbody being observed (in °K). Plotting the associated Blackbody curves for various temperatures over a broad bandwidth yields the following spectral emission profiles:

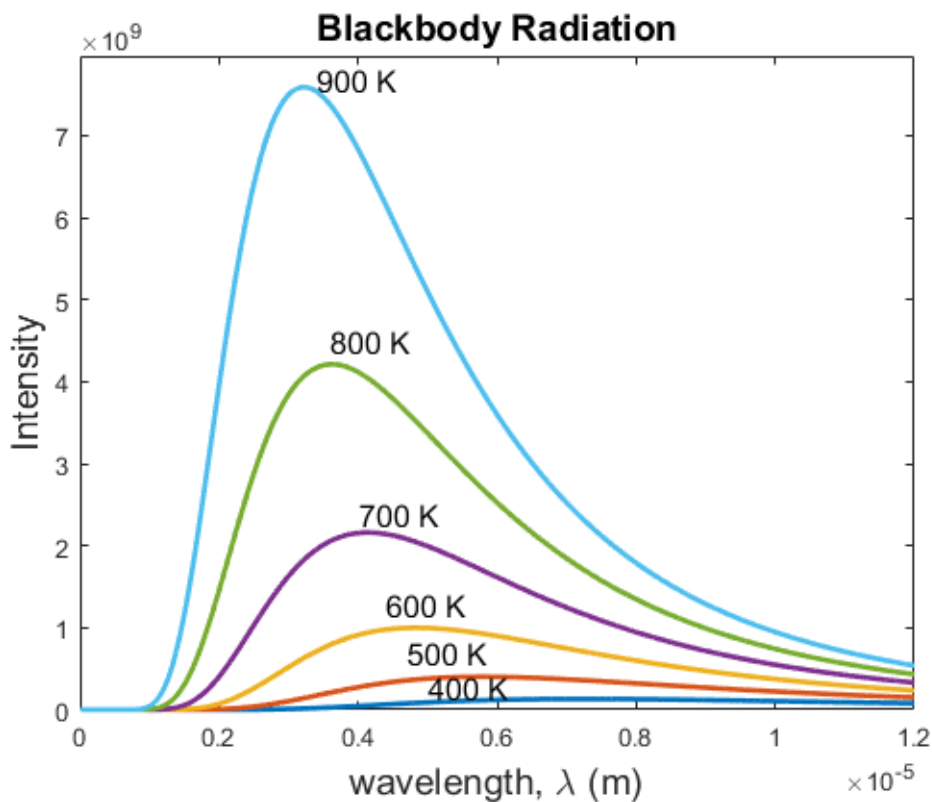


Figure 17 – spectral emission of an ideal Blackbody object at various temperatures, plotted using (2-1) in Matlab [56]

In practice, no material is a perfect blackbody, and emissivity values of up to 0.95 are accessible. A greybody refers to a material that follows a modulated Planck curve, which does not absorb all incident radiation, but its difference from the ideal emittance varies uniformly with wavelength. Finally, a non-greybody varies emissivity with wavelength. Meanwhile, transmissivity refers to the material's ability to transmit incident radiation, and reflectivity the measure of a surface to reflect incident radiation. Kirchoff's first law of radiation states the emissivity of a sample to be equal to its absorbance. Applying the law of conservation of energy, the sum of the three components is always equal to the received radiation, yielding the following relation:

$$\alpha \text{ (absorptivity)} + \rho \text{ (reflectivity)} + \tau \text{ (transmissivity)} = 1 \quad (2-2)$$

By maximising emissivity, or limiting reflectance and transmission, the measured radiance can be used to obtain a surface temperature measurement, which only needs to be multiplied with the emissivity (absorptivity) coefficient to yield the measured temperature. An emissivity value of 80-95% is regarded as good, provided any other source of radiant heat incident on the measured surface is sufficiently cooler than the measured temperature; if the emissivity value is lower, or the background temperature is similar to or higher than the target, and the reflected contribution of background radiation contributes to the measured signal, affecting the accuracy of the measurement obtained; therefore careful preparation of the scene is required, and the emissivity of the surface needs to be established.

Equipment: radiometer

A radiometer is an equipment capable of recording incident radiation intensity. When an infrared filter is applied, this becomes an infrared radiometer, colloquially referred to as an “infrared camera” or “thermal camera”. Radiometers have an output reading of digital values of recorded voltage readings specific to the sensor material’s response to a level of radiant energy, which is finely different for each pixel on the detector. A temperature – digital level response curve is required to be captured in order to translate the radiometer’s output digital levels back into a measure of temperature readings, by establishing each pixel’s unique response to a changing (uniform) temperature field, using a calibrated temperature source whose spectral profile radiates as close to a perfect blackbody as possible.

ii Active Thermography

Applying of the same principles of data capture while adding application of heat energy to the inspected component, the method becomes one of “active thermography”; the resulting temperature contrast reflecting the material’s thermo-physical properties (heat capacity, thermal conductivity, diffusivity) and its density. Control of the heat application allows for a temperature contrast to be generated over the profile of damages that may not have been exhibited under passive inspection. The method of application of heat, and direction of its propagation in the material all need to reflect the type, size and exhibited change in material property of the damage / defect being sought all need to be factored into the inspection and how it is applied, resulting in numerous methods of active thermography. Several active techniques exist, including step heating, involving

uniformly raising the temperature of the bulk material before cooling upon inspection; pulse or flash heating, where a sharp wave of heat is applied to the surface and inspection monitors either surface as the pulse flows into the material; lock-in, or 'phase' thermography, where the heat is modulated, typically varied so the passage of heat through the material to the defect matches the application of heat pulses, and so on.

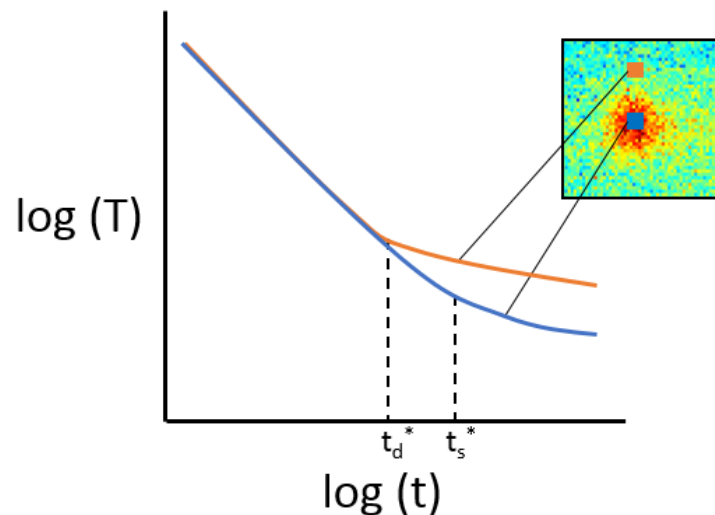


Figure 18 – Typical time-temperature $T(t)$ plot of a thermographic inspection of component and defect area (inset), plotted in logarithmic domain, yielding the time of change of log-linear cooling (t^*) of a damage / feature (t_d^*) and sound (t_s^*) region.

Pulsed thermography typically involves a blast of heat applied to the surface with either hot air, or more commonly a laser or optical flash. The rapid application of heat on the surface then dissipates into the material, cooling the temperature of the surface, while the radiometer records the temperature of the surface, and its respective temperature-time cooling profile. In homogeneous materials, the surface temperature decay is proportional to the square of the depth that the heat pulse has travelled since the flash heat application on the surface. For this reason, a sharp “Dirac” pulse is ideal, allowing the “thermal wave” diffusing into the material to exhibit a high contrast on the surface as it moves through the

material, which forms a log-linear temperature-time decay profile, with a gradient of approx. $0.5(t)$. An interruption of the material homogeneity, such as from structure, or sub-surface damage, or defects, this will confer an interruption of the flow of the thermal wave, similar to how a damage or defect obstructs the flow of sound in an ultrasonic inspection. As the heat flows around the feature, the temperature decay on the surface exhibits this change in cooling characteristics in contrast to the surrounding surface, where the thermal pulse beneath continues to diffuse into the material; all which is illustrated in Figure 18.

One significant development in pulsed thermography has been the Thermographic Signal Reconstruction process (Shepard, 2003, 2004) [57] [58]; involving the fitting of polynomials to the pixel temperature decay curves, yielding a reduction of temporal noise, smoothing the temperature decay profile, and permitting the transform into first and second order differential decay curves, representing the rate of surface cooling, and rate of the rate of cooling acceleration; the inflection of the 1st differential, or peak of the 2nd gives the time at which the heat pulse encounters a change in thermal material properties. These are useful for improved sensitivity to features with low aspect ratios, even when nothing is known about the sample prior to inspection [59] which confers advantages in reducing trained user input [60].

Some of the challenges in using active thermography include the uncertainty in the length of the heating flash, if not truncated [61], and the requirement for the emissivity of the surface of the material to be known [62], [63], or improved, such as with application of a surface treatment, such as a soot or carbon layer [64].













Active thermography: alternative heating application

In addition to optical and laser excitation sources, other methods of thermography exist. These include methods where the part can be heated via ultrasonic vibration so that close features (such as crack walls) generate heating via friction, exhibiting a detectable temperature signal, also referred to as “vibrothermography” or “thermosonics”. The application of highly oscillating magnetic currents induce eddy currents which generate heat where damage or defects interrupt their flow known as “eddy current” or “induction thermography”. Meanwhile, through the passage of an excitation laser over the surface of a part, the interruption of the heat flow laterally across the surface can exhibit an interrupted temperature profile around surface-breaking features, such as cracks. This is known as “laser-scanning thermography”.

2.3 NDT comparison chart

In order to give a general overview of these strengths and weaknesses and to make a direct comparison between different NDT methods and the damage features they encompass, a comparison chart of the different NDT techniques is shown below. This was made from a reproduced version of an NDT selection chart made available by a well-known Quality Assurance / Quality Control supervisor with 30 years of experience, who has produced numerous guides on NDT methods including a comparison chart (Pierre Dostie) [65]. This chart was expanded with additional thermography NDT methods, and two additional damage examples added to the list to incorporate changes in material properties; as the scope of this thesis is not just the visible detection of damage, but measurement of material properties with which to facilitate ageing assessment. The chart scores the suitability (i.e. 1 – most suitable, 4 – least suitable) of different techniques to a variety of damage and defect examples, including the geometry of said damage. In each damage type, method suitability could be expected to change with different materials as their conductivity / speed of sound / coefficient of attenuation (of radiation) will change. This level of understanding of the suitability of the different techniques is critical in selecting appropriate methods for any given problem, and its geometry.

Table 1 - Comparison of NDT techniques, highlighting their suitability strengths from 1 (strong) to 4 (weak) against a range of inspection tasks, adapted and expanded from an NDT trainer's online materials, [65]. Rankings are based on the ability of the technique to develop a response signal, and does not inherently imply a measurement is useful; many of the classifications are based on the author's assumptions with limited experience with all the methods.

Flaw type	Example	Illustration	Visual	Magnetic particle	Dye penetrant	Eddy current	Ultrasound (c-scan & array)	X-ray (2D scan)	Thermography (pulsed)	Thermography (laser spot)*	Vibro thermography*	Eddy current thermography*
Surface breaking linear	Surface crack		3	1	1	1	2	3	4	1	1	1
Surface breaking volume	Corrosion pit		1	1	1	1	1	1	3	2	2	1
Near surface linear, normal orientation	Near surface crack		4	2	4	1	2	3	4	4	3	2
Near surface linear, parallel orientation	Delamination		4	4	4	4	1	4	1	2	4	4
Near surface volume	Void or Delamination		4	2	4	1	1	1	1	2	4	1
Subsurface, linear, normal orientation	Subsurface crack		4	4	4	4	1	3	4	4	4	4
Subsurface, linear, parallel orientation	Sub-surface delamination i.e. in composites)		4	4	4	4	1	3	2	4	4	4
Subsurface volume	Void, delamination or subsurface structure		4	4	4	4	1	1	1	2	4	4
Thickness measurement of thin material	Wall / coat thickness		4	4	4	1	1	1	1	1	4	4
Thickness measurements thick material	Wall / bulk thickness		4	4	4	4	1	1	2	2	4	4
Surface material property change	Surface / coating material properties		3	4	4	1	2	3	2	1	4	4
Bulk material property change	Bulk material properties		4	4	4	3	3	1	1	1	4	4

2.4 TBCs & thermal properties

Optical scattering: The optical scattering of radiant heat and light by TBCs is a complex phenomena, which depends on a range of variables: the pore sizes, its size distribution, the gaps between the pores, their shape, and the refractive index of the ceramic between the pores; which has been modelled by (Li & Clarke, 2008) [66]. Li & Clarke described light scattering results from different phenomena: reflection from either side of a ceramic-air interface; refraction from a change in refractive index between air and ceramic; diffraction from structure; transmission through the semi-transparent material, etc. Instead of mere description, an illustration of these influencing factors is provided in Figure 19, displaying a photon's various options it undergoes when it has an encounter with a TBC and its microstructure (in this case, an EB-PVD TBC with vertical columnar grains, and their "feathery" walled surface, as mentioned previously. Those interactions include:

- 1) Diffuse reflection of the ceramic-air interface, such as at the columnar walls, or the angular tips of the ceramic columns
- 2) Reflection from the air-ceramic interface at pores is the ceramic
- 3) Diffraction of radiant light inside the pores
- 4) Refraction due to the refractive index of the ceramic
- 5) Transmission of incident light through the semi-transparent material

- 6) Absorption on the surface of the ceramic, where heat then propagates as phonons through the ceramic via its low thermal conductivity; and is re-emitted from the surface

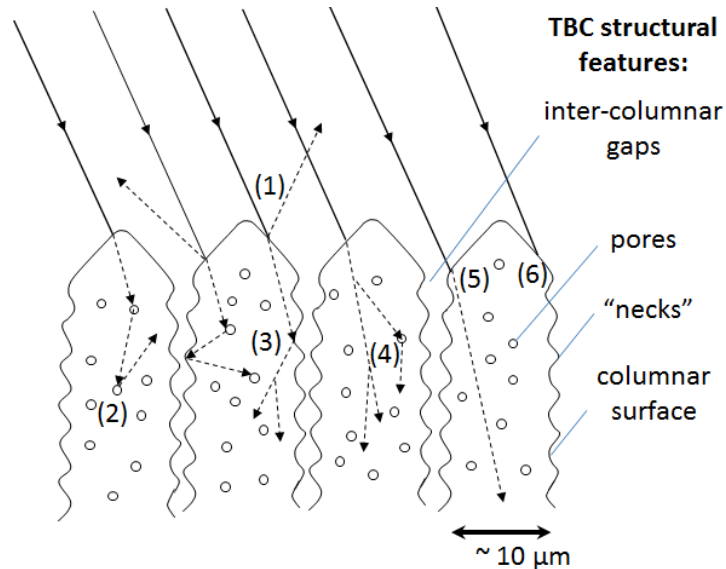


Figure 19 – propagation of incident light on a typical semi-transparent EB-PVD TBC and its structure, illustration by the author, inspired from Li and Clarke (2008) [66]

The combined effects of these can be observed in that the transparent zirconia used in EB-PVD TBCs appears white in ambient light.

Effect of ceramic grain size The grain size of polycrystalline YSZ has been found to have an effect on thermal conductivity of TBCs, valued at $\sim \pm 4\%$ (taken at room temperature) (Limarga & Clarke., 2011) [67], and is not strongly expressed at service temperatures. This effect would be useful for TBC lifing if grain size were found to change over thermal cycling; though is worth noting when comparing measurements taken at room temperature with studies of conductivity taken at high temperature to expect a temperature-dependent offset.

2.5 TBC ageing: causal factors in changes of thermal properties in TBCs

A TBC is subject to high temperature over time, various changes gradually take place in the TBC; including sintering, rumpling, buckling, creep, etc. In sintering, the air gaps and pores in the ceramic structure shift and coalesce; the fine cracks that make up the feather-tip structure “heals” as the interfaces blend together; eventually even the columns form bonds, and grains gather together, clumping and forming a “mud crack” pattern over the TBC surface. Meanwhile, the Bond Coat (BC) / Thermally Grown Oxide (TGO) interface can rumple under thermal cycling, pushing and pulling the column “hairs” of the EB-PVD’s ceramic rug to clump together and space out in different areas, thus promoting the “mud cracks” [68]. The TGO grows into voids left by the shifting microstructure under thermo-mechanical loads, exhibiting stress when the coating cools and relaxes; promoting cracks [69].

As the coating ages over thousands of cycles, cracks formed between the TGO and the bond coat eventually grow and merge, until a sufficiently large area of TBC is no longer bonded, where the stresses may cause the ceramic to “buckle”, leading to eventual spallation. An overall increase of thermal conductivity / diffusivity from TBCs has been observed in numerous publications, and ascribed to various causal factors, including sintering, evolution of porosity including their size, shape and orientation; changes in the shape / thickness / chemistry of the BC-TGO interface; growth of the TGO, to annealing of the ceramic material itself, changing its inherent thermal properties. The different mechanisms of TBC ageing affect the material and its resulting properties in a variety of ways.

2.5.1 Increase in thermal conductivity & diffusivity: Sintering, changes in microstructure surface features

When subjected to the range of high temperatures experienced by high pressure (HP) components in service, the TBC coatings can undergo a change in their microstructure, such as densification, or 'sintering', where atoms diffuse, causing particles to fuse together. This is regarded as one of the main causes for increase in the thermal conductivity of TBCs under prolonged exposure to high temperature, as cracks and microstructure are broken up and neighbouring regions become joined, physical obstructions in the material to heat transport are reduced under both isothermal or cyclic loads [70]. In cycling conditions, the top coat undergoes sintering, where cracks in the TBC 'heal', redistributing the pores and increasing the contact between the columns, increasing its thermal conductivity [71]; bringing higher temperatures with increased TGO growth.

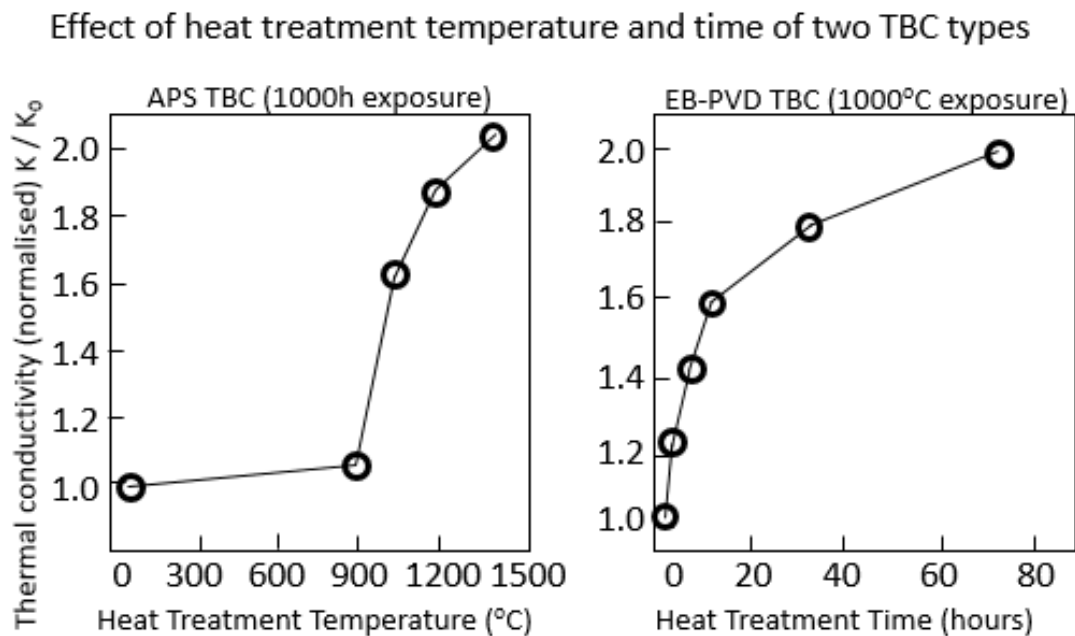


Figure 20 – The thermal conductivity change induced by heat treatment of PS TBCs at different temperatures (left), and over increasing treatment times at 1000°C. (right), adapted from (Dinwiddie et al., 1996) [72], courtesy of ASME.

It has been reported in literature that heat treatment of EB-PVD TBCs exhibit a large initial change in thermal conductivity within the first ~50 hours of heat treatment above 1000°C, as shown in Figure 20. While other researchers in the literature have found similar increase in conductivity, they noted that 1150°C is considered a low temperature to observe significant sintering of TBC, however, they also noted that the increase in thermal diffusivity was similar to results they found with sapphire substrates, and with free-standing TBCs, indicating that the change in diffusivity is related to sintering of the TBC, and would not simply be dominated by interface influence [73]. An example of the effects of this on the intra-columnar gaps in the structure of EB-PVDs, is the smoothing of the initially rough 'feathery' structure as the ceramic condenses, reducing gaps and porosity, increasing thermal conductivity of the ceramic from the structural change, which can be seen quite dramatically in Figure 21.

Changes to porosity changes the optical properties of the TBC; changes to the microstructure affects the structural conductivity of the system; while the crystal grains of the ceramic itself also undergo change, albeit more slowly than other processes. Surface diffusion of the TBC microstructure is shown in Figure 21 [74] which, taking place at temperatures as low as 900 °C, dominate early transformations at high temperature, as other studies have also found [73].

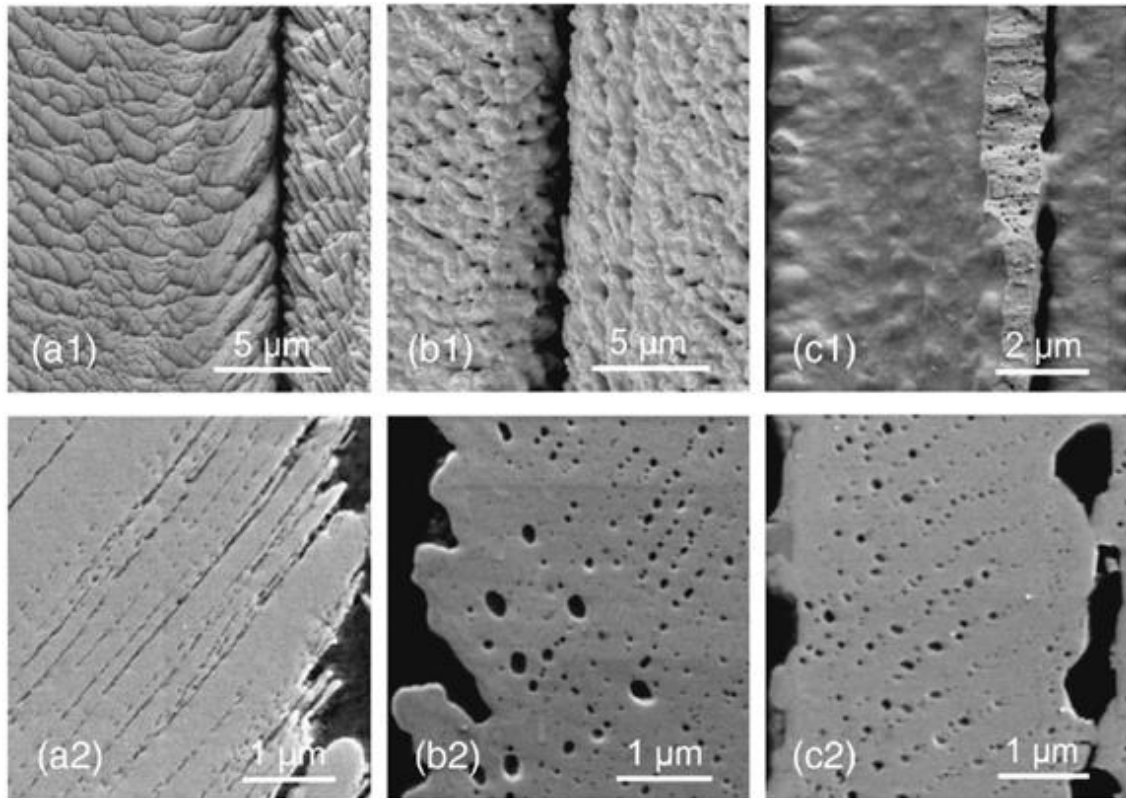


Figure 21 – changes in an EB-PVD's surface morphology & internal porosity. Shown are the surface structure (#1), cross-section of internal structure (#2), showing the deposited condition (left; a), after dwell at 1100°C in air for 200 hours (mid, b); and 900 hours (right, c). Reproduced from (Rätzer-Scheibe & Schulz, 2007), courtesy of Elsevier [74]

2.5.2 Increase in thermal conductivity: changes in porosity

In EB-PVDs, the thermal conductivity of heat flowing through the columns can be described as the sum of the products of the area fraction occupied by the TBC columns and the conductivity of the ceramic, summed with the product of the remaining area (inter-columnar gaps) multiplied by the conductivity of the gaps, which – being air – is considered negligible (at ambient pressures). Effectively, including the low conductivity of the ceramic, the gaps between the columns contribute to lowering the conductivity of the TBC, by reducing the area of material the heat energy can be conducted through. However, the columnar structure also leads in reduction of thermal conductivity, from the structure of the material split into columns, to the structure of the columns themselves; which in

turn is influenced by the volume of porosity, pore shape, and their orientation with respect to the heat flow. In a study measuring the thermal conductivity of EB-PVD TBCs subjected to high heat flux (measurements taken at high temperature, simulated service temperatures), a similar increase at isothermal temperatures, and increase –with fluctuations- under cyclic loading was observed [70] which is shown in Figure 22, showing the differences not just in the TBC materials, but also the behaviour induced from ageing conditions.

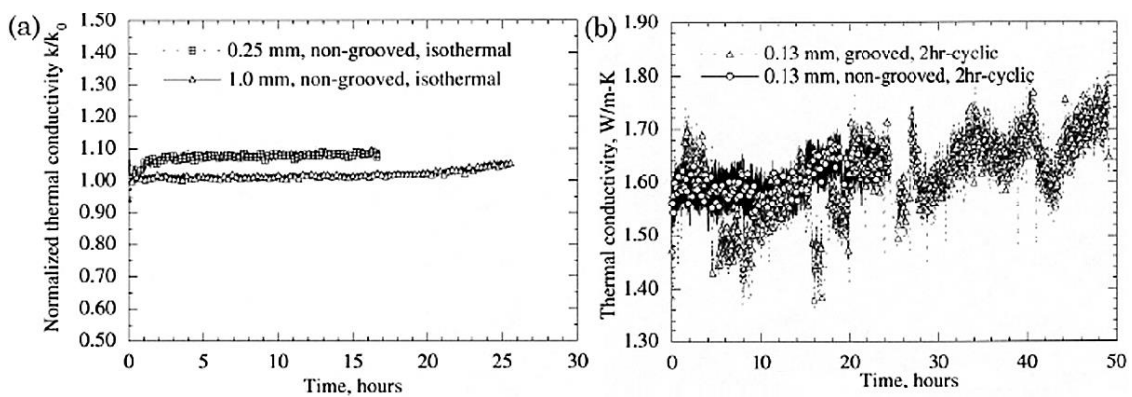


Figure 22 - changes to thermal conductivity of EB-PVD TBCs, measured under steady-state heat flux at const. temperature (left), or cyclic testing (right) (Zhu et al., 2001) [70], courtesy of Elsevier.

As previously discussed, when the feathery structure of EB-PVDs is exposed to high temperature, ‘crack-like’ gaps in the columnar structure are broken up, and pores in the ceramic coalesce and become round [75]. In one study, this has been shown to occur at temperatures as low as 900°C and increasingly so at higher temperatures, increasing further over exposure time [76]. The shape of the pores becoming spherical effectively break up cracks and increase the thermal conductivity of the columns via gap reduction, increasing the area of the column that heat can flow through the structure, along them. In the study, using a typical oxidation temperature of 1100°C, break-up of the micro-cracks is rapidly observed in the feather-like structure; while the pores become spherical. This was

observed after even 1h of exposure, which would explain the large early increase in conductivity observed in many different studies [72] [73] [70]. The authors concluded that their results pointed to atomic diffusion occurring between 900-1000°C was surface diffusion, while between 1100°C-1400°C, more mechanisms were likely to take place, further complicating analysis; from sintering beginning at 900°C+, surface diffusion from 900-1000°C, and the specification of pores after the first hour of exposure at 1100°C. TBCs exposed at over 1100 °C undergo numerous changes simultaneously. An example of these changes over different exposures at typical service temperature is shown in Figure 23.

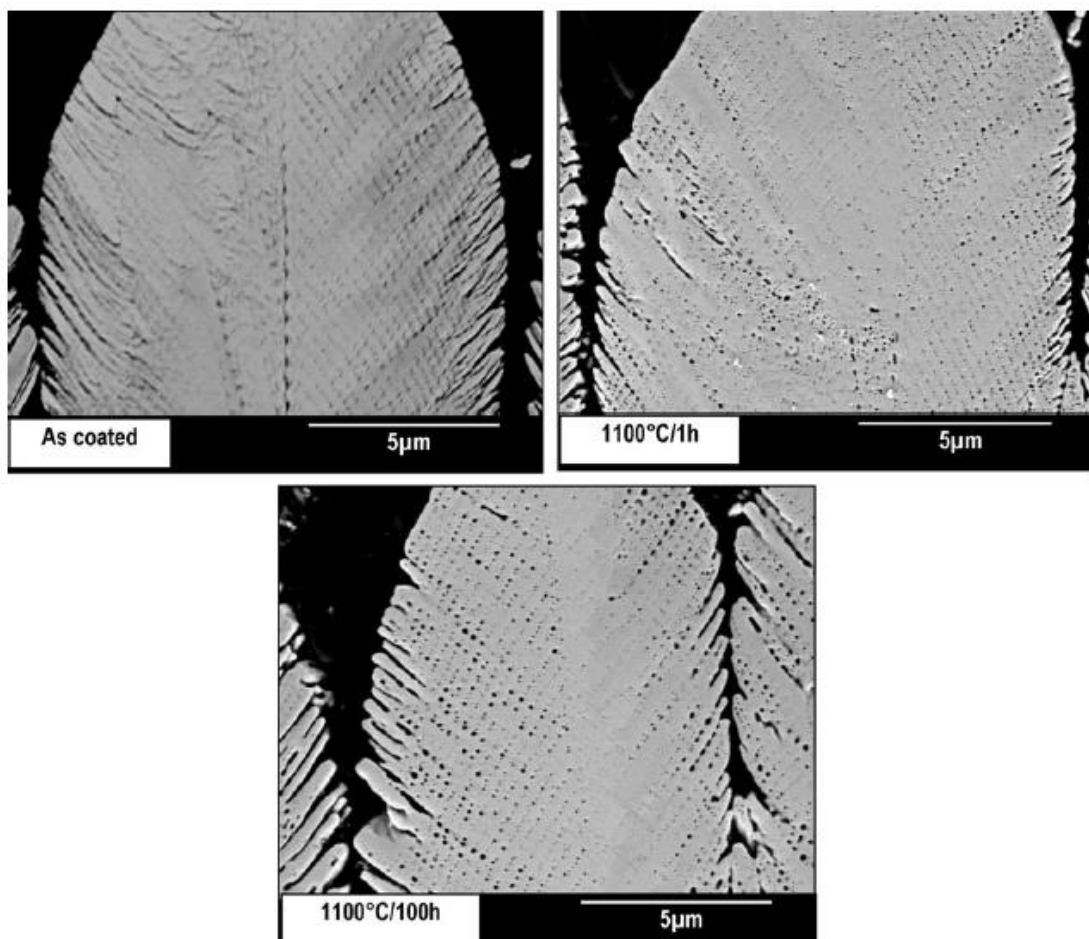


Figure 23 – SEM of EB-PVDs undergoing high temperature oxidation ageing, showing the break-up of the feathery structure giving way to spherical pores from as soon as 1 hour, and developing further by 100 hour (bottom) Reproduced from Renteria & Saruhan (2006) [76], courtesy of Elsevier.

In one study by Kakuda et. al., a large early increase in thermal conductivity was observed, which they noted was induced by exposure to 1150°C, a temperature below that at which they expected to observe sintering, which they ruled out as the dominant cause, thus attributing their observed increase to a combination of microstructural changes to the cracks and pores and the feathery structure, and a decrease in point defects in the ceramic, which they inferred from narrowing of Raman spectral peaks [73].

2.5.3 Changes in the thermally grown oxide interface associated with TGO thickening and possible interface separations.

In addition to the effects of sintering and atomic diffusion are included the effects of thermally grown oxide growth, ensuing rumpling, micro-cracks and wholesale delaminations occurring between TGO above the bondcoat, and the ceramic.

Conversely while cracks are breaking on the feathery-tips of the TBC, increasing the thermal conductivity; other cracks and delaminations are forming at the BC-TGO interface, lowering the thermal conductivity / diffusivity values, and the formation of such cracks have been credited to the cause of abrupt dips in thermal conductivity in thermal cycling tests [70], over both short term change (Figure 22) and longer durations (Figure 24), throughout the tests.

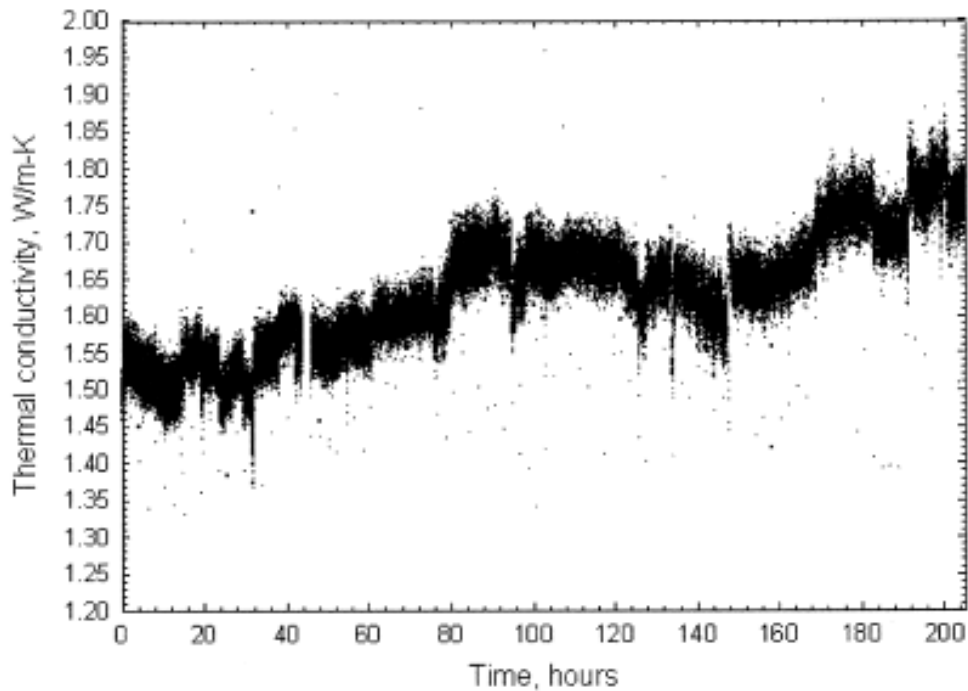


Figure 24 – cyclic behaviour of thermal conductivity of EB-PVD TBC subjected to cyclic testing (2h), reproduced from (Zhu et al., 2000, 2001) [70] [77], courtesy of Elsevier.

In their study Zhu et al., found all cyclic test conditions produced an overall increase in conductivity, interrupted by intermittent fluctuations, while fluctuations did not occur under the isothermal heat load, merely during thermal cycles. During the last few cycles, the coating significantly lowered conductivity, which was then credited to the formation and propagation of cracks.

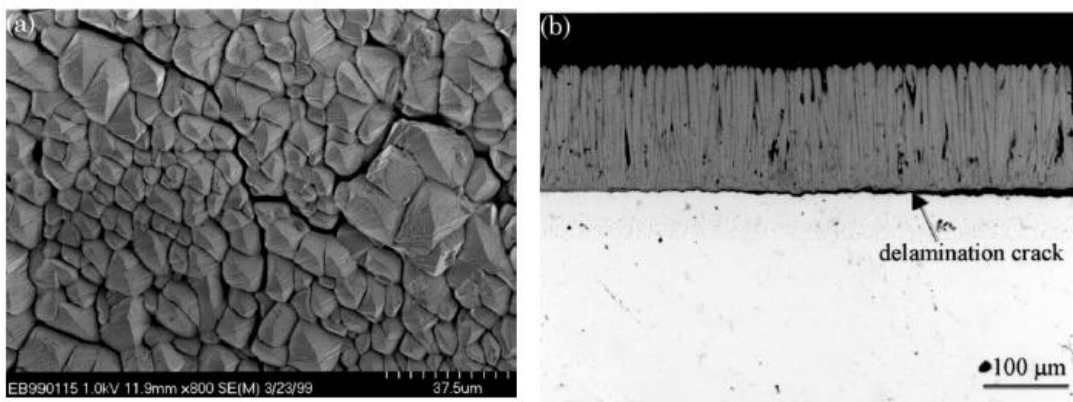


Figure 25 – EB-PVD TBC exposed to 40h of thermal cycling showing inter-columnar cracks (left), and propagation of a delamination crack at the interface (right); figure reproduced from (Zhu et al., 2001) [70], courtesy of Elsevier.

It was from such studies that the need for cyclic ageing in any experiment was noted, while different factors affecting increase / decrease of thermal properties would be occurring simultaneously, potentially complicating the problem of trying to track age, as these processes will occur at different rates and will weigh against each other.

Meanwhile, the formation and development of cracking occurs during the cool-down phase at the end of cycles due to differences in thermal expansion between coating and substrate, an example of this cracking / delamination is given in Figure 25. In addition to the change in measured thermal properties, passive mid-IR emission has been used to show severe delamination, as shown in Figure 26.

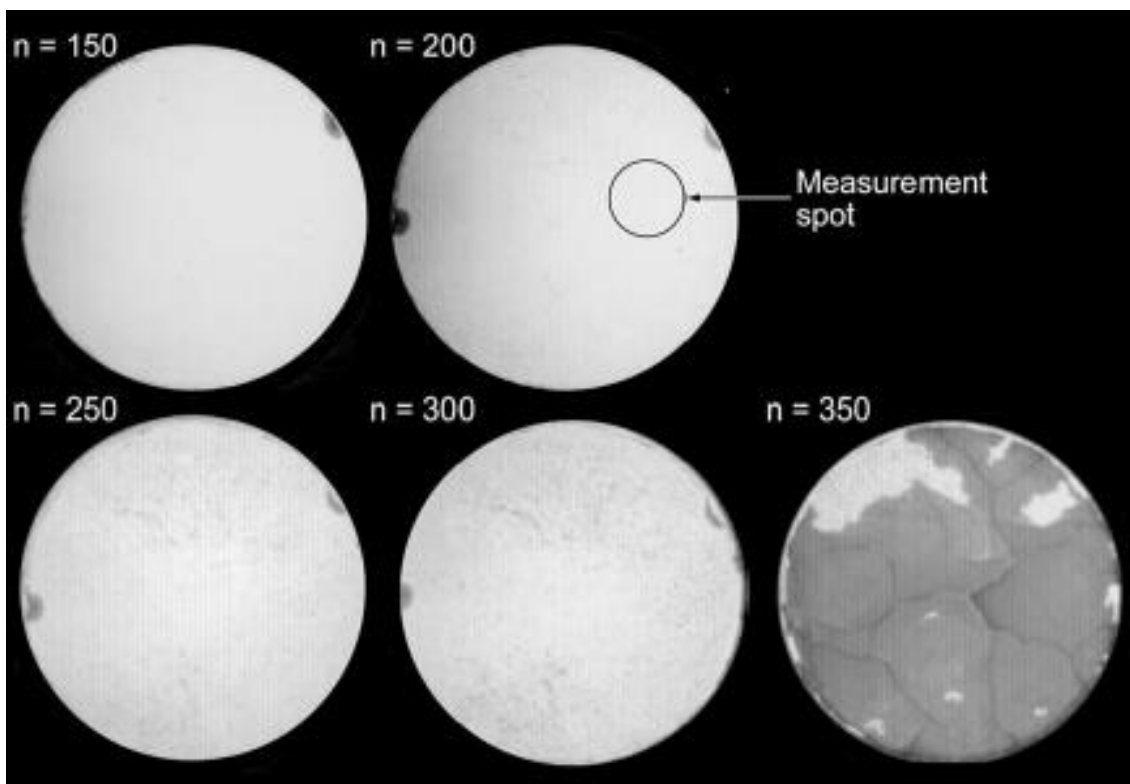


Figure 26 – Mid-IR (rear heated) emission images of a TBC showing smaller delaminations leading to coalescing of cracks and spallation. Reproduced from (Kakuda et al., 2009) [73], courtesy of Elsevier.

2.5.4 Other changes in coating properties

Ceramic density: Kakuda et. al. (2009) [73] observed an initial increase in density of approx. ~14% of initial value from initial state to the first thermal cycle, then smaller changes over the rest of the TBC life, shown in Figure 27.

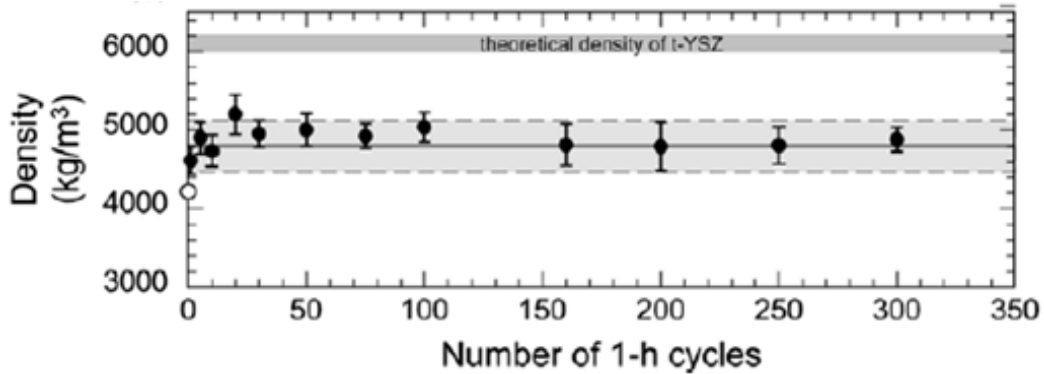


Figure 27 – changes to density with TBC thermal cycling, reproduced from (Kakuda et al., 2009) [73], courtesy of Elsevier.

Optical penetration depth The same researchers also observed other changes, including a rapid initial jump in optical penetration depth, also shown in shown in Figure 28, measured at 10.6 μm (the long wave infrared spectrum), which is highly relevant to the absorption of the initial heat flash pulse. These readings were replotted on the same time-scale as the results of this study to infer potential responsibility for the initial jump in uncoated condition, replot of optical penetration depth shown in Figure 28.

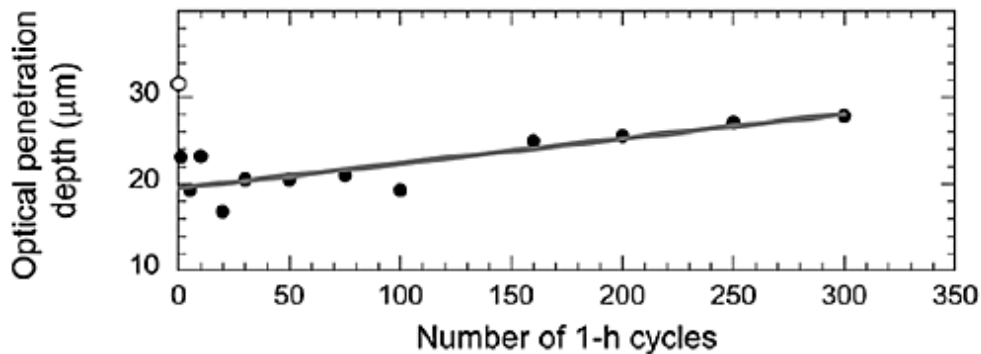


Figure 28 – optical penetration depth of a thermally cycled TBC, showing a large initial change, followed by a steady linear increase over cycle life. Reproduced from (Kakuda et al., 2009) [73], courtesy of Elsevier.

This sharp initial decline occurred at the same time the density increased, while the thermal conductivity, and diffusivity (Figure 29) exhibited a large increase.

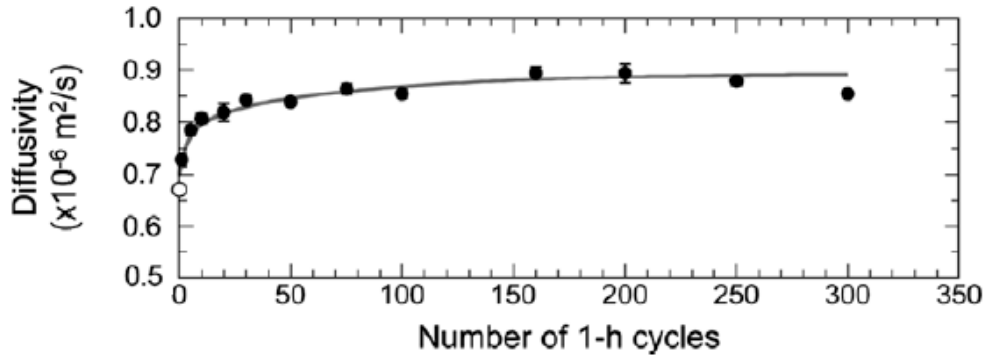


Figure 29 – thermal diffusivity change of a thermally cycled TBC, exhibiting a decaying exponential early increase, followed by a steady increase over cycle life, decreasing near end of life, reproduced from (Kakuda et al., 2009) [73], courtesy of Elsevier.

Optical scattering of TBCs can be affected by different features, such as the tips of the columns manifesting a diffuse reflector. Scattering also takes place via by the inter-columnar gaps, and the fine, “feathery” surface microstructure of the ceramic columns, and the pores between the intra-columnar gaps; their size, distribution, and shape – all of which are subject to change at high temperatures via surface diffusion. Meanwhile, reflectance of EB-PVDs has been shown to be strongly affected by differences in refractive index between the zirconia in the ceramic, and air in the gaps between the columns, and in the pores. This was applied to the detection of CMAS penetration [75] owing to its different refractive index [66]; so a change in gaps and porosity can be expected to yield a change in reflectance in some part of the spectrum (i.e. behaviour of a non-graybody). A change in increasing reflectance over longer wavelengths has been measured occurring with increasing thermal cycles [73]. These changes moved the reflectance of the TBC away from the initial condition, and toward the higher

reflectance of dense YSZ, as shown in Figure 19. Considering sintering is also known as “densification” of the TBC, this makes sense.

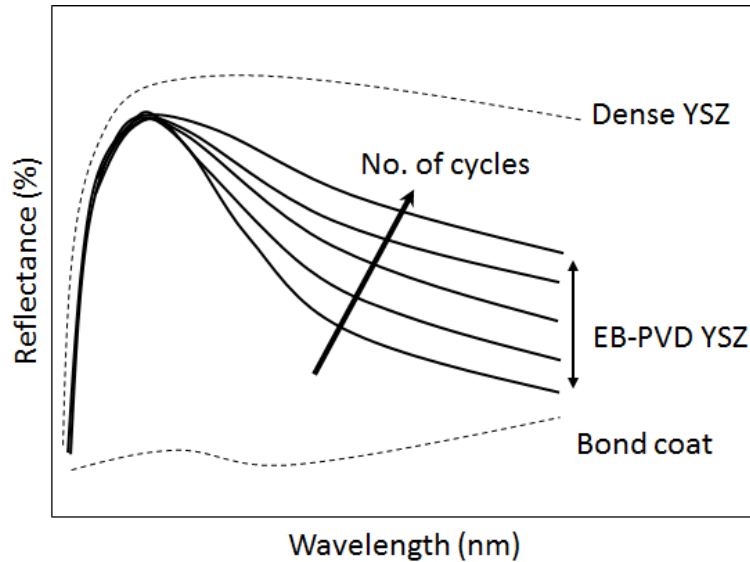


Figure 30 – changes in reflectance spectra of EB-PVD TBC when subjected to thermal cycling at 1150°C as studied by Kakuda et al., (2009) [73], courtesy of Elsevier.

As this increase in optical reflectance occurring at similar dimensions to pores in the microstructure (refer again to Figure 21, Figure 23), which indicates a strong connection with changes in porosity and optical reflectance. A decrease in diffuse scattering would entail from the smoothening of the fine-feathery structure of the EB-PVD TBCs, and removal of reflection barriers via the joining of intra-columnar gaps, coalescence of pores in the microstructure; this would be expected to decrease diffuse scattering of the TBC, which would be evidenced by an increase in optical reflectance, such as that shown in Figure 19, which would be expected to occur in the samples in this study over similar timescales.

2.6 Prediction and Assessment of TBC life

In the 1980s, as the promise of thermal barrier coatings to develop the durability, life and operating temperature of gas turbines and aero-engines was becoming realised, the complex challenges presented by the degradation and lifing was still

an under-developed subject. Early TBC lifing models were developed, assuming the stresses and strain in the TBC at temperature could be described by the thermal expansion mismatch strain – the differences between the thermal expansions of the ceramic coating with the bond coat. (Miller, 1984) [78]. This was modelled against sample weight gain during its life – the addition of weight from the growth of the TGO layer. One model assumes an accumulation of strain over oxidation life; the other approach assumed the failure strain decreases until it matches the strain in the TBC upon cooling (Miller, 1987) [79], the resulting models included power exponents to adjust for non-linear relationships between the oxidation parameter (weight gain, stress increase / failure stress decrease), and the exposure time (i.e. number of cycles). These provided preliminary models of TBC lifetimes, and highlighted the dominance of bond coat oxidation as the primary factor of TBC life limitation, but that other temperature dependent mechanisms, creep, sintering and variations in exposure conditions, needed further study to provide models useful to design engineers.

2.6.1 Turbine Engine Hot Section Technology (HOST) Project

In answer to the early life modelling and open questions, the US National Aeronautical and Space Administration (NASA) launched a major effort to understand the material behaviour and key degradation mechanisms of TBCs, and their effects on coating system life, and developing of models based on these findings. Called the Turbine Engine Hot Section Technology (HOST) project, it pioneered research into the physical mechanisms of TBC degradation, and its efforts built upon the initial lifing models, and collectively have become the primary research root of lifing of TBCs (Sokolowski, Hirschberg, 1990) [80]. The

modelling of TBC lifing was shared between the NASA Lewis Research Center, Pratt & Whitney Aircraft, Garrett Turbine Engine Co., and General Electric Co., who adopted different approaches:

Pratt & Whitney Aircraft researchers developed a life model based on fatigue model of life of the TBC. They also discovered that for plasma sprayed TBCs, plastic deformation of the ceramic was a key life-limitation, while EB-PVD TBCs were elastic with thermal cycling. Phase I: Plasma-sprayed TBCs: (DeMasi, Sheffler & Ortiz., 1989) [81]; Phase II: EB-PVD TBCs: (Meier, Nissley & Sheffler, 1992) [82]

Garrett Turbine Engine Co. researchers developed a model based on oxidation of the bond coat, and ceramic toughness loss, with damage from salt film corrosion included; (Strangman & Neumann., 1986) [83], (Strangman, Neumann & Liu., 1987) [84]

General Electric Co. researchers life prediction method adopted time-dependent finite element modelling non-linear stress and strains in the TBC, correlating with stress & strain life. (Hillery, Pilsner, McKnight, et al., 1988) [85].

In each of these, the life of a TBC is estimated using a combination of analytical or finite element models with the model coefficients derived from representative sample datasets, and extrapolated to predict the lives of other furnace-run datasets to confirm their ability with varying aging conditions. The models require reproducible coatings to reflect the training set, although the power of the methods is that they only require a few samples to facilitate a life prediction. At the end of the project, the need for more understanding in sintering, creep, plastic deformation, and the oxidation mechanism itself were emphasised.

2.6.2 Statistical life modelling

One of the most popular methods for life and reliability estimation in industry is applying a statistical treatment to sample lifetimes, such as the Weibull distribution (Weibull, 1951) [86]. Life prediction is conducted by fitting a distribution of sample life times, yielding a probability of failure against hours of exposure, or TBC lifetime (h) against different temperatures or different stress or environmental conditions, where a given population and its respective sample failure rate fits a Weibull distribution of different parameters, an illustration of Weibull life modelling is shown in Figure 31.

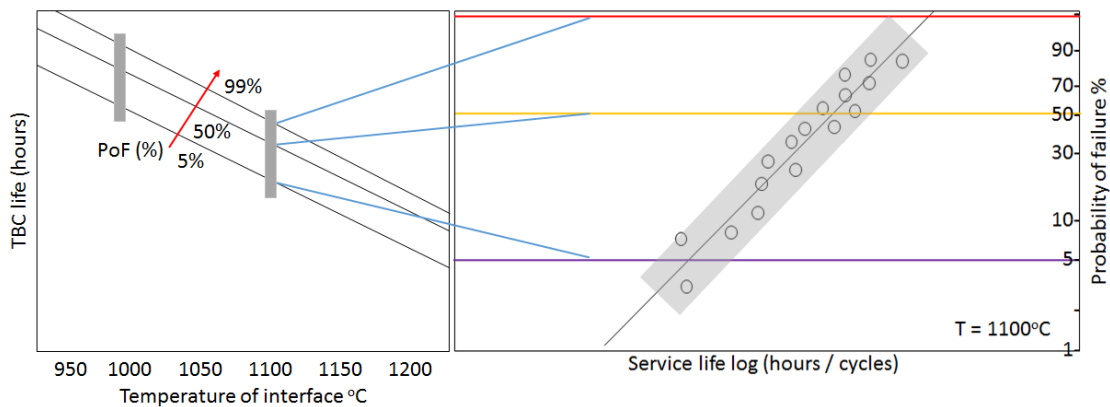


Figure 31 – expected TBC life via Weibull distribution over test temperatures, showing predicted life against temperature (left) containing populations of probability of failure of each sample set (right) in the sample life data, inspired by TBC life estimations in literature [87] [88].

2.6.3 Later developments in TBC lifing

The model from (DeMasi, Sheffler & Ortiz., 1989) [81] calculated mechanical strain in the TGO layer, applying damage power law models to TBC life data sets for cycled specimens. The model coefficients could be empirically derived from furnace cycled sample sets, then extended to TBC specimens subjected to different conditions, with similar results. The model was found to apply broadly to both APS and EB-PVD TBCs, which the authors remarked implied the same

damage mechanism of a maximum TGO tensile stress / strain was controlling TBC life, which meant that the measurement of sample strain and TGO thickness could assist in life modelling. With a stress model dependent on oxide thickness and furnace cycling, accurate measurement or prediction of the oxide layer is important. The researchers then modified an oxidation model using measurement of TGO thickness via Scanning Electron Micrographs (SEM) and non-linear regression analysis, which enabled them to fit an oxidation model (Meier, Nissley, Sheffler 1992), eq. 11, p52 [82]:

$$\delta = \left\{ \exp \left[Q \left(\frac{1}{T_0} - \frac{1}{T} \right) t \right] \right\}^n \quad (2-3)$$

where δ refers to TGO layer thickness (μm), Q = apparent activation energy / universal gas constant, R (given in their report as 27777.4); T_0 the universal temperature constant, 2423.7K; and empirically derived value of n was given as 0.332; T is the bond coat temperature, and t is time of exposure, in seconds. This relation would describe the fastest growth in its early stage, representing a faster leeching of material from the bondcoat while the oxide is thin and the BC is not yet depleted, it can be predicted from this that many small cracks would be likely to form early in the life of the TBC, though these will not be initially significant to the life of the TBC.

The majority of the work as part of HOST for life estimation was developed to estimate life prior to deployment in service, to enable designers and manufacturers to project a component life for a given manufactured TBC under different conditions, so that it can be shown how long the coating, as-manufactured, would endure a spread of simulated conditions.

Other research has built upon the life modelling in the HOST program, developing life models that reflect both the oxidation age and thermos-mechanical stress cyclic ageing of the TBC [89] applying the models in field tests [90].

While the models and new knowledge gained from the NASA HOST project were the seminal series of work for TBC lifing, their models and methods were intended largely to be applied for the purpose of design use, for optimising design and manufacture for prolonging the life of TBCs and for operating at higher temperatures while taking into account various sources of degradation. The software tools making use of these findings and statistical treatments of furnace cycled populations are useful for designers in the industry to develop new refinements, and for quality control purposes to prove the expected life of a given TBC batch. However, these methods have limited application in service context, for the in-service estimation of remaining life. It is with this angle that the main thrust of the literature review is continued.

2.6.4 Other approaches of TBC life (mechanistic, NDT & data driven)

These models have been useful in the progressive development of TBCs, and in providing a model of their expected life, useful for the scheduling of maintenance, however in order to improve inspection and maintenance of TBCs further, the assessment of remaining useful life in-situ needs to be responsive to the coating's real condition. That estimation can include information about the conditions the coating has been subjected to, such as estimations of conditions based on mission profile, use of engine use data including number of cycles performed, thermal cycling data (i.e. number & length of cycles, peak temperature, cruise temperature, respective times, instances of longer or unscheduled throttling, etc).

For example, one group developed a lifing method based on a crack growth model, which could utilise min / max temperature, and thermal cycles at dwell times (Beck et al. 2012) [91]. However this approach like previous life prediction models, makes use of model parameters from isothermal oxidation cyclic tests, and therefore also provides a prognostic method, which would be useful for in-situ lifing of TBCs in response to differences in engine usage data. In the current industrial context, not all of the engine usage data is available as standard, as it may not be available on that particular engine model, or may not be subscribed by the airline operator using it.

Another approach would be to use the actual condition of the TBC material, as captured by NDT inspections; this could involve NDT technologies already in use, or (as often the case in research literature), technologies that are not currently deployed to capture such information, but could be.

Some life prediction methods have been developed in order to utilise NDT measurements of stress in the TBC, coupled with statistical descriptions of a given TBC's microstructure at the interface, and stress modelling of the nucleation and propagation of cracks (Busso et al., 2007) [92]. By making use of in-service NDT measurements, this technique offers the potential for remaining useful life predictions, however a full description (i.e. SEM micrographs) of the interface between the bondcoat and TGO is required, as are the temperature-cycling the coating has endured.

In between the life modelling of TBCs from statistical and mechanistic approaches described above, those among them that could be responsive to in-

situ measurement of TGO thickness and stresses in the bond coat, including the method by Busso et al., there exists further literature covering the factors underlying TBC life (though are not always applied directly to life prediction methods) [93]. Meanwhile, numerous studies exist on the inspection of TBCs, which yield information either on the changes of physical properties of the TBC (conductivity, reflectivity, measurement of stress, etc), or the respective TBC health (evidence of coating delaminations), either of which may be used to update a life model, or measure changes that could feature in a new model approach. These NDT methods which can be applied to inspection of TBCs are discussed in the next section, encompassing the main thrust of the literature review.

2.7 NDT of TBCs

Unlike the earlier introduction of NDT methods, the following literature pertains only to the application to inspection of TBCs. A variety of different techniques have been used in the inspection of TBCs, either as part of characterisation of the TBC destructively (i.e. with use of SEM microscopy) or as part of otherwise destructive oxidation / cyclic ageing tests. Some NDT methods exist for inspection of externally apparent features that have been applied to components with TBCs, such as light fringe projection (Schlobohm et al., 2017) [94], digital image correlation (Mao et al., 2011) [95].

Some more exotic methods for characterisation of TBC change exist, such as use of a cyclic burner rig to measure TBC heat resistance (JIS H7851) (Takagi et al., 2007) [96], which, while a method capable of inspecting the TBC in-situ, would contribute to aging of the TBC to be applied. The method also incorporates Acoustic Emission measurements, where the measurement of the acoustic

emissions (i.e. sounds emitted by the propagation of cracks) is performed in the process of a cyclic test which is responsible for the propagation of cracks. This means that the method itself including the temperature measurement on the surface during cyclic loading are non-destructive in nature, they are applied in a destructive context for characterising the life of a TBC as representative of similarly-manufactured specimens. Methods such as this will be included in the literature table, though their applicability for NDT and in-situ RUL provision will be noted, as they could conceptually be incorporated in-situ for assistance in RUL assessment, if they could be properly integrated. Additionally, other research, such as those in life estimation which utilise NDT measurements as part of their study (even if under isothermal oxidation or cyclic loading) will also be included, to build a picture of NDT methods available for assessment of TBCs for RUL provision; whether they are applied in a non-destructive manner, or whether an NDT inspection is used for facilitation of RUL assessment; or not.

Phosphorescent doping in the concept of “sensor TBCs” has been applied for detection of coating erosion (Pilgrim et al., 2012; 2013) [97] [98], which can also permit the measurement of surface temperature in-situ, during turbine operation [99], which offers a promising method to facilitate real TBC function measurement and tracking, if the technique can be incorporated into the engine design.

2.7.1 Acoustic emissions

Acoustic emission (AE) is one of the simplest concepts of material testing, where a material under stress emits noise related to material degradation under stress, where the signal is produced by the material itself, usually as it undergoes plastic

deformation [100]. This can be applied to TBCs for the tracking of AE emitted by cracks growing in the TBC structure, (Beck et al., 2012) [91], (Mao et al., 2011) [95], (Park, Kim & Lee, 2007) [101].

Owing to the destructive nature of the tests these are applied in, the method is usually for characterisation studies, investigating the life and crack propagation of TBCs undergoing TMF cycling, and the dependency on design and manufacturing parameters. However, should the monitoring of emissions in the cooling phase be plausible in a real scenario, it would function as non-destructive monitoring of the TBC, and hence has been included in the literature results.

2.7.2 Microwave NDT

The transmission and reflection of microwaves incident on a dielectric boundary, such as the ceramic – bondcoat interface; the magnitude and phase relationship of the reflected signal depends upon the integrity of the interface, and the permittivity (resistance of a material to formation of an electric field) of the material in the topcoat. The method has been used in literature for the detection of defects under the TBC (Firdaus et al., 2016) [102], and for measurement of porosity change, as the response signal has been found to have a linear relationship with porosity (Akbar et al., 2018) [103].

2.7.3 Micro-indentation loading method

The indentation-based measurements of Young's modulus, hardness, elastic modulus have been in use previously (Doerner & Nix, 1986) [104], (Sneddon, 1965) [105], and have been applied to the measurement of TBC stiffness of TBCs with ageing, in a matter that was found to be non-destructive (Tannenbaum et al.,

2010) [106], which has been found to correlate with bond coat degradation over heating cycle life (Kang et al., 2009) [107]

2.7.4 Ultrasonic inspection

The use of ultrasonic inspection doesn't appear to receive much attention in application for TBCs, but some modifications have been undertaken to adding of a time delay between the transmission and reception of the reflected signal, allowing the method to be applied to the narrow thickness of TBCs, which can be used for measurement of Young's modulus of the TBC, as well as an early detection of delamination propagation, before exhibiting visible signs on the surface of the TBC (Chen et al., 2012) [108]. This could be applied in an MRO context, where the part is under inspection on a lab bench.

A method of applying a waterproof layer to the surface of an APS TBC has been proven to enable measurement of sound velocities in the TBC, which are affected by voids and microcracks on the resulting measurement of coating elasticity (Crutzen, Lakestani & Nicholls, 1996) [109]

In a non-contact implementation of ultrasonic inspection, a laser-induced ultrasound technique has been used for measurement of sound velocity and attenuation coefficient in the bond layer, which was found to increase with oxidation life of the TBC (Zhao, Chen & Zhang, 2015) [110]. Meanwhile, in a rather novel development of the "tap method", measuring of the ultrasonic reflectance of the TBC, the acoustic impedance and the resonant frequency shift with TGO growth can be measured (Ma et al., 2014) [111].

2.7.5 Eddy Current testing + electrical resonance-based testing

Application of eddy current NDE is possible with TBCs, where the responsive voltage signal can be used to track changes in the chemistry of the bond coat, or from the thickness of the top coat via the “lift-off” effect between the inductor coil and the electrically conductive material under the TBC (bond coat, substrate), which can measure the ceramic coating thickness

Conventional EC tests operate up to a few MHz of the induced AC current; however, in order to inspect the much thinner bond layer, the penetration depth of the signal needs to be reduced to below 100 μm with application of higher frequency signals, upto 30 MHz (Schlobohm et al., 2017) [94]

The change in the signal’s real part can be used for coating thickness, either for conformity test or for detection of erosion in the ceramic (Reimche et al., 2013) [112], while changes in imaginary part of the signal can be used for detection of changes of chemistry in the coating incurred by oxidation and corrosion (Bruchwald et al., 2016) [113] [114], with other research conducted recently on the application to TBCs [115] [116] [117].

2.7.6 Emission spectroscopy

A different approach, which requires designing into the TBC includes the use of chemical trace dopants included in layers of the ceramic material, where erosion and spallation may then cause the dopants to be released into the hot gases, which are then excited and emit a detectable signature, providing an in-situ detectable warning signal of coating decay. Originally developed for in-situ application for the rocket motor of the space shuttle, so that NASA would have a

warning of engine health they couldn't get otherwise (Madzsar, Bickford & Duncan, 1992) [118], this has been proven to be applicable to aircraft engine parts (Chen, Lee, & Tewari., 2007) [119]. This method would be applicable in-situ, however it would function as a trigger on new coatings manufactured with the dopants, and would not be useful for other types of TBCs.

2.7.7 Impedance spectroscopy (IS)

With use of electrodes applied on the topcoat and the rear surface of the substrate, the electrical impedance (complex resistance to an imposed AC current) of TBCs can be measured (Wang et al., 2004) [120], and is sensitive to the presence of cracks, and growth of the TGO (Jayaraj et al., 2004a) [121] (*Jararaj et al., 2004b*) [122], (*Wu, et al., 2004*) [123].

The technique is responsive to grains in the top coat, grain boundaries, TGO growth, TGO chemistry, top coat thickness and electrode placement has been studied (Anderson, Wang & Xiao, 2004) [124], detailing the non-destructive applicability of the technique in furnace cycle studies; typically requires the physical adherence of silver electrodes to the surface, or through the liquid penetration of an electrolyte into the ceramic (*Byeon et al., 2005*) [125].

The performance of impedance spectroscopy has been determined to be sensitive to measurement temperature, the size of silver electrode used, while the voltage of the AC applied has negligible effect (Wang et al., 2016) [120].

2.7.8 X-ray diffraction (XRD)

X-ray diffractometry (XRD) is often used in research studies for measurement of coating phase and residual stress, usually performed in conjunction with other methods, such as AE (Park, Kim & Lee 2007) [101], or impedance spectroscopy (Anderson, Wang & Xiao, 2004) [124]; both mentioned above. (Cernuschi et al., 2005) [126] found in their use of XRD, no phase transformation took place in their TBC samples exposed to high temperatures, concluding the thermal diffusivity increase was due to sintering. However, this ageing was performed under vacuum.

2.7.9 Photo-luminescent piezospectroscopy (PLPS)

In a development of Raman Spectroscopy, a laser excitation of trace Chromium ions in the TGO makes possible the calculation of change in residual stress of a material via the frequency shift of its characteristic emission spectral peaks (Christensen et al., 1996) [127]. When applied to inspection of TBCs this residual stress is directly correlated with bond coat strength and the stress change from crack propagation; and hence can be used to generate residual stress maps of the TBC, while inference of the Cr content of the oxide layer points to the possible use for estimating remaining life (Clarke, Christensen & Tolpygo, 1997) [128], (Saunders et al., 2004) [129]. An important consideration: PLPS has been found to be obstructed by presence of CMAS deposits.

Damage and stress in the TBC aren't directly correlated, hence there are problems applying the technique as a measurement of damage. In aid of

understanding the emission spectra, stress factors that cause the spectra widening and shift have been simulated (Luz, Balint & Nikbin, 2009) [130]

Almost all studies available in the literature relate to the Cr³⁺ spectra, either in APS TBCs (Heyes et al., 2008) [131], (Feist & Heyes, 2011) [132]; or the measurement of Cr³⁺ spectra in EB-PVD TBCs (Busso et al., 2007) [92], (Clarke, Christensen & Tolpygo, 1997) [128], (Hawron, 2014) [133], (Nychka & Clarke, 2001) [134], (Christensen et al., 1996) [127], (Saunders et al., 2004) [129]; or to both APS and EB-PVD (Gell et al., 2004) [135]. Aside from these, some research has been performed in the spectra of lithium dioxide applied to APS TBCs (Chen, Lee, & Tewari., 2007) [119].

2.7.10 Thermography: thermal cycle monitoring of TBC

Another thermal method involves measurement of surface temperature of the TBC while it undergoes thermal cycling. If the temperature of both sides of the sample are fixed, i.e. for a front-heated TBC, cooled on the rear surface by a cooling system, then the temperature on the surface is dependent on both the thermal properties of the metal substrate and the TBC system; hence the 'heat resistance' of the sample can be obtained (Takagi et al., 2007) [96]. The method is focused on measurement of temperature difference under a range of heat flux. In its current description this functions as a research tool for characterisation of damage progression and heat resistance change *during* heat cycles; however it could potentially be adapted to be useful in-situ, in a similar way to implementation requirements for 'sensor TBCs'.

2.7.11 Active thermography: laser flash method

A variety of active thermography methods exist, differing in heat application and data collection. The first and most widely used of such methods to be developed was the Flash Method, developed by Parker, Jenkins, Butler and Abbot (Parker et al., 1961) [136] which enabled calculation of the thermal conductivity, thermal diffusivity and the heat capacity of materials with use of a thermocouple and an oscilloscope. By capture of the temperature of the rear surface from the heating application, the time at which the temperature reaches its half-maximum is then used to calculate thermal properties, using the following relation from the Flash Method (Parker et al., 1961) [44]

$$\alpha = 0.1388 \frac{l^2}{t_{0.5}} \quad (2-4)$$

where α refers to thermal diffusivity, l the sample thickness, while $t_{1/2}$ is time at half temperature maximum. This method is very simple in concept, and is ideal for measurement of thin homogeneous materials. However, it does require a short direct heating pulse, and this needs a graphite soot coating on the surface in order for the heat pulse to be absorbed and measured (if using non-contact measurement). As the method requires access to both surfaces in a vacuum, it is more ideally suited to a lab inspection, and is difficult to apply in-situ; particularly with real components, if access to both surfaces is a challenge, as is the case with gas turbine parts. Additionally it requires modification to permit the measurement of layers in a multi-layer system.

2.7.12 Active thermography: Induction thermographic inspection

In the same manner that Eddy Current inspection induces eddy currents in the material of the part for reading of induced magnetic fields, applying the method with much higher power results in the interruption of the eddy currents by cracks and voids, which then heats the damage features, enabling them to be observed remotely by an infrared radiometer. This method is ideal for rapid observation of thin damage features (such as cracks) in electrically conductive materials. As the alloys that make up gas turbine parts are usually low in electrical conductivity and magnetic permeability required for eddy current induction methods, high frequencies are required to apply the technique (Schlobohm et al., 2017) [94]. However, this is not so much appropriate for inspection of the TBC itself and is more useful for detection of cracks in the metallic substrate (Weekes et al., 2012) [137], (Frackowiak et al., 2016) [138]. Due to spatial requirements of the heating coil and the size of the radiometer, it is not likely in the near future that the method can see any application in-situ, and is more appropriate to laboratory tests.

2.7.13 Active Thermography: Infrared reflectance technique

A novel method for evaluating TBC ageing makes use of the mid-IR translucency of TBCs, enabling the measurement of TBC reflectance value (%). This provides a measure that is responsive to the extent of cracking in the TGO-BC interface, as the changes to the interface affect its reflectance, which is dependent on TBC thickness (Eldridge, Spuckler, Markham, 2009) [139], and exhibits an increase in reflectivity from approx. 50% to 90% (Eldridge, Spuckler & Martin, 2006) [140], which has been shown to be useful to predict remaining life (Luz, Balint & Nikbin, 2009) [130]

2.7.14 Active Thermography: oscillating heat application

Other techniques in thermography include the oscillation or periodic excitation of the heat application, in what is known as “pulsed phase” thermography (PPT) (Maldague, Galmiche, Ziadi, 2002) [141], and Thermal Wave Interferometry (TWI) (Cernuschi, Figari & Fabbri, 2000) [142]. As the method is strongly reliant on the thermal wave propagation between the periodic heating cycles, the translucency of TBCs is an obstacle, that still requires a coating deposit on the surface to improve the absorption. Most studies investigating TBC life do not use this method. As with light and change in refractive index influences reflections and transmission; the difference in thermal properties between the coating and the substrate causes partial reflections and transmission, according to the thermal properties; measurement of the temperature reflected on the surface by this contains information about the coating thickness and thermal diffusivity.

2.7.15 Active Thermography: Pulsed inspection (front surface)

An adaptation of the Parker method is encompassed in the form of front-surface flash thermography, also referred to as “transient thermography”, or more commonly known as Pulsed Thermography (PT), and is useful for inspection of coating condition and material delaminations from a single-sided inspection. As with the Parker flash method, knowledge of the thickness or diffusivity of the material, or calibrated reference samples are generally required to perform quantitative inspection, for instance to determine thickness or diffusivity of a sample, given the knowledge of one, the other can be determined. Recalling the log-linear temperature-time behaviour of homogenous materials mentioned in the introduction to thermography in chapter 1, the relation between the thickness (l)

and diffusivity (α) of a material is given by the break time (t^*) of the materials' temperature time behaviour (Maldague, 2001) [143]; $L =$ by the following relation:

$$L = \sqrt{\pi\alpha t^*} \quad (2-5)$$

If the exact properties are not desired, materials and their features can be differentiated based on their contrast-time profiles without any prior information about the samples required to differentiate them by the aspect ratio of defect features within them (Shepard et al., 2004) [59]. Additionally, it is possible to use the differential of polynomials fitted to a temperature-time curve, using the patented TSR method (Shepard, 2003) [57], [58] to provide the location of the break time (t^*), which suppresses the need for use of a reference or thermal contrast methods (Shepard et al., 2006) [60]. If thickness is known, the local diffusivity can be estimated; conversely if the diffusivity is constant, the depth to a given feature can be estimated. Further away from the common streams within the literature, studies exist applying the pulsed flash thermography method for inspection of TBCs, performing a mixture of delamination detection and measurement of thermal response (Zhao et al., 2015) [144], while other studies exist applying similarly different approaches, such as the simulation of annealing to measure TBC thickness, announcing surprisingly comparable results with eddy current tests (Bu et al., 2016) [145]. Meanwhile, additional challenges arise in the pulsed thermographic inspection of TBCs, including: the reflectance of Yttria-stabilised Zirconia (YSZ) between 1-5 μm , and the semitransparency between 5-8 μm [146].

Thermal diffusion of a multi-layer system:

These methods are applied to TBCs, with further developments to the application of the technique, for instance, a method proposed by (Phillipi et al., 1995) [147] and demonstrated by (Bison, Cernuschi & Grinzato, 2007) [148] applied non-linear least-square fitting of pulsed thermography data to model of 1-dimensional heat diffusion of a geometrically uneven heating spot, simulating a two-layer (i.e. coated) part; the model permitting them to obtain both in-plane (Cernuschi et al., 2004) [149](Bison, Grinzato & Marinetti, 2004) [150] and then through-thickness diffusivity TBC evaluations (Bison et al., 2008) [151]. Unlike most infrared techniques in the literature, this method does not come at the behest of an audacious title, and instead is humbly referred to through as “thermal diffusivity measurement with flash thermography” and similar unassuming descriptions. The method has been tested on real components (Cernuschi et al., 2006) [152], to obtain a measure of diffusivity change over TBC ageing, also obtaining an estimate of cracked interface of the TBC over oxidation ageing (Cernuschi et al., 2010) [153] & (2011) [154], although this relied upon an analytical model for APS TBCs (Golsonoy, Tspas & Clyne, 2005) [155], which may not be readily adapted to EB-PVD TBCs. Upon deriving the model representative of a Dirac heating pulse on the surface, the authors (Bison, Cernuschi et al.) have noted that their solution applied equally to uniform heating, meaning that it could be equally applicable for optical flash. In more recent developments, using the estimation of the reflection coefficient of the TBC-substrate boundary that the model-fitting produces, then the porosity of the material can also be estimated, if the material’s heat capacity is known (Cernuschi, 2015) [156].

Pulsed thermal imaging–multilayer analysis (PTI–MLA) method

More recently, utilising a different approach to the same problem (Sun, 2010) [157] [158] utilised a numerical model of the 1D heat diffusion equation, also solved for multi-layers, similarly reduced to an expression of surface temperature over time. The model-derived expression permits the calculation of thermal conductivity and thickness. Similar to the previous method, thickness and diffusivity cannot be determined independently; where thickness of the top coat is known, then the thermal conductivity / diffusivity, and specific heat capacity can be found (Sun, 2014) [159]. While the method has been shown it can be applied to both APS and EB-PVD TBCs (Sun & Tao, 2016) [160], it has not seen much use in ageing characterisation studies.

2.8 Definition of “non-destructive” and “in-situ” in service / MRO contexts

A point of interest in dealing with the diverse literature on the application of NDT techniques to TBCs within the context of components in service and their respective MRO cycle, is that a relatively loose use of terms applies, concerning whether the method is applicable in real context, applicable in-situ (on-wing), applicable in-situ (in-engine, off-wing), applicable in-service (offline), and applicable in-service (online). The distinction between whether a non-destructive method is appropriate for non-destructive application, or whether a method that can be applied in-situ means it can be applied on-wing, or in the hangar, etc., becomes an important mental task when approaching the literature, and in the various occasions when literature does or does not clarify the distinction, or broadly assign either of the terms, can feel like the reader is subjected to

subjective 'splitting of hairs', which nevertheless are still placed in either of two categories; non-destructive versus destructive, in-situ versus ex-situ (almost invariably described with a sentence or three).

In addition, the precise destructive / non-destructive nature of various testing methodologies are classified in a bipolar term, abruptly assigned either to "destructive testing" (or "testing"), or to the broad category "non-destructive testing". However, some methods may be non-destructive in nature, but applied in destructive contexts in the lab, wherein application in the real-world would be non-destructive. Some methods may incur damage, but the distinction of whether the level of damage is objectionable or not, would really depend on the expectations and responsibilities of the owner of the asset, the responsible agency for asset health and integrity, or the author of the maintenance manual, or inspection standard.

For this purpose, a new all-encompassing terminology is proposed, with which to assign the various methods into more tangible categories. Breaking down NDT methods and their applicable contexts would help researchers to categorise methods that may have been applied in laboratory environments but can be applied in-situ; or methods which are historically applied under destructive contexts but could feature as a non-destructive inspection when applied in-situ, and "non-destructive testing" methods which cannot apply to real samples in the current setup.

2.9 Classification scheme: Non-destructive testing

2.9.1 Non-destructive (true) testing (NDT-A i)

This category applies to any NDT method which is truly non-destructive in nature, in that no change to the structural or material integrity, chemistry or otherwise can be measurably achieved when the method is applied within established parameters. The sub-category i, referring to the method being applicable to real components, in the service context; a “true” NDT method of universal application, depending only on its specific features.

2.9.2 Non-destructive (true) testing (NDT-X ii)

Similar to NDT-Ai, this method applies to ‘true’ NDT methods, but which may not be applicable to real parts in the ‘in-use’ service context i.e. physical access or environmental constraints.

2.9.3 Non-destructive (true) testing (NDT-X iii)

Similar to NDT-Ai, this method applies to ‘true’ NDT methods, but which may not be applicable to real parts, requiring idealised features i.e. flat surface, access to both sides of the material which may not be possible, etc. The sub-categories I-III will not be further described with later classifications as they would equally apply here-after.

2.9.4 Non-destructive (applied) testing (NDT-B)

This category applies to any NDT method which the application of the method is non-destructive in nature, but the test the method is applied in requires potentially destructive stressing / tension of the part, which generates the

measured signal – however, if the method is applied in-situ during the use of the part, it is effectively non-destructive in its implementation, while if applied in the laboratory context, it is destructive; this label would be useful to distinguish between the different contexts in its categorisation

2.9.5 Non-destructive (practical) testing (NDT-C)

This category applies to non-destructive testing methods where some damage can be theoretically inferred to take place, though the application of the technique has no measurable effect on the part's material properties or its performance characteristics, with current attempts to measure the change.

2.9.6 Non-destructive (practical) testing (NDT-D)

Similar to category NDT-C, this applies to where a non-destructive testing method where damage can be inferred to take place in the part, which has a measurable effect on its properties or performance characteristics, where the change is measurable but the scale of the change is negligible or not of interest to the operator, and can be regarded as “non-destructive” for the part's life.

2.9.7 Non-destructive (practical) testing (NDT-E)

Similar to category NDT-D, this applies to where a non-destructive testing method where damage can be measured to take place in the part, which has a measurable effect on its properties, performance characteristics, and/or the life of the part. Some types of NDT-D may not reasonably affect the properties of the material, but the damage incurred in the microstructure through performance of the technique may only be observable in the resulting life duration of the part, whereupon it may become objectionable. However, the effect on life may be

below a threshold of tolerance that may be established, and therefore the method may still be regarded as “non-destructive” for the purpose of the part’s service life, if the benefits of the technique sufficiently add to confidence in its service life, of an appreciable value to the potential reduction of that life.

2.10 Classification scheme: situational context

2.10.1 In-situ (on-line, hot) (S-A)

Applies to methods that can be applied in-situ, integrated into the operational environment, and performed live when the system is in function. The label of “on-line” in the context of this thesis means “on-wing”, implying integrated into the gas turbine / engine; however this could also infer deployment in any real part’s operational function.

2.10.2 In-situ (on-line, cool) (S-B)

Applies to methods that can be applied in-situ, integrated into the operational environment, but owing to the extremes of the operational environment, the noise, opacity or contamination of the operational / hot gas, the fast motion or vibration of the parts; cannot performed live during function.

2.10.3 In-situ (on-line, cool) (S-C)

Applies to methods which, likely due to the size of technological constraints of the equipment required, cannot be performed in-situ inside the system, until the system is not only offline, but located in an environment where the necessary equipment or environmental conditions can be introduced (i.e.

requirement of additional lighting / stimulation, spatial, chemical, gas or radiation requirement for performing the test are available.

2.10.4 Ex-situ (S-D)

Applies to methods which require the tested part to be located in a lab environment in order for the inspection to be carried out, i.e. light fringe projection, X-ray CT scanning, mechanical testing rig.

2.10.5 Ex-situ (S-E)

Applies when the method not only requires the part to be located in a laboratory environment, but that the sample be “ideal” i.e. access to both sides of a test surface, and with other restrictions that require ideal parameters, such as on test geometry, or surface conditioning.

2.11 Classification scheme: Estimation of RUL

In order to classify whether a technique has been used for the actual estimation of remaining useful life (cycles, hours, percent of total); or whether the technique has been applied to track changes in a material property or response, which changes over the coating life, the following classification has been proposed:

2.11.1 Remaining Useful Life: applied (RUL-A)

Applies to where the method has been used for the actual determination of residual or remaining useful life.

2.11.2 Remaining Useful Life: entailed (RUL-B)

Applies to where the method has been used to monitor changes in the properties or performance of the material under inspection, but this has not yet been translated into an actual prediction of remaining useful life.

2.11.3 Remaining Useful Life: plausible (RUL-C)

Applies where a method has not been used to monitor changes in properties or performance of material under degradation, but is capable of measuring a change in properties or a change in response of the material from a change in structure and respective properties, leaving it open to be applied in the context of tracking changes over material life. This is intended to be a largely irrelevant category, but one that will still catch some of the literature.

2.12 Non Destructive Testing & Remaining Useful Life of TBCs

As the sub-categories I-III depend on the method and sample design and respective real-world service context, this categorisation can be arbitrary between researchers, in accordance with the context they are describing; and any technological developments or novel applications, can shift a technology from one sub-category to the other.

Any testing that creates damage above category NDT-E, where the damage incurred has an explicitly objectionable effect on the properties, performance or life of the part would classify as the rest of the spectrum of “destructive” testing. For the sake of having a category to mark in the literature, NDT category “F” refers to destructive testing.

The categories described above can be summarised in the following tables:

Table 2 – classification scheme of NDT categories

Cat	Description
A	True NDT
B	True NDT but typically applied in destructive context
C	NDT - minor damage inferred, not measured to date
D	NDT - minor damage incurred, measurable, negligible
E	NDT - minor damage incurred, measurable, objectionable
F	Destructive testing

Table 3 – classification scheme of NDT situational (“situ”) categories

Cat	Description
IS-A	In-situ (on-line, hot)
IS-B	In-situ (on-line, cool) inside the system
IS-C	In-situ (on-line, cool) outside the system
ES-D	Ex-situ, lab environment in current application
ES-E	Ex-situ, lab environment, ideal conditions strictly required

Table 4 – classification scheme of NDT situational (“situ”) categories

Cat	Brief	Description
RUL-A	Proven	The method has been used for explicit determination of RUL
RUL-B	Likely	The method has been used to monitor changes tracked over life, but
RUL-C	Plausible	The method has been used to monitor changes in properties or
RUL-D	Possible	The method is physically capable of measuring properties or
RUL-E	Not	The method is not known or foreseen to be capable of measurement to

Applying these categories to the literature of the application of NDT techniques to the lifing of TBCs, and with respect to their application (or potential to be applied for) the estimation of remaining useful life, the literature is thus presented, as shown in Table 5.

Table 5 – summary of literature on application of NDT methods to the estimation of RUL of TBCs

NDT type	Requires	Surface access	NDT class	Situ class	RUL class	Output	Summary	Papers
Light Fringe Projection / external optics	Projection of laser / optical pattern on part surface	Front	A	B-D	C	Surface profile / geometry	Detection of cracks, shape deformations (Situation: equipment spatial considerations)	Schlobohm et al., 2017 [94] Mao et al., 2011 [95]
Reflectance imaging	< 10 fs signal precision	Front	A	C	B	Thickness measurement	Application to erosion	Zimdars et al., (2008) [161]
Acoustic emissions (AE) test	Microphone / laser: vicinity or hard contact	Front	B	A	A	Number of cracks formed over time during cyclic testing	Detection of acoustic emissions as cracks propagate during cyclic tests; difficult to apply in gas turbine context	Berndt (1989) [162] (Park, Kim, Lee, 2007) [101] (Mao et al., 2011) [95] (Beck et al., 2012) [91] (Takagi et al., 2007) [96]
Microwave NDT	Microwave transmission at TBC surface	Front	A	D	B	Phase change: thickness measurement	Appropriate for TBC<300 um, situ: equipment spatial considerations	(Lin & Berndt, 1998) [163] (Firdaus et al., 2016) [102] (Akbar et al., 2018) [103]
Micro indentation	Physical impact of sample	Front	C	B-D	A	Estimation of surface stiffness	Physical pressure on material to measure physical properties. Situ: construction in-situ, not gas turbine to date	Kang et al., (2009) [107] Tannenbaum, Kang, Alvin (2010) [164] Zhu, Miller (1999) [71]
Ultrasonic inspection	Ultrasonic probe contact with surface (often); or laser	Front	A	B-D	A	Time of flight of reflected soundwaves, speed of sound in material	Situation deployment depends on whether wet contact or laser method is used	Chen et al., 2012 [108] Crutzen, Lakestani & Nicholls 1996 [109] Zhao, Chen & Zhang, 2015 [110] Ma et al., 2014 [111]
Eddy current inspection, electrical resonance-based inspection	Probe contact with surface	Front	A	B-D	C	Lift-off, coating thickness measurement, bond coat chemistry change	Signal change responsive to chemical change in bond coat and to TBC thickness change from erosion / spallation	Yong et al., 2012 [115] Reimche et al., 2013) [112] Bruchwald et al., 2016 [113] [114]. Min et al., 2017[116] Li, Yan, Li & Li, 2016 [117] Schlobohm et al., 2017 [94]

NDT type	Requires	Surface access	NDT class	Situ class	RUL class	Output	Summary	Papers
Thermal Emission Spectroscopy / Phosphorescent TBCs	TBC dopant, sensor <1m from TBC during cycle	Front	B	A, B	A	"intensity (a.u.)"; detection of emission from doped layer	Requires direct application in-situ, live on engine	Madzsar, Bickford & Duncan 1992 [118] Bennet & Yu, 2005 [165] Chen, Lee, & Tewari., 2007 [119] Pilgrim et al., 2012 [97] Pilgrim et al., 2013 [98] Eldridge et al., 2016 [99]
Impedance spectroscopy / electrochemical impedance spectroscopy (EIS)	Direct sample surface contact; direct on sample + metal rear surface, offline	Front	B	B-D	B	Detect variation of TGO, response to TBC cracking	Measurement of electrical impedance of the TBC, responsive to chemical changes in the TGO; requires bound contact of electrode to both surfaces	Wang et al., 2004 [120], Jayaraj et al., 2004 a[121] b[122] Wu, et al., 2004 [123] Anderson, Wang & Xiao, 2004 [124] Byeon et al., 2005 [125]. Wang et al., 2016 [120]
X-ray diffraction	Large equipment considerations	Front	A	D	B	Measure crystallographic phase; phase change, stress	Usually used as an adjudicate method in parallel with laboratory based studies to explain results, not in RUL estimations	Czech et al., 1999 [166] Schulz (2000) [41] <i>Tolpygo, Clarke & Murphy (2001)</i> [167] Anderson, Wang & Xiao, 2004 [124] Cernuschi et al., 2005 [126] Park, Kim & Lee 2007 [101]
Photo Stimulated Luminescence Spectroscopy (PLPS)	Laser stimulation of TBC coating; requires TBC that accumulates Cr ³⁺ in layer	Front	A	D	A	Measure stresses in TGO through the shift of raman spectral lines	Possible to measure stress in the TBC, however the stress is not linearly correlated with ageing, as crack development relaxes and redistributes stress in the oxide layer	Lipkin & Clarke 1996 [168] Christensen et al., 1996 [127], 97 [128] Tolpyo, Clarke & Murphy 2001 [167] Nychka & Clarke, 2001 [134] Gell et al., 2004 [135]. Saunders et al., 2004 [129] Busso et al., 2007 [92] Chen, Lee, & Tewari., 2007 [119] Heyes et al., 2008) [131] Sayar, Seo & Ogawa 2009 [169] Luz, Balint, Nikbin (2009) [130] Feist & Heyes, 2011 [132] Hawron, 2014 [133]

NDT type	Requires	Surface access	NDT class	Situ class	RUL class	Output	Summary	Papers
Thermal cycling / heat flux test	Heat burner + requires heating and cooling, both sides	Front	B	D	B	Measurement of "heat resistance" and conductivity	Measures "effective thermal conductivity" with heat flux	Zhu, Miller (1999 [71] Takagi et al., 2007 [96]
Laser Flash Method / Pulsed (transmission) thermography	Heat source, IR radiometer, surface coating	Both sides	A	E	A	Diffusivity / thickness measurement	Correlates with TGO layer growth & crack nucleation; Situ E assigned w.r.t. lack of access in complex parts	Parker et al. (1961) [44] (Zhao et al., 2015) [144]
Induction thermography	Large AC induction coil, IR radiometer;	Front	A	D	A	Detection of underlying cracks: in metal substrate	Eddy current induction to reveal cracks in substrate	Weekes et al., 2012 [137] Schlobohm et al., 2016) [94] Frackowiak et al., 2016 [138] Schlobohm et al., 2017 [94]
Infrared reflectance imaging	IR imager, flash / laser heat source	Front	A	B	A	Mid-infrared reflectance %	As the TBC-BC interface rumples with age, its reflectance property changes, which is easily measured	Eldridge et al. 2003 [170] Eldridge, Spuckler & Martin, 2006 [140] Eldridge & Spuckler 2008) [171] Eldridge, Spuckler, Markham, 2009 [139] Luz, Balint & Nikbin, 2009 [130]
Modulated heating / Photo-thermal / Oscillating technique	Laser heating (modulated, i.e. chopper)	Front	A	D	C	Measurement of thermal diffusivity	Conversion of phase-amplitude response; situation context based on current equipment	Maldague, Galmiche, Ziadi, 2002 [141] Cernuschi, Figari & Fabbri, 2000) [142] (Cernuschi et al 2004) [149] Bennet & Yu, 2005 [172] aka "PopTea"
Pulsed thermography (single sided) TSR method	Flash thermographic response, front surface	Front	A	C	B	Temperature: TSR® derivative, diffusivity, thickness, defect depth	Very attractive method for estimating thermal diffusivity of thin coatings; if thickness is known. Requires adaptation to apply in-situ	Shepard, 2003) [57], [58] Shepard et al., 2004) [59] Shepard et al., 2006) [60] Shepard et al., 2007 [173]

NDT type	Requires	Surface access	NDT class	Situ class	RUL class	Output	Summary	Papers
Active thermography, multilayer model fitting approach A		Front	A	C	A	Temperature – time profile; coating thickness / diffusivity estimation; porosity, % of cracked interface	Very attractive method for estimating thermal diffusivity of thin coatings; if thickness is known. Requires adaptation to apply in-situ	Phillipi et al., 1995 [147] Cernuschi et al., 2004 [149] Bison, Grinzato & Marinetti, 2004 [150] Cernuschi et al., 2006 [152] Bison, Cernuschi & Grinzato, 2007 [148] Bison, Cernuschi Grinzato., (2008) [151] Cernuschi et al., 2010 [153] Cernuschi et al., 2011 [154] Cernuschi, 2015) [156]
Active thermography, multilayer model fitting approach B		Front	A	C	A	Temperature – time profile; coating thickness / diffusivity estimation	Very attractive method for estimating thermal diffusivity of thin coatings; if thickness is known. Requires adaptation to apply in-situ	Sun, 2010 [157] [158] [174] Jang & Sun, 2012 [175] Sun, 2014 [159] Jang, Sun et al., 2015 [176] Sun & Tao, 2016 [160]
Pulsed thermography (single sided) other methods		Front	A	C	B	Thermal conductivity / diffusivity measurement		Zhao et al., 2015) [144] Bu et al., 2016) [145] Akoshima et al., (2008) [177]

2.13 Gaps in knowledge / state of the art

Many of the significant work has been performed with the application of pulsed-active thermography for assessment of thicker Plasma Sprayed TBCs, however this has not been applied in many of the studies to EB-PVD TBCs, which due to their microstructure differences with PS TBCs, would be expected to exhibit differently-shaped ageing trends. Furthermore, which EB-PVD TBCs are more costly to manufacture, they offer greater aerodynamic performance, strain tolerance and overall life, and typically are applied to high performance components in the hot path, such as NGVs and turbine blades. This locates the use of EB-PVD TBCs in the protection of some of the most critical and high cost parts in the engine, thus ensuring that any extension or prediction of the life of the coatings on these parts would have a significant impact on the engine parts, with a significant cost-driver attached.

As EB-PVD TBCs are applied more to these high performance components, they will also be very thin; effectively reducing the number of frames available in a 'flash thermography' event, introducing challenges in the application of the technique, where the clear identification of the boundary between coating and substrate becomes critical. The measurement of thermal diffusivity as a basis for ageing assessment has already been proven with other TBCs, yet many of the studies of pulse thermography, while well applied to study of plasma sprayed TBCs, are lacking in application to thin EB-PVDs (<200 μm). Meanwhile, where many studies are performed with a graphite soot preparation, this is not ideal for a realistic context, and hence it is the application of pulsed thermographic NDT for the inspection of thin EB-PVD TBCs that forms the main scope of this thesis.

2.14 Summary: predictions of TBC cyclic ageing experiment

From consulting the literature on the many aspects of TBC ageing with isothermal temperature and cyclic oxidation tests, a number of observations should be summarised as to what can be expected from the TBC ageing test:

- 1) The effects of sintering of the TBC are frequently illustrated, as the microstructure is smoothed and microcracks that are part of the structure converge into spherical pores. This effect will be expected to increase thermal conductivity of the TBC, and this will steadily grow over the coating life and has been noted by several studies. For example: all cyclic test conditions explored by Zhu et al., (2001) [77] produced the same overall increase in conductivity in EB-PVD TBCs; this has also been observed by others in APS TBCs [126], [153], [74]
- 2) A number of studies considered large early changes in the TBC, from oxidation growth models showing a large increase in the TGO growth in the first 30-50 hours, which might be expected to generate initial microcracks which would be expected to reduce thermal conductivity of the TBC; however optical property changes were also noted (Kakada et al., 2009) which complicates the multi-faceted changing system further.
- 3) An opposite trend has also be noted by studies as exhibiting late-life decrease in conductivity from later life cracks coalescing into buckling and delamination [154], which can be ascribed to crack growth when inspected with AE [101] [91], or measurements are taken at a fine resolution to capture change (Zhu et al., 2001) [70], or TBC spalling (Takagi et al., 2007) [96].

3 Research Aims, Objectives, Methodology

3.1 Scope & Aims

The aims of this research are to identify and address the gap regarding high value manufactured components within the aerospace / MRO context, and to improve upon it; either for the reduction of maintenance service cost, or for the diagnostics and / or extension of useful component life, through the application of NDT for ageing assessment of TBCs. The research will resolve this gap by developing a technique to facilitate a reduction in maintenance time schedule, detection of damage features earlier in the inspection timeline, or for the ageing assessment of TBCs, within the scope of expected service conditions.

3.2 Objectives

The aims of the research are broken down into four key objectives. The latter objectives were written after the initial two were carried out, which informs the requirements the later objectives needed to address.

3.2.1 Objective One: Identify industry requirements, current practice

In order to identify the most exploitable gaps in the literature, there should be an engagement with industries working in the Aerospace / MRO context so that current practice can be captured, and the opportunities for research and development be highlighted. Additionally, the engagement should highlight key criteria for the research to ensure the direct applicability of results in a realistic industry setting.

3.2.2 Objective Two: Conduct TBC lifing experiment to capture degradation of TBCs

TBC coatings will need to be subjected to ageing conditions that manifest typical degradation behaviour; the samples should be aged at distinct stages in order to provide an ageing trend to be captured and analysed, and discrete opportunities to capture data in order to measure the degradation via the NDT method used. The captured data is then to be analysed and exploited to furnish an assessment of component ageing.

3.2.3 Objective Three: Development of a framework for thermographic NDT for through-life degradation assessment of thin EB-PVD TBCs

In between each ageing cycle, the pulsed thermographic data will need to be captured. In order to inspect thin TBCs and the fast thermal event that is being captured, it is vital that a strategy is employed in order to maximise the available data for the analysis within the limitations of the framerate of the thermal imaging system. The setup and parameters of the inspection should factor in a response to the requirements for application in a real industrial environment, captured in answer to the first objective; and should focus on methods to circumvent limitations of applying the method to that context, while also capturing data under “ideal” inspection conditions, for comparison of the ageing trends with the ideal scenario.

3.2.4 Objective Four: Development of an automation process to support thermographic NDT for through-life assessment

The technique used in the main experiment may be performed under realistic scenario context, but there will still exist barriers to the actual end use

deployment of that technique; these could include the speed of inspection and result, which may present an obstruction to implementation in already busy inspection routines. The cost incurred in application of the technique may not compare with the benefits offered; or the technique may need to be applied in-situ in inaccessible areas. These challenges will be outlined in response to Objective One, and would require a response to project how the inspection method used in the main thrust of the thesis could be deployed within a real service / MRO context.

3.3 Methodology

The methodology adopted to address these objectives breaks down into multiple stages, much of the work taking place simultaneously, as some of the objectives interact with each other, and the refinement of one affected another, which narrowed the outcome from the first in finer details. This process is shown in Figure 32.

Initially, a review of literature was performed in order to ascertain current state of the art, so that, in comparison with industrial requirements for longer component life, and reduced maintenance cost, knowledge gaps in use of NDT techniques can be identified, in fulfilment of Objective One. This study was covered in Chapter 2, where the methodology for the review is specified in detail.

Alongside this, it was important to capture current industrial deployment of NDT technologies, the challenges faced by new technologies in order for them to become adopted in standard practice, and identify any specific problems needing

solutions, to which techniques from the literature can be deployed or adapted to address this need.

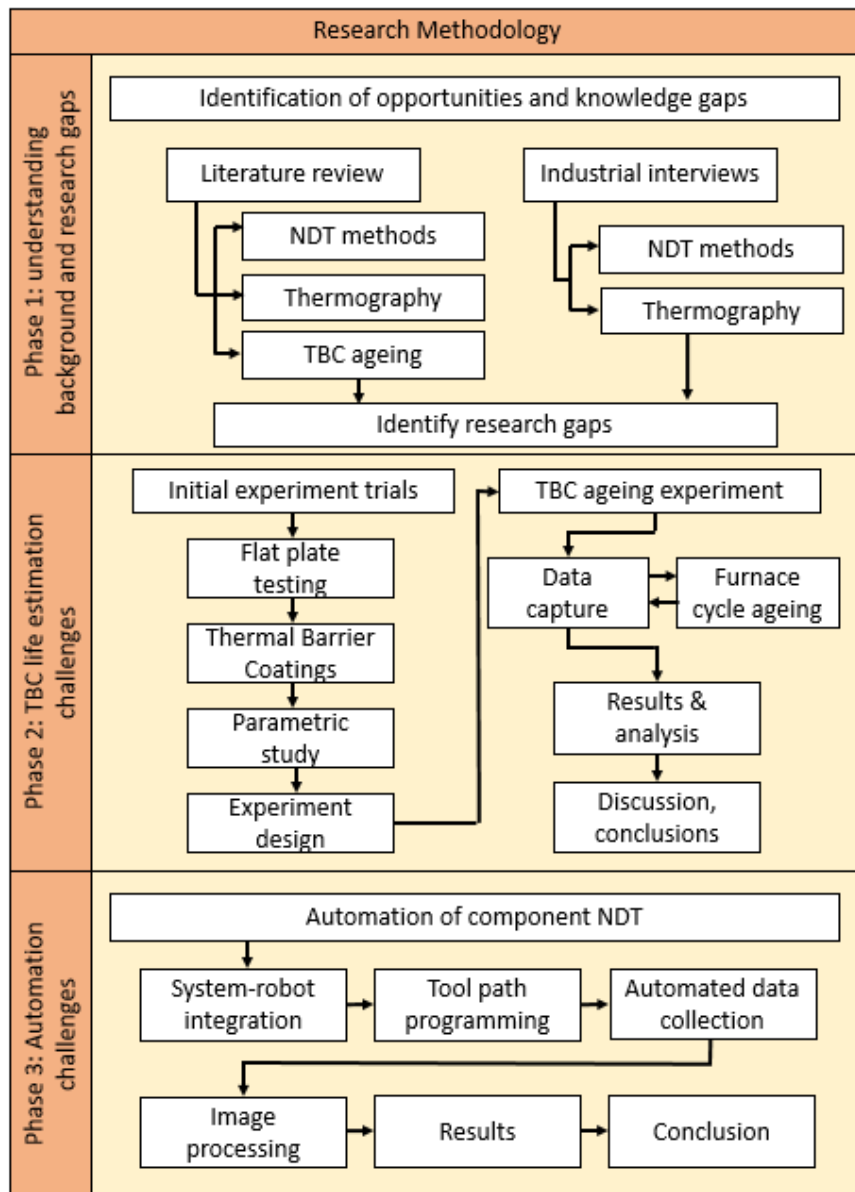


Figure 32 – illustration of the adopted research methodology

These engagements entailed a series of interviews with NDT experts and senior engineers in the aerospace / MRO sector, with a series of prepared interviews and considerable 'free discussion' surrounding them around the overall scope of the interviews. This process was in direct fulfilment of Objective Two, and is discussed in Chapter 4.

Whilst the review of literature in Chapter 2 explained that the assessment of Remaining Useful Life of EB-PVD TBCs was of interest, the surveys in Chapter 4 highlight the use of automation as a key strategy to improve NDT in use in assessment of in-service components. Due to these dual priorities, and the availability of component samples at the time of the research, the decision was taken to explore automation of pulsed thermographic inspection, while also exploring the use of PT with EB-PVD TBCs of similar thickness to those deposited on hot section components. This enabled the investigation of multiple component contexts, with detailed focus on thin EB-PVD TBCs, which presented additional research challenges and novelty; while the handful of real components available for the research provided a unique opportunity to develop automation, which the main experiment could be adapted into. As the components had spalling coating and sub-surface delaminations, these presented a different degradation inspection aspect from the ageing characterisation, and the work behind the detection of delamination that arose from the work in chapter 4 is directly related to the ageing assessment.

At this stage, the literature gaps, current practice, and industry requirements have been identified, and need to be condensed into a set of experimental parameters to plan out the experimentation that will fulfil the industrial requirements, while addressing gaps in the literature from the first two objectives. Initial trials were performed with ideal samples, highlighting the challenges in novel application of the adopted NDT method, informing the process of selection of parameters, in fulfilment of Objective Three.

In parallel with the selection of experimental parameters is the design of experiment itself, which is split between objectives two and three; the initial experiment concept came first, though its final implementation was performed after resolution of optimal experimental parameters, covered in chapter 5, with the design of the lifing experiment to be discussed in chapter 6.

Upon the completion of the experiments, the analysis was performed, identifying ageing trends in the TBC samples, detailed in chapter 7.

Additionally, experiments on automation of pulsed thermography were performed to raise the prospect of applying active thermography in an automated data capture and data analysis platform. This section of work drew on the identifying of barriers to introduction of new NDT technologies contained in Objective One and was in fulfilment of Objective Four, and is covered in chapter 8.

Specific details of the methodology for each section is covered at the start of each of their respective chapters.

4 Current industrial practice

With the objective of performing a thermographic NDT to the inspection of TBCs, and with a literature-formed focus to seek application to EB-PVD TBCs in the industrial service / MRO context, a series of interviews with companies operating in the aerospace / MRO sector has been engaged, with the aim of identifying where and how different NDTs - and particularly, thermography - is currently employed, what has been achieved, and what is still to be desired. Additionally the various barriers for a new NDT method to be utilised in industry will be sought, in order that they may be part of the objective of the research, in aim to deliver directly applicable results.

In order to capture the inspection requirements from the industry, a few key companies in the sector have been engaged in the form of a case study approach to build research around existing practices. A semi-structured interview was performed with these industries in the manufacturing and MRO context of aerospace in order to identify how thermographic NDT had already been employed, what had been attempted (in order to get a grasp beyond the contents of the literature), how the technology is perceived by those who would be intended to use it, how well other NDTs are currently used, and what challenges thermographic NDT faces to become more widely adopted.

4.1 Questionnaire design: the key questions

A series of interviews were held with aerospace industries involved in supply and servicing of aero engines, to capture a current view on the use of NDT on aero engine components in the service context. Two companies, including different

departments of the same company were approached, to enable focus on NDT in the whole life cycle, from design and manufacturing to service.

The main focus of the interviews was pitched around a series of questions targeted to the individuals being interviewed; whether they work in design, manufacturing, or service. In addition to this, a large amount of free conversation resulted from the meetings. These interviews can be found in Appendix A. A summary of the key questions included:

1. What types of NDT do you perform?
2. Of those, what is the extent of manual and automatic evaluation in each?
3. What are the common types of damage you inspect for?
4. What are the standards you perform to / where do you get them?
5. Are these static documents, or live? Can they be changed?
6. For a new NDT process, what time constraints would it need to have?
7. Do you use thermography, and in what context?
8. Has there been any work on automation of thermography?
9. Has PT been used for remaining useful life prediction?
10. What are the obstacles to applying new NDT in your industry?

These interviews were prepared as printed questionnaires which were completed by the author by hand during the interview. Some questions were not relevant to all departments, and many questions became apparent during the interview.

4.1.1 People involved: background, years of experience

Two engineering companies were interviewed; one interviewed once on their only site, the other interviewed in four business units. Company A was interviewed in

the design, manufacturing and service context; with a further separate interview in the manufacturing context; company B was interviewed in their only function of MRO/service context. In the service context, used components were being sent for service inspection and repair, and subsequent inspection; in other contexts inspection was on new, unused components, or the discussion was pre-empting future inspection context.

Those interviewed varied from senior engineers high in the management structure who participate actively in the guidance of testing processes and introduction of new ones; to those working on the factory floor in performing the tests on a regular basis. While other interviews with other industries were undertaken in search of relevant applications for NDT, for the sake of the thesis that developed and its scope, only the interviews with aerospace industry experts will be discussed.

The profiles of those interviewed are as follows:

- Head of NDT, 40+ years of experience
- Corporate Specialist - Surface Engineering, 30+ years of experience
- Life Cycle Engineering, 20+ years of experience
- Manufacturing Engineer, 15+ years of experience
- NDT specialist, 20+ years
- NDT specialist, several years

Part of the process involved interactions with other members of staff, though their full status and opinion was not fully captured in the same manner; key details were followed up in later questions & discussion with those in the above list.

4.1.2 Summary of results

1. NDT types in regular use were similar to those discussed in Chapter 1, including; visual inspection, dye penetrant inspection, x-ray radiography, ultrasound thickness measurement, and pulsed thermographic inspection.
2. The vast majority of these techniques were applied manually, by trained technicians, while if the sample was placed on a fixture jig for automated assisted data capture, the data analysis was still a manual process.
3. Common damage types included visibly obvious material erosion, surface-breaking cracks, hidden cracks on internal surfaces, insufficient wall thickness, component shape / geometry mis-match with design specifications, and coating delamination.
4. The inspections were performed to internal standards, tied to the part as part of the OEM manual. These standards had been accredited via a national board to confidently fulfil this purpose.
5. As some repairs required modification of the method specified, the documentation prescribing repair strategies were live. Updates or changes are subject to approval mechanisms by the OEM that supplied the parts.
6. For new NDT to compete with the other methods, it would need to reduce total turn-around time. The time requirement desired was 3 weeks.
7. Thermography was used for inspection of combustor insulation and for sentencing of some specific features of specific TBC coated parts, after repair. There was no thermographic work at present with coatings where it is used to sentence parts.

8. There had been studies on the automation of thermography, but the influence of dirt was found to be a prohibiting factor.
9. No application of PT for RUL prediction was specified.
10. Obstacles to deploying new techniques and technologies require special purpose application to address a specified problem, concerning individual features; as well as the technique needing to reduce turn-around time by more than it consumes to implement into the schedule.

4.1.3 Interview analysis

The first observations were the similarities and differences between the interviewed groups, which closely followed the scope of their work.

Similarities

There were applications for pulsed thermography in both manufacturing and service, though both contexts were for specific issues.

Each aspect, from design, manufacturing and service, in both companies, all had a strong focus on reduction of waste. In design and manufacturing this focus was on material waste; in service the focus was on waste of useful components not returned to service; or waste of man-hours or consumables during inspection of components that would be scrapped. Many of the NDT techniques in use in the main sentencing process were the well-established, older techniques, such as those discussed previously in the 'Introduction to Non-destructive Testing' in chapter 2, i.e., visual inspection, dye penetrant, ultrasound, etc. There were specific components and features, sometimes with very specific problems with narrow context, to which more advanced NDT techniques were applied.

A considerable amount of research had been performed in investigating the viability of other advanced techniques, though often these identified their own challenges and obstacles that made them difficult to apply in service context.

Concerning expansion of the NDT portfolio, there were concerns that new NDT techniques would need to address specific problems uniquely attractive to using the new technique, or would need to reduce turn-around time greater than the time the inspection required, on average, and this requirement typically hinders introduction of new techniques.

A vast majority of the NDT techniques in use were lacking in automation. This was due to the uncertainty of methods that require a trained operator to interpret.

Differences & unique attributes

In manufacturing, PT was not mentioned to be applied to TBCs, while in service / MRO context, it was; although this was for one specific application.

Manufacturing faults can occur: voids, inclusions, machining – currently they have a good understanding of the possible issues.

In-service faults were temperature and service environment dependent; thermal cycle, chemical contaminants etc., each batch of components' damages would vary according to their age, and the particular service conditions they experienced.

While the manufacturing stage was seeking extension of the maximum useful component life, the MRO / service side are seeking to increase yield – parts returned to service – wherever possible.

Service degradation context involves parts that have been subject to a wide variety of damaging conditions, and not just those that can be simulated in lab-based batch tests at the manufacturing stage, and as such contains a wider variety of features that are not as well understood as those arising from manufacturing.

The MRO company interviewed commented that they can't perform full NDT evaluation with TBC coating on, which they remove between visual inspection and the first NDTs.

Of components with concessions, further tests later in the component life would not account for the concessions made. This would be raised during the custom repair requests and introduce additional delay.

A workshop interviewed did not always have access to complete service records, and only if a customer had subscribed to the service. This introduces a gap in the information flow between design, service and manufacturing.

While the manufacturing stage can test components before and after coating, the service side receives a "complete" but damaged part, and has to remove the TBC coating to perform their tests.

The application of NDT was only found to be used to determine strictly if the measurement meets the part specification criteria, and no assessment of remaining life was observed by the author, indicating that perhaps the various developments of NDT for life assessment in literature are lacking in real service use, however the scope of these interviews was a little too broad and the

sampling of the organisations too limited for the author to assert this observation with conviction.

4.1.4 Key degradation mechanisms

For the purpose of identifying an application for automation of active thermographic inspection, different damage types were described during the interview process, including, as mentioned in the previous section: material erosion, surface-breaking cracks, hidden cracks on internal surfaces, insufficient wall thickness, component shape / geometry mis-match with design specifications, and TBC delamination. Additionally, blockage of channels and corrosion product build-up was of strong interest. This was to assist in the selection of damages that active thermography is appropriate for, drawing upon the strengths and weaknesses of various NDT techniques as discussed in section 1, which generated background for work in automation of thermography of TBCs, which is presented in section 8, as development of how the main ageing experiment could be applied in an MRO context.

Table 6 - A summary of typical degradations in aerospace components which were identified as being potentially accessible to thermography NDT (reproduced from Mehnen, Tinsley & Roy 2014), [178], courtesy of Elsevier.

Damage type	Location	Direction	Geometry
Blocked channels	Surface	Area, surface	Surface breaking
Metal thickness sizing	Sub-surface	Normal to surface	Linear
Detection of internal corrosion product	Sub-surface	Area	Volumetric
Substrate / corrosion differentiation	Sub-surface	Area	Volumetric
Surface coating thickness sizing	Thickness	Parallel to surface	Linear
Surface coating delamination	Near surface	Parallel to surface	Linear
Subsurface oxide layer	Near surface	Parallel to surface	Linear
Differentiation between oxide & sulphide product	Surface breaking	Area	Volumetric
Detection of cracks in substrate	Near surface	Normal to surface	Linear

4.1.5 Summary and gap analysis

As should be expected, the aerospace industry in the MRO context has a significant portfolio of proven NDT techniques already in regular use; it has also conducted research into new types of NDT and further developments, and is engaging with R&D developments as an on-going process.

The gaps identified in the interviews are two-fold; firstly, there is a considerable lack of automation of thermographic NDT, in both the data collection aspect, and of greater interest, in data analysis.

While techniques such as active thermography receives some use in the MRO business, it is under-exploited, as there is a lack of specific problems that require the inspection, and the additional time requirement to expand a method, while already in use, to other component features, comes at the cost of additional data collection and analysis time of trained technicians, which without a specified problem requiring a solution, is unnecessary.

One of the key findings from the interview process was a limitation of automation of thermographic NDT, and while thermography had application, this was largely as an additional check / in a quality control aspect, indicating that methods being developed in literature capable of capturing changes of material property evolution with ageing, appropriate for estimation of RUL, still require further development to prepare them for direct implementation. Lastly this prospect of implementation came with the caveat that, unless the method covers a safety-critical pass gate on a specific component problem; any additional method introduced would be required to reduce maintenance cost greater than the cost

of implementation, which would be subject to a cost-benefit analysis to this effect. However, it was also strongly stressed there is a considerable value in reducing turn-around time, and that any significant time saving in reducing other NDT applications would be worth additional expense, if it sufficiently relaxed the schedule.

It was therefore concluded from these interviews that in order for new NDT techniques to be attractive for deployment in current MRO inspections, the technique must respond either to specific problems, or be suitable for automation and detection of features that may already be covered by other NDT techniques, but turn-around and wastage can be reduced where the technique may identify part failure earlier in the inspection cycle (including the potential from estimation of RUL), and thus reduce overall resources in time and man-hours committed to inspection of each batch of components.

5 Thermographic NDT & parametric study

As TBCs undergo ageing at exposure to high temperatures, one of the key changes they express as part of this age is the change of their designed purpose; their thermal properties. As a result, a large volume of the literature apply a variety of NDTs for the inspection of TBCs, and a large number of them focus on infrared / thermographic techniques for the measurement of these thermal properties. The application of infrared is relatively rapid and non-invasive, and is directly relevant to the problem of the ageing of TBCs. It has been demonstrated in various studies that these properties change over time, however they do not appear to have sufficient deployment in current industrial use; while their application is perfectly suited for the service / MRO environment, where a rapid inspection of thermal properties may yield a number of answers regarding the remaining useful life of the TBC. This could be potentially applied in the inspection lab setting in an automated context, in answer to research objective two: *conduct TBC lifing experiment to capture degradation of TBCs*, and would provide a method which could be implemented in an automated inspection process in objective four: *development of an automation process to support thermographic NDT for through-life assessment*. However, in order to fulfil these objectives, the main experiment needs to overcome some problematic issues, and the setup and parameters of the experiment needs to be resolved, hence giving rise to the need for objective three.

The aim of this chapter is to outline the setup of the experiment, from the data capture experimental setup, to the creation of samples, to preparing their ageing

over which to measure their changing properties, and the selection of parameters required for the measurement of change of thermal property.

The capture of a “fast thermal event”, such as a thermal wave propagating through a thin coating, requires a fast framerate; however in the implementation with optical flash lamps carries the problem of uncertainty regarding when the termination of the heat pulse enables the usable data to begin, and when exactly the heat pulse reaches the substrate, shortly beyond which the collection of data should terminate, before the wave reaches the far surface of that layer. In order to respond to these difficulties, without knowing the ideal parameters before beginning the experiment, a parametric study approach was conducted, in order to select the optimum data capture and analysis parameters required. The through-thickness diffusivity was the objective to be measured throughout the TBC life at various stages of its oxidation life with the objective of returning repeatable trends in the calculated diffusivity properties’ change over time, which it was hypothesised would still be expressed in the non-soot coated condition, albeit with an unknown quantity of errors and uncertainties.

5.1 Setup and samples

Six thermal barrier coating samples were manufactured to represent service coatings for turbine blades, which are the intended application of this research. The samples were round coupons, 12.5mm wide, 0.9mm thick, made from CMSX-4 as a substrate, to provide the same material properties [179], the basic design is shown in Figure 33, and the resulting samples in Figure 34.

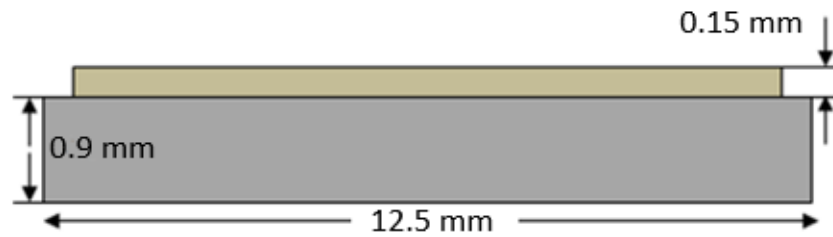


Figure 33 – drawing of TBC coupons manufactured for preliminary experiment

The samples were manufactured with a platinum-diffused bond coat, $\sim 24\mu\text{m}$ thick; the ceramic was 7wt. %, P-YSZ (Yttria partially-stabilised Zirconia) with thickness of approximately $152\mu\text{m} \pm 7\mu\text{m}$, as shown in Figure 34. The deposition of the TBC was performed by EB-PVD; deposited at a chamber pressure of $6\mu\text{Bar}$. The substrate temperature was $1305\text{ }^\circ\text{K}$, the atmosphere 1:9 Ar:O₂. The substrate was rotated at 8 rotations per minute, with an electron gun operating at 4kW. Six as-manufactured samples were used, numbered: S01, S03, S05, S07, S09, S11; while 3 pre-aged samples were also provided, numbered S21, S23, S25 to distinguish them. This was to allow for parallel samples manufactured in the same location in the coating furnace, so they could fit in the dataset next to their twin if tests needed to be repeated. It was unknown to the author prior to the experiment how well the samples would perform, and this convention was maintained in case of any unforeseen circumstances.

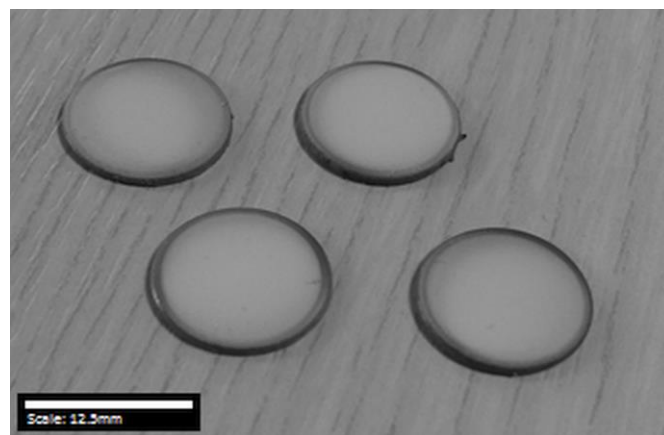


Figure 34 – Image of round coupon samples

5.1.1 Equipment

For application of heat and triggering and management of data capture, the thermographic system to be used for the experiment was the Thermoscope® II by Thermal Wave Imaging Inc. [180]. The infrared system was a FLIR SC7600 series radiometer; hosting an Indium antimonide sensor, with a full spatial resolution of 640x512 pixels. The system possesses mid-IR filters for 3.1-5 μm ; with a noise-equivalent temperature difference (NETD) of 20-25mK measured at 25°C. The samples were placed on a custom made fixture in front of an internally reflective flash hood, with two Xenon flash lamps as the flash heat source. The infrared “camera” observes the data capture through a viewport in between the flash bulbs, at a distance of approx. ~230mm from the sample position, with the sample oriented normal to the inspection plane, as illustrated in Figure 35.

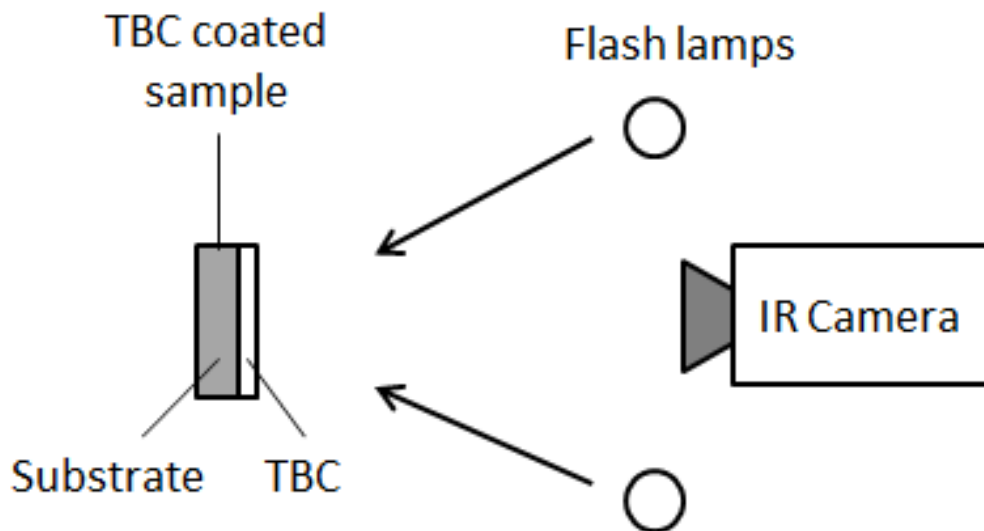


Figure 35 – Thermographic data capture experimental setup.

An advantage conferred by the Thermoscope system is that it can synchronise the triggering of the flash heating with the timestamp of the captured frames, ensuring a set number of frames are captured pre-flash, where the start of the

flash heating is also known. This helps resolve one of the problematic issues in PT, regarding the timing of the start of the flash pulse. The implementation of the system setup is shown in Figure 36.

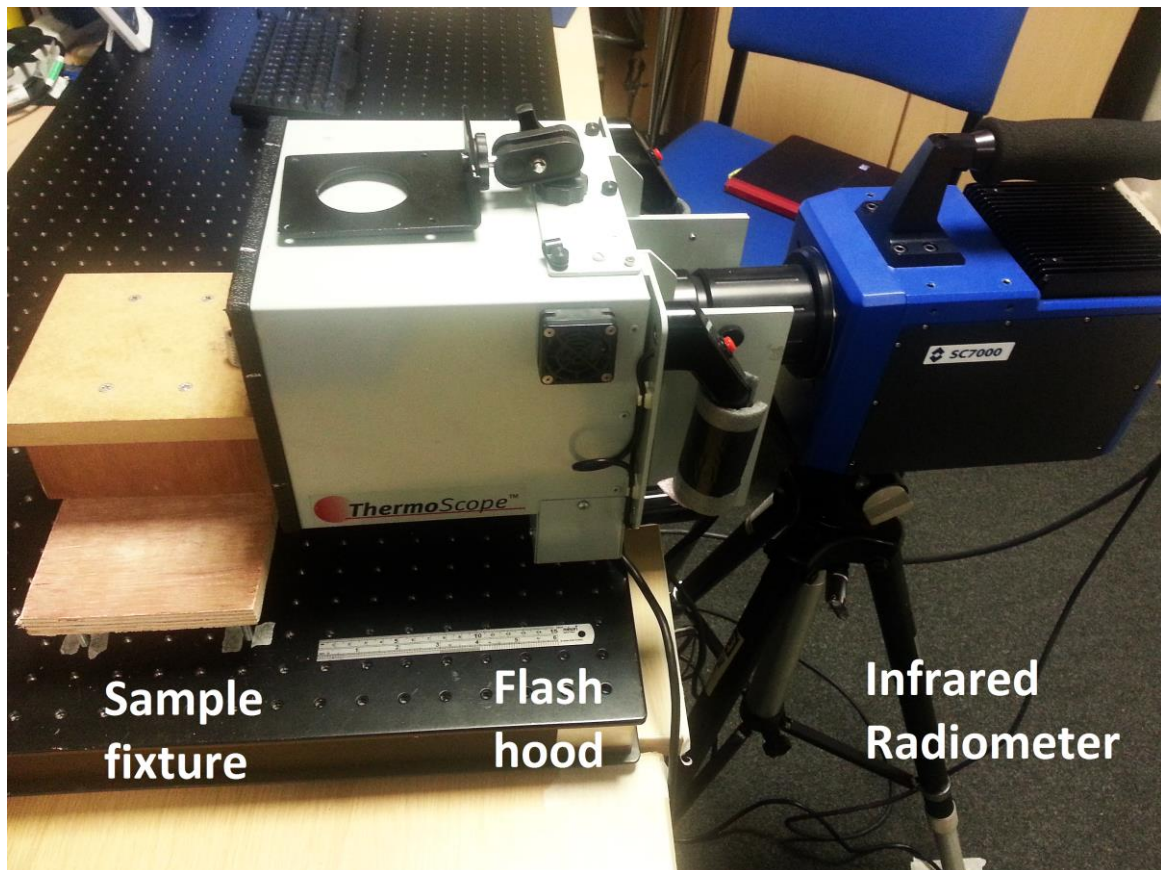


Figure 36 – Experimental setup of flash thermography equipment, showing the sample fixture (left), flash hood with xenon flash lamps (center), and radiometer (right).

The system captures raw radiance of the target in the infrared spectrum, recording a series of thermograms. These are recorded in data cubes as camera digital level in a ‘raw’ data format produced by the system.

5.1.2 Data processing: Two-layer thermal pulse model

Applying the 1D solution for heat diffusion of a non-uniform ideal (Dirac) pulse on the surface of a thin homogeneous layer, as proposed by Philippi, Batsale, Maillet & Degiovanni, (1994) [147], and further developed by Bison, Grinzato, Marinetti

(2004) [150]; & Robba, Lorenzoni (2006) [152], (2007) [148], the in-plane and through-thickness diffusivities can be estimated – if the thickness of the TBC is known. The model is given by:

$$T(t) = \frac{Q_0}{\varepsilon_c \sqrt{\pi t}} \left[1 + 2 \sum_{n=1}^{\infty} \Gamma^n e^{-\frac{n^2 l_c^2}{\alpha_c t}} \right] \quad (5-1)$$

where $\varepsilon = \sqrt{k\rho C_p}$ is thermal effusivity, $\Gamma = (\varepsilon_c - \varepsilon_s) / (\varepsilon_c + \varepsilon_s)$ the reflection coefficient between the coating (c) and substrate (s), α_c is coating diffusivity in (m²s⁻¹) and l_c refers to coating thickness; t is the time after the flash heat application (s). By fitting this model to the data it describes, returns an estimation of thermal thickness (thickness² / diffusivity), effective effusivity, and coefficient of reflection [148].

In modelling the heat conduction of a gaussian heating profile of a laser spot, applying Hankel and Laplace transforms, Bison et al. noted that their solution integrated the surface temperature as a general solution that also corresponded with the solution for a spatially uniform pulse [150][148]. This was an exciting development, as it equated the method with the ideal flash condition.

5.1.3 Data calibration: digital level to temperature

One of the aspects of the Thermoscope II[®] system is that its interface with the camera extracts the raw Digital Level data, which does not come temperature-calibrated. While this confers advantages in that the system can synchronise data capture with the timestamp of the radiometer framerate, in the system setup used, it records in raw digital level format. A critical step, therefore, before fitting the two-layer model to the temperature data, as described in the previous section, is to convert the output data into the temperature domain. This step was performed

by first using the manufacturer’s software to generate calibration curves for the selected integration time, which generate a series of points along the calibration curve, shown in Figure 37.

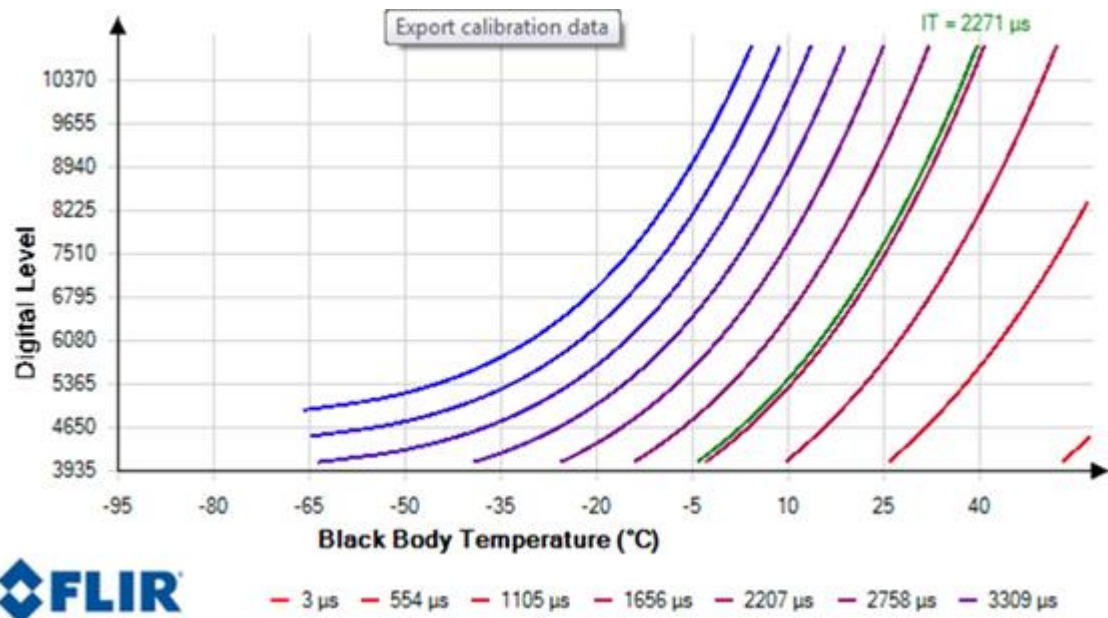


Figure 37 – Integration time adjustment for FLIR SC7600 with calibration curves for integration time vs temperature range as produced by the manufacturer’s software.

A low-order polynomial was fitted to these curves to enable the calibration of points in the integration time range to be interpolated and converted from the sensor’s digital level outputs into the temperature domain, as shown in Figure 38. This fitting solution would enable calibration of the raw temperature data measurements, however, readings below 0 or above 40°C could have a significant error introduced into the reading, observable in Figure 38 and shown exclusively in Figure 40.

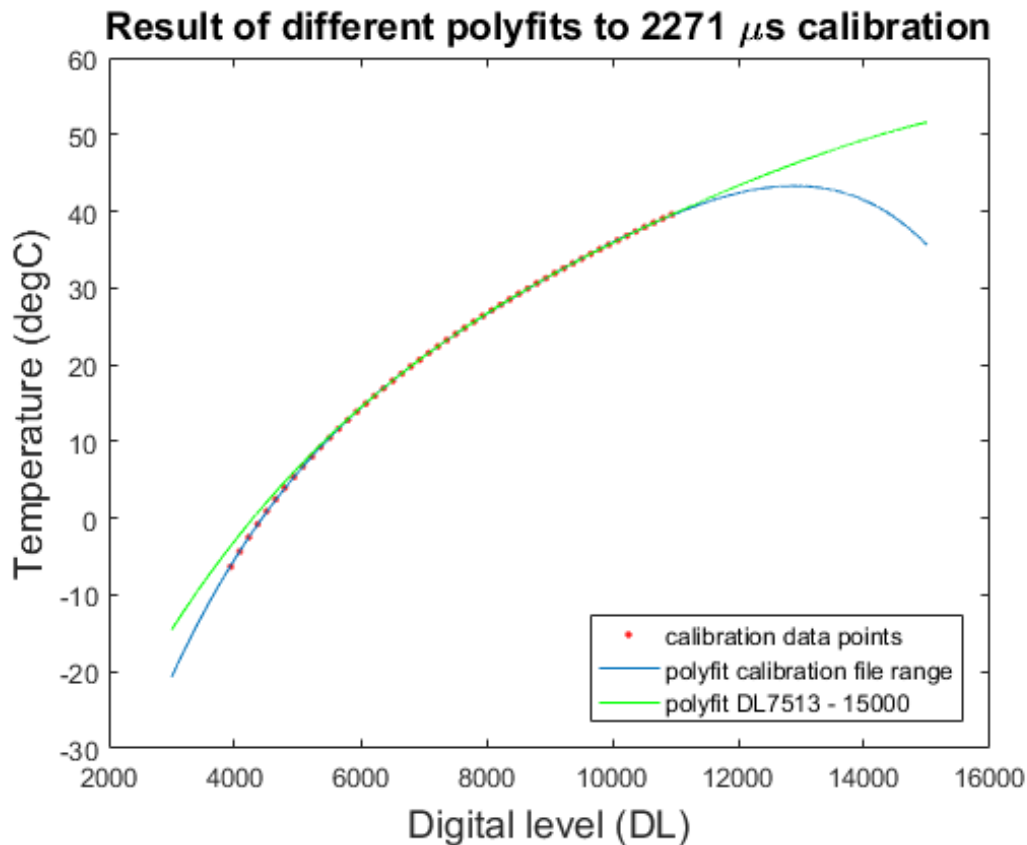


Figure 38 – displaying and fitting to camera temperature calibration curves and the problem encountered attempting to calibrate pixels captured beyond the data range.

Considering the time of year, data captured during the experiment would not be expected to fall below 10°C, but post-flash frames could be expected to exceed 40 degrees or more, introducing an unnecessary source of error to the data that is to be used for measurement of diffusivity. The calibration curve was fitted in two steps, to allow the shape of each end of the calibration curve to be captured; these two curves were extended beyond their range to encompass the actual temperature and digital level range that could be recorded by the system, and the projected data points were then fitted again, to enable the full range of captured data to be fitted, and accurately. This hybrid calibration curve is shown in Figure 39, its significant reduction in error of fit against the calibration curve shown in Figure 40 in comparison with the other preliminary fits.

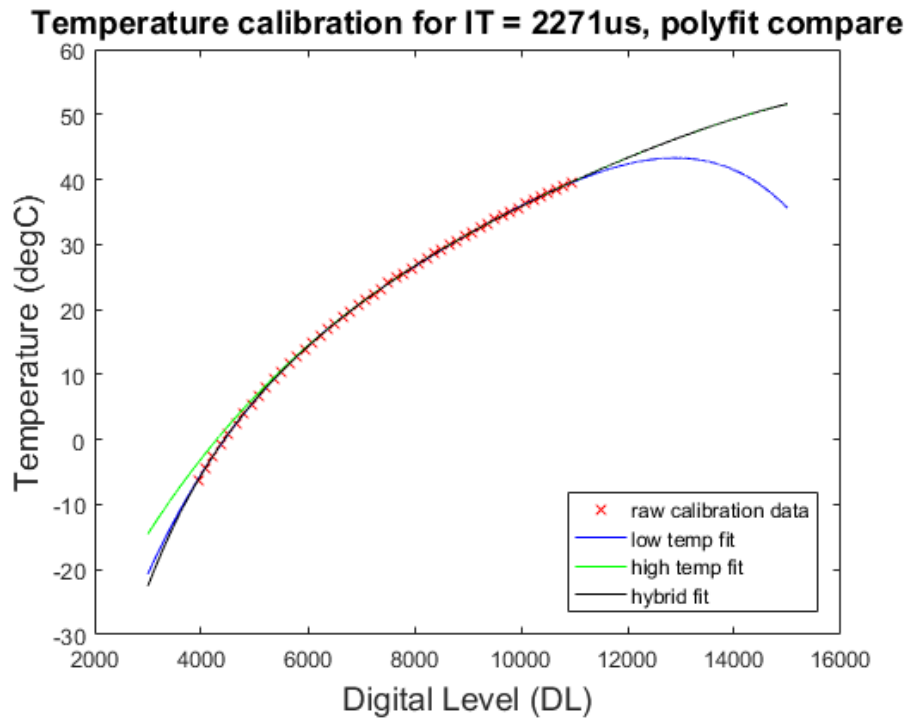


Figure 39 – final calibration curve: fitting a hybrid of low and high range data points, extending beyond the range to follow calibration curve; then re-fitting to full range.

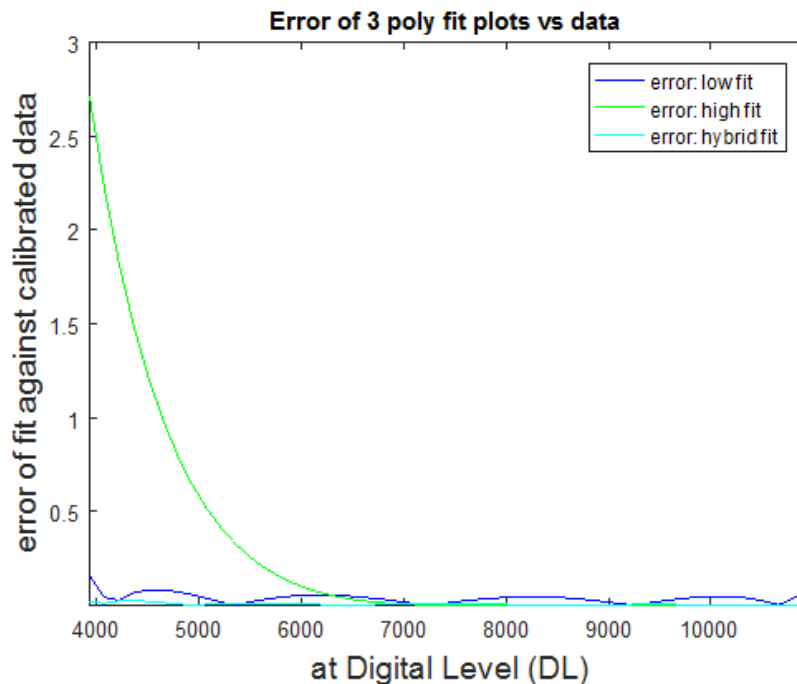


Figure 40 – plotting error of each calibration fit against the calibration curve data, for low temperature range, high temperature range, and the hybrid fit (lowest error)

For illustration of the scale of the error, this was plotted over the temperature range, and compared to the “Noise Equivalent Temperature Difference” i.e. the

smallest detectable temperature difference (the level of noise) expected from the system when operated at 25 degrees. This is shown in Figure 41, indicating the low error produced by the hybrid fitting step. It is impossible to compare the fit beyond the calibration curve, however the error reduces towards the higher temperature range. While the other fits both used exclusively the real calibration curve produced by the tool, both their fits when carried beyond the edge of their respective ranges (fit to the whole set, or to the high or low temperature range), expressed error above the system's lowest temperature error rating, or "noise-equivalent temperature difference", the smallest resolvable temperature difference detectable by the system, given by the manufacturer as $\sim 0.02^\circ\text{K}$. In comparison, the error of the hybrid fit is shown in Figure 41, < 0.02 , over 5°C .

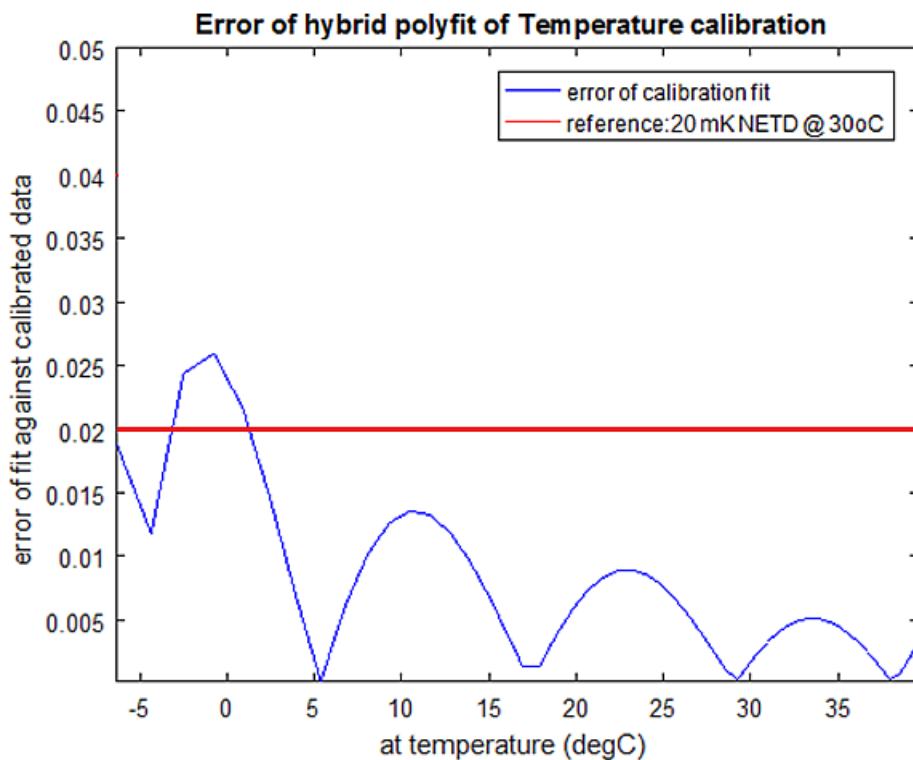


Figure 41 – plotting hybrid calibration curve error over temperature range, compared to 20mK, given as the camera's NETD

Integration time is the length of time (usually given in microseconds) between each frame readout, that the pixels are “open” to collecting incident radiation, before they are read and cleared. One issue is that the framerate is limited in a trade-off with the integration time, in that a long integration time yields a short framerate, but to get a high framerate requires a short integration time, which may not be sufficient for the radiometer to accurately capture the incident thermal radiation; much like a fast shutter speed on a camera in low light can result in an under-saturated image. To enable the system to achieve the highest framerate, the field of view was reduced to 25% of its full pixel window size, enabling the hardware to capture at that rate over less pixels, called “window mode”. Longer integration times would reduce the maximum framerate, while lower framerates would reduce the amount of data available to fit the model to, both of which are important for capturing a sensitive, fast thermal event, such as a heat pulse diffusing through a TBC. The highest framerate at 25% window mode that was accessible to the longest integration time selected of 4000 μs (the ideal integration time according to pixel well fill estimations), was 200 Hz. This was therefore used as the highest framerate for the tests, as it was both greater than those used by other researchers for coatings down to 170-250 μm , and would be available to all other experimental factors equally, therefore eliminating framerate as a factor.

5.2 Data capture parameters

In order to ascertain the key data capture parameters for the experiment, an analysis was required. However, because the objective sought from the study was the response parameter, and its real value was not known a-priori, the

approach carried a different objective of seeking a 'stable region' of the response that would occur around the ideal parameters, instead of the classic approach of minimising / maximising the response parameter, or producing results close to the pre-known value. This approach was not easily exploitable in traditional experiment design; thus, the approach for the parametric study followed a quasi-experimental design [181], loosely following a Fractional Factorial design.

An important consideration in this experiment is that a broad set of parameters affect the temperature readings which in this inspection method are all feeding into the diffusivity estimation. The full range of factors can be substantial, depending on the number of levels selected for each factor, and particular differences in equipment available. For instance, a laser would deliver a large heat burst in a short pulse, which is ideally suited for the Dirac pulse modelled in equation (5-1). Meanwhile, in the setup used, which uses flash lamps, the lamps may need to be used on higher settings to deliver the required pulse, but this may come additionally with an additional post-flash afterglow; making the problem recursive in nature when attempting to select the optimum parameters, when numerous factors apply. In order to respond to this, a parametric approach was adopted.

5.2.1 Parametric Study

From the setup apparatus described above, the tests entailed 5 key factors, each with different levels available for selection with each:

(a) Integration time of the infrared detector, which is similar to shutter speed for a photographic camera i.e. exposure time before read-out of a shutter free detector.

(b) The heat application energy, which in this case is given as a % of maximum flash power, referring to the % of the capacitor bank's full output

(c) The application of a soot coating to the surface to improve emissivity, which is usually applied in all experiments considering the translucency of TBCs in infrared and visible light [182] [183], however, it is desirable for real-world tests to forego this, hence the soot-free inspection requirement

(d) the start (offset), and (e) end (window length) of the data capture required to accurately the model to fit to, which needs to approximately follow the 1D modelled scenario.

The last two factors are important at the analysis stage because of difficulty in determining the termination of the flash and its afterglow, as well as the need with a fast thermal event to use a sufficient number of frames for calculation without inclusion of the rear wall of the sample.

The experiment required the resolution of multiple parameters in two classes; data capture (factors A, B, C), and analysis (D & E). The full series of factors and their broad range of level options can be seen in Table 7.

Table 7 – initial setup parameters options

Index	Factor	Units	Level (1)	Level (2)	Level (3)	Level (4)	Level (5)	Level (6)	Level (7)
A	Integration time	μs	1000	2000	2271	3000	4000	-	-
B	Flash intensity	% max power	25	50	75	100	-	-	-
C	Soot coating	applied	No	Yes	-	-	-	-	-
D	Frame offset	number	0	1	2	3	4	-	-
E	Window limit	number	10	12	14	16	20	30	40

Integration time and flash powers were selected at broad steps representing barely sufficient (1000 μs , 25%) to full (4000 μs , 100%). In the case of IT = 4000 μs , this was the value that returned the sufficient quantum well saturation, discussed shortly. Soot coating had only two levels, while frame offset and window limit were selected by a quick estimation of diffusion depth using approximate values for TBC thickness and diffusivity, setting a window length range that is insufficient (10), and in excess of the break time for the heat pulse, at the given maximum framerate accessible (200Hz). The offset frames of 0-4 was selected from 0 offset, arriving during the the post-flash afterglow, to 4 frames, arriving $4/f = 0.02\text{s}$ later.

In the preliminary experiments, a variety of ‘soft’ experimental influences included: differing waiting duration between data captures; captures taken at different points through the day, between different days, entailing differing ambient conditions during data captures. This involved a series of repeat measurements to capture the inherent variability in the experiment. Aside from confirming the necessity to wait for 15 minutes between data captures, and finding a poor signal from an integration time of 1000 μs (as was expected from estimation of quantum well saturation falling below the minimum recommended 20% given, for that exposure time), very little insight was gained from these initial

trials, the results of which can be found in the full preliminary results presented in the appendices.

Integration time, quantum well saturation

The levels for these were selected along the following basis: the radiometer was calibrated at an integration time (IT) of 2271 μs , and this was used as a benchmark for the low setting, with variations higher, and lower, along the following argument: Integration Time for thermographic imagers is the exposure time for filling each pixel with light. A longer IT gives a stronger saturation at a given temperature, and a shorter IT permits an increased framerate, however with reduced saturation, and with it an increase in relative noise. The recommended working region for filling the sensor pixels at a given temperature is stated by the manufacturer to be between 20-80% saturation. An IT of 2271 μs , for example, fills each pixel $\sim 12\%$ at 20 degrees, and 17% at 30 degrees (the approximate temperature range of the flash test). These values were obtained using the Planck Calculator applet that is provided from the manufacturer, and enables an estimation of well saturation from incident radiant light that should pass through the lens and IR filter. This calculation depends on the temperature of the target, the bandpass of the filter used, and the integration time parameter used during the capture.

Meanwhile, an IT of 4000 μs fills the well $\sim 20\%$ at 20 degrees, and 30% at 30 degrees. This is within the recommended working region of 20-80% saturation, and theoretically is the best integration time to use, provided it yields a sufficient framerate. Longer integration time limits the maximum framerate; an IT of 4000 μs permits 200 Hz, and this integration time will be used to provide sufficient

saturation, while setting the maximum framerate at 200 Hz. This is in excess of other active thermography experiments on thin TBCs, which can be found in Table 5 in the literature review, and utilise framerates of 120-150 Hz. The integration times and their saturation values were estimated using Planck Calculator, estimating pixel saturation for a user-specified integration time and scene temperature described above; the well saturations are shown in Table 8.

Table 8 – Quantum well saturation of the detector for a set of integration times

Integration time (μs)	Well fill (% saturation) at 20 degC	Well fill (% saturation) at 30 degC
2271	12%	17%
3000	15.50%	22%
4000	21%	30%

It is possible to use 4000 μs within specific analysis parameters. The result and stability of the fitted diffusivity outputs obtained at each of the various framerates were captured for analysis and comparison, in parallel to the main focus of the parametric study; these results will be discussed in Step three: Integration time. In order to ascertain how those values were selected, it is necessary to cover additional steps; however, in Step Four, the level options for IT were reduced to two, further reducing the total number of experiments while still covering the calibrated setting of 2271 μs , and the estimated “ideal” saturation setting of 4000 μs , as shown in Table 8. This reduced the 5 integration time levels from Table 7, with Flash Power (FP) still varied at 4 settings alongside the 2 soot coating condition parameters. This design matrix is shown in Table 9.

Table 9 – High (+) and Low (-1) settings for parametric study

Factor	SC	IT	FP
Levels	2	2	2
+	yes	4000	25%
-	no	2271	50%
			75%
			100%

These settings can then be used in a Full Factorial Design of Experiments, with full variation of the parameters against each other, in a series of 16 experiments, the set-up of which is shown, also with level settings used in Table 10.

Table 10 – 2³ Three Factor, 2(2), 1(4) mixed-mode design of experiments tabulation, with runs in ‘standard order’ (left), and full factorial design of experiments, with factor levels used (right)

Run	SC	IT	FP
1	-1	-1	1
2	1	-1	1
3	-1	1	1
4	1	1	1
5	-1	-1	2
6	1	-1	2
7	-1	1	2
8	1	1	2
9	-1	-1	3
10	1	-1	3
11	-1	1	3
12	1	1	3
13	-1	-1	4
14	1	-1	4
15	-1	1	4
16	1	1	4

Run	SC	IT	FP
1	no	2271	25%
2	yes	2271	25%
3	no	4000	25%
4	yes	4000	25%
5	no	2271	50%
6	yes	2271	50%
7	no	4000	50%
8	yes	4000	50%
9	no	2271	75%
10	yes	2271	75%
11	no	4000	75%
12	yes	4000	75%
13	no	2271	100%
14	yes	2271	100%
15	no	4000	100%
16	yes	4000	100%

5.2.2 Step one: background parameters

Framerate Using the TBC thickness, and thermal properties of similar TBCs from literature, provided the following properties to get an initial idea of the parameters required:

Table 11 – estimation of manufactured TBC coupon properties

Property	Value	Units	Source
Thickness	150	µm	SEM scan
Density	3600	kg / m ³	Zhao et. al. [184], Fig.8
Conductivity	1.0	W / m.K	Zhao et. al. [184] Fig.8
Pore fraction	40	%	Zhao et. al. [184] Fig.9
Diffusivity1	6.7 x 10 ⁻⁷	m ² /s	Kakuda et. al. [73], Fig.3 @ t=0 hr
Diffusivity2	8.6 x 10 ⁻⁷	m ² /s	Kakuda et. al. [73], Fig.3 @ mean (t=1-

These values can be utilised with relation (2-5), which can be arranged:

$$t^* = \frac{L^2}{\pi\alpha} \quad (5-2)$$

yielding the expected transition point to correspond to: $t^* = 0.0830 - 0.0107$ s

where the shorter of these times corresponded to the following frame numbers:

$$frame = frequency \times time \quad (5-3)$$

which for the shorter break time, yields:

@30 Hz = frame 2.49 @50 Hz = frame 4.15 @200Hz = frame 16

Considering the noise expected from the post-flash afterglow in the early frames, it is entirely impossible to expect the fitting process to be able to extract any

information from the first two frames, while using only 4 or 8 frames are similarly insufficient; for this reason, a high framerate of at least 200 Hz is required.

Flash temperature & flash duration

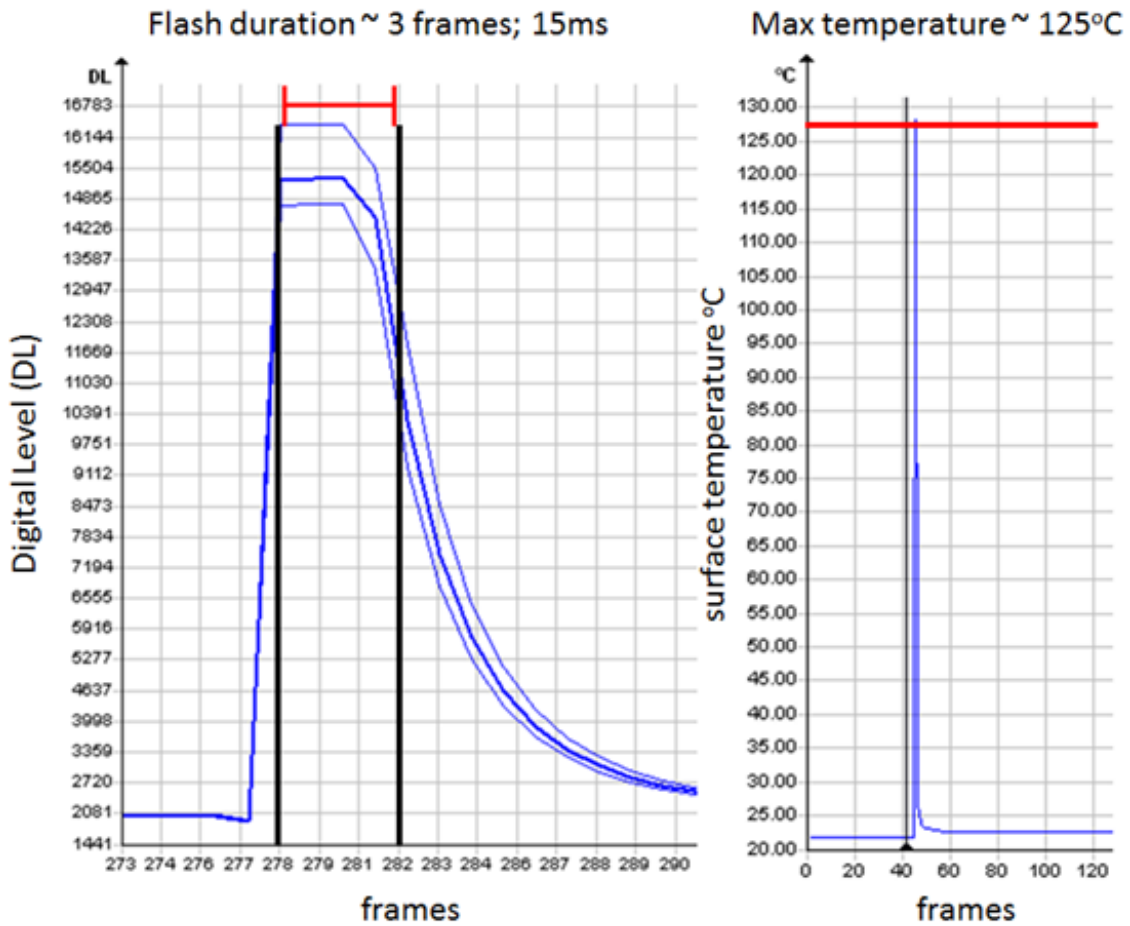


Figure 42 – estimation of flash temperature to predict data range, and duration of flash for estimation of afterglow effects for preliminary trial settings.

In order to properly select the appropriate integration time, as discussed in Parametric Study, and Step three: Integration time, it was important to capture the expected temperature range within which data would reside, and investigate the flash pulse and afterglow effects. This was captured at an integration time of 4000 μ s, and indicated that the flash itself exhibited a “hot” flash temperature of over 125°C+. The real temperature would possibly be beyond accuracy of any

integration time selected, however since the flash frame is saturated and not of interest for the data fitting stage, the post-flash data itself after 1 frame resided within the 20-30 degree range; this was key for selection of appropriate integration time, to enable a calculation of sensor saturation using the manufacturer's tool, giving the temperature range for Table 8.

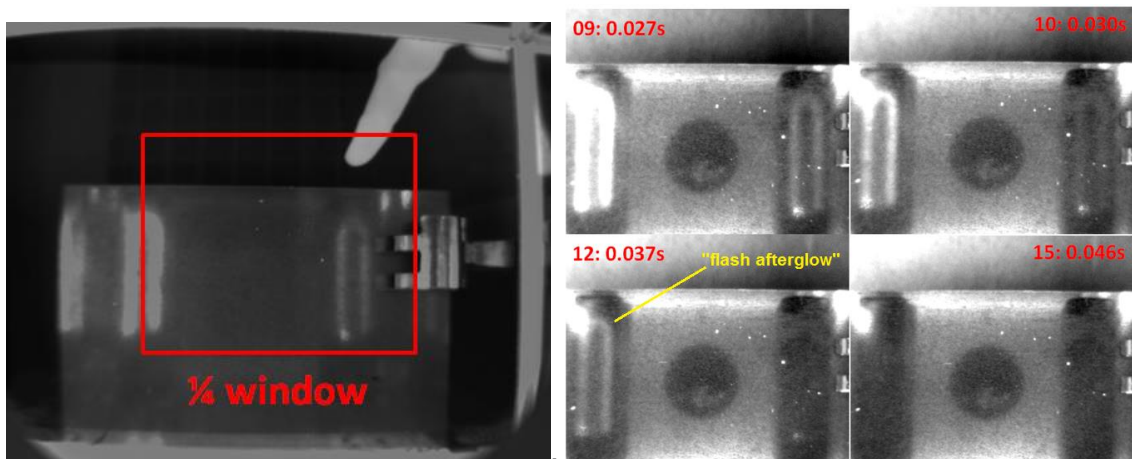


Figure 43 – investigation of flash afterglow (marked), demonstrating a number of frames after the flash, introducing problems to inspection without soot condition

Additionally, the afterglow was investigated at high framerate 328 Hz, IT 2271 μ s, as detailed in 10.1Appendix B. This experiment determined that the post-flash “afterglow” could no longer be detected in direct reflection on a plain aluminium surface beyond 0.04s after the flash. At 200 Hz, frame length is 0.005s, meaning that the afterglow would be present in heating the sample over up to 8 frames at 200Hz, and therefore the afterglow was considered a significant and uncontrollable factor, which had to be accounted for in the data analysis step discussed in the next sub-section; Step two: data window.

Flash intensity; wait time

One consideration in the experiment is the selection of flash power and the wait time required between inspections. An experiment was conducted by flashing samples with a capture of 20 minutes at 10 Hz, as shown in Figure 44 showing that the inspection for each flash power level had returned to its initial temperature (22.3°C for 25%, 22.4°C: 50%, 22.6 °C: 75% & 22.9°C: 100%) after less than 15 minutes (900s), and the “cool-down” time of 15 minutes between inspections was selected, for data captures on the same sample. For fresh change-overs, if proper care had been taken not to transfer body heat to the samples upon placement before the inspection system, a wait time of 5 minutes was observed.

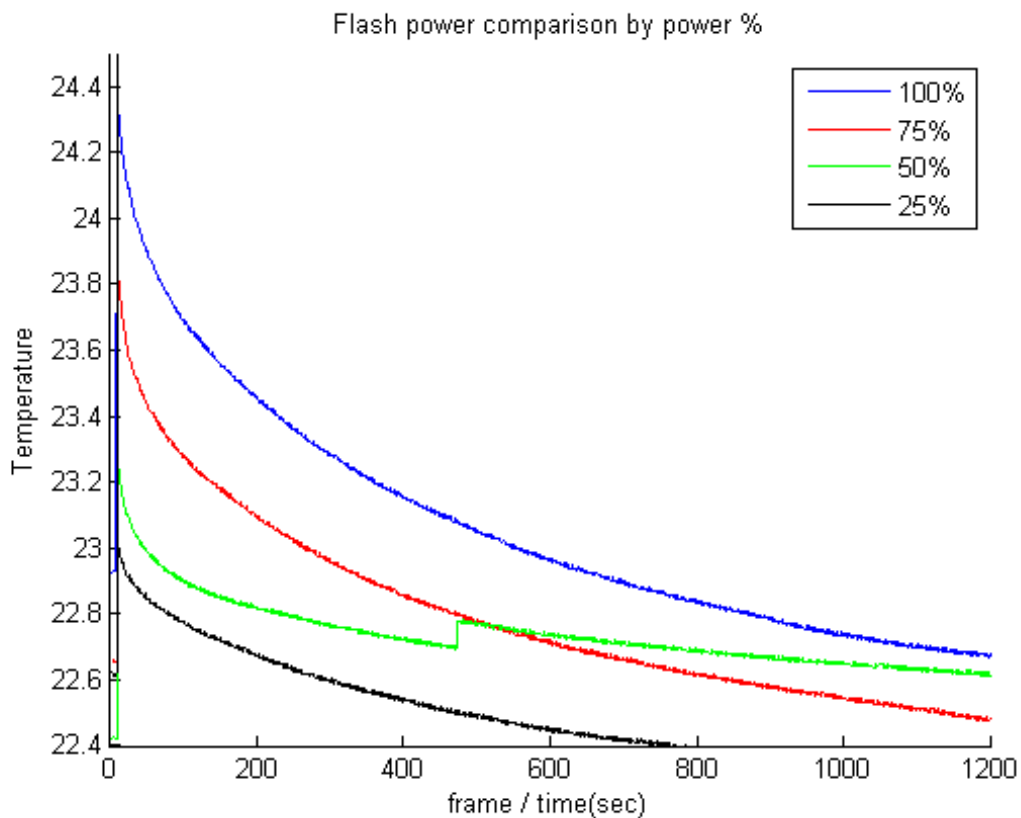


Figure 44 – comparison of different flash intensities on sample cool-down. Effect of ambient light leaking into inspection cell via removal of protective cover also indicated by the mid-recording ‘step’ in the data capture for 50%.

Sample emissivity

Prior to the main experiments, the selection of emissivity of TBC coating was performed. This was conducted by placing electrical tape (thermal emissivity ~95%) on the surface of a TBC coated sample, recording a video of the scene as the sample is heated with hot air. A data box for measuring effective temperature was placed on each side of the sample (in this case, a real TBC from a guest component), and the averages displayed. The software enables manual tuning of emissivity for temperature corrections, related to radiated power to the fourth power of body temperature via the Stefan-Boltzmann law:

$$P_r = e\sigma AT^4 \quad (5-4)$$

where P_r is the emitted radiated power in watts, e the emissivity of the material (between 0 and 1), A surface area, σ Stefan's constant ($5.67 \times 10^{-8} \text{ W/m}^2 \text{ K}^4$) and T is the object temperature. The contribution of atmospheric absorption and reflected ambient temperature via kirchoff's first law (2-2) also needs to be incorporated. The emissivity setting was varied until the temperature measurements agreed. By limit of emissivity setting available, this gives an uncertainty in the emissivity value (measured at approx. 35°C) of 0.89 ± 0.005 .

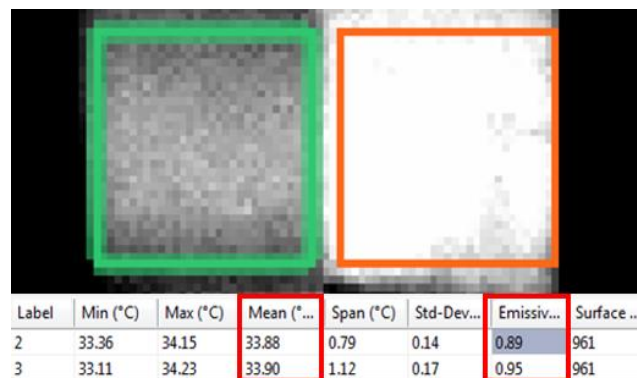


Figure 45 – emissivity estimation of TBC using manufacturer's software to match emissivity estimate to yield the same temperature (2, left) as the electrical tape (3, right)

5.2.3 Step two: data window

One major problem introduced with thin coatings being investigated, is that the thermal event being investigated is a very rapid event, yielding few frames for the data analysis process before the event is over. As discussed above, the duration of the afterglow when using flash lamps is one aspect that needs mitigation. It was not known that the offset of up to 4 would be sufficient with the uncoated condition, but from preliminary trials the data fitting went well, and the analysis parameters could always be changed later. Another key aspect is the need to use sufficient frames for the heat pulse, but without the excess of either the post-flash afterglow, or beyond the substrate, as illustrated in Figure 46.

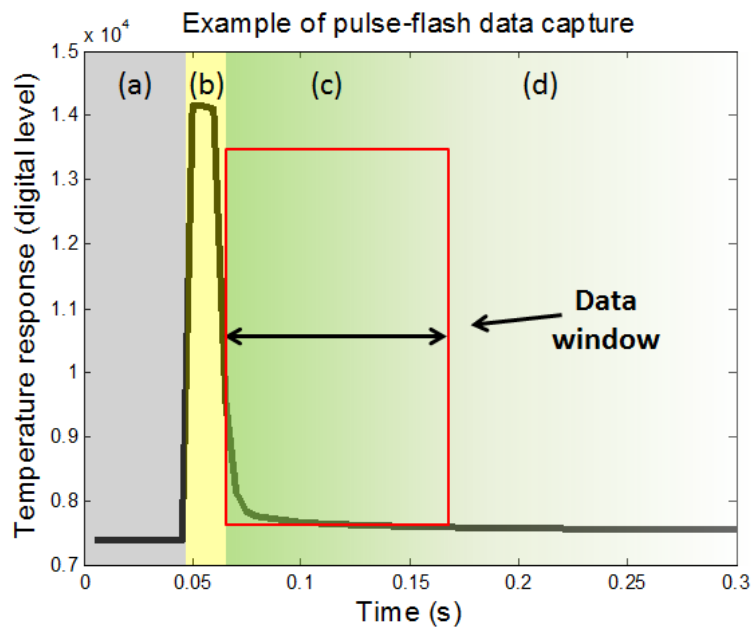


Figure 46 - Illustration of the data output showing different regions within the data, from pre-flash (a), flash duration and post-flash heating effects (b), coating data window (c) and heat pulse diffusion into the substrate material (d).

The trend sought from the parametric study was for a stable region of thermal diffusivity, coupled with a high value of R^2 (coefficient of determination between the model-fit and the data). Initially, a data offset is required to start capture after

the flash to begin after the afterglow has sufficiently diminished; while the second part of the window is the cut-off, which needs to terminate data capture before the recordings reflect the un-modelled behaviour of the thermal wave encountering the rear surface of the substrate. For flash lamps, the termination of the afterglow can be uncertain, as it falls over multiple spectra – and even with application of a filter, does not change the heating being still being applied to the surface of the material while the data capture begins. Meanwhile, it is important to have data that occurs both sides of the transition of the heat pulse into the substrate, but that it does not reflect any further behaviour than described by the model, or the calculated value of diffusivity will be less accurate. This can be easily approximated for thick coatings and large substrates, where the thermal event is slow with respect to the data capture framerate, and an approximate calculation can be sufficient; however when it comes to a thin coating, especially when the real location of the transition is unknown and the substrate is metallic, both layers can experience a fast thermal event as far as the number of frames being captured can describe. Hence, obtaining the optimum data window for calculating the diffusivity is a key exercise. With only a few dozen frames within the diffusion time available at accessible framerates, any initial frame still in the flash pulse will result in under fitting the solution to the data. Without knowing when the heat pulse encounters the interface, and having the constraints at both the start and the end of the data capture, this places limits on how the correct answer can be identified; which becomes useful for identification of the data window, as the fitting process should yield substantially different results as the parameters are changed further from the reality, either side of the ideal

parameters which contain the true value and a series of values close to it; the resulting approach is similar to optimisation, seeking a series of parameters which achieve a stable output of results obtained, either side of the optimum setting/s.

To illustrate the approach taken in the parametric study, a single experiment of it is shown in Figure 47; in it is contained a single data capture, where the x-axis entails 5 offset values (0-5), and in each subset contains a series of window variations (10, 12, 14, 16, 20, 30, 40) as described previously in Table 7. The full variations of this table in the estimations of resulting diffusivity estimation are contained in Appendix D; this was an early series of experiments and a very wide variety of parameters were varied, including waiting time between captures, captures on different days, captures with different integration times than otherwise detailed, and differences in practice of soot application. Parameter variations that are valuable to detailing are discussed in the text. A row of the matrix shown in Appendix D is essentially the plot of Figure 47 (in this case, it refers to y-axis 20, IT 2271, 50% flash power + other parameters).

The aim of this approach was to seek out 'stable regions' in which the estimation of diffusivity does not differ substantially with, for instance, flash power, and offset and window size, or how the inspection differs with repeat captures, under different ambient conditions and different wait times between captures, for example; hence the plot in Figure 47 is a partial solution to narrowing down and obtaining the solution to multiple optimal parameters simultaneously; as parameter conflicts would be expected to influence readings in any combination meaning that no parameter could be singularly evaluated without others being resolved, reduced or otherwise eliminated.

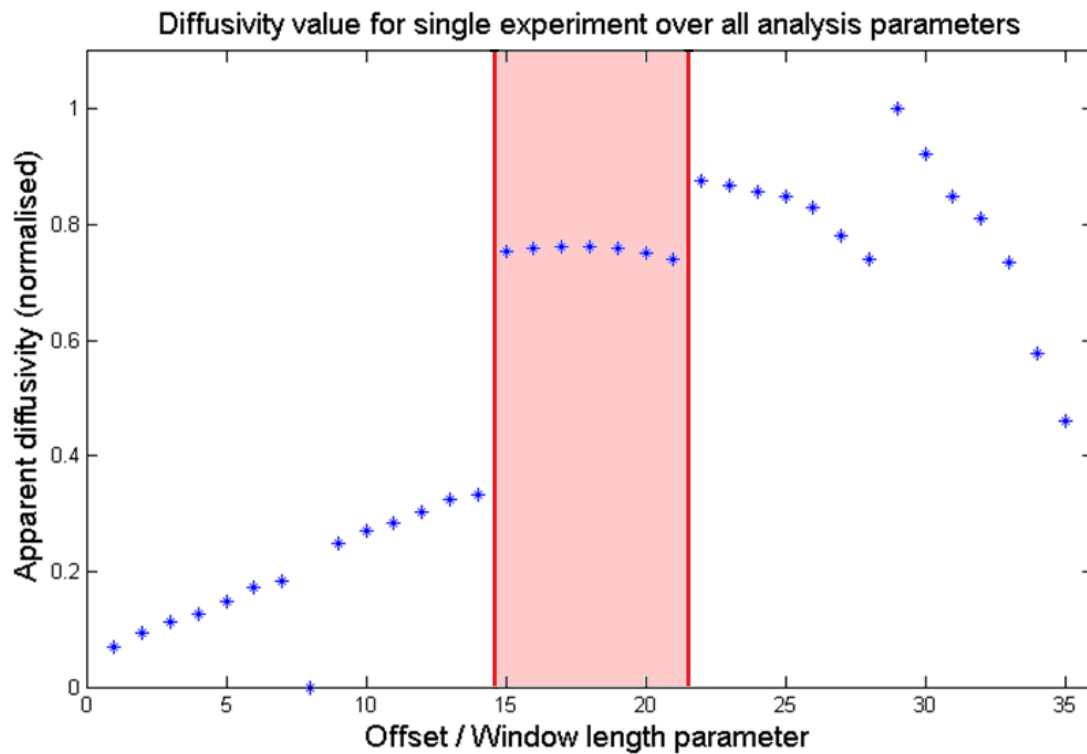


Figure 47 – plot of diffusivity results of a single data capture varied with analysis parameters (x-axis) taken with an integration time (2271us) and flash power (50%), cycling through data capture parameters in series from left to right: data offset (0), window length 10, 12, 14, 16..; data offset (1), window length (10, 12,..); (2), (10, 12..)

This approach permitted the selection of optimum parameter combinations simultaneously that result in stable regions of results, shown in Figure 47 (highlighted), where offsets (initial frame after flash) varied in the x-axis follows steps from 0-5 frames, with window length of 10, 12, 14, 16, 20, 30, 40 frames after the offset, in batches for each offset which in most examples showed a similar pattern within each group, yielding offsets of 0, 1, 3, and 4 as unstable offsets, with all window variations in each of these bands (Figure 47, unhighlighted) resulting in a marked gradient of difference in the values per subset; while offset of 2 is stable, giving the post-flash start frame, with minor variation for all window lengths. The sensitivity of this response down to the single-frame offset was not expected, but was not surprising considering the

amount of temperature information that is lost every frame after the flash, and the amount of post-flash interference in the first two frames; thus highlighting the importance of having taken this approach, when such a task was more sensitive than was initially understood. For a series of experiments at the two integration times, the estimated diffusivity was shown, indicating a strong ‘stable region’ under IT 2271 μ s, shown in Figure 48, which yielded the desired stable region.

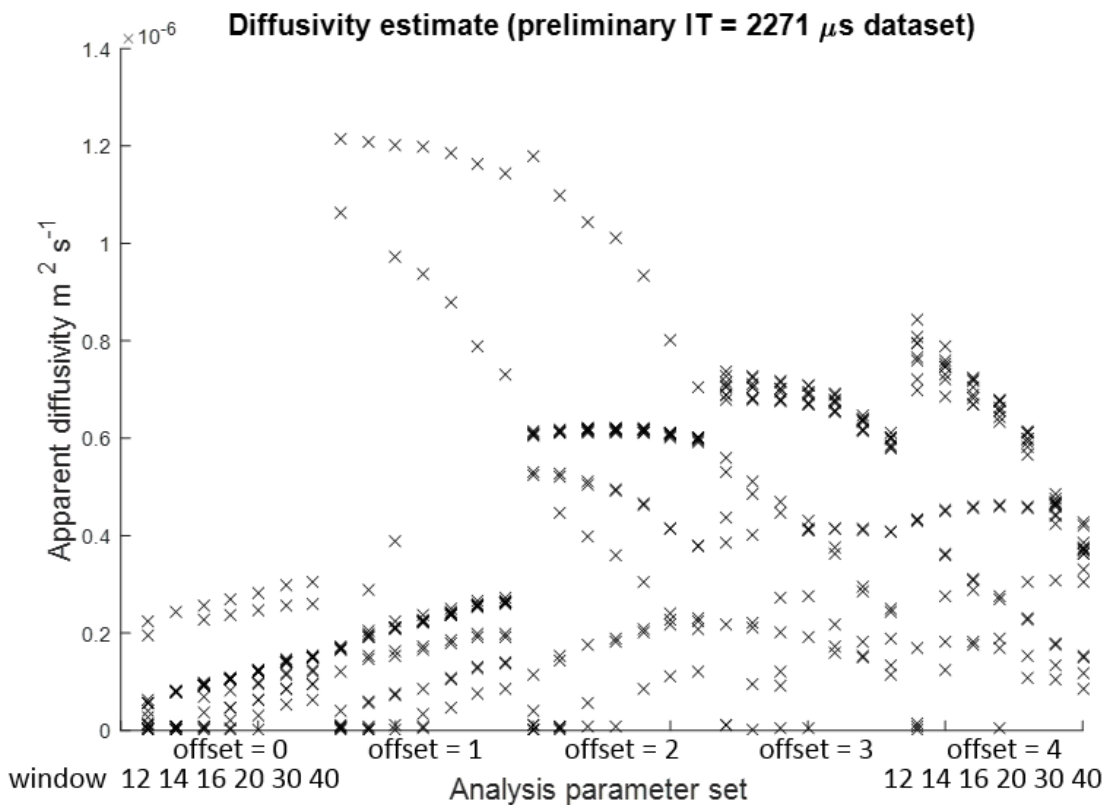


Figure 48 – estimated diffusivity values, for a range of data window parameters (offset 0, left, 4, right; and within each offset a variation of data window length 12, left, to 40, right); IT 2271 μ s.

Meanwhile the value varied quite strongly under IT of 4000 μ s was noisy over most analysis parameters, with strong noise in early offset values, and very little stability in the result estimation, becoming more consistent with greater offset values; as shown in Figure 49 for the 4000 μ s dataset.

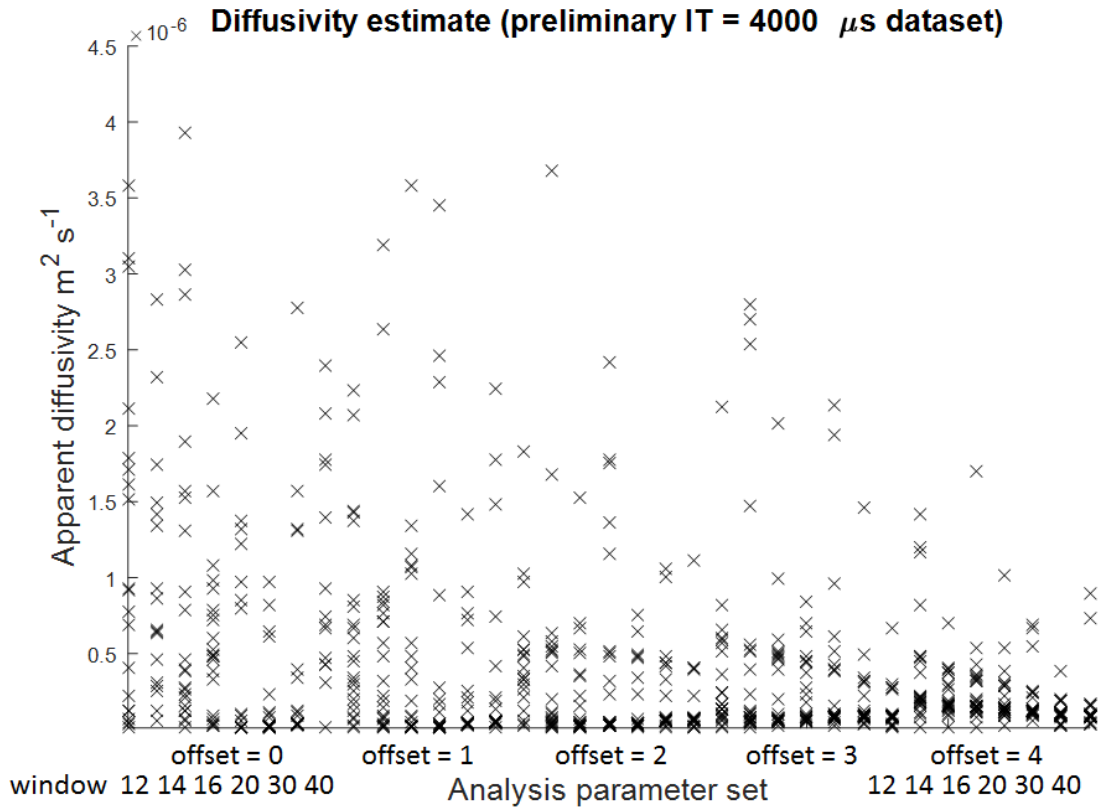


Figure 49 - estimated diffusivity values, for a range of data window parameters (offset 0, left, 4, right; and within each offset a variation of data window length 12, left, to 40, right); IT 4000 μs .

5.2.4 Step three: Integration time

While integration time of 1000 μs gave a strong consistent R^2 response, the output estimation of diffusivities (shown in Figure_Apx 6, Appendix D: y-axis 50-54 respectively) – showed a strong output correlation between integration times of 1000-2271 in terms of the estimation of diffusivity. Integration time is an important factor since shorter values are required for faster framerates, while longer integration times are required for lower temperatures. A short integration time at a given temperature may achieve a low saturation of the sensor. The range of saturation recommended by the manufacturer is 20-80%, and from use of the manufacturer’s Planck calculator mentioned previously, an integration time of 1000 μs , for a surface emissivity of 0.9 yields 5.3% saturation at 20°C, to 7.5%

at 30°C. This is the range of sample surface temperatures during the post-flash heat diffusion event (particularly the case after the first two frames have been skipped with the offset value), meanwhile, at the same range, an integration time of 4000 μs provides 21.1% and 30.0% well saturation respectively. Simultaneously, all offsets 2 and above yield similar results in R^2 response (the coefficient of determination of the fitted model to the temperature-time data), which is shown in Figure 50 for each integration time variation, where each horizontal data line is plot similar to Figure 47, the values of which actually makes up the central y-axis plot, for 2271 μs . While 1000 μs in Figure 50 yields the most high coefficient results, it also deviates from the others where an offset below 2 significantly spoils the result. The dominance of the post-flash afterglow expected in the first few frames may be sufficient to neglect the high coefficient of 1000 μs in the second frame. For offsets of 2 or more, and window limits of 14 or more (3rd value in each offset subset from the left); all integration times hold similar behaviour in their coefficient values, *except* the integration time of 1000 μs , raising doubt on its value, which was already expected to yield different results from the other sets from its low well saturation. In comparing the actual readings of diffusivity integration times, 1000-3000 μs conformed well to similar values; while 4000 μs differed substantially, and below the expected value from literature. Since 1000-3000 μs were consistently similarly stable around the literature value for offset 2+, (Figure_Apx 6, Appendix D; y-axis 50-53) compared to 4000 μs (y-axis 54), one of the three were selected: the IT at which the camera was calibrated (2271 μs), and the longer integration time (4000 μs), owing to its expected appropriate well saturation.

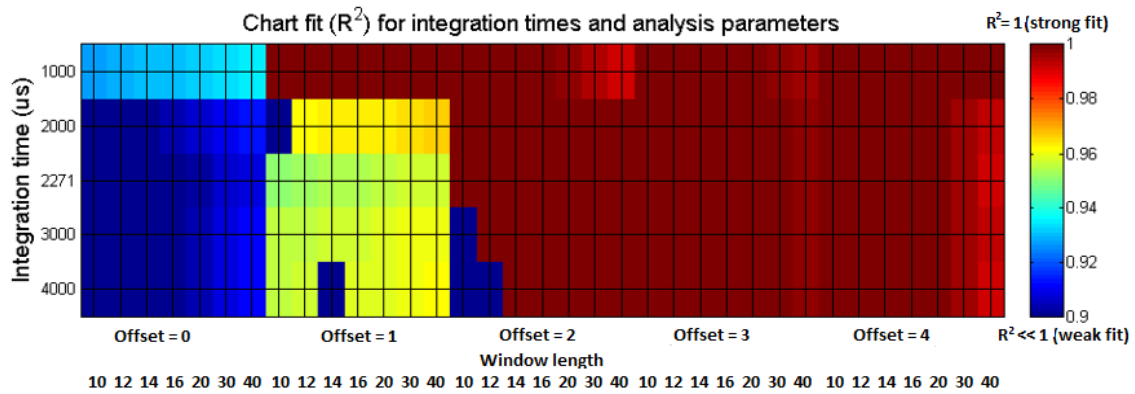


Figure 50 – Searching for stable settings using R^2 indicating accuracy of fit of the two-layer model to the data under the given experimental conditions, showing R^2 values for 5 experiments over different integration times at 50% flash power. Reproduced from Tinsley et al., (2017) [185], courtesy of Elsevier.

The resulting estimation of TBC diffusivity for each of the two IT levels were compared and found that the lower value of 2271 achieved resulting output that were less consistent over the variation of parameters, though closer to the reference value for EB-PVD TBC diffusivity. For this reason, both integration times were retained for the final parameter selections for the main experiment, to ensure that both aspects can be contained in the final data.

5.2.5 Step four: flash power intensity

Next, the effects of flash power intensity was investigated, varied from 25-100%. The low power was shown to achieve a closer fit of the model, with a higher R^2 , (see Figure 51), however the values for estimated thermal diffusivity changed more rapidly from one subset of varied parameters (varying 4 parameter per flash power, shown in Table 10, right), while the flash power of 50% approached the expected value of diffusivity for EB-PVD TBCs of between $6-8 \times 10^{-6}$ (see Figure 52), with less of an abrupt change either side of the expected value between the with and without soot condition, as is the case with the 25% parametric quartet.

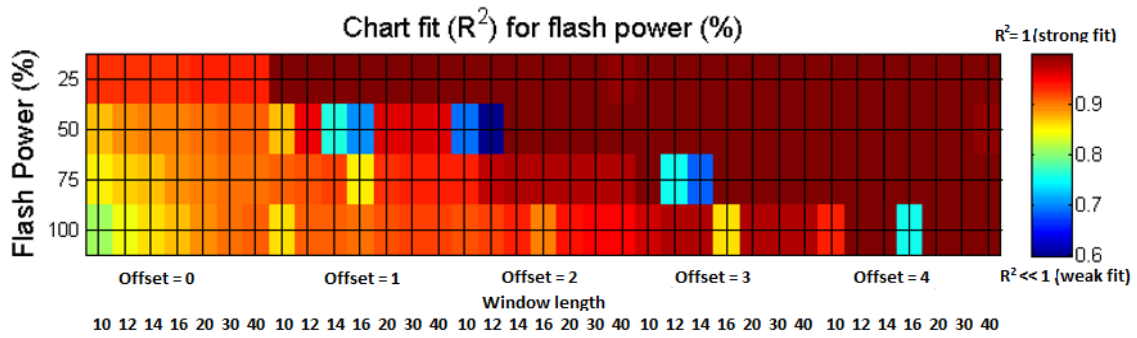


Figure 51 – maintaining a constant IT of 2271 μs , the result of different levels of flash power are tested for their R^2 stability over different fitting parameters., figure reproduced from Tinsley et al., (2017) [185]., courtesy of Elsevier.

Additionally, the higher flash powers yielded substantially lower than expected values ($< 3 \times 10^{-6}$) in with soot and without soot combinations, thereby eliminating them from selection.

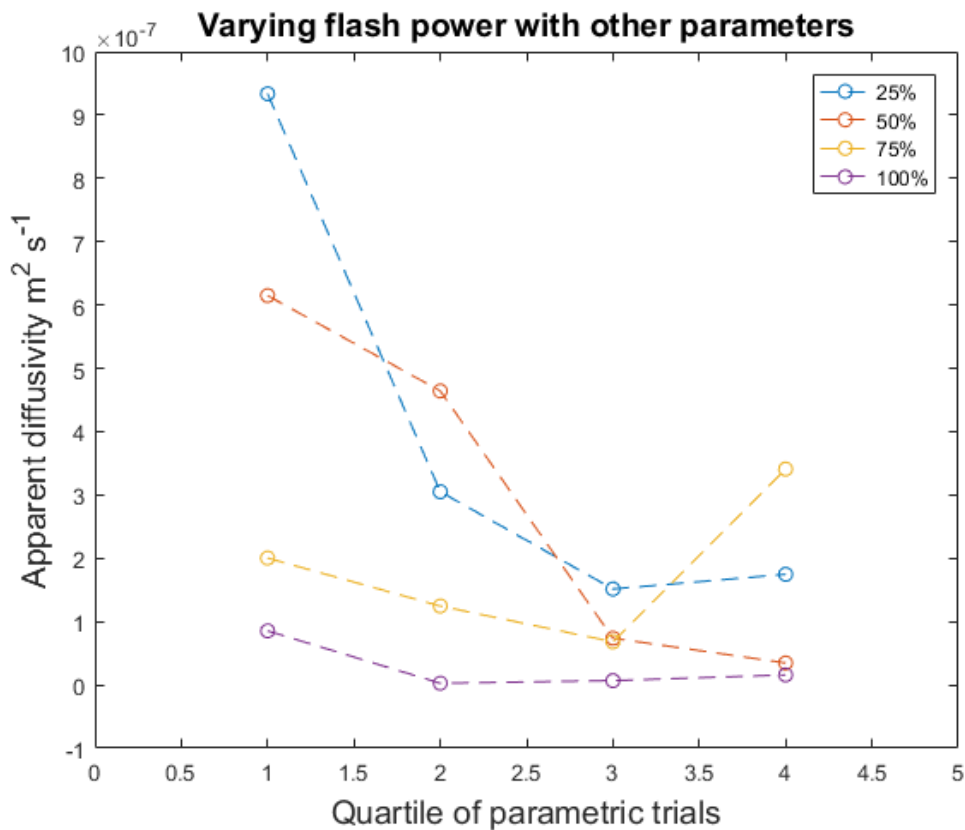


Figure 52 - Sensitivity analysis: flash power – result value with 4 parametric combinations for each flash power, identifying closest subset (50%, combinations 1, 2), where each data series is a quartet of parameter observations integration time (2271, left, Q1-2; and 4000, Q3-4, right), without soot condition (Q1, Q3) and with soot condition (Q2, Q4); refer to Table 12.

5.2.6 Step five: Soot coating influence

It was important to factor in the consideration of application of soot coating to the samples, and its effect on the resulting diffusivity calculation. While it is a given that the resulting temperature measurement without a soot coating will be less than the ideal data capture setup, and the measurement would yield a reduced estimation, it is of essential interest to this research whether the trend in the change of measured diffusivity values sought in the main experiment would exhibit a similar pattern that might be replicable without the application of soot coating. This would show the suitability of the test for application in real industrial context. The effect of this comparison on accuracy of the fitting step can be seen in Figure 53, and indicated that a strong similarity in stability of the fitting process would hold, showing that that the trend should be worth investigating as part of the main experiment. The resulting estimation of diffusivity for the with and without soot coating application in these cases can be found, in combination with variation in flash power and integration time, in Table 12, which are also displayed in Figure 52, where inspection without soot is shown in Q1, Q3, and with soot, Q2, Q4, where it can be seen that soot application reduces apparent diffusivity.

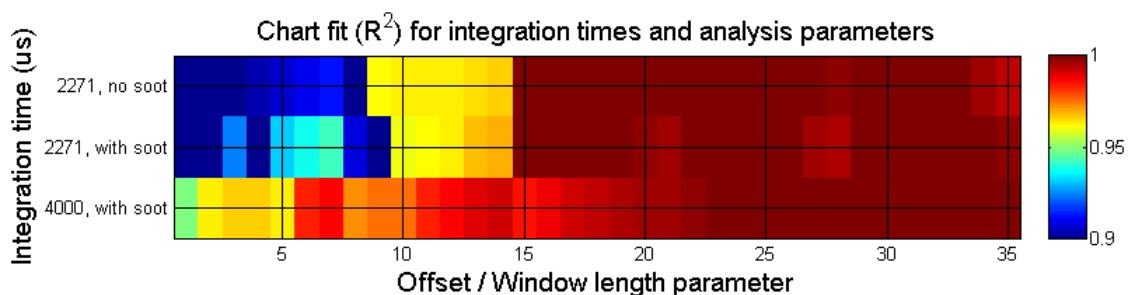


Figure 53 – R^2 difference achieved without soot, compared to with soot, and with soot at the integration time of 4000 μs . This shows that offset of 0 and 1 frame (x-axis 1-14) are particularly erroneous and unstable, resulting in poor fits of the model to the data, while the uncoated condition (top row) is similarly stable as the coated condition (mid row). Plot reproduced from Tinsley et al.,(2017) [185], courtesy of Elsevier.

5.3 Final parameter selection

Following these steps, the resulting outcome of these factors and level variations, computed using the data analysis levels of offset (2), window length (20), are shown in Table 12. All data recordings used a capture rate of 200Hz.

Table 12 – Full Factorial study results, based upon offset = 2, window length = 20

Run	SC	IT	FP	Alpha
1	no	2271	25%	9.34E-07
2	yes	2271	25%	3.05E-07
3	no	4000	25%	1.51E-07
4	yes	4000	25%	1.75E-07
5	no	2271	50%	6.15E-07
6	yes	2271	50%	4.64E-07
7	no	4000	50%	7.37E-08
8	yes	4000	50%	3.46E-08
9	no	2271	75%	2.00E-07
10	yes	2271	75%	1.25E-07
11	no	4000	75%	6.81E-08
12	yes	4000	75%	3.41E-07
13	no	2271	100%	8.54E-08
14	yes	2271	100%	2.57E-09
15	no	4000	100%	6.79E-09
16	yes	4000	100%	1.58E-08

Following from the discussion in the previous section, the final factor selections were reduced to 1 level for each factor; except for soot coating, which was retained in its two-level variation to enable the study of suitability for real industrial context requirement to be investigated. Additionally, while IT 4000 data was captured as part of the experiment to ensure the “ideal case” data could be captured for future reference, the experiment will focus on the more accurate results of IT 2271. These selections are shown in Table 13.

Table 13 – Final experiment setup, reproduced from Tinsley et al.,(2017) [185], courtesy of Elsevier.

Factor	Name	Units	Levels	Levels
A	Integration time	μs	1	2271
B	Flash intensity	% max power	1	50
C	Soot coating	Yes/No	2	Yes/No
D	Frame offset	number	1	2
E	Window limit	number	1	20

5.3.1 Summary

Following the employment of a full factorial experiment setup to investigate the broad range of available factors and their various levels, the data capture and analysis factors were reduced, particularly regarding the offset / window parameters, which were effectively eliminated, shown by Figure 47 - Figure 48. Additionally, the retainment of inspection with and without soot coating has been justified as plausible by the stable regions being repeatable in both conditions and the approach with expected reference diffusivity value; enabling the experiment to proceed, taking into account real context while also having inspection of the ideal case (with soot coating condition) to compare it with, throughout the ageing experiment. The justifications for full data capture setup, including discussion of the details themselves are not usually explained in literature reporting of similar works, and it was this knowledge gap that this part of the thesis has addressed. To conclude the experimental setup, the final parameter variations shown in Table 13 were the selected parameters for the full furnace cycling experiment, in the next chapter.

6 TBC lifing experiment

In order to artificially age the TBC samples, isothermal oxidation runs were conducted. Following from the selection of data capture and analysis parameters for use in the sample ageing furnace runs, the layout of the furnace runs was laid out, detailing how the samples were to be aged, and inspection performed. The decisions behind this setup were based on interviews with OEMs detailed in Chapter Four, and with other researchers at Cranfield University who have a strong background in study of TBCs. The samples for the lifing experiment were realistic to coatings provided by industry, to allow for the results to reflect real materials as close to the target scenario as possible. These were manufactured with parameters similar to the coupons in the previous section. Each of the samples were exposed in a box furnace at 1100°C in air, to provide a standard oxidation ageing mechanism for the inspection of TBC diffusivity properties over coating life cycle.

6.1 Inspection-exposure methodology

The TBC samples were subjected to oxidation ageing over time at temperature, aged at over 1100°C, using temperatures inspired by literature [74] for up to 144 hours in 16 hour intervals, which enabled rapid ageing of the TBC with regular intervals for inspection of the TBCs throughout their life. The thermal diffusivity was 'measured' between each 16 hour cycle in order to capture the change in material properties over TBC life, so that any trend could be captured, and with a whole population of samples for each stage of the life cycle, enabling any patterns to be shown regarding how repeatable they are exhibited between samples, and so an isothermal furnace-inspection methodology needed to be developed.

Shorter cycles were considered to offer greater resolution in the experiment, however, initial inspections were performed to ensure timing and feasibility, and to assist in planning of the furnace schedule, which also had to fit within a demanding schedule for the furnace itself.

6.1.1 Initial experiment run

An initial inspection trial on the samples at exposure time $t=0$ was carried out to evaluate the time requirement for each of the steps required to conduct data capture for the experiment, thus utilising all of the factors to determine the inspection time requirement, balanced with lab time during the day, and appropriate time for furnace exposure. This became the results for $t=0$ hours.

The logic steps involved were as follows:

- i. Parametric study, involving variation of factors and parameters to determine resulting parameters, as detailed in the previous chapter. The data from this step was reduced to form the first set of data for the initial state, exposure time, $t = 0$.
- ii. Performance of thermographic data capture at both integration times, $IT = 2271 \mu s$, $4000 \mu s$. While $IT = 4000 \mu s$ had been reduced from the factors, data was still captured at this IT for comparison.
- iii. Application of graphite soot coating to sample surface
- iv. Repeat capture of thermographic data, as in step ii
- v. Remove soot coating in ultrasonic bath for 15 minutes
- vi. Insert into oxidation box furnace at over $1100^{\circ}C$ for X hours

- vii. Remove from furnace
- viii. Allow to cool for 15 minutes
- ix. Quench samples with distilled water.
- x. Return to step ii, repeat cycle until sample coating failure / spallation

At the end of each furnace exposure run, the samples would be removed from the furnace and allowed to cool for 15 minutes, at which point they would have cooled to approx. 60°C – this was measured after the first furnace run with an infrared spotmeter – and were then to be quenched in distilled water. This was performed in order to apply a thermal shock to the coating to accelerate the nucleation and propagation of cracks, ensuring coating would exhibit sufficient ageing, as has been applied by other researchers in oxidation of TBCs [123]. The TBCs were then inspected with thermography without graphite soot coating; a soot coating was then applied to perform the same inspection under ideal emissivity parameters. Prior to re-entry into the furnace, the soot coatings were washed with an ultrasonic bath in isopropanol, partially removing them, before the samples were returned to the furnace.

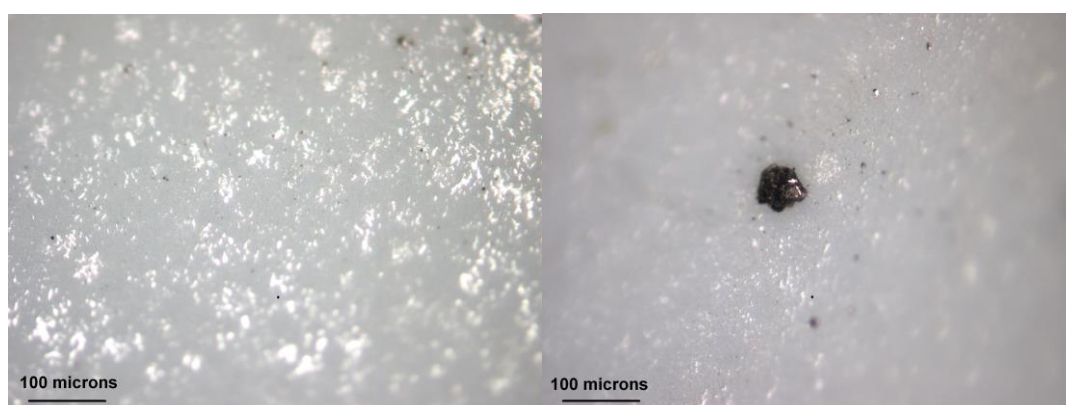


Figure 54 – Micrograph (10x zoom) of post-wash sample S11 in different locations, before (left) and after (right) soot coating contamination, at $t = 0$; contamination residue (right) survived ultrasonic path stage, step v.

During the initial dry-run, the pre and post wash condition of the TBC surface was observed to be still containing soot residue, and this was inspected via microscope to examine how well the samples had been cleaned. Examples of remaining soot coating are shown in Figure 54 and Figure 55.

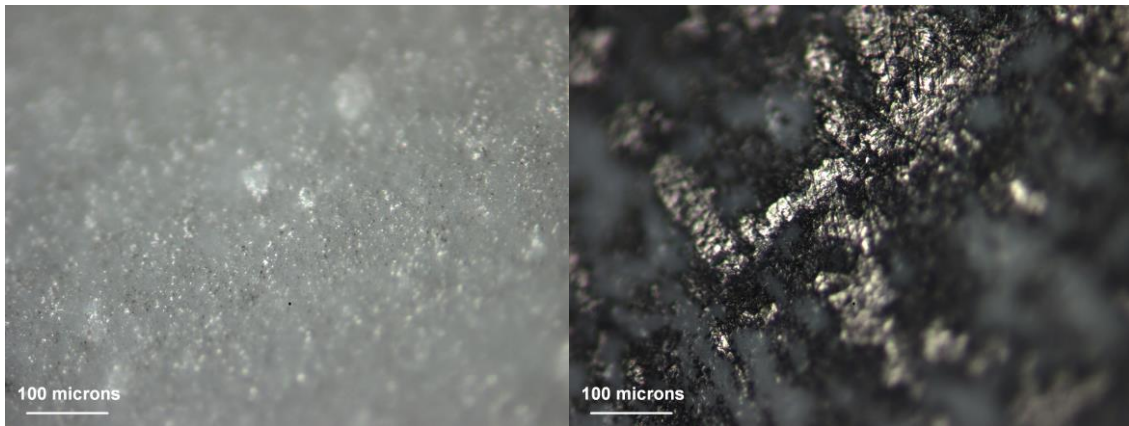


Figure 55 – Micrograph (10x zoom) of post-wash sample S05 in different locations, before (left) and after (right) soot coating contamination, at $t = 0$; contamination residue (right) survived ultrasonic path stage, step v.

It was expected from expert advice that remaining soot residue should vaporise in the high temperature of the ageing test, where the TBC surface should be clean and uncontaminated for the post-furnace inspection cycles, and that the experiment should proceed with that assumption.



Figure 56 – Micrograph (10x zoom) of post-furnace sample S05 at $t = 16$, showing the coating free from soot.

Upon inspection of the samples at $t = 16$ hours - after the first cycle - some of the samples were inspected via microscope and this was revealed to have been the case, as indicated in Figure 56. The experiment could then proceed with less concern about lingering contamination of the soot coating on uncoated inspections. The entire sequence listed earlier in this sub-section was carried out in a dry-run prior to furnace exposure, simulating each step to ensure appropriate planning to optimise the furnace runs in as short a total experiment duration as possible.

6.1.2 Limitations

It was important to limit the total experiment duration because the furnace was in relatively high demand, and lengthy runs would be more difficult to schedule and would delay the experiment.

It was also important not to be present in the lab in evenings or early morning, as students are not permitted to use the lab unattended out of hours for health and safety reasons; while special cases could be made for experiments to be conducted with evening supervision, this requirement would need to be sufficiently justified, which this was not considered necessary for this experiment. This was one of the limitations that factored heavily in the selection of furnace exposure time, based on the time schedule that was available in balance between time at temperature when the student was not available to be in the lab, and removal from the furnace when the student was available to remove and re-insert the samples to the furnace, with requirement for sufficient inspection time in between.

6.1.3 Inspection process layout

At this stage, the number of factors for consideration have been substantially reduced, allowing inspection of all the samples at each stage of the cycle, with all tests for each cycle being able to fit within one day; returned to the oxidation furnace until the onset of coating spallation. The full cycle layout of this process has been mapped out and is shown in Figure 57.

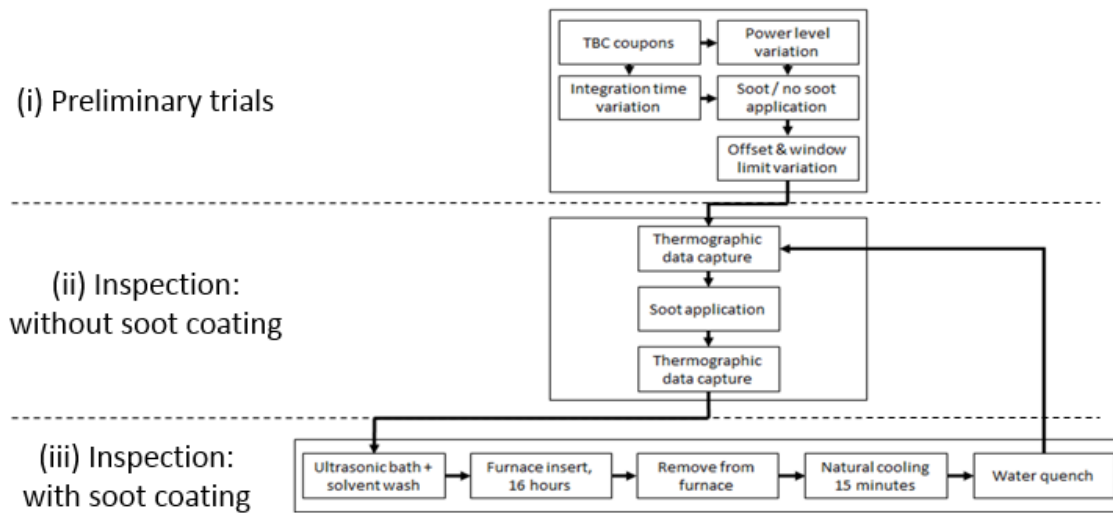


Figure 57 – Flowchart illustrating the process stages of the oxidation ageing cycle, showing the different stages; from preliminary trials (i), through to inspections without (ii) and with the soot coating condition (iii). The process cycles through stages (ii)-(iii) until visible spallation in either of the last two stages

After the initial trial run at $t = 0$ hours, the first furnace cycle was performed. This was still initially regarded as part of the preliminary trial, however was conducted based on the furnace cycle that is to be laid out in the next sub-section, and was a first test of the entire procedure, to confirm that timings had been correctly accounted for, including supervised practice of the procedure for health and safety considerations that naturally coincide with handling high temperature samples, shown in Figure 58. A microscopic evaluation of some of the samples at

this stage confirmed one of the initial concerns from the initial dry-run, that the soot coating residue had evaporated as discussed previously.



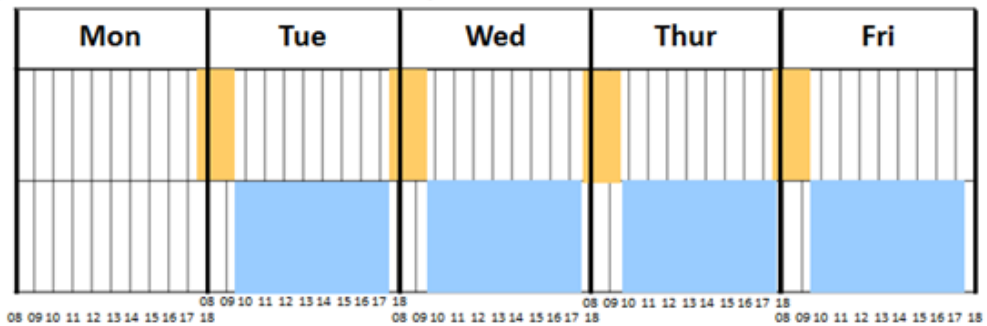
Figure 58 – Extraction of samples in-between oxidation cycles at $t = 016$ hours, before the sample is allowed to cool in their holder on a ceramic brick.

6.2 Furnace cycle runs

From initial inspection trials in a practice run for $t=0$, it was determined that the full inspection cycle, with sample cooling and washing, transport between laboratory and carrying out the full inspection series, it was determined that the time required for an inspection was around four hours. As the samples had to be retrieved and returned to the furnace promptly, and the limitation of lone-working access to the lab outside of working hours being an unfavourable option, it was decided that the furnace exposure runs should set as 16 hours, to enable an entry

to the furnace at 18:00 one evening, and extraction at 10:00 the next morning. This choice of timing enabled ample time for the four hours of inspection, while ensuring the furnace runs provided sufficient number of opportunities up until failure, offering ~8 data windows over the life of the TBCs, if the coatings failed at approx. 120 hours.

16 hours: 1730-0930 furnace
(showing time as 0800 – 1800 work hours)



Furnace hours:
Mon-Fri 1730 - 0930 (16 hrs)

Inspection hours:
Mon-Fri 1000 – 1700 (7 hrs)

Figure 59 – layout of furnace cycle planning (orange highlight), with inspection cycles (blue highlight), permitting four ageing runs and inspections per week.

The choice of 16-hour furnace runs, scheduled to end at the beginning and start at the end of each day permitted four furnace runs and four inspection cycles per week, where 140 hours furnace exposure could be met in just over two weeks.

The oxidation-inspection schedule is outlined in Figure 59, while the furnace runs and their resulting time at temperature is shown in Figure 60.

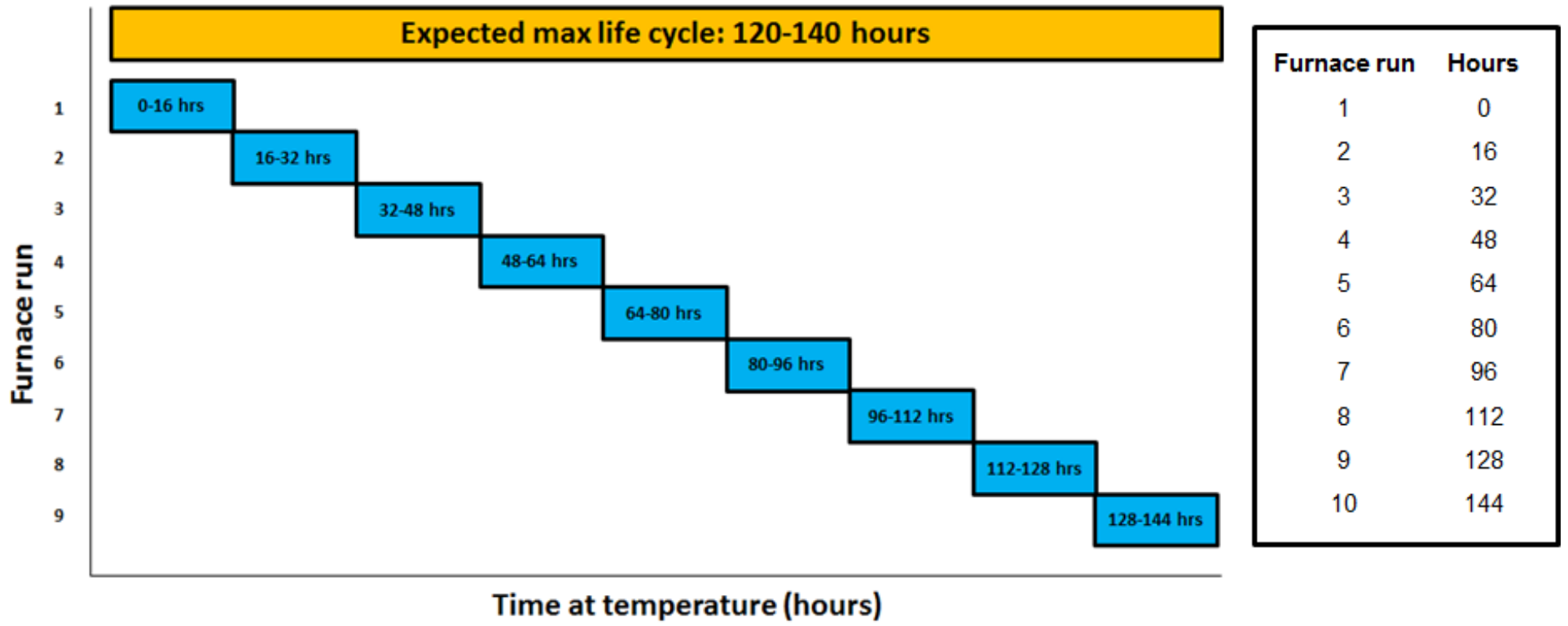


Figure 60 – Chart of furnace cycles displaying time at temperature for each furnace run.

6.3 Trend identification

The main aim of the research, as outlined in objective two, §3.2.2, is the identification of trends in TBC ageing that can be detected and assessed using the NDT. From the observation of exploitable trends in Plasma Sprayed TBCs, a similar trend is expected in EB-PVD TBCs from the increase due to sintering; however, due to the different structure of EB-PVD TBC to PS TBC, the difference in cracks propagating through the top coat in APS but only through rumpling in EB-PVD, and the difference in thickness used in most APS studies; the trend is expected to be different, and owing to the additional source of error from use of optical flash for whole-area inspection, as opposed to the ideal heat source of a laser which does not entail afterglow effects, this trend is expected to also be more difficult to identify. Some trends in change of thermal conductivity in EB-PVD TBCs have been discussed in the literature; there are expected to be an overall increase from sintering at the furnace temperature, with intermittent “dips” from crack growth, however the true trend is not known, prior to results.

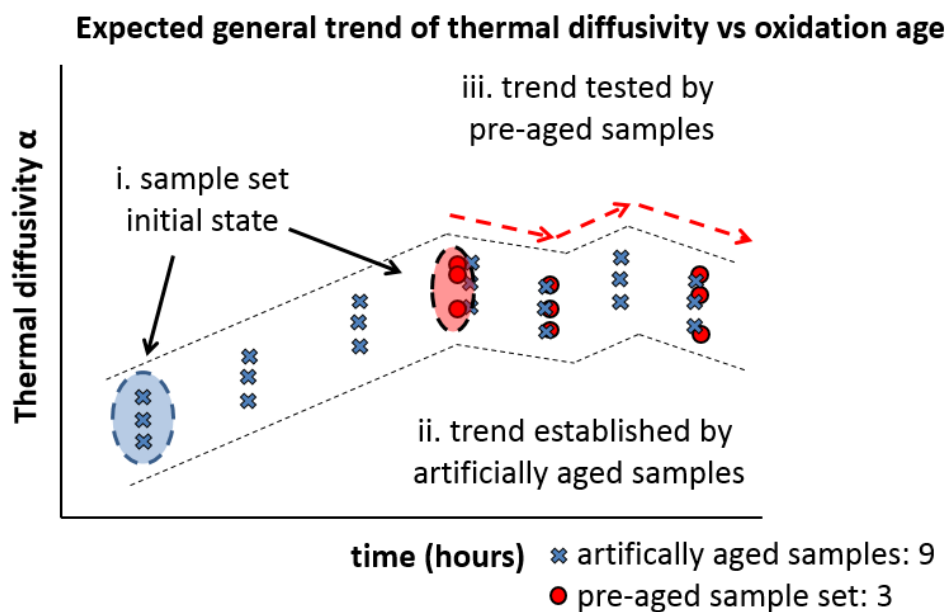


Figure 61 – Sketch of expected experimental results.

A rough outline of expected outcome from the experiment is provided in Figure 61. If the expected trend can be identified in the as-deposited TBCs, a portion of that trend and diffusivity values should be exhibited by the pre-aged TBCs, and therefore may prove the trend exploitable for ageing characterisation.

6.4 Results

The samples were exposed to time at temperature, and their apparent diffusivity was measured according to the setup detailed in 5.2 - Data capture and the inspection-furnace cycle shown in Figure 57.

6.4.1 Sample lifetime

Each of the as-new samples survived an average of ~110 hours, ranging from 80-128 hours at temperature, before visible spallation on removal from the next 16 hour furnace cycle. The pre-aged samples only lasted 1-3 furnace cycles, ranging from 16-48 hours, with spallation occurring at 96-144 for the as-new samples, and 32-64 hours for the aged samples respectively. These lifetimes are shown in Table 14, and displayed visually in Figure 62. Samples were labelled reflecting parallel copies (S02, S04 etc), which were kept aside in case of repeat trials, which were not conducted.

Table 14 – Sample lifetime until failure (samples labeled to enable repeats)

Sample	Data captured until	Spallation at
S01	112	128
S03	128	144
S05	80	96
S07	96	112
S09	112	128
S11	128	144

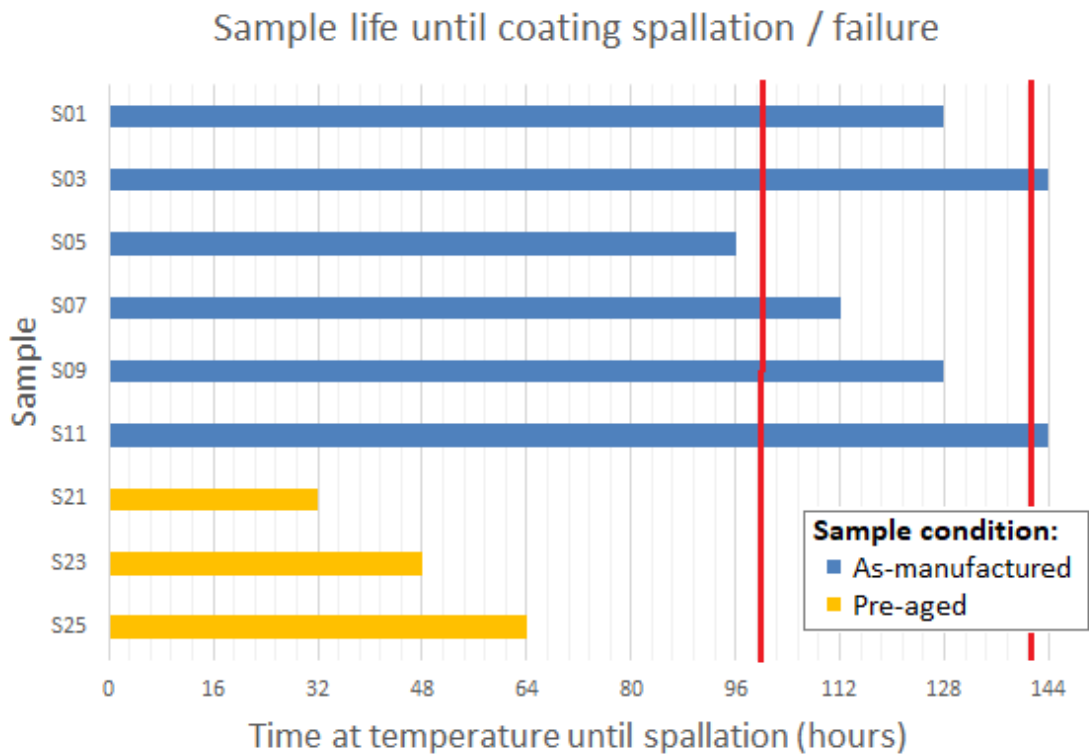


Figure 62 – Sample life duration over time at temperature until coating failure (expected lifetime ~100-140 hours, (vertical lines)).

6.4.2 Results: tabulated

The results for the full experiment are shown from Table 15 to Table 23 below, where sigma is the standard deviation between model and data at each step; both values, and the R^2 value of model fit, were useful during the parametric study, and in determining if the data extracted was sufficient, or if it had significant errors.

Table 15 – Data table for Sample S01

Furnace exposure	without soot		with soot	
	sigma	Diffusivity	sigma	Diffusivity
0	3.04E-02	6.26E-07	1.29E-01	4.79E-07
16	1.89E-01	4.96E-07	1.08E-01	4.67E-07
32	2.46E-01	4.56E-07	8.94E-02	4.52E-07
48	2.55E-01	4.43E-07	1.01E-01	4.58E-07
64	2.83E-03	4.48E-07	1.13E-01	4.93E-07
80	2.33E-01	4.53E-07	1.15E-01	4.86E-07
96	2.07E-01	4.67E-07	1.11E-01	4.93E-07
112	2.25E-01	4.66E-07	1.01E-01	4.86E-07
128	-	-	-	-

Table 16 – Data table for Sample S03

Furnace exposure	without soot		with soot	
	sigma	Diffusivity	sigma	Diffusivity
0	3.00E-02	6.42E-07	1.03E-01	4.51E-07
16	1.81E-01	5.01E-07	9.94E-02	4.56E-07
32	2.22E-01	4.67E-07	9.38E-02	4.33E-07
48	2.55E-01	4.41E-07	9.02E-02	4.50E-07
64	2.68E-01	4.32E-07	9.40E-02	4.56E-07
80	2.61E-01	4.33E-07	9.16E-02	4.62E-07
96	2.11E-01	4.39E-07	1.00E-01	4.76E-07
112	2.37E-01	4.54E-07	9.17E-02	4.90E-07
128	-	-	-	-

Table 17 – Data table for Sample S05

Furnace exposure	without soot		with soot	
	sigma	Diffusivity	sigma	Diffusivity
0	3.62E-02	6.29E-07	-	-
16	2.21E-01	4.79E-07	1.05E-01	4.66E-07
32	3.10E-01	4.33E-07	9.71E-02	4.39E-07
48	2.52E-01	4.39E-07	9.08E-02	4.40E-07
64	3.43E-01	4.07E-07	9.74E-02	4.49E-07
80	3.28E-01	4.08E-07	1.17E-01	5.02E-07
96	-	-	-	-
112	-	-	-	-
128	-	-	-	-

Table 18 – Data table for Sample S07

Furnace exposure	without soot		with soot	
	sigma	Diffusivity	sigma	Diffusivity
0	2.85E-02	6.29E-07	1.15E-01	4.68E-07
16	2.10E-01	4.87E-07	1.01E-01	4.61E-07
32	1.46E-01	4.70E-07	1.00E-01	4.54E-07
48	3.08E-01	4.19E-07	9.31E-02	4.58E-07
64	2.84E-01	4.30E-07	9.01E-02	4.64E-07
80	2.39E-01	4.49E-07	9.67E-02	4.81E-07
96	2.34E-01	4.37E-07	1.12E-01	4.88E-07
112	-	-	-	-
128	-	-	-	-

Table 19 – Data table for Sample S09

Furnace exposure	without soot		with soot	
	sigma	Diffusivity	sigma	Diffusivity
0	3.26E-02	6.09E-07	1.35E-01	4.77E-07
16	1.79E-01	4.88E-07	1.13E-01	4.84E-07
32	2.28E-01	4.62E-07	9.75E-02	4.43E-07
48	2.46E-01	4.54E-07	9.09E-02	4.54E-07
64	3.01E-01	4.14E-07	1.04E-01	4.77E-07
80	2.27E-01	4.51E-07	1.12E-01	4.79E-07
96	2.84E-01	4.22E-07	1.05E-01	4.73E-07
112	2.72E-01	4.78E-07	9.87E-02	4.78E-07
128	-	-	-	-

Table 20 – Data table for Sample S11

Furnace exposure	without soot		with soot	
	sigma	Diffusivity	sigma	Diffusivity
0	4.51E-02	6.05E-07	1.08E-01	4.84E-07
16	2.49E-01	4.54E-07	1.08E-01	4.84E-07
32	2.95E-01	4.34E-07	9.30E-02	4.45E-07
48	3.46E-01	4.06E-07	9.91E-02	4.38E-07
64	3.33E-01	4.06E-07	1.01E-01	4.46E-07
80	3.89E-01	3.93E-07	8.63E-02	4.59E-07
96	3.89E-01	3.82E-07	9.16E-02	4.65E-07
112	3.62E-01	4.04E-07	9.24E-02	4.81E-07
128	3.29E-01	3.92E-07	8.93E-02	4.72E-07

Table 21 – Data table for Sample S21

Furnace exposure	without soot		with soot	
	sigma	Diffusivity	sigma	Diffusivity
0	4.69E-02	5.96E-07	1.06E-01	4.74E-07
16	2.44E-01	5.49E-07	2.24E-02	6.31E-07
32	-	-	-	-
...	-	-	-	-

Table 22 – Data table for Sample S23

Furnace exposure	without soot		with soot	
	sigma	Diffusivity	sigma	Diffusivity
0	1.25E-01	5.15E-07	1.10E-01	4.73E-07
16	1.51E-01	5.11E-07	1.03E-01	4.76E-07
32	4.70E-01	4.21E-07	7.36E-02	4.40E-07
...	-	-	-	-

Table 23 – Data table for Sample S25

Furnace exposure	without soot		with soot	
	sigma	Diffusivity	sigma	Diffusivity
0	8.82E-02	5.53E-07	1.07E-01	4.69E-07
16	2.27E-01	4.61E-07	7.21E-02	5.12E-07
32	2.18E-01	4.52E-07	9.21E-02	4.37E-07
48	2.63E-01	4.33E-07	9.90E-02	4.48E-07
...	-	-	-	-

6.4.3 Results: plotted

As can be observed in the data tables in the previous sub-section, the aged samples lasted from 1 to 3 furnace runs, while the as-new samples lasted 5-8 runs. Any data points not captured were due to coating spallation, and have been

marked as blank (“ – “). The coating spallation event was determined by direct observation: upon cooling from removal from the furnace, the coating would emit small cracking noises, and if the coating failed; it would rapidly fracture, and shed from the surface, exposing the underlying metallic bond coat and substrate. The samples for the uncoated inspections are plotted in Figure 63, and coated condition dataset is plotted in Figure 64.

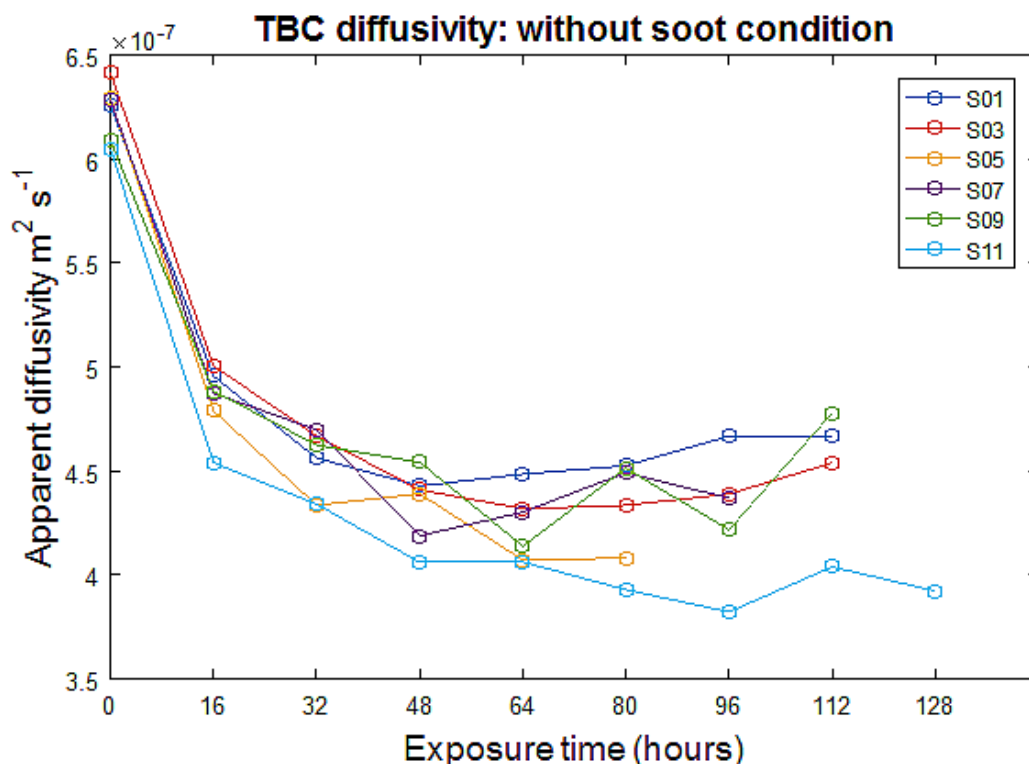


Figure 63 – Plot of as-new sample diffusivity versus furnace cycle hours, without soot coating

The data was plotted as follows: each of the sample sets were broken into two populations, the “as-new” and “aged” populations. First was to establish the ideal case that can be used to search for trends, to then be sought for repetition in the uncoated condition; then extending further as to whether the test would still be applicable in realistic test conditions, which will be covered in the next chapter.

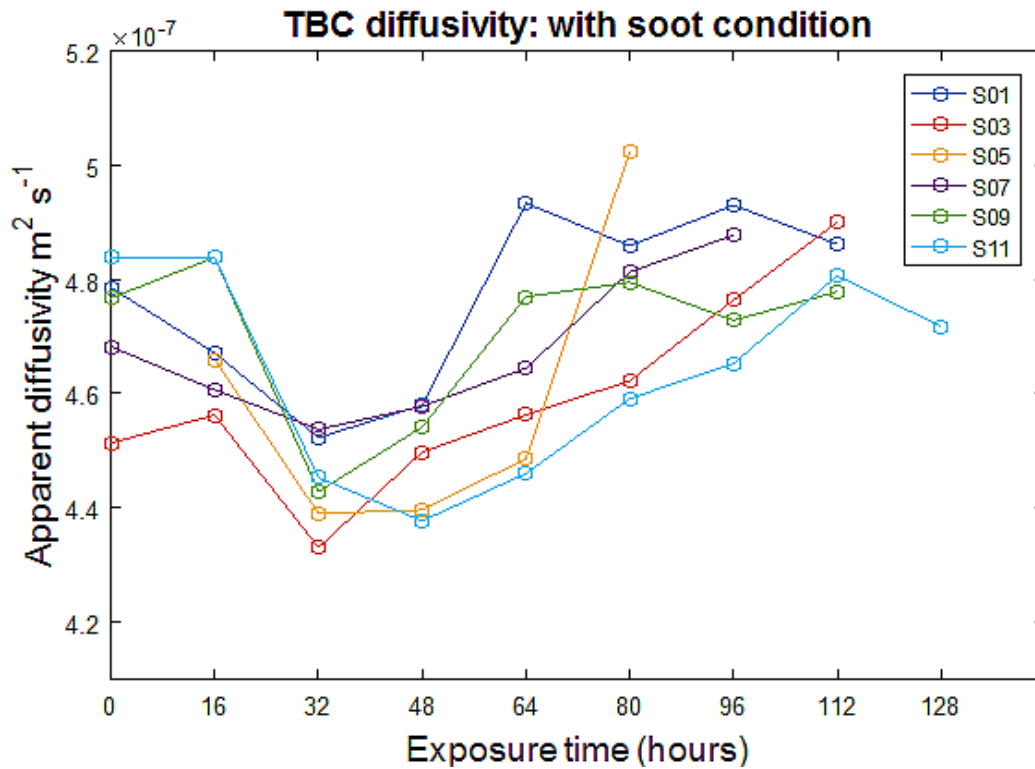


Figure 64 - Plot of as-new sample diffusivity versus furnace cycle hours, with soot coating

6.5 Summary

The samples were exposed to temperature for up to the 140 hours duration they were expected to endure; the as-manufactured samples began spallation failure at 96 hours and all the last failures occurred at 144 hours. The pre-aged coats failed much earlier as was expected, lasting 32-64 hours. Data was captured up to 16 hours prior to their failure upon cooling when removed from the furnace. Data was captured for all samples at each stage. Results for each inspection has been collected and the standard deviation for each fitting stage has been captured and utilised in this chapter ready for analysis.

7 Diffusivity Analysis and pattern seeking

Some of the results presented in this section have already been published and are here reproduced, from (Tinsley et al., 2017) [185].

Having tabulated and plotted the data, it can now be interrogated and analysed, seeking patterns, which can then be attempted for exploitation. Plainly apparent issues will be raised and discussed first, reducing the problem task so the ageing characterisation can then be pursued.

7.1 Anomaly resolution

As an essential pre-requisite for data analysis, anomalies need to be identified and discussed. There were a couple of anomalies in the dataset, as highlighted in Figure 65.

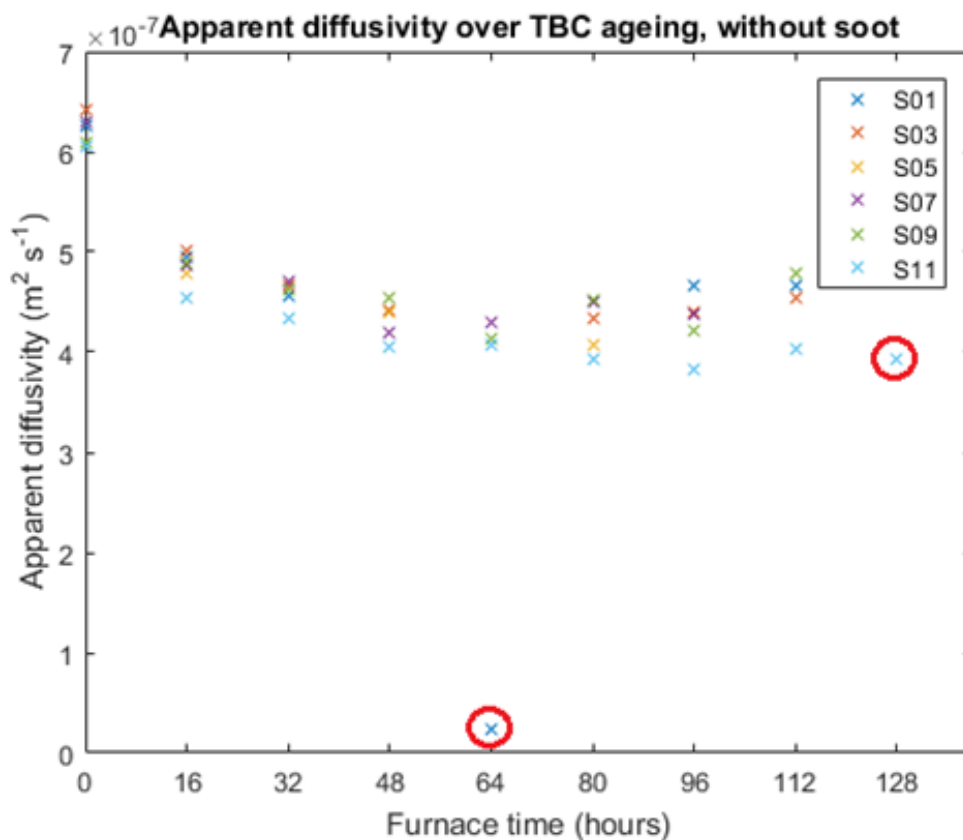


Figure 65 – Identifying anomalies and outliers in the results, S01 at t=64 (lower middle), and S11 t=128 (right) are regarded as anomalous.

A data capture of sample S01, at $t = 64$ was more than several standard deviations separated from any value in the dataset. Upon repeating the analysis, it was discovered that the file for this data capture was captured at 30 Hz from a previous user's settings; but that this had also been noticed at the time, and a repeat capture performed; though this had initially been missed during early data processing. This anomaly was thus resolved and no longer appears in the dataset. A capture for sample S05 at $t = 0$ hrs in the with soot condition failed to record data, while the data captured for S11 at $t = 128$ hrs may not be anomalous, however, its lone presence as shown in Figure 65 at the extreme end of life leaves its value to be suspect, as its measure is likely to be dominated by late-life delamination effects, which it does appear to exhibit.

As can be seen in Figure 66, one of the sample data captures in the with soot condition failed to record data capture at $t = 0$. Lab notes were consulted and the sample was checked as having been inspected, however the data was not recorded. It is suggested that this may be that the system encountered an error that then failed to record the data capture, or human error in conducting the first set of inspections in haste. The absence of data for this sample at this time is irretrievable, and was only noted at the 16 hour interval when initial comparisons of the data captures at both time intervals were being made, and increased care was taken to ensure all inspections had data recorded, performing repeat captures when in doubt, ensuring that this error wasn't repeated. As shown by the account of data captures per time interval in Figure 66, the time for 128 hours only had one sample, reducing confidence in sample behaviour at that late stage.

While the data capture at this time would not be ignored, it should be remembered that it is only represented once.

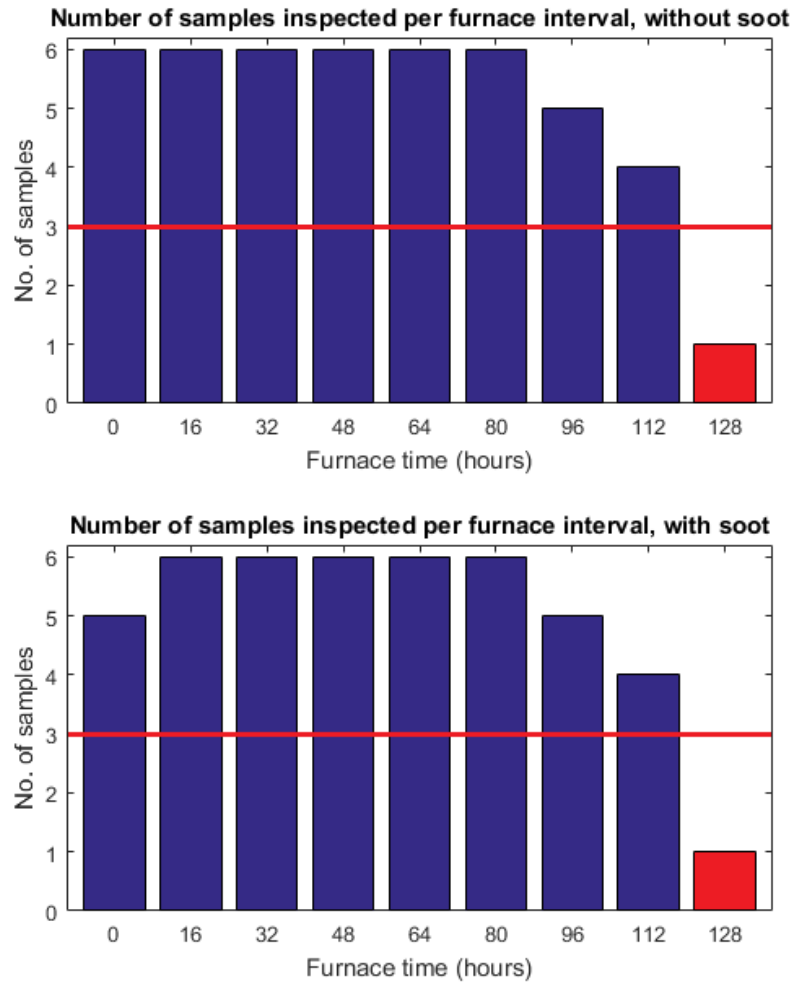


Figure 66 – histogram showing number of sample data captures per time slot, indicating a failure to record data capture for S05 (with soot) at t = 0 hrs, and a reduction of data samples for later time periods, where all available samples were captured, reducing below the minimum requirement of 3 for reliable pattern inspection at t = 128 hrs. Data captures for as-new samples, only; pre-aged samples expired at 16-32 hours.

7.2 Analysis of results

Correcting the S01 t = 64 hrs anomaly from the without soot condition from the dataset and plotting to the same scale to include all data points from the updated version of each dataset allows the underlying pattern followed by the samples to begin to emerge, with average values plotted, as shown in Figure 67.

One of the first observations to be made is that there is not a linear proportional relationship between coating diffusivity property and age. It should also be noted that there is a very strong step change during the first cycle between $t = 0$ to 16 hours in the uncoated condition inspection set – but not in the coated condition.

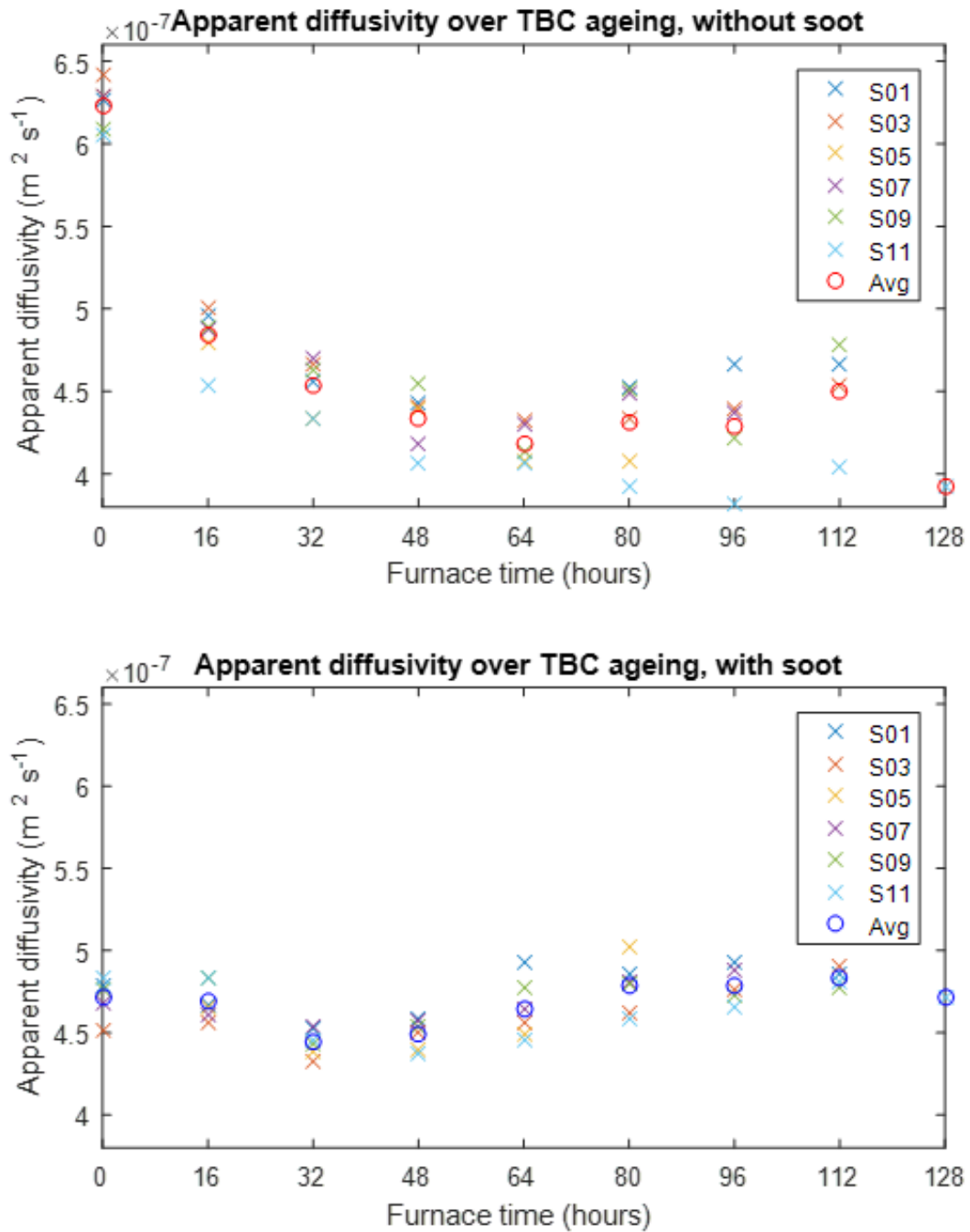


Figure 67 - Plotting all results in the raw as-calculated value, without soot coating (above), and with soot coating (below), excluding the anomaly at $t = 64$ hrs for the without soot condition.

Finally, it is noted that the change exhibited is not a trend, where a change in one parameter (hours of exposure) results in a matched or proportional change in the measured variable; but a pattern, where a set of values cannot by themselves be used to categorise the sample age, however, this pattern appears to be repeated among each the samples, which offers alternative methods for characterisation.

7.3 Pattern seeking

For simplification of viewing of the results, the values of each dataset was normalised between 0 and 1 with the following relation, in order to compare the datasets to the same scale:

$$\alpha(t_i)_{norm} = \frac{(\alpha(t_i) - \alpha_{min})}{(\alpha_{max} - \alpha_{min})} \quad (7-1)$$

where $\alpha(t_i)$ is the measured value of diffusivity at time t, for sample i for any given soot coating condition; $\alpha(t_i)_{norm}$ is its' normalised counterpart, while α_{min} and α_{max} are the min-max values of measured α for the full dataset. After being normalised to the same axis, the two datasets can now be plotted together as an initial look in search for a common pattern exhibited between both sets, which is shown in Figure 68, below:

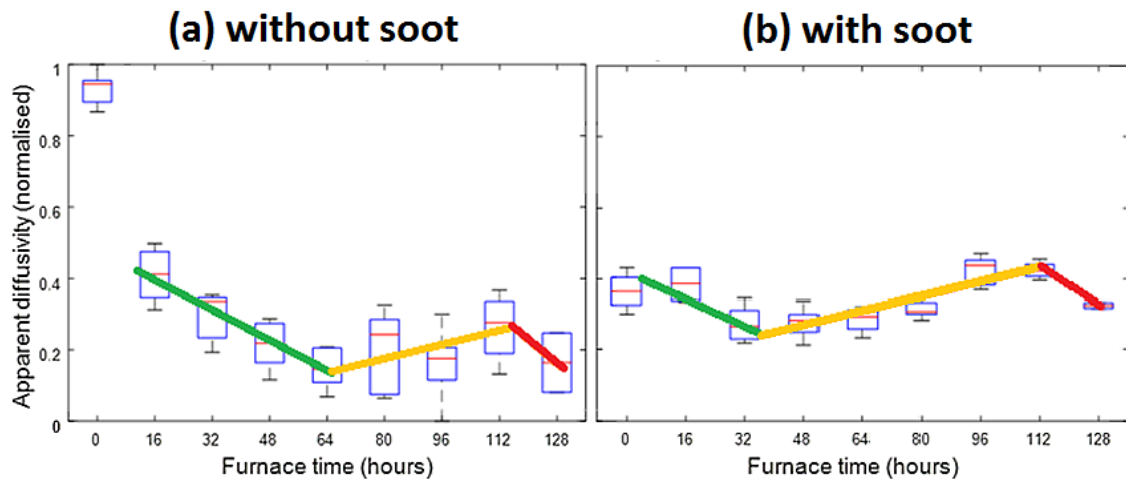


Figure 68 – A plot of thermal diffusivity (normalised) box plot of all as-deposited samples plotted against cycle time (hours). Data shown in the without soot condition (left) and with soot condition (right), showing a pattern between the samples over ageing (illustrated). Plot adapted from Tinsley et al., (2017) [185], courtesy of Elsevier.

As-new samples

All 6 of the as-deposited samples were put through oxidation ageing cycles of up to 144 hours, where coatings failed at 80-128 hours, with final sample failure at 144 hours; while pre-aged TBCs lasted only until 32 hours, providing few data points. The results are shown in Figure 68. One of the reasons for normalising the dataset was to reduce the context to change of arbitrary units. Additionally it was necessary to include the graphs in their as-published presentation, with a brief visual summary of the observations made, before moving on with further analysis for the thesis. Henceforth, the data shall be presented in original units. At this stage it can be readily observed that the desirable direct trend that can be exploited in a linear or proportional relationship is not the case, however an underlying pattern does appear to be evident.

The presentation of the results in Figure 68 shows the data in raw form, only seeking patterns in the raw data as-plotted; this direct approach neglects the

spread of the pattern in the horizontal axis, and the patterns exhibited by each sample, which sometimes occur at different points in the overall furnace cycle. By neglecting how some samples may age at different rates from each other, this approach obfuscates the seeking of patterns within the dataset, as some samples may exhibit the same pattern along the same number of hot hours, but may be offset in the y-axis somewhat, as demonstrated in Figure 69 (right).

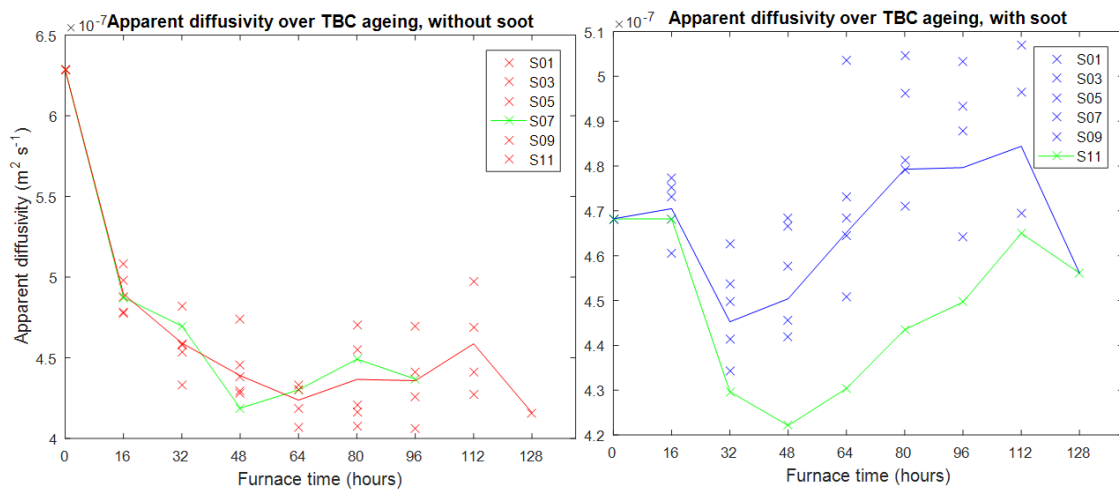


Figure 69 – highlight of S07 in ‘without soot’ series, (left) versus average, and S11 in ‘with soot’ data series versus average (right); demonstrating similar pattern to the average, with an offset in x-axis from t=48 (left), offset in y-axis from the average (right); where the red and blue lines refer to the average of the dataset, while the green plots show the plots for individual samples S07 (left), and S11 (right), highlighting some of the variance in the sets between the samples, in both soot conditions.

Transversely, some samples may exhibit the same pattern but may be offset along the x (time) axis, where the pattern, or parts, or ‘features’ of the pattern may occur over different exposure times, and may be exhibited over different lengths of time, as shown in Figure 69 (left), where the trough of the pattern may be occurring 8-16 hours sooner.

Features of the underlying pattern between the samples will not occur at the same point in time, while the discrete measurement points are not directly

translatable to the underlying shape itself, but rather represent points on that shape, i.e. the trough of S07 at $t=48$ in the 'without soot' condition, as shown in Figure 69 (left) cannot simply be expressed as being the same trough as $t=64$ of the average, 16 hours to its right, as the true trough of the diffusivity change in both the average and may actually take place at any point in between the two, which could only be resolved if more frequent inspections were to be undertaken. Should additional data captures in between the two points have been taken, the additional points could be level, or lower, below that exhibited at $t=64$, either for the average, or for S07; this example highlights how the underlying pattern does not fit rigidly in the 16 hour cycles monitored, that the shape of the pattern for each sample captured at this frequency may be similar but translated differently along the x-axis, while offset differently along the y-axis, and in each case: occurring at different points along each axis, for each of the features of the pattern. A full display of each sample's pattern against the average is shown in Figure 70 - Figure 71. To seek these patterns, a more detailed analysis than simply the average is required.

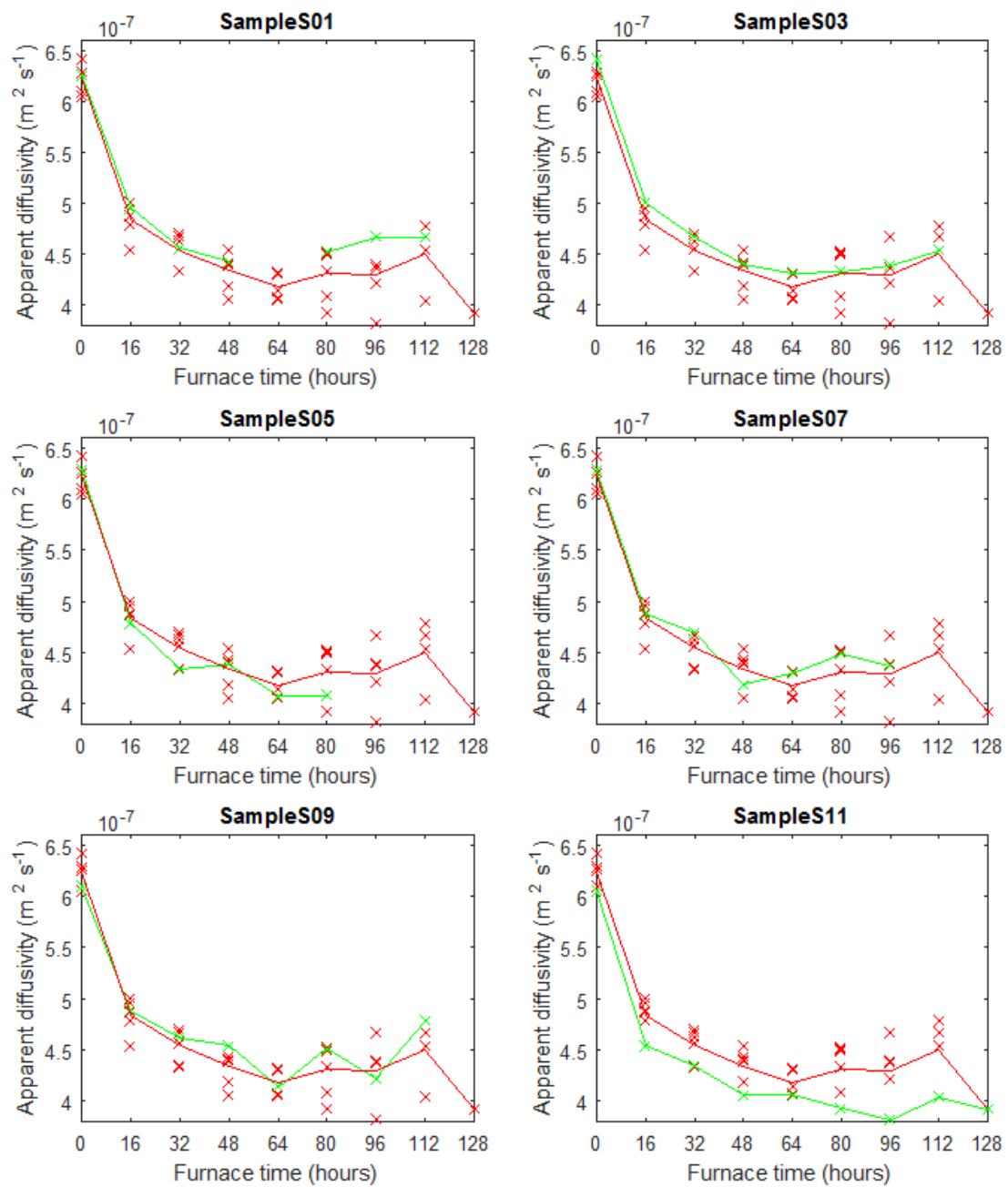


Figure 70 – raw plots of all samples in the ‘without soot’ condition, displaying each sample’s pattern (green) against the average (red).

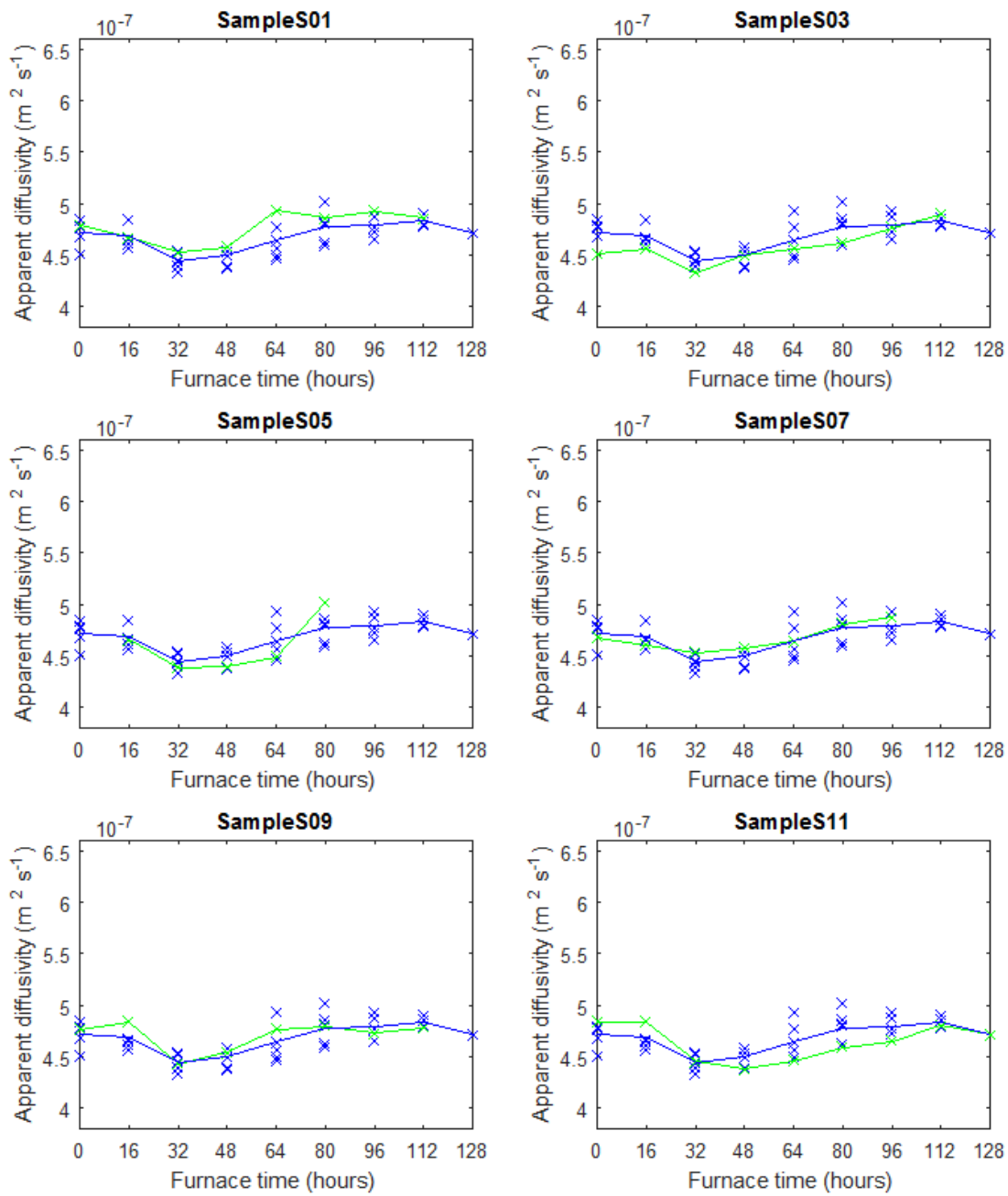


Figure 71 - raw plots of all samples in the 'with soot' condition, displaying each sample's pattern (green) against the average (blue).

Initially, an adjustment of the dataset is attempted, where each of the samples were shifted in the y-axis at a given time, subtracting the difference from each sample compared to the same sample - sample S07 - hoping to minimise the spread of the data between the samples in the y axis.

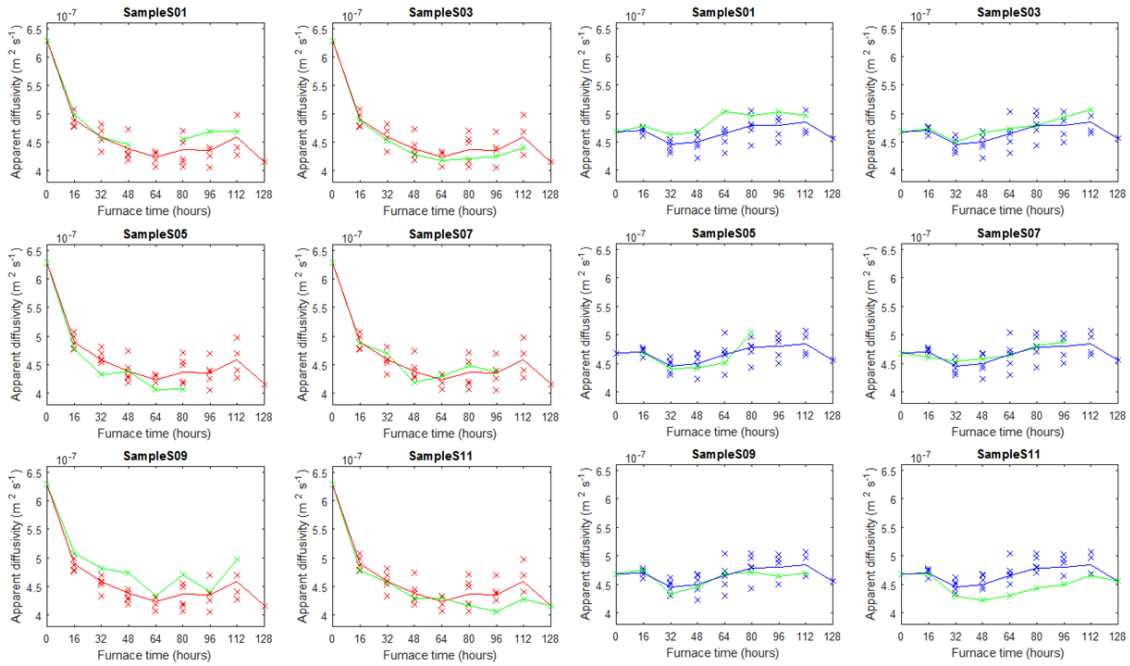


Figure 72 – adjusted plots of all samples, showing sample’s pattern (green) against the average (blue); modified: normalised for initial reading at, 0 hours.

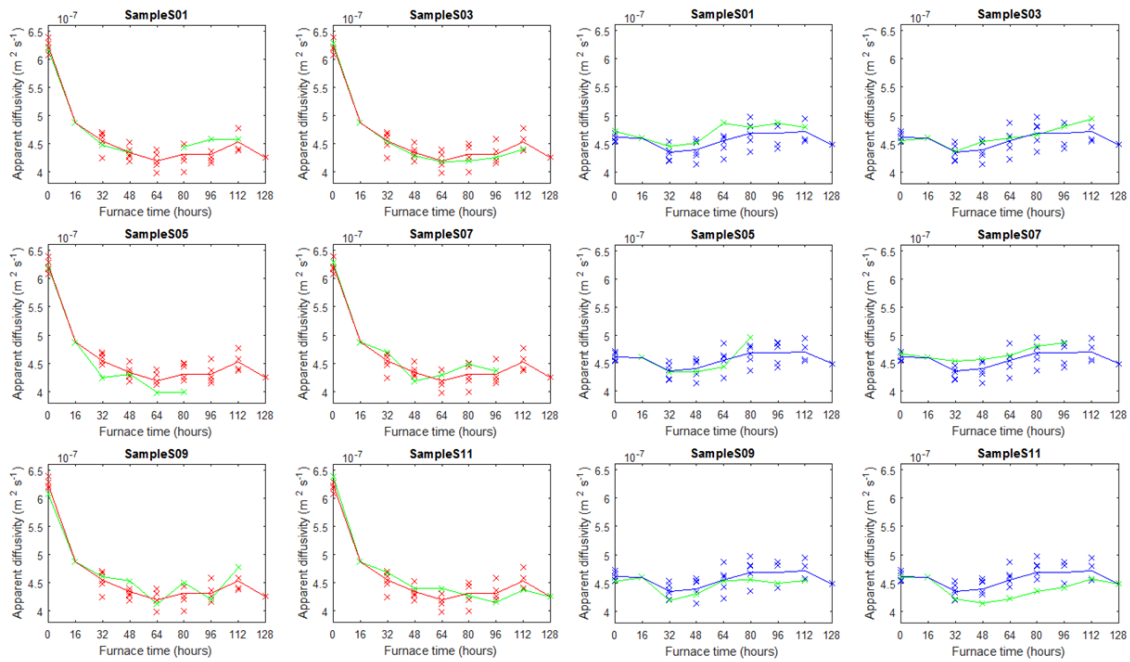


Figure 73 – adjusted plots of all samples, showing sample pattern (green) against the average (blue); modified: normalised for first cycle, at 16 hours.

The sample of sample S07, that was arbitrarily selected to shift the other data samples to the same diffusivity value at a given time; as the only difference would be in the collective starting (for $t = 0$) or shift point (for any other times). It was hoped that this would reduce their deviation to reinforce the underlying pattern. These can be seen in Figure 72 for adjustment at $t=0$, and Figure 73 for adjustment at $t=16$. The standard deviation of the datasets (whole samples) are shown in Table 24.

Table 24 – standard deviation of datasets, in the original and adjusted conditions.

Time	Standard deviation 'without soot'	Standard deviation 'with soot'
original	6.85E-08	1.74E-08
t = 0	6.72E-08	2.05E-08
t = 16	6.61E-08	1.99E-08

Further exploring the dataset with adjustments, a polynomial was fitted to the average, in preference to plotting straight-line plots connecting the average points, raising the underlying pattern features more clearly. Between Figure 74 and Figure 75, the different feature regions are more plainly apparent, from those in common between the two coating conditions, and those that differ. Additionally, other features that are unique to each sample also becomes more apparent by this comparison, as the polynomial suppresses behaviours from individual samples not shared between them, occurring at the same time in the furnace cycle. With the suppression of these behaviours, the common patterns of initial decrease then late-life increase becomes more apparent – but so also does the

delay in exhibit of the increase in values with the uncoated condition, yielding information useful to analysis for interpretation of the results, and what is taking place as the coatings are aged.

At this point it is important to explore some basic aspects of TBC aging, in order to ascertain how much of the trend features can be eliminated and what can be explored as features of the trend.

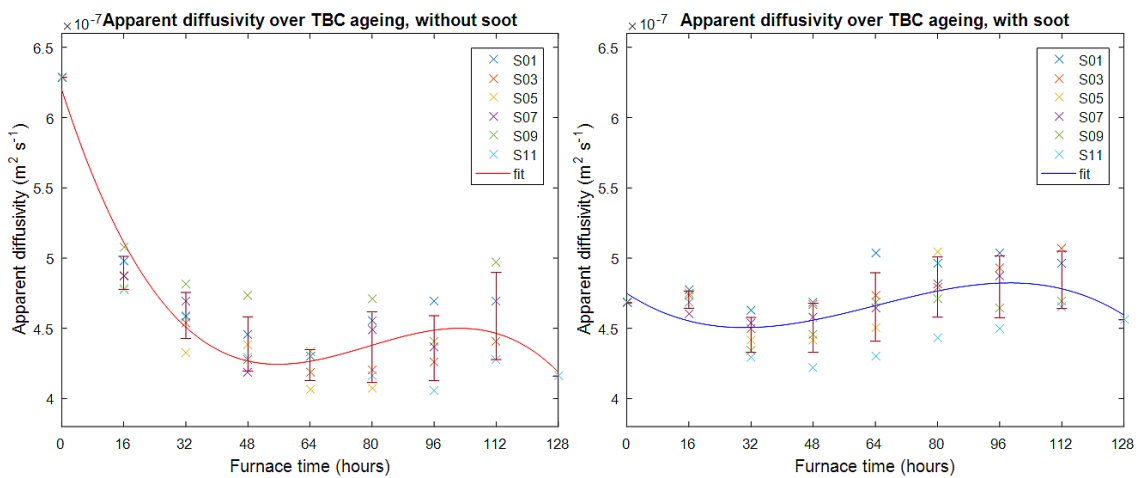


Figure 74 – polynomial fit of data, adjusted to $t = 0$, coeff = 4, full time series

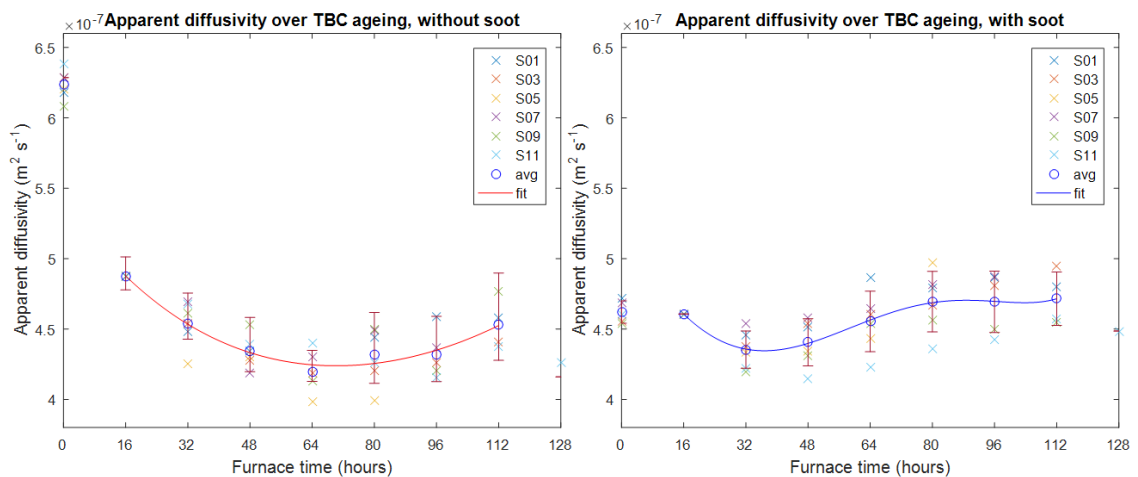


Figure 75 – polynomial fit of data, adjusted to $t = 16$, coeff = 4, between $t=16 - 112$.

It should be noted that the “uncoated” inspection after the first furnace cycle has had a soot coating applied to it, and then removed; at each stage of the

removal, the coatings had a lingering contamination on the surface (Figure 54, Figure 55) that was expected to evaporate in the furnace – and, indeed, the contaminations were not visibly present upon removal from the furnace. However, the coating itself may likely have been contaminated in the process, with soot penetrating into the intercolumnar gaps of the EB-PVD TBC, which would change the optical characteristics – how the heat pulse is reflected and absorbed – from the initial clean state. The difference in the uncoated condition, from $t=0$ hours to $t=16$ hours, which is a change not present in the coated condition, was considered an anomaly in the dataset, that may be neglected, requiring further investigation into the specific cause, suspecting a change in reflectance properties from soot contamination that, once initiated, remained constant through the rest of the uncoated condition dataset. From this reasoning, the $t=0$ initial data points of the uncoated condition should be neglected in the search for the underlying patterns, which was the adjustment made to the analysis, shown in the difference between Figure 74 and Figure 75, where the $t=0$ data points were then ignored in a repeat of the polynomial fitting step, shown in Figure 76, to further raise the underlying patterns.

7.4 Pattern detail summary

In summary of the different features exhibited in the data, there are four apparent behavioural pattern features that will be considered:

- Firstly, feature 1 (F1), is a behavioural pattern which shows a strong initial decrease in thermal diffusivity in the uncoated condition samples, that is not present in the soot coated condition inspections.
- Feature 2 (F2) is the early stage decrease in diffusivity values present in both data sets, that persists until a minimum, ~48-64 hours for the uncoated condition samples, and 32-48 hours in the soot coated condition. In the journal publication, these first two observations were regarded as one common feature, however, are being regarded as distinct features in the thesis, for reasons that will be discussed in the upcoming subsections.
- Feature 3 (F3) exhibits a steady, long-term increase in the thermal diffusivity, which builds until failure.
- Feature 4 (F4) of the dataset entails sudden jumps and variations in the dataset, which presents an abrupt jump in the diffusivity value, before resuming behaviour of the other features (largely: feature 3)

The regions of these features have been identified from the results, later to be shown in detail per-sample, and is displayed in Figure 76. With these features identified, each of the samples results were inspected, seeking out features that follow the pattern rules outlined above, interrogating each sample individually and marking the sample age/s at which each feature can be observed, using the individual plots shown in Figure 72 & Figure 73. The furnace cycle time at which the features were identified are laid out in Table 25.

Table 25 – Summary of observed features from each dataset, where ‘-’ is used to indicate absence of the feature for that sample, in the specified soot coating condition.

Sample	Feature 1	
	Uncoated	Coated
S01	t00 - t16	-
S03	t00 - t16	-
S05	t00 - t16	-
S07	t00 - t16	-
S09	t00 - t16	-
S11	t00 - t16	-

Sample	Feature 3	
	Uncoated	Coated
S01	t64+	t32+
S03	t64+	t32+
S05	-	t32+
S07	t48+	t32+
S09	t64+	t32+
S11	t96+	t48+

Sample	Feature 2	
	Uncoated	Coated
S01	t32-t48	t00-t32
S03	t32-t64	t00-t32
S05	t32-80	t00-t32
S07	t32-32	t00-t32
S09	t32-48	t00-t32
S11	t32-t80	t00-t48

Sample	Feature 4	
	Uncoated	Coated
S01	-	t64+
S03	-	-
S05	t48+	t80++
S07	t48-, 96-	-
S09	t64-,80+,96-	t96-
S11	t112+ t128-	t128-

The behavioural features identified can now be used to highlight the “phase” regions of the dataset in which they occur, indicating regions of the life cycle and approximate times for each, interpreted from Table 25 & illustrated in Figure 76:

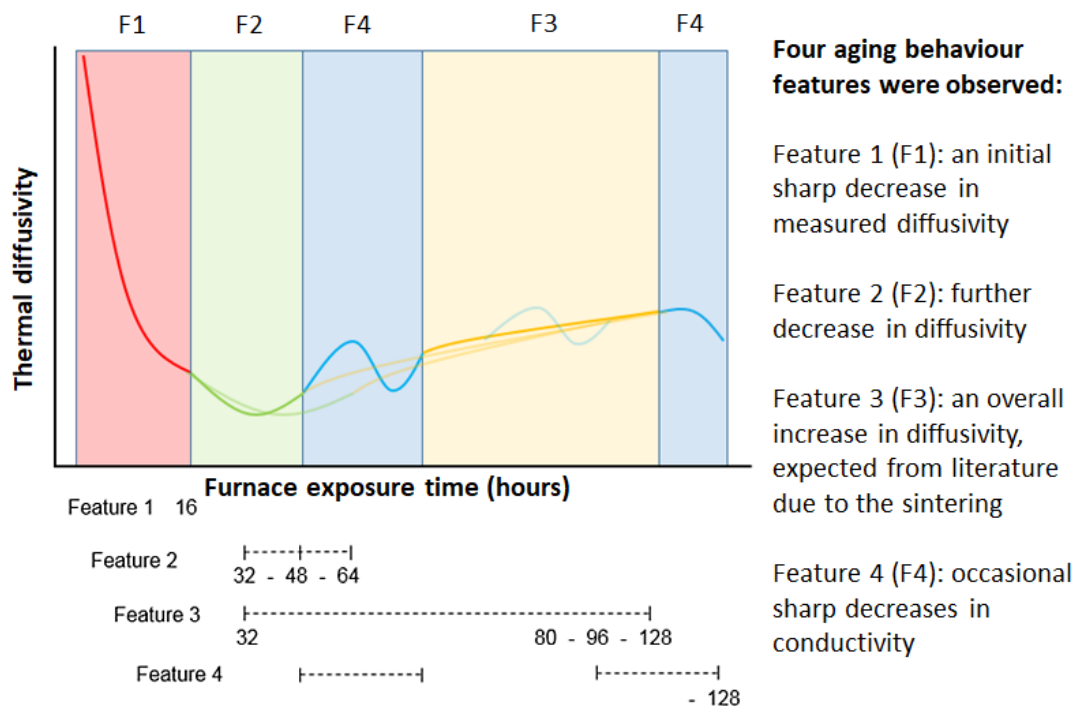


Figure 76 – pattern features of diffusivity behaviour over coating life, approximately detailing how each of the regions vary, and over their respective timeframes. If feature (4) exists, it is not fixed to regions indicated, and the regions are variable for each sample and coating condition.

Having identified the regions, they can be replotted again in the individual results form as in Figure 76, with the identified pattern features as identified in Table 25 overlaid, displaying the results again, with the pattern regions shown; see Figure 77, Figure 78. These feature regions are useful for breaking down the complications from different behaviours being exhibited simultaneously. Additionally, the full expressions of these features can be seen individually for each feature, over both soot conditions, shown in Figure 79-Figure 80; where the overlapping between feature 3 and the others, particularly with the sporadic later-life nature of feature 4 introducing interference in the ageing characterisation.

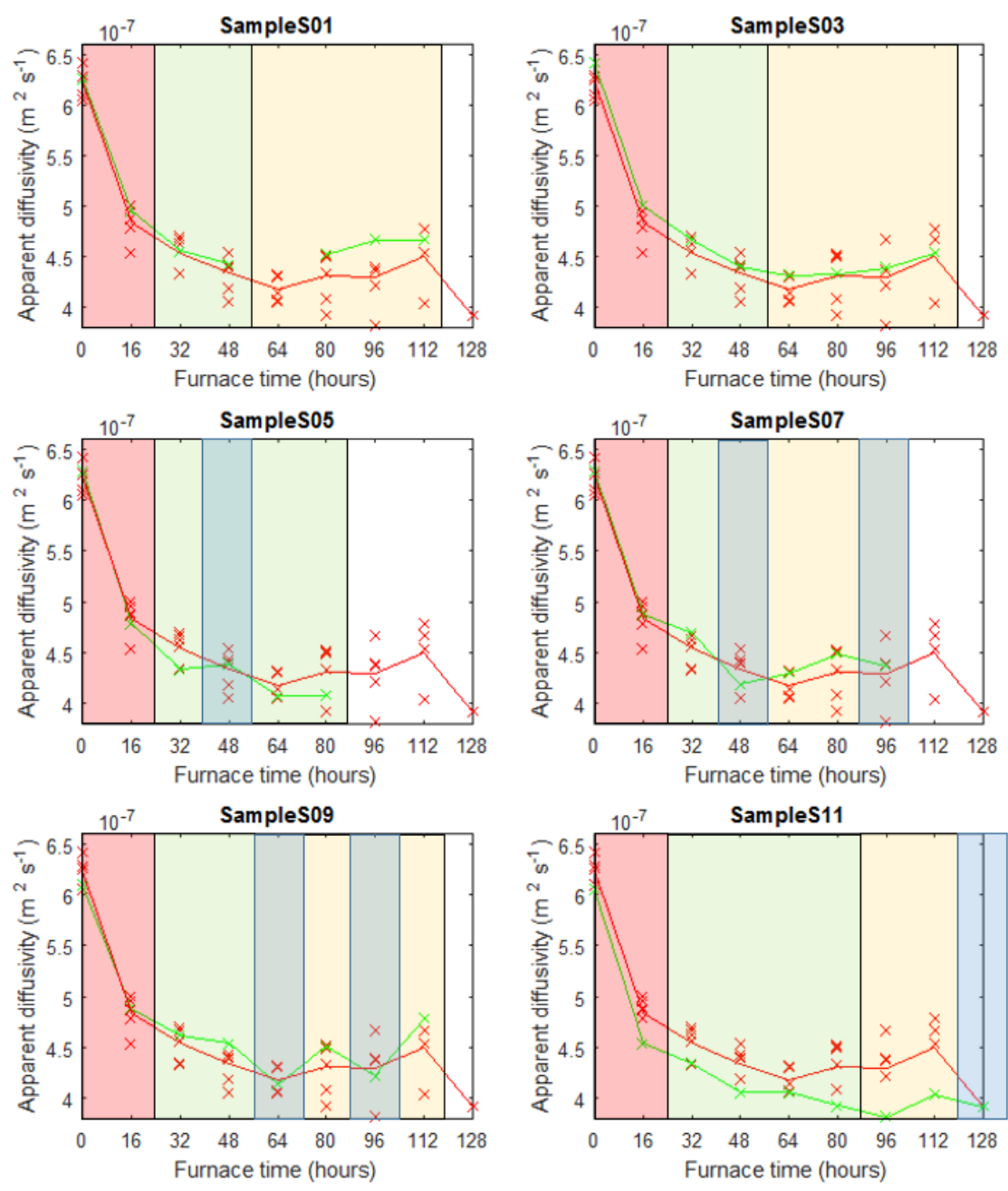


Figure 77 – replotting individual results, with pattern features overlaid, shown here for samples without the soot condition, with each sample’s pattern (green line) plotted against average values: without soot (red line).

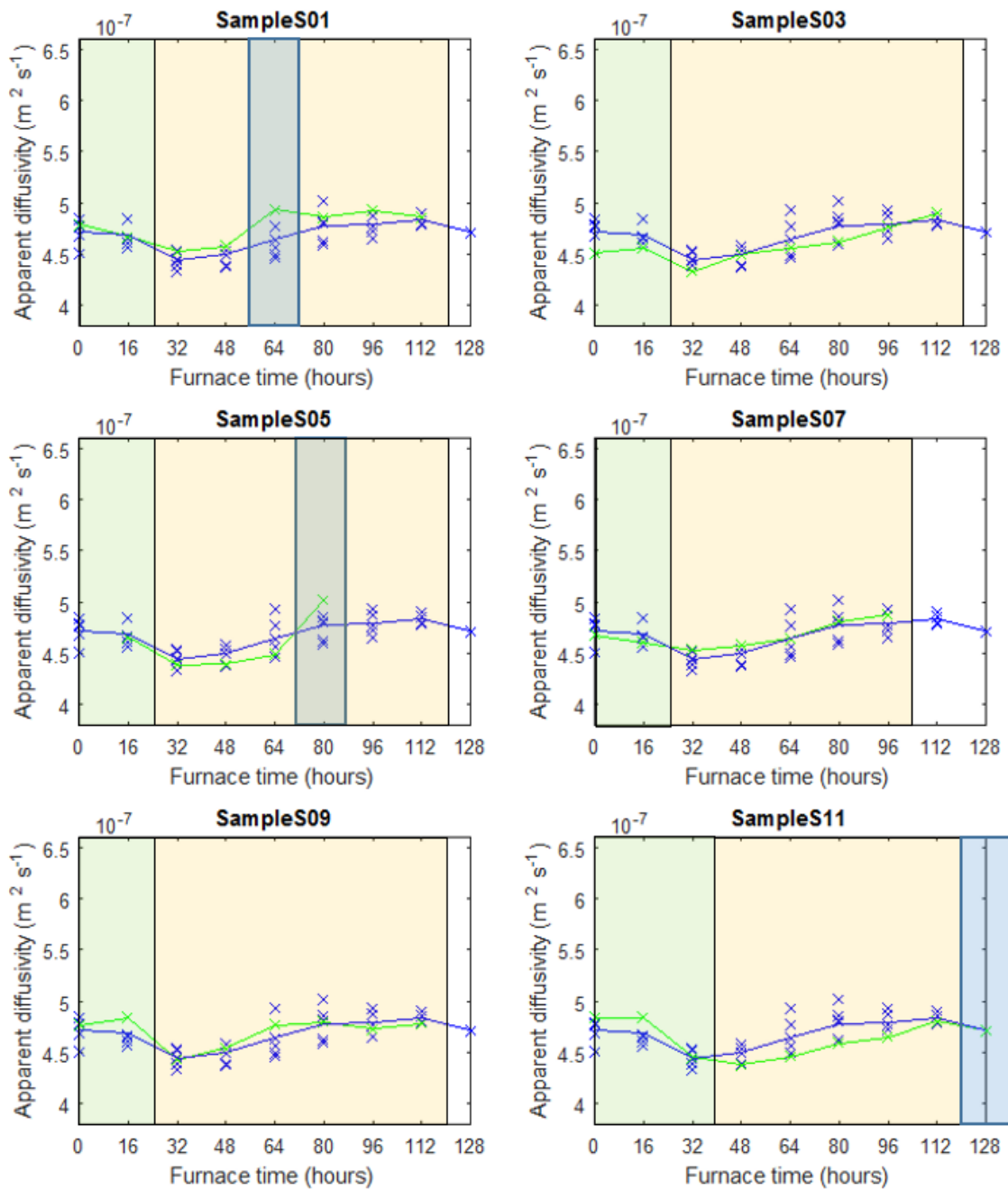


Figure 78 – replotting individual results, with pattern features overlaid, shown here for samples without the soot condition with each sample’s pattern (green line) plotted against average values: with soot condition (blue line).

Having identified the pattern features in the dataset, and their locations, explanations for the phenomena can now be explored. An aggregate plot of each of the regions over the data series are displayed in Figure 79, and Figure 80:

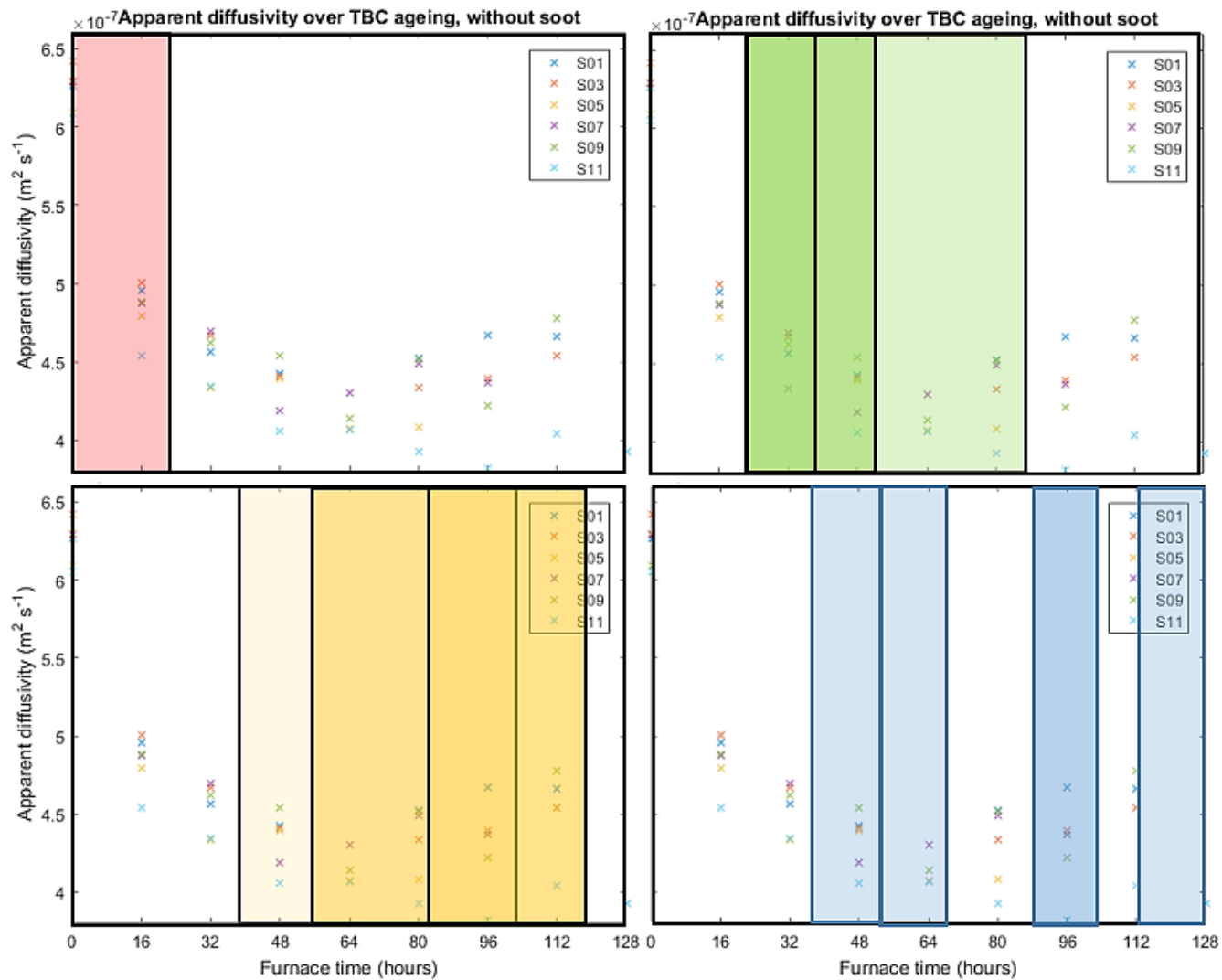


Figure 79 – replotting results, showing distribution of pattern features over life cycle (without soot condition), feature 1 (top left), 2 (top right), 3 (bottom left), 4 (bottom right), emphasising the presence of each feature to be shown in their full expression.

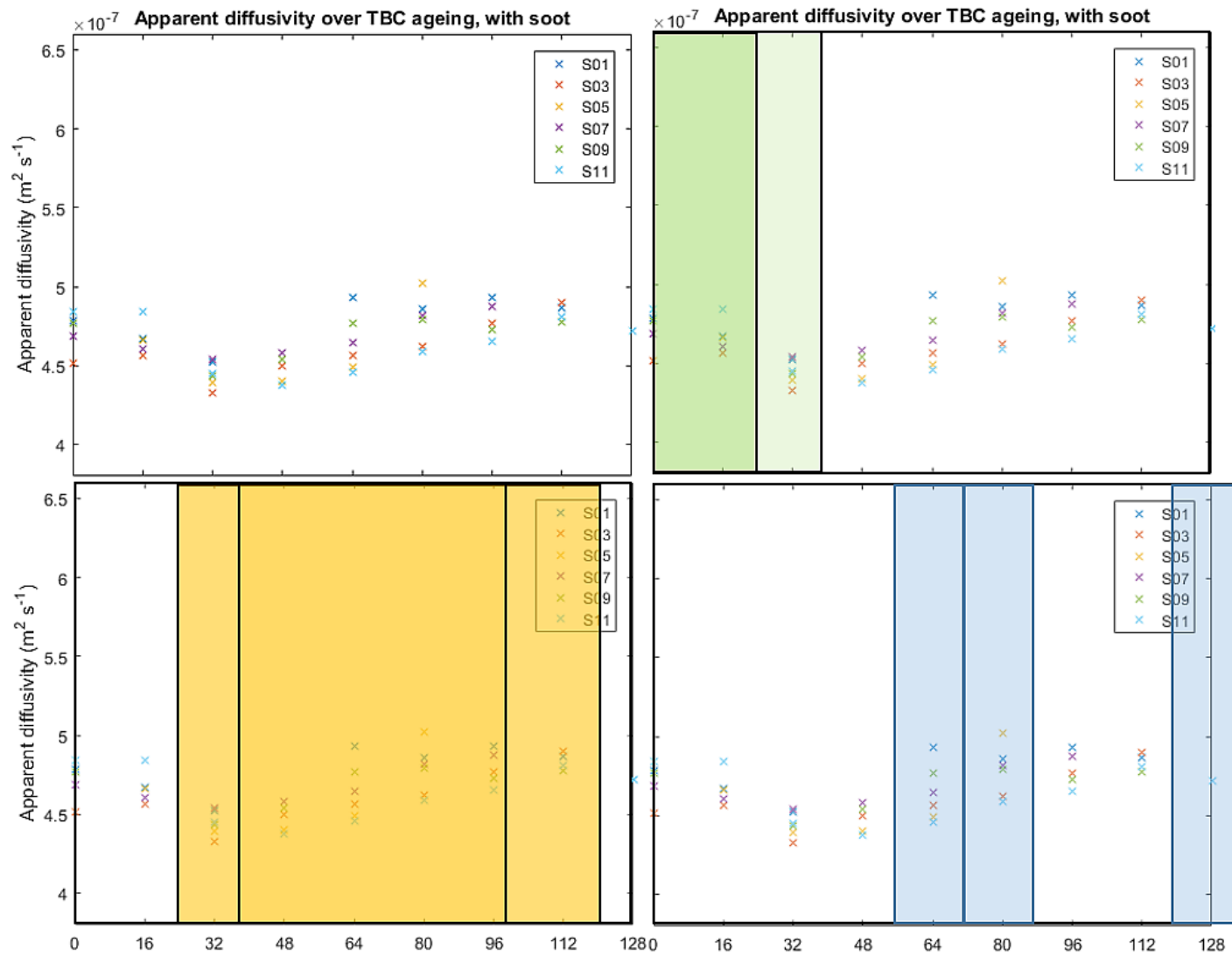


Figure 80 – replotting results, showing distribution of pattern features over life cycle (with soot condition), feature 1 (top left), 2 (top right), 3 (bottom left), 4 (bottom right), emphasising the presence of each feature to be shown in their full expression.

7.5 Comparison with pre-aged coatings of unknown age

Now that a few trends have been teased out from the dataset, the pre-aged samples, whose cyclic conditions are not known to the author, can be inspected to consider how well the trends compare, shown in Figure 81-Figure 82, below. The pre-aged TBCs did not last many furnace cycles, while their response showed that it is possible to measure TBC diffusivity in the same manner as has been performed for as-new samples under ideal and simulated conditions, though it can be observed that the ideal inspection condition with the soot coating condition does offer more intriguing results, and two of the samples exhibit a sudden drop that has been discussed previously to be characteristic of delamination. Furthermore, the uncoated condition inspections are close to the values expressed by the samples aged under isothermal heating; however some differences apply, and these would need to be explored.

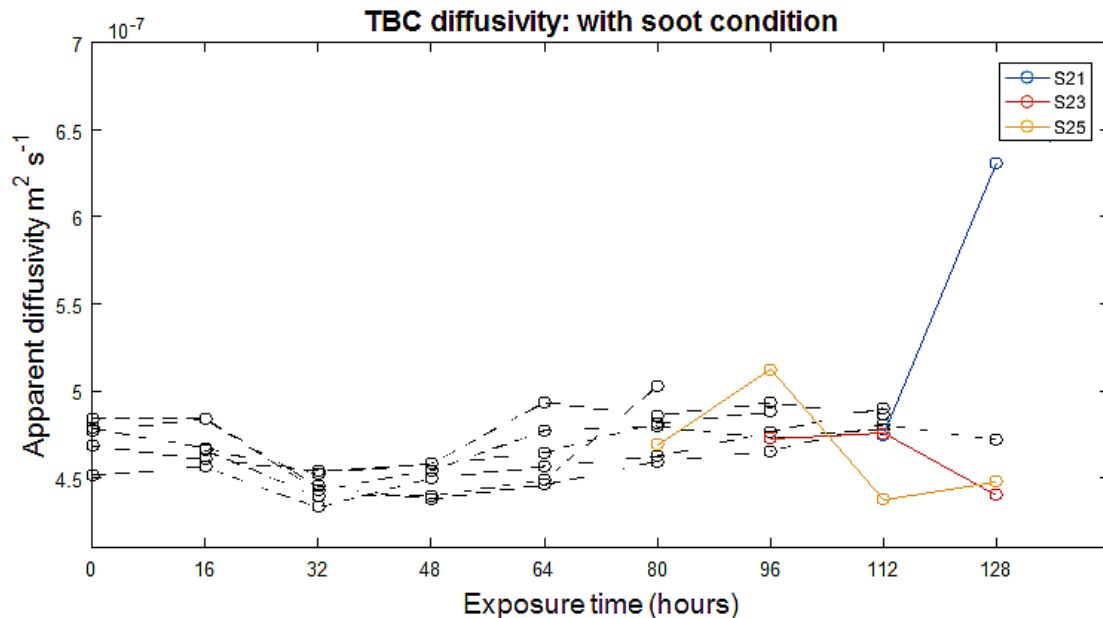


Figure 81 - Plot sample diffusivity versus furnace cycle hours, with soot coating condition: pre-aged coatings; with pre-aged samples over-plotted from $t=128$, in reverse.

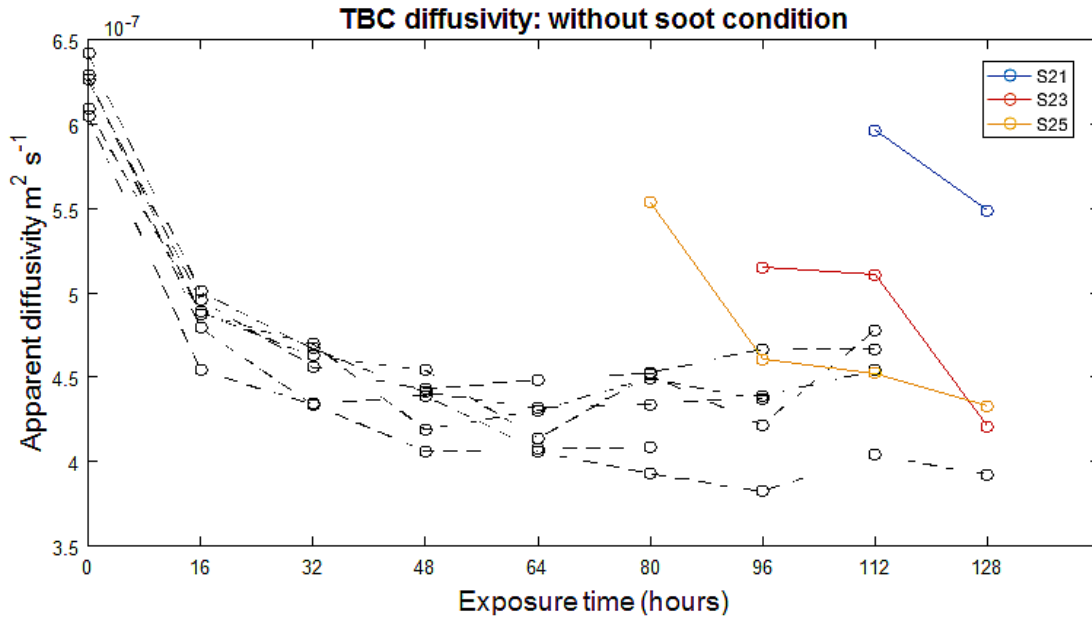


Figure 82 - Plot of pre-aged sample diffusivity versus furnace cycle hours, with soot coating, with pre-aged samples over-plotted from t=128, in reverse.

7.6 Summary

Four features have been identified from the both soot condition inspection series. From the aggregate pattern plots in Figure 79 and Figure 80, it can clearly be observed that the feature region 1 only exists in the uncoated condition dataset, and that there may be some overlap between region 1 and 2, though this does not occur in the coating condition dataset, which exhibits feature 2 independently; where no significant difference between the initial and first inspection was observed. The observation of feature 2 occurs at a different time in the uncoated dataset, and therefore could be instead a continuation of feature 1, with the expression of feature 2, which may exist in the uncoated set, potentially smothered under the dominant expression of feature 1. These observations aside, feature 3, the continuous increase in thermal diffusivity property that was expected, sought-after, and can be found in the literature, which this study was

attempting to seek in the uncoated condition. This feature has been identified in *both* the soot coated and uncoated datasets. However, the expression of feature 3 is considerably much stronger in the soot coated condition than it is in the uncoated condition, where in S05 the expression of feature 3 was not exhibited at all, likely due to its earlier failure, at a point where the expression of feature 2 still dominates in all the other samples – while in S11 in the uncoated condition, feature 3 was only observed at the end of the sample's life. Feature 4, the sudden abrupt changes in measured diffusivity was exhibited at the middle (48-80) hours of coating life, and at the end of coating life – though this expression only occurred in sample S11, for both datasets), with two further expressions near the end of coating life (96 hours) in the uncoated condition.

8 Automation of data capture and feature detection

The data and graphs contained in this subsection have already been published in a journal paper (Mehnen, Roy & Tinsley, 2012) [178].

As discussed in §1-2, Non-Destructive Testing (NDT) methods are instrumental in the prolonging of component life and reducing service disruption from unscheduled failure and maintenance. A wide variety of NDTs are available, depending on the material and form of deterioration involved; however NDT and component inspection has often taken a qualitative approach, where the tests frequently require to be conducted and the results interpreted by a trained operator. This chapter presents developments in robotic thermographic NDT to automate data capture, identification of damage and sizing in real components, in order to improve upon the advantages of the system as a low-cost, rapid inspection method that can provide automation for component inspection.

8.1 Industry requirements

Initially, the requirements for a new NDT application needed to be established, where two companies were engaged in the form of a series of structured interviews in order to set out applicable inspections for thermography and its automation, reflecting the NDT methods in current use in MRO context, which was discussed in detail in Chapter 4. Among the key findings was the indication that while thermography had featured in inspections, regular applications were limited, while implementation of inspection automation with thermography was also limited, while the main barriers to further development and making use of the advantages of thermography would have to remain within the cost constraints of

limited technician time, and consumption of time on the component's turn-around schedule. With quasi-manual inspection methods and data interpretation consuming considerable time from trained technicians, thermography has more potential for regular use than it can currently be afforded, and in order to make use of its advantages, it would need to not only offer valuable inspection capability (for instance, detection of delamination or measurement of thermal property as part of the main experiment in this thesis); it would also need to be developed to be quick and undistruptive in its implementation.

Two other key issues that were raised were the lack of application of thermography for prediction of remaining useful life, and the constraint that any additional NDT method introduced or application of existing methods expanded would not incur a cost burden above the advantages the method confers, unless it was in answer to a specific problem. In this instance this becomes the preference for thermography to reduce inspection turn-around time, underlining the need for automation, if its current application were to be expanded. For this purpose - and prior to the results of the main experiment being generated - a study on the automation of thermographic inspection was undertaken.

8.2 Experimental method

The experimental setup included the same thermoscope system described in §5-7, the Thermoscope® II, using the same capacitor bank and computer control unit. The IR radiometer used was an uncooled micro-bolometer model Gobi Xenics384, using a lower resolution of 384x288 pixels, and a framerate of < 30Hz. The diagram of equipment setup in Figure 35 is equally relevant in this instance, however, instead of the radiometer being held on a tripod to view through the

reflective flash hood's view port, the camera is small enough to be mounted on the flash hood, which could then be mounted in-situ, for automated data capture.

8.3 Automated inspection cell for damage detection

Automation can be broken down into two categories: automation of data capture, and of analysis. The first was addressed by use of an M-20iA robotic arm from the Fanuc Europe Corporation. The use of a robotic arm or other mechanised system permits the part to be accurately presented to the inspection system over a large volume of inspections with rapid performance, and repeatable precision, encompassing flexible rotation of components to present their features at the required inspection angles, while maintaining a high inspection speed, with minimal interference from operators required, even for changes of component. For this purpose, a robotic arm was used for automation of data collection, and is shown in Figure 83. With the M-20iA robotic system used, this repeatability can be maintained to within ± 0.1 mm positional accuracy; smaller than the thermography system's resulting pixel resolution at standard distance ($\sim 30\text{cm} +$).

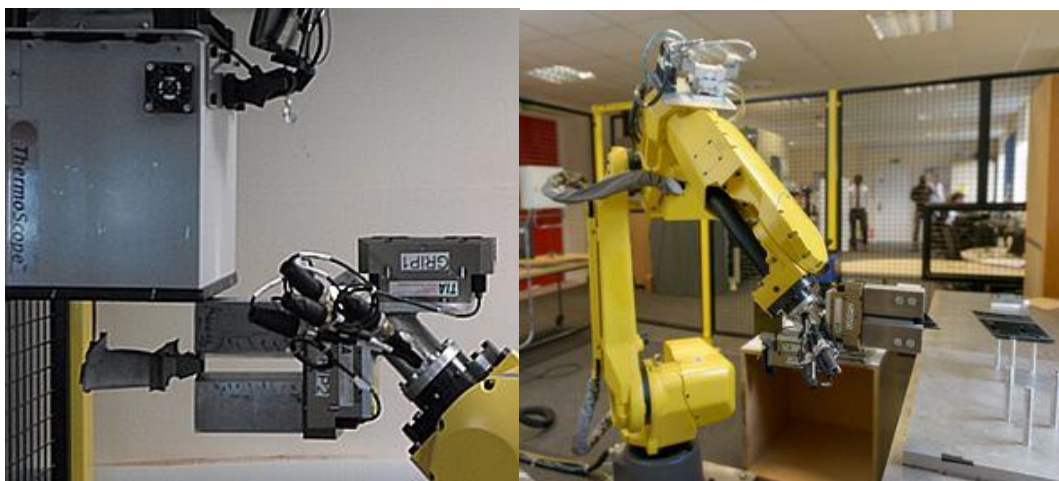


Figure 83 – Automated NDT inspection system with use of the Fanuc M-20iA robotic arm, showing presentation of one type of component to the inspection system (left), and the collection of another type of component for inspection, (right); image reproduced from (Mehnen, Tinsley & Roy, 2014) [178], courtesy of Elsevier.

8.4 Pulsed thermography: delamination detection

The type of components available for inspection during this work did not contain the same coating as inspected in Chapters 5-7, and so the application of pulsed-active thermography, though essentially the same in principle, was developed around the target damage type of delamination of the TBC, as this was an appropriate inspection application for the component. While the work in earlier chapters would be ideal targets for inspection automation with the analysis performed integrated into the inspection system, the availability of samples with TBC delaminations invisible on the surface were used as the demonstration of automation of the inspection technique confers similar advantages, in either inspection scenario. These components had TBC coatings, with delaminations causing the parts to be rejected from being released, providing ideal features to develop and demonstrate inspection automation.

8.5 Automated analysis: image processing

Once the data has been collected by the robotic system, the next stage of automation requires damages to be identified without human operator input.

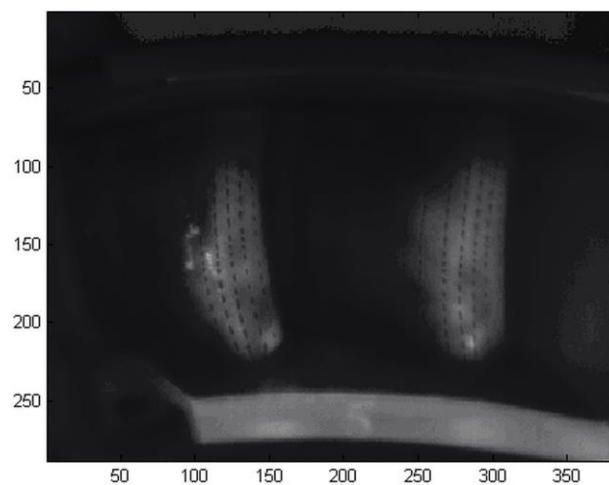


Figure 84 – Raw output image of component under inspection (greyscale); image reproduced from (Mehnen, Tinsley & Roy, 2014) [178], courtesy of Elsevier.

For this purpose, software has been written using Matlab with Image Processing Toolbox R2012b [186]. An example of the raw data image output by the system is shown in Figure 84. The first frame after flash was selected for development of the automated image processing (this was a subjective decision based on the peak signal-to-noise signal for apparent features, also due to the low frame rate of the radiometer used, and the features in the sample, the peak contrast for most of the features was within the first post-flash frame. In further developments, this would be relevant to the frame at which the depth of feature or penetration of the substrate occurs; or a compound image, such as 2nd differential / diffusivity map, which would make appropriate use of the method developed for chapters 5-7.

Once the data was acquired, a threshold level was set at the upper-quartile (75%) of pixel intensity range. The location of the line segments can be set since the component presentation from the data capture stage is repeatable, where it can be assumed that for every inspection, the position of the component is within <0.1mm accuracy; meanwhile, the inspection system has an effective resolution on the sample surface at standard distance of approx. ~ 0.25mm per pixel [187]. Owing to the positional accuracy of the end-effector of the robot system being significantly smaller than the effective resolution of the inspection system at standard distance, the positioning of the line segment can be set at the very first inspection so that it includes key structural features, in areas that are normal to the inspection plane of the camera lens, and do not contain background behind the target subject; these initial line segments can be maintained for all inspections of components at the same angle; in thermography, an angle of less than 50° from the inspection plane (a line perpendicular to the surface) is advisable,

though a detailed study of the spectral emittance of the material under inspection could enable shallower angles (with respect to the surface) to be applicable, if desired. In this case, an angle of 5° (85° from the mounting rail surfaces) was used. The output produced by the thresholding step is a binary map of “hot spots”: any feature or area above the prescribed threshold. After the thresholding process, multiple feature regions with temperature contrasts above the background were highlighted isolating them in the remaining plots. The borders of these regions are captured using the Moore boundary trace algorithm that defines the border of regions in the threshold-resulting binary images [188].

8.6 Segmentation of features of interest from structure

While the method readily yields detection of sub-surface defects and damages, a number of structural features are also passed to the results list of “features of interest” that remains from the threshold-filter. For this purpose a structure feature mask was created to obstruct features not of interest to the inspection (the outer edges, cooling holes, etc), so that any unwanted structural features can be masked from the detected “hot spots” in the resulting binary image. Examples of the binary image output from the thresholding stage, its filter mask and respective threshold binary map output, are shown in Figure 85.

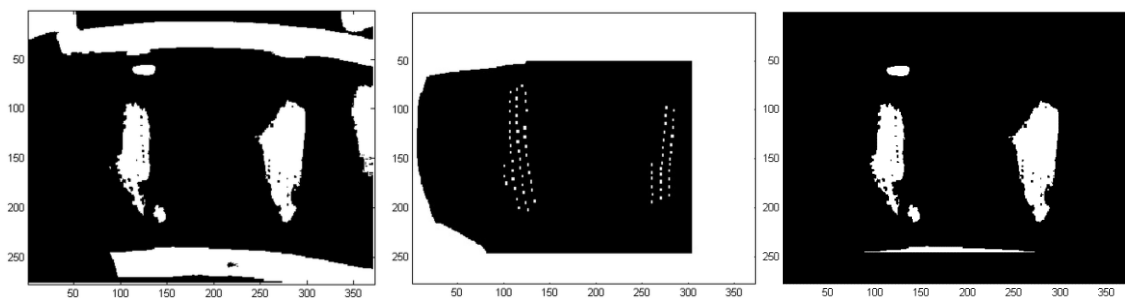


Figure 85 – example of binary image (left), respective filter mask (mid), resulting binary map (right); reproduced from (Mehnen, Tinsley & Roy, 2014) [178], courtesy of Elsevier.

The boundary trace algorithm is then applied to the resulting binary map, tracing all ‘regions of interest’ (ROI) remaining in the image. A minimum feature size of 2-3 pixels is often recommended to classify a feature as a valid detection [189], and was applied as part of the algorithm. This step filtered potentially false positive hits which were picked up surrounding the cooling holes on the leading edges, as shown in Figure 86. Since the samples were loaned, they could not be dissected for a proper investigation, and any attempt to investigate the validity of such small detections would need a more thorough investigation. For features that fall within the 2-pixel criteria that has been applied, (in this case, 0.5mm), the effects of the edge of the cooling holes would need to be included in the analysis, and a higher effective resolution on the surface of the component employed.

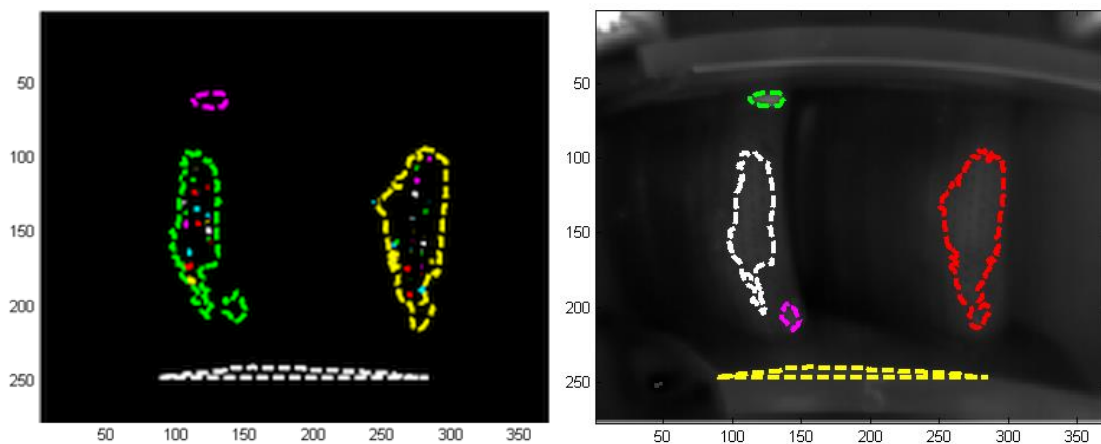


Figure 86 – application of boundary trace algorithm to binary map, regions of interest plotted in rotating colour palette (left), filtered results plotted on original image (right); image reproduced from (Mehnen, Tinsley & Roy, 2014) [178], courtesy of Elsevier.

8.7 Automated sizing

Sizing in thermography is usually undertaken by manually placing a calibrated scale over the feature of interest [190]. In this study, the distance between the furthest pixels in the boundary region may be used; however other methods are useful, such as the full width at half maximum (FWHM). Application of a fitting a

2D Gaussian function to data (Nootz, G., 2012) [191] was set to each “feature of interest” region using the least-squares technique [192], where each feature region was able to be removed from the background data. An initial set of guess parameters for x-y location, size and amplitude and feature rotation are required, the fitting process fitting an estimate for size, center location, spread, amplitude and rotation of the features given; or (if the data is temperature-calibrated), an estimate of temperature contrast and the FWHM can be applied, simplifying and standardising the detection and post-processing of damage features, shown in Figure 87, below:

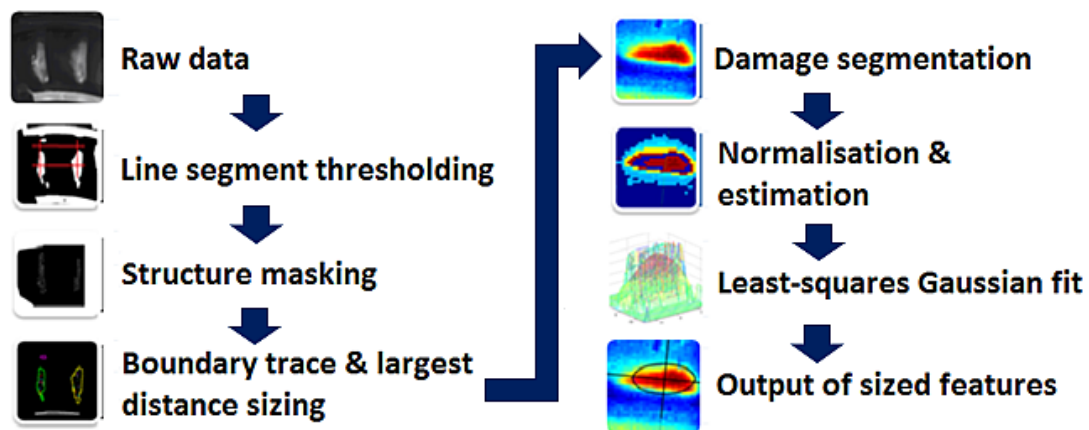


Figure 87 – A process flowchart showing the automated detection & sizing stages; image reproduced from (Mehnen, Tinsley & Roy, 2014) [178], courtesy of Elsevier.

8.8 Results and discussion

This automated data capture and inspection technique was performed on a series of aerospace components with surface-breaking (spallation) and sub-surface (disband, delamination) features. Since many perspectives are required for full part inspection, a filter mask for each inspection angle was created by highlighting the pixels of structure features overlaid on top of one of the pre-flash frames.

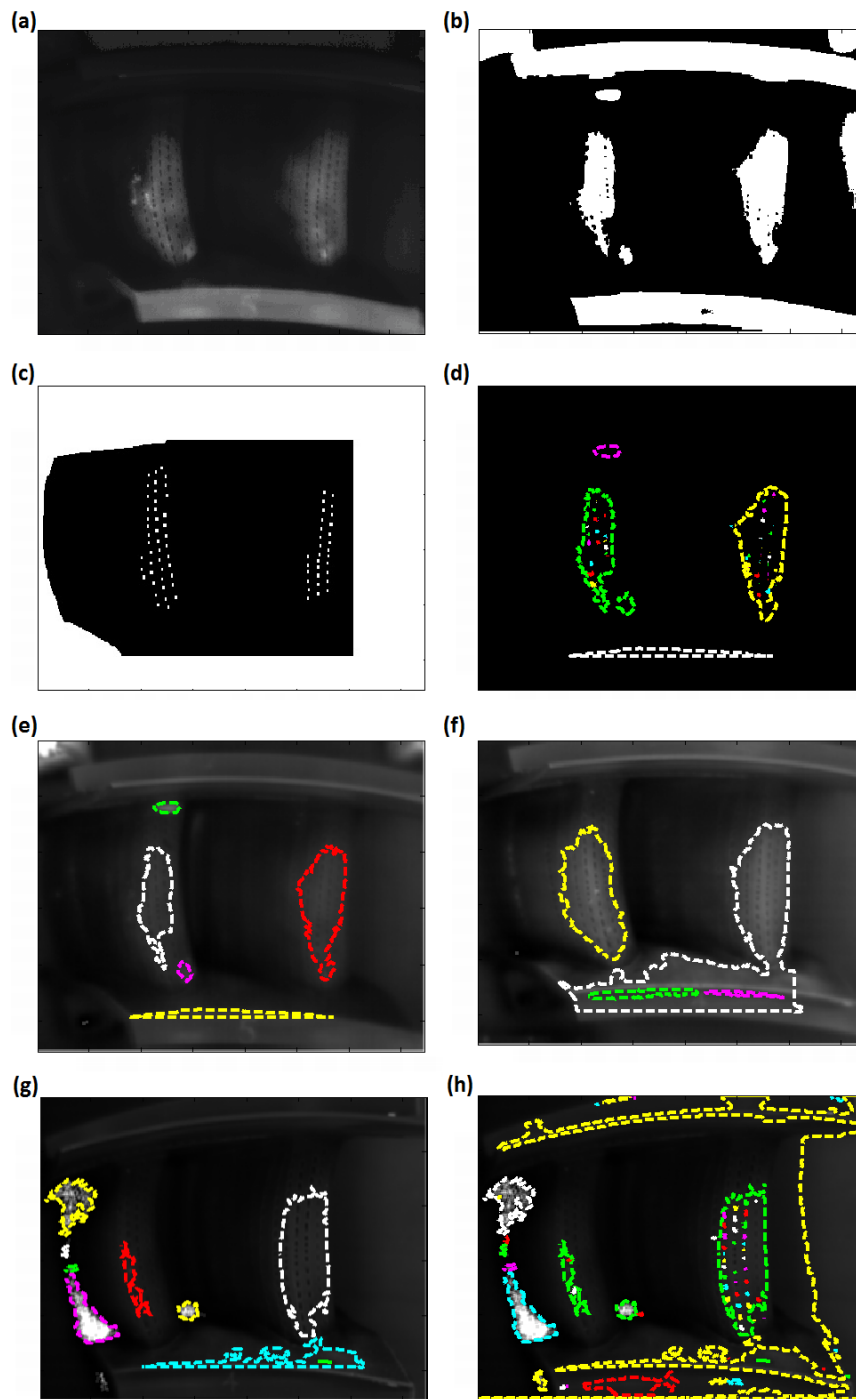


Figure 88 – Automated damage detection and segmentation process; image reproduced from (Mehnen, Tinsley & Roy, 2014) [178], courtesy of Elsevier.

The inspection process and a handful of examples at different stages of inspection are shown in Figure 88, where the automated data processing steps are as follows: firstly the raw temperature data (a) was converted into a binary map using a threshold (b), this is used to form a filter mask (c). Numerous features

could be seen in the resulting image, including much of the part structure, most of which is not of interest to any one inspection method (d), which necessitates their addition into the feature-filter mask. Once the filtering process is applied, few regions of interest remain (e). When one filter mask has been constructed for the respective inspection angles, new components may be presented for inspection, (f), (g), respectively. Structure that has been excluded is also displayed (g) (h).

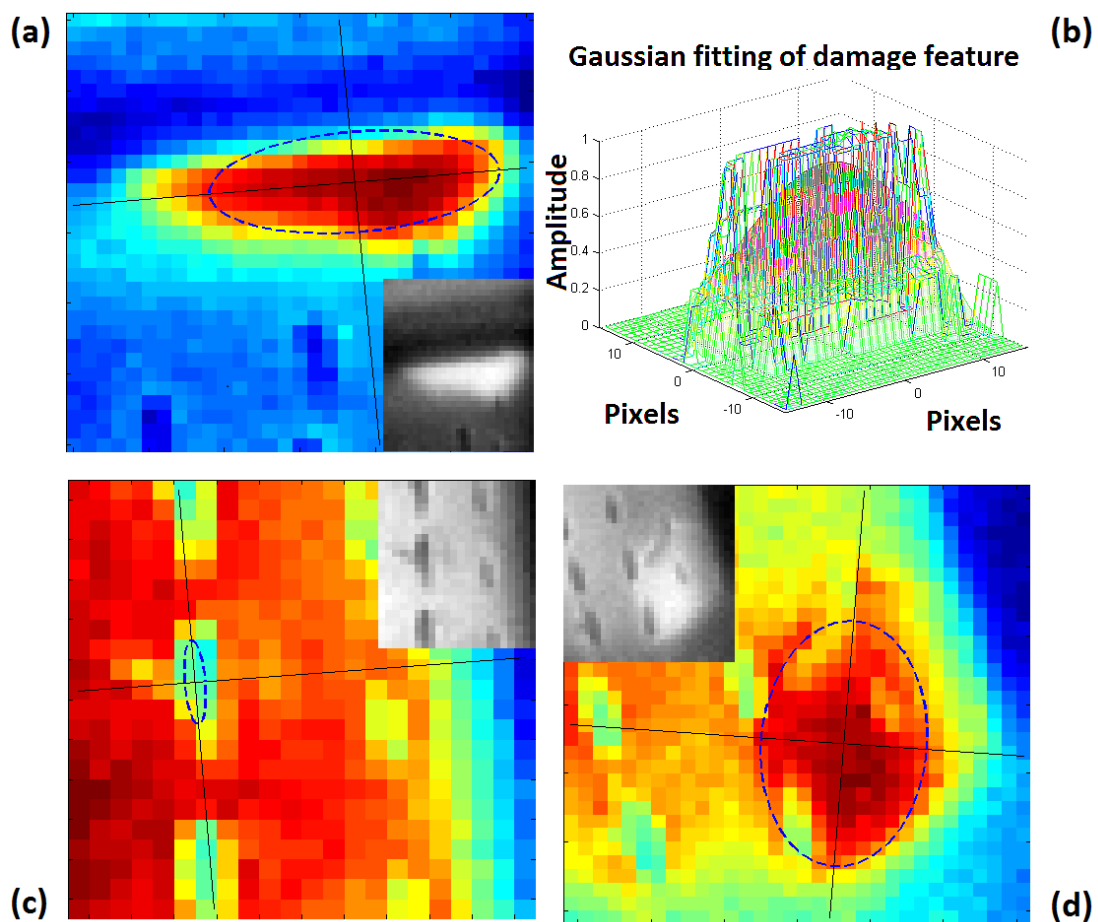


Figure 89 – Three damage types auto-segmented for Gaussian fitting, with fit results plotted over the damages. The fitting process is shown. Image reproduced from (Mehnen, Tinsley & Roy, 2014) [178], courtesy of Elsevier.

A few examples of fitted damage features are shown in Figure 89, with results displayed in Table 26. The fitting enables significantly more information than a single measurement about damage regions, including length, width, orientation,

and eccentricity of the damage feature, providing an initial proxy for shape. It also provides pixel co-ordinates of the centre of the fitted shape, as well as the co-ordinates of each of the feature boundary points from the boundary trace stage.

Table 26 – Examples of detected features output by the algorithm

Damage	Minor	Major	Eccentricity	Amplitude	Angle
A	1.06	2.9	0.93	0.9	5.3
C	0.28	4.18	0.99	1.4	4.6
D	1.70	2.68	0.60	0.8	4.4

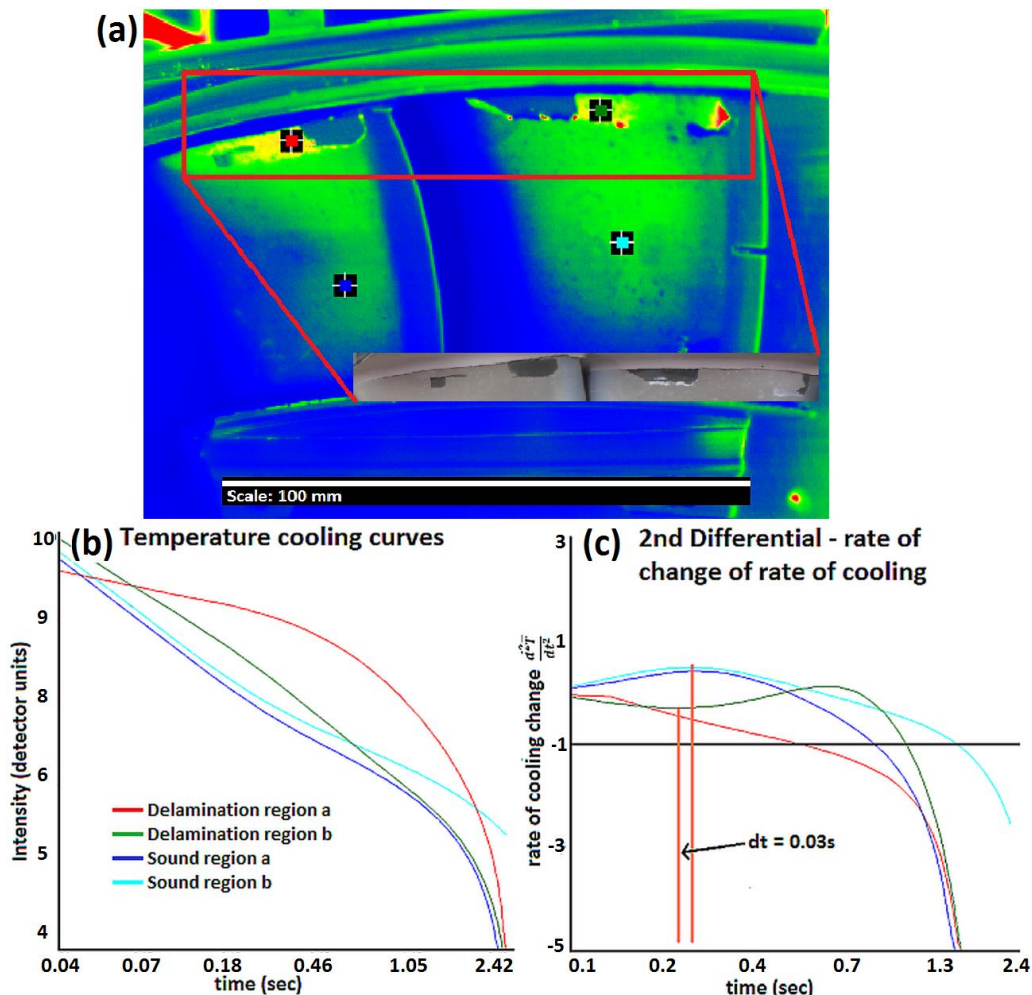


Figure 90 – Example of thermography inspection of TBC delamination (situated next to spallation regions), top-left (a), red, & top right (b), green, showing log-log (T,t) plot (b) containing thermal contrast of the delam regions from the “sound” in-tact TBC (a), (blue, mid), with 2nd differential plot giving different time of peak contrast change (c). Image reproduced from (Mehnen, Tinsley & Roy, 2014) [178], courtesy of Elsevier.

A pair of sub-surface damage features exhibited a temperature contrast, though owing to the low frame-rate of the radiometer used, these were impossible to investigate further, with their contrast peak occurring in the first two frames.

8.9 Summary

The automated data collection and post-processing of a complex-geometry aero engine component was performed on two components with various features of interest (TBC delamination, spallation), and structural features. The data capture was collected with 3 angles for each component, with <15s movement required between inspection, and 5 mins cool-down between inspections, resulting in a total inspection time of <32 minutes for two components, with automated damage inspection for spallation / delamination features. Faster inspection is possible for coarser inspection with lower sensitivity appropriate for larger features. The automated generation of part inspection for delamination detection with filtering of false positives was almost-instantaneous (<1m), highlighting the applicability of thermography for automation for rapid inspection, offering the measurement of TBC diffusivity for ageing characterisation used in the main experiment the potential for rapid implementation in a commercial context.

9 Discussion

The literature surrounding the NDT inspection of TBCs was presented in the first and second chapters, while specific interest and requirements from industry were explored in the fourth chapter. After filtering the available literature for their appropriate application to the inspection of TBCs, an oxidation ageing experiment was proposed, planned, trialled and carried out, which has been described in chapters 5 & 6. The results were then produced, and the patterns exhibited analysed for both coating conditions, raising the underlying trends and their respective features explored in chapter 7. Following on from the cyclic ageing degradation experiments, an automated application of pulse thermography NDT for TBCs has been explored and implemented in chapter 8. This was performed with a detection of delamination inspection method, which could be adapted instead of location of hot spots, to location and sizing of diffusivity regions that the main experiment could yield in real practice. This has demonstrated how the assessment of TBC life could be applied in a real context, in response to the associated cost-benefit barriers such a method would need to overcome. In summary: the patterns exhibited in the life assessment results require discussion in light of the stated objectives and literature context, with particular regard for the realistic applicability of the technique applied (i.e. whether without soot coating condition is appropriate). Also, the strengths and weaknesses of the methodology need to be included, with recommendations of improvements.

9.1 Causal factors in changes of thermal properties in TBCs

As covered in the literature review, the thermal and optical properties of TBCs are rooted in the ceramic material's intrinsic low conductivity property, in the ceramic's crystal structure's respective grain size, and the microstructure of the deposited TBC, and all of these are expected to shift and change over sintering from exposure to high temperatures, including changes to pore size and shape, smoothing of the "feather shape" of the EB-PVD columnar surface, thus increasing the conductivity of the columns over time. This effect was expected to be counter-balanced and punctuated by a decrease in interface thermal conductivity associated with the propagation of cracks, reducing the cross-section through which heat can flow to the substrate, matched with an increase in reflectivity of the interface. Meanwhile, dislocations at the interface would be expected to change optical properties, such as the reflection coefficient owing to the now-growing mis-match between the ceramic and air, while the changes in porosity would also be expected to have an effect, discussed in later sections.

All of these processes occur simultaneously during high temperature oxidation ageing of TBC, which was expected from the literature findings to exhibit an overall long-term increase in conductivity / diffusivity with sintering and porosity change, along with intermittent drops that increase towards the later stages of TBC life as cracks grow and converge, detaching from the bond coat. Additionally, other sources of change to TBC properties were expected to affect the measured properties, although how exactly this would unfold was not fully understood prior to the experiment. In some instances this was because the changes mentioned or exhibited by the data in other studies, were reflective of

changes in APS TBCs; while in other studies the change in a property in an ageing EB-PVD TBC was measured, though how the results would translate into influence a measurement of thermal diffusivity would not be immediately apparent without a model or matching experimental results, which the main experiment of this thesis was expected to express. Those results can now be reflected upon, in light of the various findings in literature.

9.1.1 Feature 2: Growth of TGO with ageing?

Referring back to the literature and attempting to find use of the life prediction methods developed from project HOST, specifically the oxidation model given in (2-3), and using the model and figures by (Meier, Nissley, Sheffler 1991) [82], we can model curves of TGO growth over the first two furnace cycles, yielding the curves shown in Figure 91.

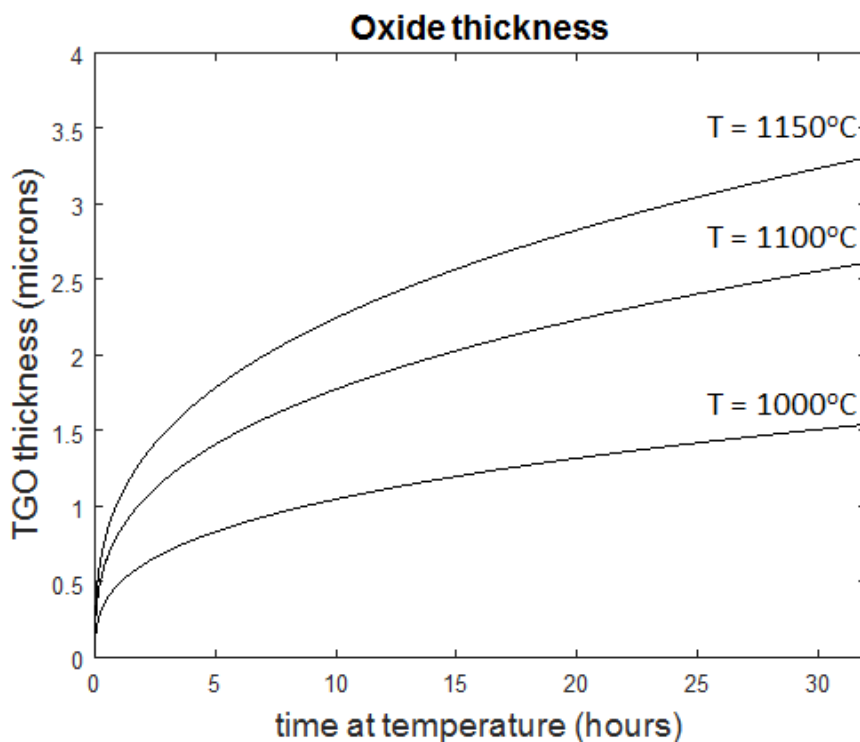


Figure 91 – model of TGO growth as a function of temperature & time at t

As can be seen, a considerably rapid growth of TGO can be expected in the first 16-32 hours (or the first two isothermal exposure cycles). It was suggested during the literature review that this early rapid increase of the oxidation thickness might generate a large number of small microcracks, which could present a marked decrease in thermal conductivity of the system that may be detectable. This process could explain the second feature observed in both coated and uncoated datasets, before the growth of oxide reduces into the medium length of TBC life, while the effects of sintering become more pronounced.

Meanwhile, the additional growth of oxide could also be expected to change the infrared reflectance of the ceramic-bond coat interface. A growth in this layer would need comparison with the reflectance of the original condition, and a wider reflectance spectra to comment on whether the early TGO may have altered the absorption of the heating flash, potentially affecting the results from which the diffusivity is calculated. The interplay between the expected conductivity decrease and the potential for an interference with the flash heating would need to be probed further.

9.1.2 Increase in thermal conductivity and diffusivity: Sintering, changes in microstructure surface features

As covered in § 2.5 the literature review, the TBC was expected to exhibit a steady increase in thermal conductivity due to sintering over exposure to high temperature; phase change and grain size increase in the TBC ceramic (Limarga et al., 2012) [193]; and this steady increase was observed in other studies of TBCs, which featured behind the prediction in § 6.3.

This steady increase has been described as having been observed in the results, referred to as feature 3 in § 7.4.

Referring back to the literature on the effects of heat treatment on TBCs, a large early increase in thermal properties has been exhibited in other studies in the first 50 hours of heat treatment, as had been observed in APS (Cernuschi et al., 2010) [153] and EB-PVDs (Kakuda et al., 2009; shown in Figure 20) [73].

However, this leap in conductivity from their study was the wrong direction to explain the abrupt change observed in feature one for the uncoated inspections, and would be conspicuous if it were only expressed in the uncoated inspections; the change in conductivity / diffusivity would be expected to increase by approximately 10%, compared to that observed, shown in Figure 74 and Figure 75, which is also in the wrong direction to this increase for the large initial change in the uncoated condition, and is not observed in the soot coated condition, as can be observed in more detail in Figure 71, where only two of the samples exhibited an initial increase in diffusivity, of approximately 2% of their initial value. It would be alarming that this sharp early rise is not exhibited in either datasets, however the rise occurs in the first 10-15 hours

From the comparison with the series of results (particularly the coated condition) and those of early heat treatment and early cycle induced rapid increase in conductivity / diffusivity that can be observed in literature [70] [72] [73], it can be concluded that early sintering / heat treatment behaviour observed in literature is not responsible for the change (feature one) in the uncoated condition, which is also not exhibited by the coated condition inspections, which suggests the

difference exhibiting feature one to be optical in nature, and not related to the material's thermal conductivity.

Aside from the steady increase in conductivity, abrupt changes are noted in the literature to occur with thermal cycling (see Figure 22), which share similarity with feature four.

Researchers have mentioned that 1150°C is considered a low temperature for the observation of sintering effects, though this has been observed affecting the microstructure of EB-PVD TBCs at temperatures as low as 900°C [76]; while an early increase in diffusivity has been found to be exhibited by free-standing TBCs, and smoothing the wall surface features (see Figure 21) and transforming the feather structure of EB-PVDs into pores, decreasing scattering at the walls, and increasing the conductivity of the columns [73] [74].

This overall increase in conductivity can be observed in the data in feature 3, as predicted, however this cannot explain either of features 1 or 2, as the expected initial increase is not present.

9.1.3 Increase in thermal conductivity and diffusivity: changes in porosity

As the conductivity of EB-PVD TBCs is predominantly a result of the columnar structure, which is affected by the porosity interrupting the cross-sectional area for heat to flow through (§ 2.5.2); in the literature review it was noted that pores in the TBC coalesce at high temperatures [75], where, as the coalescence at the columnar walls effectively 'consumes' the feathery structure, reduces the effective porosity of the structure, then the area for thermal

conduction is increased; hence the conductivity can be expected to steadily increase, which would feature behind the development of feather three.

Both the smoothening of the feathery structure and the coalescence of porosity can be seen to occur dramatically within 1 and 100 hours of exposure, which can be observed in Figure 23. The researchers behind this finding (Renteria & Saruhan, 2006) pointed their sharp increase to surface atomic diffusion process, [76], meanwhile Kakuda et al, (2009) attributed a combination of microstructural changes to the feathery structure (essentially pointing to the same dominant cause).

If the change in the TBC microstructure is known, it is possible to estimate the change in conductivity from changes to porosity in the columns, and the merging of inter-column gaps (Lu et al., 2001) [194]. If the experiment had more samples, sacrificial samples could be removed throughout the test, and a visual inspection performed to assess porosity to estimate this effect.

9.1.4 TC – TGO interface changes from with TGO growth, with possible interface separations

As known from the literature, cracks and delaminations between the TGO and bond coat develops over time, which reduces the thermal conductivity of the combined system, as the lattice vibrations can't cross the gap. The effects of the formation and propagation of cracks have been inferred from abrupt dips in thermal cyclic tests, shown as part of the literature exhibited both in the short term (see Figure 22), and over the entire coating life (see Figure 24) (Zhu et al., 2001) [70]. Under cyclic testing, all test conditions explored by Zhu et al., produced the

same overall increase in conductivity (feature 3), which has been observed by others in APS TBCs [126] [153].

Feature 4: propagation of cracks

The fluctuations in the diffusivity, which represent feature 4-like dips were suppressed in the literature studies for isothermal and steady-state tests; but were exhibited in all thermal cyclic tests, indicating that the formation of cracks (and thus the sudden drops in conductivity measured), which further indicates the ‘shock’ of thermal property mismatch driving crack formation, which further supports the explanation of feature 4 in the dataset. In the same research [73] a large and steady decline in conductivity was observed, which the authors assigned to crack / delamination propagation just prior to failure, an example of which can be seen in Figure 25.

The effects of an abrupt delamination-caused sharp decrease in thermal conductivity can be observed in mid-infrared reflectance imaging used in the through-transmission mode as part of research by Kakuda et al., 2009 [73], Figure 26, where the localised delaminations can clearly be observed; while other research measured abrupt drops in conductivity with their methods (Zhu et al., 2001) [70]. Reflecting on this and the abrupt changes recorded as feature 4 in Table 25, §7.4 and shown in Figure 77 - Figure 78, are the following observations:

In the uncoated (no soot, Figure 77) condition:

- 1 fluctuations up
- 5 down in the
- with 3 of the latter occurring within 1 cycle of end of life.

These end-of-life decreases indicate the presence of pre-spallation delaminations, validating the capability of the method to measure feature 4 as an end-of-life “warning trigger”, even in the uncoated condition.

Meanwhile, in the (with soot, Figure 78) coated condition:

- 2 fluctuations involve decrease
- 1 decrease increase
- with 1 increase & 1 decrease occurring within 1 cycle of end of sample life

Considering how a change in coating diffusivity incurred by cracks and delaminations, which should be the same for both test conditions, this reduces the list of Feature 4 that fits the description of expected delamination behaviour to just one sample: S11, at t = 128 hours, where this behaviour is demonstrated consistently. By filtering the instances of feature 4 in Table 25 to only comparing matches between the two conditions, leaves the other observations of Feature 4 to be as shown in Table 27, below.

Table 27 – reproduction of table Table 25, feature 4, filtering to show only co-expressed instances of feature 4;

Sample	Feature 4	
	Uncoated	Coated
S01	-	-
S03	-	-
S05	-	-
S07	-	-
S09	t96 -	t96 -
S11	t128 -	t128 -

In order to produce this table, a feature of t96- was added to the dataset for the soot coating condition. This was performed since taking a now-informed observation of the data (expecting to see the feature having already observed

one in the uncoated condition); it can be seen that there is a marked decrease at t96h for the coated condition, as expressed more prominently in the uncoated condition, however this expression was very small in the coated condition. If the data had been processed as a record of increase / decrease, or $\Delta\alpha/\alpha_0$ as is popular among studies of TBC ageing; this would have been more visible.

It should be noted that of the expressions of feature 4 in the as-coated (with soot) condition dataset, those that have been filtered out by lacking matching expressions in the soot-coated set, are all positive increases; the uncoated condition expressed more “jumps”, and many in the positive direction. This indicates that the ‘jumps’ are not expressions of conductivity, and may relate more to optical properties of the TBC, that are changing in addition to the density and thermal conductivity and diffusivity properties.

Feature 2: the effect of optical properties?

This disparity between the coated and uncoated inspections, while they can both agree detection of the long-term increase, and the effect of common end-of-life delaminations, the disparity between the two sets heavily implies a strong effect of optical & reflectance properties, influencing the measurement of temperature behind the diffusivity calculation.

The sharp increase in conductivity and diffusivity noted in literature studies occurred in conjunction with an approx. 14% increase in density of the TBC, as seen in Figure 27 [73]. While the increase in thermal properties differs from the observation for the uncoated condition in the data in this thesis, the change in density may yet play a role in influencing other factors around the estimation of

diffusivity that may be responsible for the measured plunge. In the same research, a very significant decrease in the optical penetration depth of the TBC was observed, shown previously in Figure 28. This also make play a part behind the initial jump, as the sudden drop's expression solely in the uncoated condition is clearly not related to thermal properties.

Referring to optical properties, as discussed previously, the infrared reflectance spectra of an EB-PVD has been found to increase over time; shown in Figure 30. This would exhibit a role in the altering of the absorption & re-emission of the initial heating flash, and perhaps the through-thickness initial heating condition – which in the uncoated (without soot) inspection, as is already beyond the modelled ideal scenario; any change in optical properties would be highly influential in the resulting calculation. The same researchers applied a temperature-phase method (Bennet & Yu, 2004) [172] for measuring thermal diffusivity, and noted a striking change in phase-lag between the initial as-deposited condition of their TBC samples (also EB-PVD), and the first cycle. The significance of this “leap” from initial value was not adequately discussed to be of use to the thesis, but since the phase-lag would be related to more than just diffusivity properties, which expressed an initial jump, but not of the same scale; other factors that may be related to the sudden step-drop in feature 1 are thus inferred to be present in literature datasets, while they are not expressed in the same way. This is suggested to be related to other researchers not applying this method without soot condition, unless applying the oscillating heating (PopTea) method [172].

9.1.5 Changes in porosity: phonon scattering relation

Meanwhile, the coalescence of pores would both cause a reduction of number of defects present in the material for phonon scattering in the TBC, while at the same time increasing the defect size. Simultaneously, the smoothening of the rough TBC surface effectively removes a large volume of “point defects”, which. At the longer-term growth of the crystal grains, each of these factors effectively alters the inherent properties of the TBC itself [195], an exploration of which appears to be missing in the literature; and addressing that gap would be out of the scope of the thesis. In addition to microstructural changes, Kakuda et al., attributed their observed initial increase in diffusivity to a decrease in point defects, inferred from the narrowing of their Raman spectral response peaks [73]. This inspection method, coupled with the phonon scattering modelling by Klemens for modelling changes from defects (1993) [195] and grain boundaries (Klemens, 1994) [196] would be worth pursuing in conjunction with investigating the optical properties for performance of the flash method without an emissivity-improving soot coating.

9.2 Reflection on pre-aged coating samples

Of the pre-aged coatings, interestingly, samples S23 and S25 exhibited strong expressions of feature 4; the sudden drop in conductivity / diffusivity that is associated with the development of delaminations;

The sample S21 exhibits a very anomalous measurement upon exit from the first cycle, however it should be noted that the samples – particularly the pre exposed samples – emitted noises upon their first quenching, and the early failure, particularly of S21, was the author’s first direct experience of TBC failure;

it is suggested that this sample would not have been inspected in its condition if it had occurred later in the experiment.

The overall aim of the research was to be able perform an inspection and with the results to “locate” pre-aged TBCs along their point in the life cycle, from whence a prediction of remaining useful life may be possible; however with only a few inspections it is clear that multiple factors are influencing the change in thermal properties. It is however pertinent to remind the reader that from the literature review, this finding is not entirely surprising. The thickness of the aged coatings is only an estimate, therefore it can be expected that the displacement of the measured diffusivity values would not be correct, and the thickness should have been measured prior to exposure. Simultaneously, the location of the used coatings has been arranged back-to-front at the end of the cycle, to highlight any familiar shape the samples may exhibit in common with the as-manufactured TBCs. However, this does not necessarily assume that their oxidation life is at the point where their first inspections are now plotted, as this age is in fact unknown, & without a means to locate them accurately (as was the desire of this research); unknowable without use of other tests, destructive or otherwise.

9.3 Discussion: TBC lifing experiment

In comparing results from section 6 with observed changes that EB-PVD TBCs undergo during similar thermal ageing identified in the literature in section 2, many of the changes predicted from the literature §2.14 were observed in the main experiment; including early stage decline (feature 2), possibly related to micro cracking from rapid growth of the TGO; to the overall increase identified in literature related to ceramic sintering; with intermittent drops in conductivity

related to crack propagation and delamination. However, further testing would be required as part of the experiment to determine the extent to which these mechanisms feature. Even limited to oxidation ageing, these mechanisms occur simultaneously, both reinforcing and counteracting each other, all occurring at different rates, which is sufficiently complex for the case of isothermal tests alone. The inspection in the uncoated soot condition was carried out with some success, replicating many key features between the soot coated and uncoated condition; although additional property changes were also inferred from the preferential nature of some of the changes to feature only in the uncoated inspections.

The core aim was to identify a unique relationship between coating thermal diffusivity and TBC life. Four aging behaviour features were observed, which were covered in in section 7.4, and illustrated in Figure 76: feature 1, an initial sharp decrease in measured diffusivity which was unexpected, and expressed only in the inspections without the soot coating application; feature 2, a further diffusivity decrease, was only mildly expected, and was expressed in both datasets (though this appeared to be an extension of the first feature in the uncoated condition inspections, being also expressed in the coated condition distinguished the feature from the first, reflecting an actual decrease in thermal conductivity. Feature 3 presented an overall increase in diffusivity, was expected from literature due to the sintering of the TBC; and finally occasional sharp decreases in conductivity as cracks grow and propagate, known as feature 4.

Changes to optical penetration depth and increase in optical reflectance were suggested to be consistent with changes in optical scattering resulting from changes in the coating microstructure due to thermal cyclic aging. These changes

appear to be rather abrupt during early cycles, and it is these changes in optical properties that are attributed to the cause for the first two features. As such, this highlights a significant weakness of applying the front surface flash test in the uncoated condition, at least during early coat life, where the two features are most prevalent; especially if using flash thermography, with optical flash lamps, without a soot coating. It is suggested that this weakness is inherent in the application of flash bulbs over laser heating.

While multiple examples of feature 4 – fluctuations in thermal property value during ageing – were encountered, 6 were identified in the uncoated condition dataset, 3 in the coated condition. Of the uncoated dataset, 1 sample exhibited feature 4 as a jump increase, the rest exhibited a marked decrease, as expected from literature findings; 3 of the features present were in the last 2 thermal cycles of coating life, with 2 occurring in the last cycle and the other just previous. In the coated condition, only 3 examples of feature 4 were observed; 2 at the end of life, 1 in a sharp increase, the other in characteristic decrease. While the remaining observation of feature 4 in the coated condition exhibited a sharp increase, it may be possible that this is an expression of feature 3 increase, surrounded by feature 4 decreases on either side. Without an increase in resolution of furnace cycles or method to determine interface cracking, this problem is difficult to resolve further.

Aside from changing the thermal conductivity / diffusivity of the ceramic itself, which is expected to exhibit a steady increase (observed as feature 3), any changes to the optical properties i.e. penetration depth (Figure 28) or reflectance (Figure 30), would have a significant effect on the interaction between the coating and the incident light flash used to heat the sample, and therefore, potentially

interferes with the inspection method itself. Such interference in how the heating flash is initially absorbed could explain some of the unexpected observations, however in order to test these explanations, future testing are recommended to make more frequent capture of coating properties, along with capturing the other characteristics to enable a stronger comparison with literature observations.

Lastly, the relationship for coating material properties with ageing was identified in feature 3, found in both the soot coated and uncoated condition datasets. This progressive increase could enable age estimation, however, it can be argued that more than one feature is being expressed at any one time. Despite that, the exhibition of feature 3 has been found to initiate much later in the uncoated condition than in the coated condition, as the expression of the feature is likely suppressed by changes in optical characteristics of the TBC, affected by how the flash is absorbed through the material, reflected and reduced during the flash event, and the re-emission of absorbed flash may also be exhibiting a mis-match between the surface and TGO interface, which itself changes over ageing, affecting the diffusivity measurement, and not just the actual coating diffusivity itself. This problem raises the issue of weakness in the method, requiring further study if measurement of material thermal properties are to be exploited further for aging characterisation. Many of the limitations encountered will be related to the use of optical flash lamps instead of a laser, which would dramatically improve the modelled Dirac heating, and virtually eliminate the afterglow effect of the flash, also unlocking modulated heating methods and the possibility of estimating porosity. Additionally, other methods such as eddy current inspection would be useful for coating thickness measurement for the data inversion stage.

One further consideration is the discrepancy of diffusivity values between the samples, where the material property is not an objective fixed threshold for a particular coating age, as each of the samples have stochastic offsets from each other, exhibiting a spread of ~ 6-18% of group average values at any particular moment during the life of the batch. While the steady increase in coating values would be useful for ageing characterisation, this discrepancy between samples shifts the application of the method toward a sample-subjective analysis, where it may be considerably more useful to match each measurement of coating property measurement with its own history – however, in the soot coated condition, this issue is considerably less important, as the dataset is more consistent and the patterns are more concise. Nevertheless, it appears to be important to have a record of previous diffusivity measurements for each sample, as the shape of the property change appears to be more individually distinct over life for characterisation purposes.

Two of the samples in the uncoated condition, samples S05 and S11 would not be able to be characterised using feature 3 unless a more detailed study were able to capture change in optical properties and compensate for them, required if the front-face flash method were desired without soot coating.

The pre-aged coats offered promise with respect to demonstrating a potential example of end-of-life feature, in expression of feature four, but little is known about their true condition to make a comparison, as with only a few samples and ensuing end-of-life captures. Meanwhile, an expression of feature 3, the intended method for ageing characterisation, was incompatible with the pre-aged samples without additional inspection methods, or a history of diffusivity measurements.

This brings the discussion to conclude that objective one was met, in identification of the current practice of NDT and an overview of life estimation of TBCs, along with a set of requirements from industry interest in new developments of NDT for TBCs. In response to this, a TBC lifing experiment was developed to capture the degradation of TBCs, which required the development of an approach to the method, to apply it in consideration of limitations. The effects of these limitations are considerable and have been identified from the lifing experiment with some findings and cautions made for future developments; these fulfilled objectives two and three. Lastly, the automation of an application of thermography NDT was developed for a different material requirement – delamination detection, rather than measurement of material property – however, the approach would be adaptable and would offer a more advanced implementation of an inspection method such as diffusivity measurement, giving it a much stronger platform to enter service use in industrial context.

9.4 Limitations of research

A series of limitations were present in this research, including

- The requirement to infer coating thickness from SEM micrographs introduced a $\pm 7-10 \mu\text{m}$ uncertainty in the thickness of the TBC, which in turn would affect estimation of diffusivity measurement
- The use of optical flash lamps is not the ideal implementation of the method, however great effort was undertaken to work around these limitations successfully. A laser would enable heating closer to the ideal Dirac pulse, without the afterglow effects to work around

- While the method works successfully on both soot coated and uncoated inspections; it has been shown by the results that the uncoated inspection is not an ideal scenario and multiple factors are interfering with the signal that would be desirable to be used for ageing characterisation
- Direct measurement of coating thickness, inference of porosity, and application of other techniques, such as mid-IR reflectance imaging, eddy current testing, and laser heating, enabling application of the technique's in-plane thermal diffusivity capability, would dramatically improve the implementation of the technique
- Additional samples would enable sacrificial interruptive tests to be performed, allowing micrographs for direct characterisation of material behaviour that the change in physical properties represent; rather than inference of the behaviour from similar studies in literature
- A higher frequency of tests, particularly at the start and end of the life cycle would dramatically improve evaluation of the change and evolution of material property patterns.
- No models were used to simulate thermal conductivity of a TBC to explain the results; such a model would be considerably useful in this type of study
- The optical properties of TBCs and their evolution with high temperatures may require more study in the literature
- The limitations of applying this method for assessing the life of TBCs over their high temperature oxidation ageing would require further address before direct application to real TBCs in the engine environment can be more seriously engaged.

- The automated data capture and image processing approach described in Chapter 8 is demonstrated on multiple data captures individually, requiring further development to be applied in practice i.e., with merged captures over a larger area.
- The image processing in the automated data capture and analysis are limited through the application of threshold application on one post-flash frame of the thermographic inspection. Additionally, the boundary trace algorithm is limited to continuous-contact boundaries.

10 Conclusions

Reflecting on the objectives of the thesis, the following conclusions can be drawn:

- The industry engagement successfully captured the requirements and current practice from industry, though the scope of this was limited to the requirements of informing the direction of the thesis.
- Responding to both the literature gap and to industry interest, an oxidation ageing experiment of TBCs was undertaken, and this provided a measurable change in thermal diffusivity properties of EB-PVD TBCs over their oxidation life, which were captured by thermographic NDT.
- From the results, four signature features of the TBC evolution of thermal properties has been observed; while three were expected from literature studies; a fourth (feature 1) was unexpected, and is identified either as a challenge for application of the technique, or as a new response to change in the TBC that occurs at the start of TBC life, the origin of which is explored, but could not be fully understood.
- Pertinent to the application of thermographic NDT with the equipment available to the author, the difficult problem of identifying the correct parameters through a methodical process was developed and carried out. Without the correct optimisation of the array of parameters, the main experiment would have been difficult to perform. In the process it was identified that the 'ideal' integration time did not appear to be as theorised. This is suggested to be due to the difference in integration time used from the calibration setting, and an additional calibration would be required. It

was noted by the author that this aspect is rarely discussed in the literature, leaving researchers to some amount of guesswork and interpretation.

- In answer to the perceived barriers by industry for addition of thermographic (or any new NDT) technique to their inspection profile, an automation of thermographic NDT was carried out. This was performed with automated inspection of delaminations on complex geometry parts; however this could be readily be adapted to the measurement of thermal diffusivity in the main thesis experiment, which the two would combine well.

10.1 Further research

Further research could entail a variety of options, including:

- The post-flash afterglow and the translucency of TBCs are particularly problematic with pulsed thermography applied to the ageing of TBCs. Application of alternative heat sources (i.e. laser) could suppress the problem of the afterglow, and enable in-plane diffusivity measurement.
- Integration with other NDT methods such as mid-IR reflectance imaging, in order to yield clues as to the severity of delamination taking place
- Measurement of other features in a further study, such as density, or optical penetration depth (requires the use of a laser), to enable probing of various causal factors of change in measured thermal diffusivity (not to be confused with actual change of diffusivity)
- Integration with modelling approaches for thermal properties based on estimations of porosity etc, to further narrow / eliminate sources of change in thermal properties.

- Increased resolution of inspection / increase thermal cycling, with application of acoustic emissions data capture to capture build-up of cracks up until spallation.
- Increase number of samples, particularly with the purpose of adding sacrificial samples for SEM image analysis to enable a more informed approach for explanation of results.
- The method could be adjusted; while models of interface cracking has seen exciting application with ageing APS TBCs, an equivalent for EB-PVD TBCs would substantially add to the study of ageing of TBCs using pulsed thermography, which has been shown to be rich in generating characteristic features for the assessment of TBC life, which are traceable in inspection with and without the coated condition, though errors due to the non-ideal inspection conditions are evident and significant.
- The automated data capture and feature extraction would benefit from combination of multiple data captures into a single data object. This could be informed by a CAD model, or combination of a model with a 3D surface scan. In this instance, features could be readily selected by a trained operator, or inferred from image processing linked to the component's established baseline and CAD model; while the robotic arm used for the data capture enables rotation between data captures to be incorporated.
- Improvements to the data capture method, an account and compensation of the unexpected feature pattern for the un-coated soot condition, and then further comparison with pre-aged TBCs would be required in order to offer the method for industrial applications.

REFERENCES

- [1] R. Roy, R. Stark, K. Tracht, S. Takata, and M. Mori, "Continuous maintenance and the future – Foundations and technological challenges," *CIRP Ann. - Manuf. Technol.*, vol. 65, no. 2, pp. 667–688, 2016.
- [2] T. S. Baines *et al.*, "State-of-the-art in product-service systems," *Proc. Inst. Mech. Eng. Part B J. Eng. Manuf.*, vol. 221, no. 10, pp. 1543–1552, 2007.
- [3] H. Meier, R. Roy, and G. Seliger, "Industrial Product-Service Systems—IPS2," *CIRP Ann. - Manuf. Technol.*, vol. 59, no. 2, pp. 607–627, 2010.
- [4] "Rolls-Royce celebrates 50th anniversary of Power-by-the-Hour", 30th October 2012." [Online]. Available: <https://www.rolls-royce.com/media/press-releases-archive/yr-2012/121030-the-hour.aspx>. [Accessed: 23-May-2019].
- [5] L. T. Miller and C. S. Park, "Economic analysis in the maintenance, repair, and overhaul industry: An options approach," *Eng. Econ.*, vol. 49, no. 1, pp. 21–41, 2004.
- [6] K. Michaels, "MRO Industry Outlook," MRO Conference, Faire Du MRO Au Canada, 28 April, 2016.
- [7] Y. Allinson, "'Aircraft Repair, Maintenance & Overhaul in the UK', IBISWorld Industry Report C33.160," 2018.
- [8] H. Al-kaabi, A. Potter, and M. Naim, "An outsourcing decision model for airlines' MRO activities," *J. Qual. Maint. Eng.*, vol. 13, no. 3, pp. 217–227, 2007.
- [9] P. Ayeni, B. T.S., L. H, and B. P.D., "State-of-the-art of 'Lean' in the aviation maintenance, repair, and overhaul industry," in *Proceedings of the Institute of Mechanical Engineers, Part B: Journal of Engineering Manufacture*, 2011, pp. 2108–2123.
- [10] L. E. Bakken and R. Skorping, "Optimum Operation and Maintenance of Gas Turbines Offshore," in *ASME 1996 International Gas Turbine and*

Aeroengine Congress and Exhibition, GT 1996; Birmingham; United Kingdom; 10-13 June 1996.

- [11] Dr. Hans-Henrich Altfeld (Airbus), *Commercial Aircraft Projects, Managing the development of highly complex product*. London: Routledge Ltd, 2016.
- [12] M. Dixon, "The Maintenance Costs of Aging Aircraft. Insights from Commercial Aviation," 2006.
- [13] Y. G. Li and P. Nilkitsaranont, "Gas turbine performance prognostic for condition-based maintenance," *Appl. Energy*, vol. 86, no. 10, pp. 2152–2161, 2009.
- [14] H. Bernstein, "Materials issues for users of gas turbines," *Proc. 27th Texas A&M ...*, pp. 1–16, 1998.
- [15] R. Kurz and K. Brun, "Degradation in Gas Turbine Systems," in *International Gas Turbine & Aeroengine Congress & Exhibition Munich, Germany, May 8-11, 2000*.
- [16] A. I. Zwebek and P. Pilidis, "Degradation Effects on Combined Cycle Power Plant Performance—Part I: Gas Turbine Cycle Component Degradation Effects," *J. Eng. Gas Turbines Power*, vol. 125, no. 3, pp. 651–657, 2003.
- [17] A. N. Lakshminarasimha, M. P. Boyce, and C. B. Meher-Homji, "Modeling and Analysis of Gas Turbine Performance Deterioration," *ASME 1992 Int. Gas Turbine Aeroengine Congr. Expo. GT 1992; Col. Ger. 1-4 June 1992; Code 111210*, 1992.
- [18] E. Mohammadi and M. Montazeri-Gh, "A fuzzy-based gas turbine fault detection and identification system for full and part-load performance deterioration," *Aerosp. Sci. Technol.*, vol. 46, pp. 82–93, 2015.
- [19] P. C. Escher, "Pythia: An Object-Oriented Gas Path Analysis Computer Program for General Applications," PhD Thesis, Cranfield University, 1995.
- [20] J. Sun, H. Zuo, W. Wang, and M. G. Pecht, "Application of a state space modeling technique to system prognostics based on a health index for

- condition-based maintenance,” *Mech. Syst. Signal Process.*, vol. 28, pp. 585–596, 2012.
- [21] I. S. Diakunchak, “Performance Deterioration in Industrial Gas Turbines,” *J. Eng. Gas Turbines Power*, vol. 114, no. 2, pp. 161–168, 1992.
- [22] M. R. V. Lakshmi, A. K. Mondal, C. K. Jadhav, B. V. Ravi Dutta, and S. Sreedhar, “Overview of NDT methods applied on an aero engine turbine rotor blade,” *Insight Non-Destructive Test. Cond. Monit.*, vol. 55, no. 9, pp. 482–486, 2013.
- [23] B. Raj, T. Jayakumar, and M. Thavasimuthu, *Practical Non-Destructive Testing*, 3rd editio. Oxford, UK: Alpha Science International LTD., 2007.
- [24] H. Saravanamuttoo, G. Rogers, and H. Cohen, *Gas Turbine Theory*, 5th editio. Pearson Prentice Hall, 2001.
- [25] M. P. Boyce, *Gas Turbine Engineering Handbook*, Second Edi. Gulf Publishing Company, Houston, TX, USA, 2002.
- [26] X. T. Centrich, E. Shehab, P. Sydor, T. Mackley, P. John, and A. Harrison, “An aerospace requirements setting model to improve system design,” *Procedia CIRP*, vol. 22, no. 1, pp. 287–292, 2014.
- [27] “Theory and basic mechanics,” in *The Jet Engine*, London, UK: Rolls-Royce plc, 65 Bunckingham Gate, London, SW1E 6AT, 2005, pp. 12–17, ISBN:0 902121 2 35.
- [28] W. N. Harrison, D. G. Moore, and J. C. Richmond, “Review of an Investigation of Ceramic Coatings for Aeronautics’, National Advisory Committee for Aeronautics, NACA TN-1186,” 1947.
- [29] F. S. Stepka and R. O. Hickel, “Experimental Investigation of Air-cooled Turbine Blades in Turbojet Engine IX: Evaluation of the Durability of Noncritical Rotor Blades in Engine Operation,” 1951.
- [30] F. B. Garrett and C. A. Gyorgak, “Adhesive and Protective Characteristics of Ceramic Coating A-417 and Its Effect on Engine Life of Forged

- Refractaloy-26 (AMS 5760) and Cast Stellite 21 (AMS 585) Turbine Blades,” 1953.
- [31] B. R. Bornhorst and L. V. Hjelm, “Development of improved ceramic coatings to increase the life of XLR99 thrust chamber,” 1961.
- [32] “Photo: X-15 #2 just after launch, NASA Photo: EC88-0180-1 (cropped), NASA Dryden Flight Research Center Photo Collection.” [Online]. Available: <https://www.dfrc.nasa.gov/Gallery/Photo/X-15/HTML/EC88-0180-1.html>. [Accessed: 10-Jun-2019].
- [33] Cliff1066 <https://www.flickr.com/people/nostri-imago/>, “Photo: ‘North American X-15 Nozzle.jpg’, This work is licensed under a Creative Commons Attribution 2.0 Generic License, (CC BY 4.0), used without modification.” [Online]. Available: <https://www.flickr.com/photos/nostri-imago/3333560982/in/photostream/>.
- [34] R. J. Quentmeyer, “‘Thrust Chamber Thermal Barrier Coating Techniques’, NASA Technical Memorandum 100933,” 1988.
- [35] D. R. Clarke, M. Oechsner, and N. P. Padture, “Thermal-barrier coatings for more efficient gas-turbine engines,” *MRS Bull.*, vol. 37, no. 10, pp. 891–898, 2012.
- [36] P. Morrell and D. Rickerby, “Advantages/disadvantages of various TBC systems as perceived by the engine manufacturer,” in *AGARD-R-823-18, chapter 20*, 1998, pp. 1–9.
- [37] U. Schulz *et al.*, “Some recent trends in research and technology of advanced thermal barrier coatings,” *Aerosp. Sci. Technol.*, vol. 7, pp. 73–80, 2003.
- [38] U. Shulz, B. Saruhan, K. Fritscher, and C. Leyens, “Review on advanced EB-PVD Ceramic topcoats for TBC applications,” *Appl. Ceram. Technol.*, vol. 1, no. 4, pp. 302–315, 2004.
- [39] J. A. Nesbitt, “Thermal modeling of various thermal barrier coatings in a

- high heat flux rocket engine,” *Surf. Coatings Technol.*, vol. 130, pp. 141–151, 2000.
- [40] U. Schulz, M. Menzebach, C. Leyens, and Y. Q. Yang, “Influence of substrate material on oxidation behavior and cyclic lifetime of EB-PVD TBC systems,” *Surf. Coatings Technol.*, vol. 146–147, pp. 117–123, 2001.
- [41] U. Schulz, “Phase transformation in EB-PVD yttria partially stabilized zirconia thermal barrier coatings during annealing,” *J. Am. Ceram. Soc.*, vol. 83, no. 4, pp. 904–910, 2000.
- [42] G. Chen, “Non-destructive evaluation (NDE) of the failure of thermal barrier coatings,” in *Thermal Barrier Coatings*, H. Xu and H. Guo, Eds. Woodhead Publishing Ltd, 2011, pp. 243–262.
- [43] N. P. Padture, M. Gell, and E. H. Jordan, “Thermal Barrier Coatings for Gas-Turbine Engine Applications,” *Science (80-.)*, vol. 296, no. 5566, pp. 280–284, 2002.
- [44] W. J. Parker, R. J. Jenkins, C. P. Butler, and G. L. Abbott, “Flash method of determining thermal diffusivity, heat capacity, and thermal conductivity,” *J. Appl. Phys.*, vol. 32, pp. 1679–1684, 1961.
- [45] T. A. Cruse, S. Stewart, and M. Ortiz, “Thermal barrier coating life prediction model development,” *J. Eng. Gas Turbines Power*, vol. 110, no. 4, pp. 610–616, 1988.
- [46] R. A. Miller, “Life Modeling of Thermal Barrier Coatings for Aircraft Gas Turbine Engines,” *J. Eng. Gas Turbines Power*, vol. 111, pp. 301–305, 1989.
- [47] S. M. Shepard, D. Wang, J. R. Lhota, B. A. Rubadeux, and T. Ahmed, “Reconstruction and Enhancement of Thermographic Sequence Data,” vol. 4704, pp. 74–77, 2002.
- [48] “Non destructive testing in the aerospace industry,” *The Engineer*, 2011. [Online]. Available: <https://www.theengineer.co.uk/non-destructive-testing->

- in-the-aerospace-industry/. [Accessed: 10-Oct-2018].
- [49] S. Chaudhuri, "At IKEA, Ensuring 'Quality as an Enabler of Lower Cost,'" *Wall Street Journal*, 2015. [Online]. Available: <https://blogs.wsj.com/corporate-intelligence/2015/06/17/at-ikea-ensuring-quality-as-an-enabler-of-lower-cost/>. [Accessed: 10-Jun-2019].
- [50] T. Pratchett and N. Gaiman, *Good Omens*. Harper Collins, Victor Gollancz Ltd, 1990.
- [51] "Introduction to Nondestructive Testing, the Collaboration for NDT Education," *NDT Education Resource Center, Iowa State University, USA*. [Online]. Available: https://www.nde-ed.org/GeneralResources/IntroToNDT/Intro_to_NDT.ppt. [Accessed: 10-Feb-2018].
- [52] P. J. Shull, "Eddy Current," in *Nondestructive Evaluation Theory, Techniques and Applications*, Marcel Dekker, 2002, pp. 261–368.
- [53] "BS ISO 10878:2013 - Non-destructive testing. Infrared thermography. Vocabulary." British Standards Institute, 2013.
- [54] S. M. Richard, "Infrared Transmission of the Atmosphere, NRL Report 5453," 1960.
- [55] M. L. Kutner, "Planck's law and photons," in *Astronomy: A Physical Perspective*, 2nd ed., Cambridge, UK: Cambridge University Press, 2003, pp. 15–16.
- [56] "Matlab." The MathWorks, Inc. 3 Apple Hill Drive, Natick, Massachusetts.
- [57] S. Shepard, "'Temporal Noise Reduction and Analysis of Thermographic Image Data Sequences', US Patent USOO6516084B2, Feb 4 2003," US6516084B2.
- [58] S. M. Shepard, "Reconstruction and enhancement of active thermographic image sequences," *Opt. Eng.*, vol. 42, no. 5, p. 1337, 2003.
- [59] S. M. Shepard, J. R. Lhota, Y. L. Hou, and T. Ahmed, "Blind

- characterization of materials using single-sided thermography,” *Thermosense XXVI, Proc SPIE*, vol. 5405, pp. 442–446, 2004.
- [60] S. M. Shepard, Y. Hou, T. Ahmed, and J. R. Lhota, “Reference-free interpretation of flash thermography data,” *Insight Non-Destructive Test. Cond. Monit.*, vol. 48, no. 5, pp. 298–301, 2006.
- [61] S. M. Shepard and J. R. Lhota, “Flash duration and timing effects in thermographic NDT,” vol. 5782, pp. 352–358, 2005.
- [62] S. Bagavathiappan, B. B. Lahiri, T. Saravanan, J. Philip, and T. Jayakumar, “Infrared thermography for condition monitoring – A review,” *Infrared Phys. Technol.*, vol. 60, pp. 35–55, 2013.
- [63] S. Taib and M. Jadin, “Thermal Imaging for Enhancing Inspection Reliability: Detection and Characterization,” *InTech, Rijeka, Croat.*, 2012.
- [64] G. Holst, *Common sense approach to thermal imaging*. JCD Publishing, Winter Park, Florida USA; SPIE Optical Engineering Press, Bellingham, Washington USA, 2000.
- [65] P. Dostie, “NDT method selection chart.” [Online]. Available: http://pages.videotron.com/quality/index_pierredostie_download.html.
- [66] L. Li and D. R. Clarke, “Effect of CMAS infiltration on radiative transport Through an EB-PVD thermal barrier coating,” *Int. J. Appl. Ceram. Technol.*, vol. 5, no. 3, pp. 278–288, 2008.
- [67] A. M. Limarga and D. R. Clarke, “The grain size and temperature dependence of the thermal conductivity of polycrystalline, tetragonal yttria-stabilized zirconia,” *Appl. Phys. Lett.*, vol. 98, 2011.
- [68] V. Lughi, V. K. Tolpygo, and D. R. Clarke, “Microstructural aspects of the sintering of thermal barrier coatings,” *Mater. Sci. Eng. A*, vol. 368, no. 1–2, pp. 212–221, 2004.
- [69] L. Zhou, S. Mukherjee, K. Huang, Y. W. Park, and Y. Sohn, “Failure characteristics and mechanisms of EB-PVD TBCs with Pt-modified NiAl

- bond coats," *Mater. Sci. Eng. A*, vol. 637, pp. 98–106, 2015.
- [70] D. Zhu, R. A. Miller, B. A. Nagaraj, and R. W. Bruce, "Thermal conductivity of EB-PVD thermal barrier coatings evaluated by a steady-state laser heat flux technique," *Surf. Coatings Technol.*, vol. 138, no. 1, pp. 1–8, 2001.
- [71] D. Zhu and R. a. Miller, "Thermal Conductivity and Elastic Modulus Evolution of Thermal Barrier Coatings under High Heat Flux Conditions," *J. Therm. Spray Technol.*, vol. 9, no. 2, pp. 175–180, 2000.
- [72] R. B. Dinwiddie, S. C. Beecher, W. D. Porter, and B. A. Nagaraj, "The Effect Of Thermal Aging On The Thermal Conductivity Of Plasma Sprayed And EB-PVD Thermal Barrier Coatings," in *International Gas Turbine and Aeroengine Congress & Exhibition, Birmingham, UK - June 10-13 1996 - 96-GT-282*.
- [73] T. R. Kakuda, A. M. Limarga, T. D. Bennett, and D. R. Clarke, "Evolution of thermal properties of EB-PVD 7YSZ thermal barrier coatings with thermal cycling," *Acta Mater.*, vol. 57, no. 8, pp. 2583–2591, 2009.
- [74] H. J. Rätzer-Scheibe and U. Schulz, "The effects of heat treatment and gas atmosphere on the thermal conductivity of APS and EB-PVD PYSZ thermal barrier coatings," *Surf. Coatings Technol.*, vol. 201, no. 18, pp. 7880–7888, 2007.
- [75] A. M. Limarga and D. R. Clarke, "Characterization of electron beam physical vapor-deposited thermal barrier coatings using diffuse optical reflectance," *Int. J. Appl. Ceram. Technol.*, vol. 6, no. 3, pp. 400–409, 2009.
- [76] A. F. Renteria and B. Saruhan, "Effect of ageing on microstructure changes in EB-PVD manufactured standard PYSZ top coat of thermal barrier coatings," *J. Eur. Ceram. Soc.*, vol. 26, no. 12, pp. 2249–2255, 2006.
- [77] D. Zhu, A. Miller, B. A. Nagaraj, and W. Bruce, "Thermal conductivity of EB-PVD thermal barrier coatings evaluated by a steady-state laser heat flux technique, NASA TM-2000-210238," 2000.

- [78] R. A. Miller, "Oxidation-Based Thermal Barrier Coating Life Prediction Model," *J. Am. Ceram. Soc.*, vol. 67, no. 8, pp. 517–521, 1984.
- [79] R. A. Miller, "Current Status Of Thermal Barrier Coatings — An Overview," *Surf. Coatings Technol.*, vol. 30, pp. 1–11, 1987.
- [80] D. E. Sokolowski and M. H. Hirschberg, "Aircraft Engine Hot Section Technology - An Overview of the HOST Project, available from Internet Archive:
https://archive.org/details/nasa_techdoc_19920013292/page/n15," 1990.
- [81] J. T. DeMasi, K. D. Sheffler, and M. Ortiz, "Thermal Barrier Coating Life Prediction Model Development, Phase I - Final Report, NASA Contractor Report 182230," 1989.
- [82] R. Miller and C. Lowell, "Thermal Barrier Coating Life Prediction Model Development, NASA Contractor Report 189111," 1991.
- [83] T. E. Strangman, J. F. Neumann, and A. Liu, "Thermal barrier coating life prediction model development," *Turbine Engine Hot Sect. Technol. NASA Conf. Publ. 2444*, pp. 435–446, 1986.
- [84] T. E. Strangman, J. Neumann, and A. Liu, "Thermal Barrier Coating Life Prediction Model Development, Final Report, NASA CR-179648," 1987.
- [85] R. V Hillery, B. . Pilsner, and R. . McKnight, "'Thermal Barrier Coating Model Life Prediction Development Final Report', NASA Contractor Report 180807," 1988.
- [86] W. Weibull, "A Statistical Distribution Function of Wide Applicability," *J. Appl. Mech.*, vol. 103, no. 3, pp. 293–297, 1951.
- [87] T. Strangman, D. Raybould, A. Jameel, and W. Baker, "Damage mechanisms, life prediction, and development of EB-PVD thermal barrier coatings for turbine airfoils," *Surf. Coatings Technol.*, vol. 202, no. 4–7, pp. 658–664, 2007.
- [88] L. Chirivi and J. R. Nicholls, "Influence of surface finish on the cyclic

- oxidation lifetime of an eb-pvd tbc, deposited on PtAl and Pt-diffused bondcoats," *Oxid. Met.*, vol. 81, no. 1–2, pp. 17–31, 2014.
- [89] K. Chan, S. Cheruvu, and R. Viswanathan, "Development of a Thermal Barrier Coating Life Model," in *ASME Turbo Expo 2003, collocated with the 2003 International Joint Power Generation Conference, GT2003-38171, 16-19th June, Atlanta, Georgia, 2003*.
- [90] K. S. Chan and N. S. Cheruvu, "Field Validation of a TBC Life-Prediction Model For Land-based Gas Turbines," in *Proceedings of ASME Turbo Expo 2010: Power for Land, Sea and Air, 2010*.
- [91] T. Beck, O. Trunova, R. Herzog, and L. Singheiser, "TBCs for Gas Turbines under Thermomechanical Loadings: Failure Behaviour and Life Prediction," in *EPJ Web of Conferences, 2012*, vol. 33.
- [92] E. P. Busso *et al.*, "A physics-based life prediction methodology for thermal barrier coating systems," *Acta Mater.*, vol. 55, pp. 1491–1503, 2007.
- [93] B. A. Pint, I. G. Wright, W. Y. Lee, Y. Zhang, K. Prüssner, and K. B. Alexander, "Substrate and bond coat compositions: factors affecting alumina scale adhesion," *Mater. Sci. Eng. A*, vol. 245, no. 2, pp. 201–211, 1998.
- [94] J. Schlobohm *et al.*, "Advanced Characterization Techniques for Turbine Blade Wear and Damage," *Procedia CIRP*, vol. 59, pp. 83–88, 2017.
- [95] W. G. Mao, D. J. Wu, W. B. Yao, M. Zhou, and C. Lu, "Multiscale monitoring of interface failure of brittle coating/ductile substrate systems: A non-destructive evaluation method combined digital image correlation with acoustic emission," *J. Appl. Phys.*, vol. 110, 2011.
- [96] K. Takagi, A. Kawasaki, Y. Itoh, Y. Harada, and F. Ono, "Testing Method for Heat Resistance Under Temperature Gradient," *J. Therm. Spray Technol.*, vol. 16, no. December, pp. 974–977, 2007.
- [97] C. C. Pilgrim, S. Berthier, J. P. Feist, R. G. Wellman, and A. L. Heyes,

- “Photoluminescence for quantitative non-destructive evaluation of thermal barrier coating erosion,” *Surf. Coat. Technol.*, vol. 209, pp. 44–51, 2012.
- [98] C. C. Pilgrim, S. Berthier, J. P. Feist, and A. L. Heyes, “High resolution erosion detection in thermal barrier coatings using photoluminescent layers,” *Surf. Coatings Technol.*, vol. 232, pp. 116–122, 2013.
- [99] J. I. Eldridge, S. W. Allison, T. P. Jenkins, S. L. Gollub, C. A. Hall, and D. G. Walker, “Surface temperature measurements from a stator vane doublet in a turbine afterburner flame using a YAG : Tm thermographic phosphor,” *Meas. Sci. Technol.*, p. 125205, 2016.
- [100] W. H. Prosser, “Acoustic Emission,” in *Nondestructive Evaluation Theory, Techniques and Applications*, P. J. Shull, Ed. Marcel Dekker, 2002, p. 369.
- [101] J. H. Park, J. S. Kim, and K. H. Lee, “Acoustic emission characteristics for diagnosis of TBC damaged by high-temperature thermal fatigue,” *J. Mater. Process. Technol.*, vol. 187–188, pp. 537–541, 2007.
- [102] M. Firdaus, R. Sloan, C. I. Duff, M. Wielgat, and J. F. Knowles, “Microwave Nondestructive Evaluation of Thermal Barrier Coated Turbine Blades using Microwave Techniques,” *Mater. Eval.*, vol. 74, no. 4, pp. 543–551, 2016.
- [103] M. F. Akbar, G. N. Jawad, C. I. Duff, and R. Sloan, “Porosity evaluation of in-service thermal barrier coated turbine blades using a microwave nondestructive technique,” *NDT E Int.*, vol. 93, no. May 2017, pp. 64–77, 2018.
- [104] M. F. Doerner and W. D. Nix, “A method for interpreting the data from depth-sensing indentation instruments,” *J. Mater. Res.*, vol. 1, no. 4, pp. 601–609, 1986.
- [105] I. N. Sneddon, “The relation between load and penetration in the axisymmetric boussinesq problem for a punch of arbitrary profile,” *Int. J. Eng. Sci.*, vol. 3, no. 1, pp. 47–57, 1965.
- [106] J. M. Tannenbaum, K. Lee, B. S. Kang, and M. A. Alvin, “Non-destructive

- spallation prediction of thermal barrier coatings by a load-based micro-indentation technique,” in *Proceedings of the ASME 2010 International Mechanical Engineering Congress & Exposition, IMECE2010-37696*, 2010.
- [107] B. S. Kang, M. A. Alvin, C. Feng, and J. M. Tannenbaum, “A Load-Based Depth-Sensing Indentation Technique for Damage Assessment of Thermal Barrier Coatings,” in *Proceedings of ASME Turbo Expo 2009: Power for Land, Sea and Air GT2009-59985*, 2009.
- [108] H. R. Chen, B. Zhang, M. A. Alvin, and Y. Lin, “Ultrasonic Detection of Delamination and Material Characterization of Thermal Barrier Coatings,” *J. Therm. Spray Technol.*, vol. 21, no. 6, pp. 1184–1194, 2012.
- [109] H. P. Crutzen, F. Lakestani, and J. R. Nicholls, “Ultrasonic characterisation of thermal barrier coatings,” *Proc. IEEE Ultrason. Symp.*, vol. 1, pp. 731–736, 1996.
- [110] Y. Zhao, J. Chen, and Z. Zhang, “Nondestructive characterization of thermal barrier coating by noncontact laser ultrasonic technique,” *Opt. Eng.*, vol. 54, no. 9, p. Article 094104, 2015.
- [111] Z. Ma, Y. Zhao, Z. Luo, and L. Lin, “Ultrasonic characterization of thermally grown oxide in thermal barrier coating by reflection coefficient amplitude spectrum,” *Ultrasonics*, vol. 54, no. 4, pp. 1005–1009, 2014.
- [112] W. Reimche, O. Bruchwald, W. Frackowiak, F.-W. Back, and H. J. Maier, “Non-destructive determination of local damage and material condition in high-performance components,” *HTM - J. Heat Treat. Mater.*, vol. 68, no. 2, pp. 59–67, 2013.
- [113] O. Bruchwald, M. Nicolaus, W. Frackowiak, W. Reimche, K. Möhwald, and H. J. Maier, “Material Characterization of Thin Coatings Using High Frequency Eddy Current Technology,” in *19th World Conference on Non-Destructive Testing 2016*, 2016, no. June.
- [114] Oliver Bruchwald, Wojciech Frackowiak, Wilfried Reimche, and H. J. Maier,

- “Applications of High Frequency Eddy Current Technology for Material Characterization of Thin Coatings,” *J. Mater. Sci. Eng. A*, vol. 6, no. (7-8), pp. 185–191, 2016.
- [115] L. Yong, Z. Chen, Y. Mao, and Q. Yong, “Quantitative evaluation of thermal barrier coating based on eddy current technique,” *NDT E Int.*, vol. 50, pp. 29–35, 2012.
- [116] J. Min, K. J. Park, H. Girl, L. H. Kim, and C. S. Y. Lee, “An Effective Electrical Resonance-Based Method to Detect Delamination in Thermal Barrier Coating,” *J. Therm. Spray Technol.*, pp. 1–8, 2017.
- [117] Y. Li, B. Yan, W. Li, and D. Li, “Thickness Assessment of Thermal Barrier Coatings of Aeroengine Blades Via Dual-Frequency Eddy Current Evaluation,” *IEEE Magn. Lett.*, vol. 7, 2016.
- [118] G. Madzsar, R. Bickford, and D. Duncan, “An overview of in-flight plume diagnostics for rocket engines,” in *NASA TM-105727*, 1992.
- [119] G. Chen, K. N. Lee, and S. N. Tewari, “The concept and development of emission spectroscopy for the non-destructive evaluation (NDE) of the failure of thermal barrier coatings,” *NDT E Int.*, vol. 40, no. 4, pp. 265–270, 2007.
- [120] N. Wang, C. Li, L. Yang, Y. Zhou, W. Zhu, and C. Cai, “Experimental testing and FEM calculation of impedance spectra of thermal barrier coatings: Effect of measuring conditions,” *Corros. Sciencie*, vol. 107, pp. 155–171, 2016.
- [121] B. Jayaraj, V. H. Desai, C. K. Lee, and Y. H. Sohn, “Electrochemical impedance spectroscopy of porous ZrO₂-8 wt.% Y₂O₃ and thermally grown oxide on nickel aluminide,” *Mater. Sci. Eng. A*, vol. 372, no. 1–2, pp. 278–286, 2004.
- [122] B. Jayaraj, S. Vishweswaraiah, V. H. Desai, and Y. H. Sohn, “Electrochemical impedance spectroscopy of thermal barrier coatings as a function of isothermal and cyclic thermal exposure,” *Surf. Coatings*

- Technol.*, vol. 177–178, pp. 140–151, 2004.
- [123] N. Q. Wu, K. Ogawa, M. Chyu, and S. X. Mao, “Failure detection of thermal barrier coatings using impedance spectroscopy,” *Thin Solid Films*, vol. 457, no. 2, pp. 301–306, 2004.
- [124] P. S. Anderson, X. Wang, and P. Xiao, “Impedance spectroscopy study of plasma sprayed and EB-PVD thermal barrier coatings,” *Surf. Coatings Technol.*, vol. 185, no. 1, pp. 106–119, 2004.
- [125] J. W. Byeon, B. Jayaraj, S. Vishweswaraiyah, S. Rhee, V. H. Desai, and Y. H. Sohn, “Non-destructive evaluation of degradation in multi-layered thermal barrier coatings by electrochemical impedance spectroscopy,” *Mater. Sci. Eng. A*, vol. 407, no. 1–2, pp. 213–225, 2005.
- [126] F. Cernuschi, L. Lorenzoni, S. Ahmaniemi, P. Vuoristo, and T. Mäntylä, “Studies of the sintering kinetics of thick thermal barrier coatings by thermal diffusivity measurements,” *J. Eur. Ceram. Soc.*, vol. 25, no. 4, pp. 393–400, 2005.
- [127] R. J. Christensen, D. M. Lipkin, D. R. Clarke, and K. Murphy, “Nondestructive evaluation of the oxidation stresses through thermal barrier coatings using Cr³⁺ piezospectroscopy,” *Appl. Phys. Lett.*, vol. 69, no. 24, pp. 3754–3756, 1996.
- [128] D. R. Clarke, R. J. Christensen, and V. Tolpygo, “The evolution of oxidation stresses in zirconia thermal barrier coated superalloy leading to spalling failure,” *Surf. Coat. Technol.*, vol. 94–95, pp. 89–93, 1997.
- [129] S. R. J. Saunders, J. P. Banks, G. Chen, and C. J. Chunnillall, “Measurement of residual stress in thermally grown oxide layers in thermal barrier coating systems - Development of non-destructive test methods,” *Mater. Sci. Forum*, vol. 461–464, pp. 383–390, 2004.
- [130] A. M. G. Luz, D. Balint, and K. Nikbin, “A Multiscale NDT System For Damage Detection In Thermal Barrier Coatings,” in *Proceedings of the ASME 2009 International Mechanical Engineering Congress & Exposition*,

IMECE2009-10694, 2009.

- [131] A. L. Heyes, J. P. Feist, X. Chen, Z. Mutasim, and J. R. Nicholls, "Optical Nondestructive Condition Monitoring of Thermal Barrier Coatings," *J. Eng. Gas Turbines Power*, vol. 130, no. November 2008, pp. 1–8, 2008.
- [132] J. P. Feist and A. L. Heyes, "Photo-Stimulated Phosphorescence for Thermal Condition Monitoring and Nondestructive Evaluation in Thermal Barrier Coatings," *Heat Transf. Eng.*, vol. 30, no. 13, pp. 1087–1095, 2011.
- [133] M. P. Hawron, "Non-Destructive Evaluation and Maintenance of Thermal Barrier Coatings," MSc Thesis, University of Connecticut, 2014.
- [134] J. A. Nychka and D. R. Clarke, "Damage quantification in TBCs by photo-stimulated luminescence spectroscopy," vol. 147, pp. 110–116, 2001.
- [135] M. Gell, S. Sridharan, M. Wen, and E. H. Jordan, "Photoluminescence Piezospectroscopy: A Multi-Purpose Quality Control and NDI Technique for Thermal Barrier Coatings," *Ceram. Prod. Dev.*, vol. 1, no. 4, pp. 316–329, 2004.
- [136] W. J. Parker, R. J. Jenkins, C. P. Butler, and G. L. Abbott, "Flash method of determining thermal diffusivity, heat capacity, and thermal conductivity," *J. Appl. Phys.*, vol. 32, pp. 1679–1684, 1961.
- [137] B. Weekes, D. P. Almond, P. Cawley, and T. Barden, "Eddy-current induced thermography - Probability of detection study of small fatigue cracks in steel, titanium and nickel-based superalloy," *NDT E Int.*, vol. 49, pp. 47–56, 2012.
- [138] W. Frackowiak, O. Bruchwald, S. Zwoch, W. Reimche, and H. J. Maier, "Non-Destructive Damage Detection and Material Characterization of Turbine Components Using Megahertz Range Induction Thermography in Pulsed Mode," in *19th World Conference on Non-Destructive Testing June 2016*.
- [139] J. I. Eldridge, C. M. Spuckler, and J. R. Markham, "Determination of

- scattering and absorption coefficients for plasma-sprayed yttria-stabilized zirconia thermal barrier coatings at elevated temperatures," *J. Am. Ceram. Soc.*, vol. 92, no. 10, pp. 2276–2285, 2009.
- [140] J. I. Eldridge, C. M. Spuckler, and R. E. Martin, "Monitoring delamination progression in thermal barrier coatings by mid-infrared reflectance imaging," *Int. J. Appl. Ceram. Technol.*, vol. 3, no. 2, pp. 94–104, 2006.
- [141] X. Maldague, F. Galmiche, and a. Ziadi, "Advances in pulsed phase thermography," *Infrared Phys. Technol.*, vol. 43, pp. 175–181, 2002.
- [142] F. Cernuschi, a. Figari, and L. Fabbri, "Thermal wave interferometry for measuring the thermal diffusivity of thin slabs," *J. Mater. Sci.*, vol. 35, no. 23, pp. 5891–5897, 2000.
- [143] X. Maldague, "Theory and Practice of Infrared Technology for Nondestructive Testing," in *Theory and Practice of Infrared Technology for Nondestructive Testing*, Wiley-Blackwell, 2001, pp. 214–224.
- [144] S. Zhao, H. Wang, N. Wu, and C. Zhang, "Nondestructive testing of the fatigue properties of air plasma sprayed thermal barrier coatings by pulsed thermography," *Russ. J. Nondestruct. Test.*, vol. 51, no. 7, pp. 445–456, 2015.
- [145] C. Bu, Q. Tang, Y. Liu, F. Yu, C. Mei, and Y. Zhao, "Quantitative detection of thermal barrier coating thickness based on simulated annealing algorithm using pulsed infrared thermography technology," *Appl. Therm. Eng.*, vol. 99, pp. 751–755, 2016.
- [146] J. Manara, M. Arduini-Schuster, H. J. Rätzer-Scheibe, and U. Schulz, "Infrared-optical properties and heat transfer coefficients of semitransparent thermal barrier coatings," *Surf. Coatings Technol.*, vol. 203, no. 8, pp. 1059–1068, 2009.
- [147] I. Philippi, J. C. Batsale, D. Maillet, and A. Degiovanni, "Measurement of thermal diffusivities through processing of infrared images," *Rev. Sci. Instruments/Instruments*, vol. 66, no. 1, 1995.

- [148] P. G. Bison, F. Cernuschi, E. Grinzato, S. Marinetti, and D. Robba, "Ageing evaluation of thermal barrier coatings by thermal diffusivity," *Infrared Phys. Technol.*, vol. 49, no. 3, pp. 286–291, 2007.
- [149] F. Cernuschi, P. G. Bison, A. Figari, S. Marinetti, and E. Grinzato, "Thermal diffusivity measurements by photothermal and thermographic techniques," *Int. J. Thermophys.*, vol. 25, no. 2, pp. 439–457, 2004.
- [150] P. G. Bison, E. Grinzato, and S. Marinetti, "Local thermal diffusivity measurement," in *Quantitative InfraRed Thermography Journal 1:2*, 2004, pp. 241–250.
- [151] P. Bison, F. Cernuschi, and E. Grinzato, "In-depth and in-plane thermal diffusivity measurements of thermal barrier coatings by IR camera: Evaluation of ageing," *Int. J. Thermophys.*, vol. 29, no. 6, pp. 2149–2161, 2008.
- [152] F. Cernuschi, P. Bison, S. Marinetti, D. Robba, E. Grinzato, and L. Lorenzoni, "Photothermal and thermographic techniques for NDT control and thermophysical characterisation of TBC," in *European Turbine Forum*, 2006, no. January 2016.
- [153] F. Cernuschi, P. Bison, S. Marinetti, and E. Campagnoli, "Thermal diffusivity measurement by thermographic technique for the non-destructive integrity assessment of TBCs coupons," *Surf. Coatings Technol.*, vol. 205, no. 2, pp. 498–505, 2010.
- [154] F. Cernuschi *et al.*, "Non-destructive thermographic monitoring of crack evolution of thermal barrier coating coupons during cyclic oxidation aging," *Acta Mater.*, vol. 59, no. 16, pp. 6351–6361, 2011.
- [155] I. O. Golosnoy, S. A. Tsipas, and T. W. Clyne, "An analytical model for simulation of heat flow in plasma-sprayed thermal barrier coatings," *J. Therm. Spray Technol.*, vol. 14, no. 2, pp. 205–214, 2005.
- [156] F. Cernuschi, "Can TBC porosity be estimated by non-destructive infrared techniques? A theoretical and experimental analysis," *Surf. Coatings*

- Technol.*, vol. 272, pp. 387–394, 2015.
- [157] J. G. Sun, “Measurement of thermal barrier coating conductivity by thermal imaging method,” in *Ceramic Engineering and Science Proceedings*, 2010, vol. 30, no. 3, pp. 97–103.
- [158] “Sun, J. G., 2010, ‘Method for Analyzing Multi-Layer Materials From One-Sided Thermal Imaging,’ U.S. Patent No. 7,769,201.”
- [159] J. G. Sun, “Pulsed Thermal Imaging Measurement of Thermal Properties for Thermal Barrier Coatings Based on a Multilayer Heat Transfer Model,” *J. Heat Transfer*, vol. 136, no. 8, pp. 08160: 1–5, 2014.
- [160] J. G. Sun and N. Tao, “Thermal Property Measurement for Thermal Barrier Coatings Using Pulsed Thermal Imaging – Multilayer Analysis Method,” *AIP Conf. Proc. 1706, 100004*, 2016.
- [161] D. Zimdars, J. White, G. Fichter, A. Chernovsky, and S. L. Williamson, “Quantitative measurement of laminar material properties and structure using time domain reflection imaging,” *Proc. SPIE, Terahertz Mil. Secur. Appl. VI, SPIE Def. Secur. Symp. 2008, Orlando, Florida, United States, 15th April 2008*, vol. 6949.
- [162] C. C. Berndt, “Failure processes within ceramic coatings at high temperatures,” *J. Mater. Sci.*, vol. 24, no. 10, pp. 3511–3520, 1989.
- [163] C. K. Lin and C. C. Berndt, “Acoustic emission studies on thermal spray materials,” *Surf. Coatings Technol.*, vol. 102, no. 1–2, pp. 1–7, 1998.
- [164] J. M. Tannenbaum, B. S.-J. Kang, and M. A. Alvin, “Non-Destructive TBC Spallation Detection By A Micro-Indentation Method,” in *Proceedings of ASME Turbo Expo 2010: Power for Land, Sea and Air, GT2010 June 14-18th, 2010, Glasgow, UK*, 2010, pp. 1–10.
- [165] F. Yu and T. D. Bennett, “Phase of thermal emission spectroscopy for properties measurements of delaminating thermal barrier coatings,” *J. Appl. Phys.*, vol. 98, no. 10, pp. 103501:1–8, 2005.

- [166] N. Czech, H. Fietzek, M. Juez-Lorenzo, V. Kolarik, and W. Stamm, "Studies of the bond-coat oxidation and phase structure of TBCs," *Surf. Coatings Technol.*, vol. 113, no. 1–2, pp. 157–164, 1999.
- [167] V. K. Tolpygo, D. R. Clarke, and K. S. Murphy, "Oxidation-induced failure of EB-PVD thermal barrier coatings," *Surf. Coatings Technol.*, vol. 146–147, pp. 124–131, 2001.
- [168] D. M. Lipkin and D. R. Clarke, "Measurement of the stress in oxide scales formed by oxidation of alumina-forming alloys," *Oxid. Met.*, vol. 45, no. 3–4, pp. 267–280, 1996.
- [169] M. Sayar, D. Seo, and K. Ogawa, "Non-destructive microwave detection of layer thickness in degraded thermal barrier coatings using K- and W-band frequency range," *NDT E Int.*, vol. 42, no. 5, pp. 398–403, 2009.
- [170] J. I. Eldridge, C. M. Spuckler, J. A. Nesbitt, and K. W. Street, "Health Monitoring of Thermal Barrier Coatings by Mid-Infrared Reflectance," in *27th Annual Cocoa Beach Conference on Advanced Ceramics and Composites: A: Ceramic Engineering and Science Proceedings, Volume 24*, 2003.
- [171] J. I. Eldridge and C. M. Spuckler, "Determination of scattering and absorption coefficients for plasma-sprayed yttria-stabilized zirconia thermal barrier coatings," *J. Am. Ceram. Soc.*, vol. 91, no. 5, pp. 1603–1611, 2008.
- [172] T. D. Bennett and F. Yu, "A nondestructive technique for determining thermal properties of thermal barrier coatings," *J. Appl. Phys.*, vol. 97, no. 1, 2005.
- [173] S. M. Shepard, J. Hou, J. R. Lhota, and J. M. Golden, "Automated processing of thermographic derivatives for quality assurance," *Opt. Eng.*, vol. 46, no. 5, pp. 051008: 1–6, 2007.
- [174] J. G. Sun, "Thermal Property Measurement for Thermal Barrier Coatings by Thermal Imaging Method," in *Advanced Ceramic Coatings and*

Interfaces V: Ceramic Engineering and Science Proceedings, vol. 31, D. Zhu, H. Lin, S. Mathur, and T. Ohji, Eds. 2010.

- [175] B. K. Jang, J. G. Sun, S. W. Kim, Y. S. Oh, and H. T. Kim, "Characterization of the thermal conductivity of EB-PVD ZrO₂-Y₂O₃ coatings with a pulsed thermal imaging method," *Surf. Coatings Technol.*, vol. 207, pp. 177–181, 2012.
- [176] B. K. Jang, J. Sun, S. Kim, Y. S. Oh, S. M. Lee, and H. T. Kim, "Thermal conductivity of ZrO₂-4mol%Y₂O₃ thin coatings by pulsed thermal imaging method," *Surf. Coatings Technol.*, vol. 284, pp. 57–62, 2015.
- [177] M. Akoshima, M. Ogawa, T. Baba, and M. Mizuno, "The Thermal Diffusivity Measurement of the Two Layer Ceramics Using the Laser Flash Method," *J. High Temp. Soc.*, vol. 34, no. 5, pp. 227–233, 2008.
- [178] J. Mehnen, L. Tinsley, and R. Roy, "Automated in-service damage identification," *CIRP Ann. - Manuf. Technol.*, vol. 63, no. 1, pp. 33–36, 2014.
- [179] T. Matsushita, H. J. Fecht, R. K. Wunderlich, I. Egry, and S. Seetharaman, "Studies of the thermophysical properties of commercial CMSX-4 alloy," *J. Chem. Eng. Data*, vol. 54, no. 9, pp. 2584–2592, 2009.
- [180] Thermal Wave Imaging Inc., "Thermoscope II: Advanced Thermography for In-Service Inspection." [Online]. Available: http://www.thermalwave.com/1/376/thermoscope_ii.asp. [Accessed: 10-Jan-2016].
- [181] T. P. Ryan, "Section 1.12," in *Modern Experimental Design*, John Wiley & Sons Inc., 2007, p. 23.
- [182] C. H. Liebert, "Emittance and absorptance of NASA ceramic thermal barrier coating system, NASA Technical Paper 1190," in *International Conference on Metal Coatings, San Francisco, California, April 3-7, 1978*, no. 2, pp. 235–240.
- [183] G. Ptaszek, P. Cawley, D. Almond, and S. Pickering, "Transient

- thermography testing of unpainted thermal barrier coating (TBC) systems,” *NDT E Int.*, vol. 59, no. C, pp. 48–56, 2013.
- [184] H. Zhao, F. Yu, T. D. Bennett, and H. N. G. Wadley, “Morphology and thermal conductivity of yttria-stabilized zirconia coatings,” *Acta Mater.*, vol. 54, no. 19, pp. 5195–5207, 2006.
- [185] L. Tinsley, C. Chalk, J. Nicholls, J. Mehnert, and R. Roy, “A study of pulsed thermography for life assessment of thin EB-PVD TBCs undergoing oxidation ageing,” *NDT E Int.*, vol. 92, no. August, pp. 67–74, 2017.
- [186] U. S. The Mathworks Inc. Natick, Massachusetts, “NN, 2012, MATLAB version 7.14.0.739 and Image Processing Toolbox Release 2012b.” 2012.
- [187] T. Widjanarko, L. Tinsley, R. Roy, and J. Mehnert, “Characterisation and Performance assessment of a Pulsed-thermography Camera System for component degradation inspection,” *Proc. 1st Int. Conf. Through-life Eng. Serv. Cranf.*, no. November, pp. 297–308, 2012.
- [188] R. Gonzalez and R. Woods, “Digital Image Processing Using MATLAB,” Pearson Prentice Hall, 2008, pp. 796–797.
- [189] X. Maldague, “Theory and Practice of Infrared Technology for Nondestructive Testing,” in *Theory and Practice of Infrared Technology for Nondestructive Testing*, Wiley-Blackwell, 2001, pp. 214–224.
- [190] “ThermoScope II - handbook and manual, Thermal Wave Imaging, Ferndale, Michigan, US.” 2011.
- [191] G. Nootz, “Fit 2D gaussian function to data,” *MATLAB Central File Exchange*. [Online]. Available: <http://www.mathworks.co.uk/matlabcentral/fileexchange/37087-fit-2d-gaussian-function-to-data/content/mainD2GaussFitRot.m>. [Accessed: 22-Apr-2013].
- [192] T. F. Coleman and Y. Li, “An Interior Trust Region Approach for Nonlinear Minimization Subject to Bounds,” *SIAM J. Optim.*, vol. 6, no. 2, pp. 418–

445, 1996.

- [193] A. M. Limarga, S. Shian, M. Baram, and D. R. Clarke, "Effect of high-temperature aging on the thermal conductivity of nanocrystalline tetragonal yttria-stabilized zirconia," *Acta Mater.*, vol. 60, no. 15, pp. 5417–5424, 2012.
- [194] T. J. Lu, C. G. Levi, H. N. G. Wadley, and A. G. Evans, "Distributed Porosity as a Control Parameter for Oxide Thermal Barriers Made by Physical Vapor Deposition," *J. Am. Ceram. Soc.*, vol. 84, no. 12, pp. 2937–2946, 2001.
- [195] P. G. Klemens, "Heat conduction in solids by phonons," *Thermochim. Acta*, vol. 218, pp. 247–255, 1993.
- [196] P. G. Klemens, "Phonon Scattering and Thermal Resistance Due to Grain Boundaries," *Int. J. Thermophys.*, vol. 15, no. 6, pp. 1345–1351, 1994.

APPENDICES

Appendix A Industry Interviews

A.1 Interview A: Company A, Manufacturing dept.

Date: 02nd December, 2013;

Interviewee: Head of NDT, 40+ years of experience

Q: In your industry, how do the technicians test TBC components that have been returned to MRO? What is the structure of the testing regime?

[confidential details: redacted]

Q: Do you use thermography, and in what context?

A: Why thermography? UT thickness gauging is quick & accurate to standard for measure wall thickness, while for multi-walled inspection, CT is used.

Current focus in on using thermography: detect blocked channels..

Q: Is IRT an approved technique in your maintenance schedule? And how can we use introduce new techniques in thermography in your company?

A manufacturer-specific process in place for thermography was developed in house and accredited by providing necessary evidence and expert opinion for the particular inspection process.

Interviewee is aware PT is used for composites. Used as a manual tool – video, 2D data comparison in pulsed mode – only one attempt to automate so far.

Not much on sizing as they compare the inspection data w.r.t performance characteristics of the part

Q: Do you use PT in maintenance and repair processes?

A: Yes, to detect delamination, damage and wall thickness measurement in specific parts in specific context

Q: Has there been any work on automation of PT?

A: No automation with thermography

Q: Has PT been used for remaining useful life prediction?

A: Interviewee not currently aware of thermography being used in remaining life capacity predictions.

Q: Any research in laser scanning thermography, or related techniques?

A: looked into laser scanning thermography which is suitable for large cracks approximately 6-7 mm in length.

Have looked at wall thickness measurement with using thermography

Have studied induction thermography for cracks; thin coatings

Also looked at fluorescence characteristics

For used parts, dirt can be a problem

Q: How is the data viewed, and are any measurements performed?

PT data is viewed as video, raw data, and difference / contrast. Searching for: visibly observable detection: local manual comparison. Nothing performed in sizing of features.

Q: What are the obstacles to applying PT more in your industry?

A: lack of standards for inspections, internal training requirement, lack of automation; unless it provides a unique benefit, or an already existing benefit at reduced cost or turn-around time, it is difficult to justify the cost of expanding inspections; unless it confers a unique advantage worth its cost. It would have to confer a unique advantage, or reduce time cost, or financial cost.

A.2 Interview B: Company A, Design

Date: 03rd March 2014;

Interviewee: Corporate Specialist - Surface Engineering, ~30 years
Life Cycle Engineering, ~20 years of experience

Scope: Proposal of thermographic coatings inspection experiment & its rejection

Outcomes: The use of thermographic NDT for coating remaining life based on oxide layer measurement of less interest, more open inspection of part life and respective change of properties over ageing accepted as being of greater interest

Q: (This part is from a lengthy interview that was more dynamic than structured here)

coating life well defined by statistical models, oxide growth is well understood. Are there any characteristics of the coating interface that can be monitored and assessed?

Verification for manufacturing is largely destructive sample testing statistics based; service / MRO context would be more promising for thermography.

The focus of requirements from the findings has been narrowed to suitability with the scope of the thesis.

There is no thermographic work currently with coatings where it is used to authorise parts or to fix a manufacturing method, though it has been used where appropriate as an additional inspection method. It would be interesting to see how material property changes with age, if it has service application in real context.

A.3 Interview C: Company A, Servicing

Date: 02nd April 2014;

Interviewee: NDT specialist, 7 years, NDT specialist, 20+ years

Company: provides bespoke maintenance for aero engine parts

Q: How are NDT tasks structured in your company? What is the routine?

NDT jobs are controlled by manufacturer specifications

Repair note specifies i.e. "check for no cracking here, these limits on crack sizes there, with techniques A, B.." i.e. "if (this) then (do this)" etc

Part comes in, print off technical drawings and relevant repair card

If new type of damage and no card for it, a "variance request" made: i.e. "found [damage description], [repair] suggested". Wait until manufacturer accepts or rejects the suggestion.

Repairs are not as repeatable in terms of tasks involved for each batch of parts returned from service, not regular as the manufacturing environment is.

Q: What NDT techniques are in use?

UT, x-ray inspection used on repairs, various metrology methods; all set by acceptance standard set for each component

PT: acceptance standard refers to the repair note for standards. Repair note comes from the manufacturer / technical manual.

If it clears as serviceable and it's going to be returned to service, thermographic inspection is applied to ensure it is sound as an additional precaution

Damage indications will be sent to senior technician who evaluates it against inspection standard.

A.4 A.1 Interview D: Company B, Service (MRO)

Date: 07th April 2014;

Interviewee: NDT specialist, 20+ years

Company: provides maintenance for aero engine parts

Interviewee: senior NDT technician trained to, 20+ years of experience.

Brief: Structured questions on NDT process, requirements and acceptance / reject criteria

Summary: Overview of NDT process with a focus on requirements for two types of HVM parts

Q: What types of NDT do you perform?

Dye pen, X-ray, Ut, Borescope (visual check)

Q: Of those, what is the extent of manual and automatic evaluation in each?

Interviewee stated as manual

Q: What are the common types of damage you inspect for?

Erosion, wall thickness check, cracking, coating deterioration. Experience says it's better to remove coating than pass it for it to fail at a later inspection anyway; if that 'fail' could be determined quick and early, would be advantageous

Q: What are the standards you perform to / where do you get them?

Standards are as specified by the part manufacturer / system manual

Q: What happens with bespoke / unexpected repair requirements?

If we see damage and can't see appropriate spec for it, then a variance request is made; may continue work while waiting answer

Q: In what ways is this done usually?

1) one-off requests on unusual damage

2) request for repeat of previous request on similar part, or for update to manual if frequently occurring

Company will continue working on the part while they wait for response to the request, if they feel confident it will be confirmed (a cost risk)

Q: What information comes with the part when it is delivered?

Can include service hours it has run, and number of cycles run; full details depends on the customer

Q: How is that validated / authorized

Inspection regime / criteria is authorized and held by the manufacturer (specified in the system manual)

Q: For a new process, what time constraints would it need to have?

Flexible: if it increases profitability or decreases process time, for example, cleaning for UT adds turn-time but is key

Q: Any other concerns?

For cleaning the component, dye penetrant sticks to the component, cleaning is performed by default.

Would like to be able to do quick NDT prior to removing the coating to save costs on wasted preparation if component is going to be rejected; the sooner the better.

It is expensive to pass a component that might fail after repair, to repair. The company is looking to increase yield. Stripping components costs time and money

Sometimes reject a repairable component because it would affect turn-around time, for which are contractually obliged to a fixed door-to-door contract; time is money; if any method can reduce time, there will be more time for repairable parts; improved yield.

It is not often that a part passed to final repairs fails later tests, due to strength of assessment process but it is a problem when that does happen (incurred cost); a quick method to help with this would be advantageous

A.5 Interview E: Company A,

Date: 24th April 2014;

Interviewee: Manufacturing Engineer, 15 years; Head of NDT, 40+ years of experience

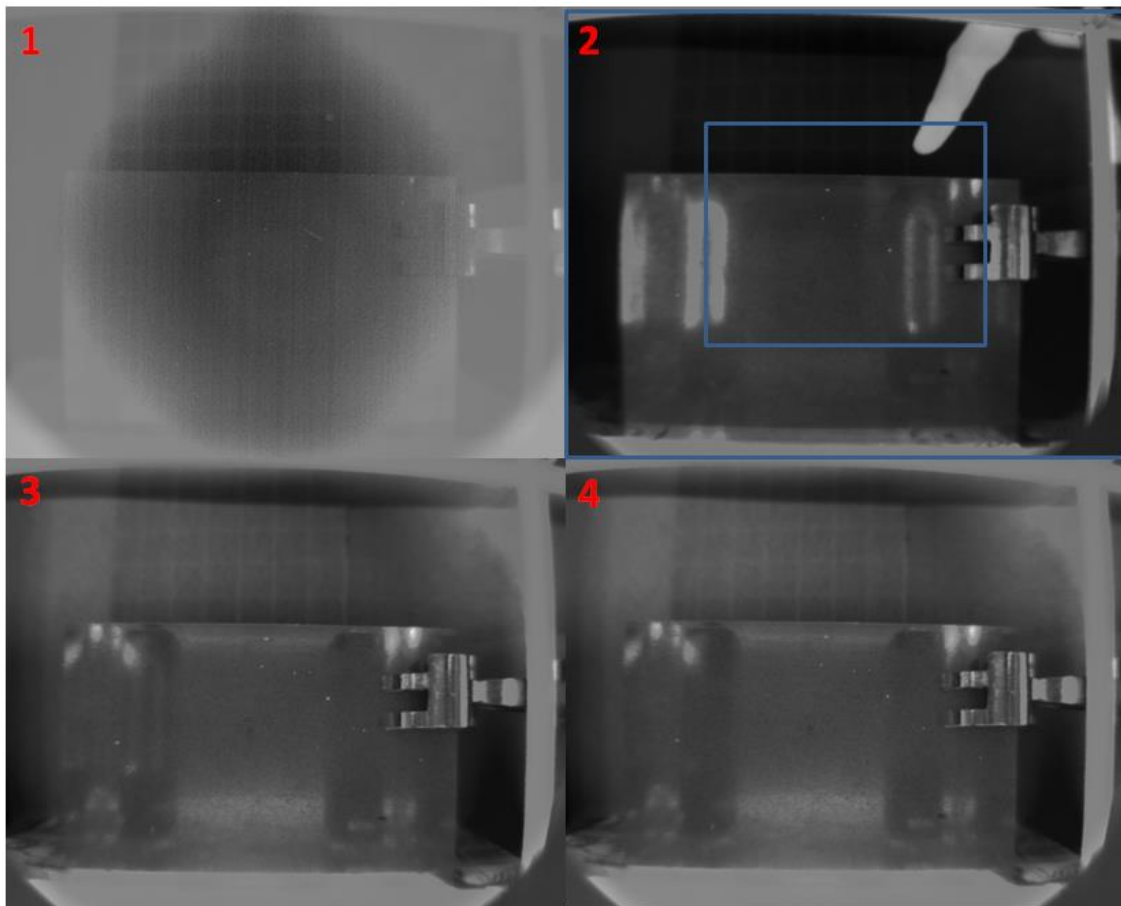
This interview was prepared with most of the same questions as previously, however, from the manufacturing context related to this interview, most of the service-related questions were either repeated or irrelevant. Other notes were taken during this meeting regarding NDT R&D being engaged by the company; these particular details were kept confidential. Some general insights were taken from this interview which helped set a few required markers of areas to be covered for the literature review i.e. to look also at methods d, e, f..

Appendix B – Report on flash bulb intensity

B.1 Test One: Initial inspection (check both bulb functionality) 03 August 2015

Setup: Present steel plate (uncoated) with no subsurface features to reflect pulse flash to show flash bulb operation and assess the status of both bulbs. Settings:

Integration Time: 2271 us
Window: 100%
Framerate: 100 Hz
Flash: 50%
Folder D:\Cranfield\Coatings Experiment\TBCTest12
File: Test12 06 001



Figure_Apx 1 – Initial inspection, data captured at IT2271 us, 50 Hz, full window
Flash bulbs both still working, both appear similar in temperature post flash, though one appears slightly dimmer than the other (right hand side if looking from behind hood, left hand bulb if looking into the hood).

- Flash frame shows homogenous saturation.

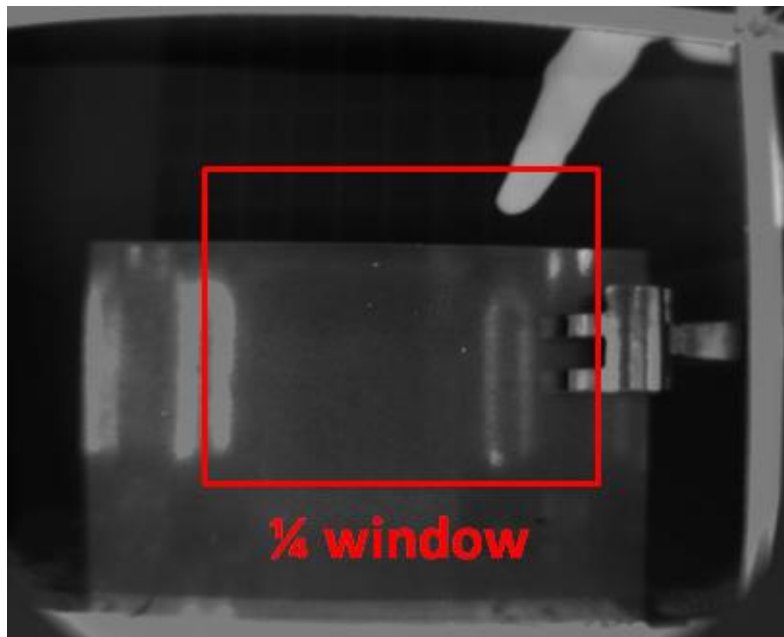
- One frame after shows difference between bulbs. (0.02s post flash / PF)
- Two frames after the flash shows a very slight disparity (0.04s PF)
- Three frames after flash shows homogenous bulb intensity (0.06s PF)

Possible conclusions

- Dimmer bulb is close to failure
- Dimmer bulb has always been dimmer and we weren't aware of this before
- Time difference between flash release among the bulbs, dimmer bulb has reached max intensity just before 0.02s and is now cooling at 0.02s while other bulb is closer to its (later) intensity peak.
- Should have captured this data previously
- Recommended action: not to ask Shayz, he could easily say it is failing even if it isn't, to get a fresh sale worth thousands.
- Repeat test at framerate with window that can still see the two bulbs

B.2 Test two: higher framerate 04 August 2015

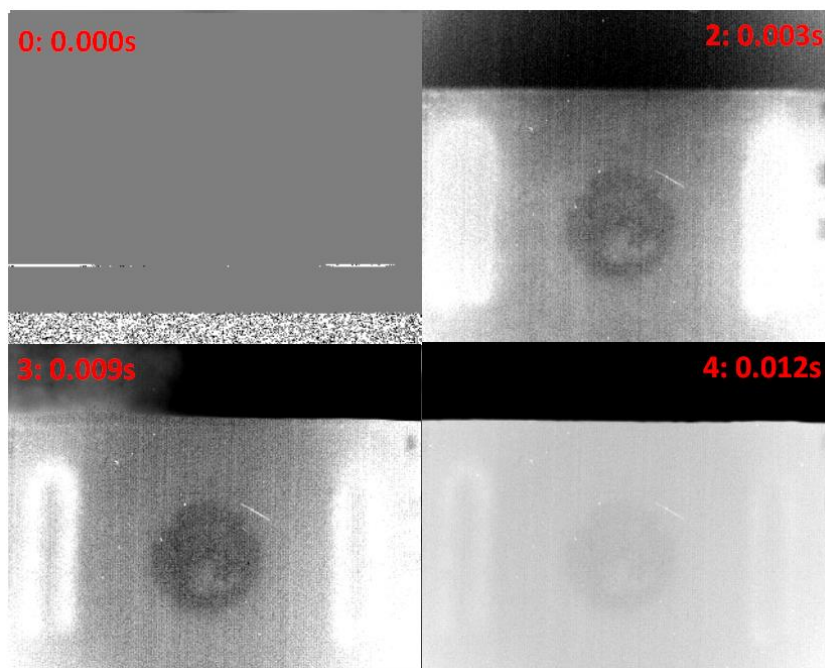
Setup: Present steel plate (uncoated) with no subsurface features to reflect pulse flash to show flash bulb operation and assess the status of both bulbs.



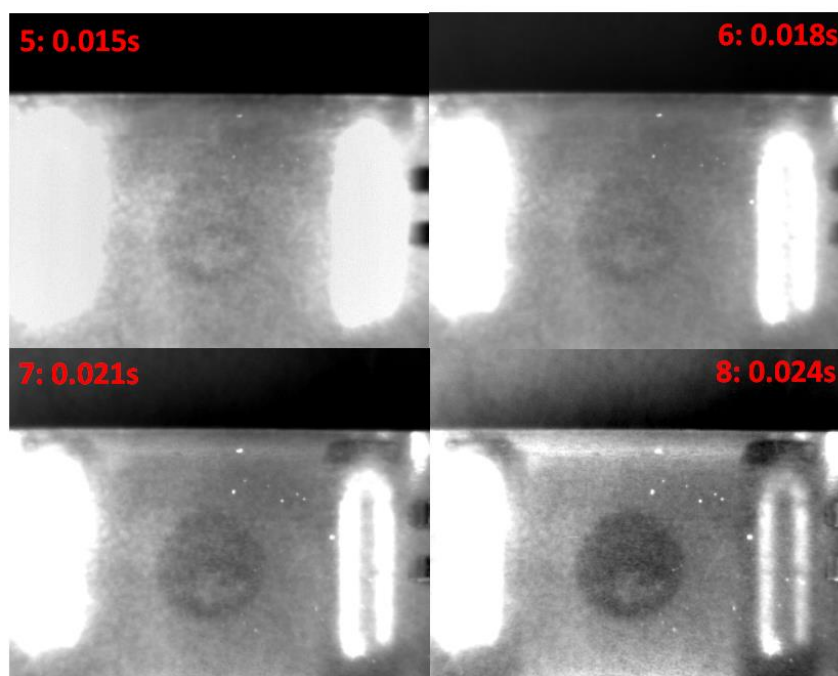
Figure_Apx 2 – narrowing inspection window to 25%

Integration Time: 2271 us

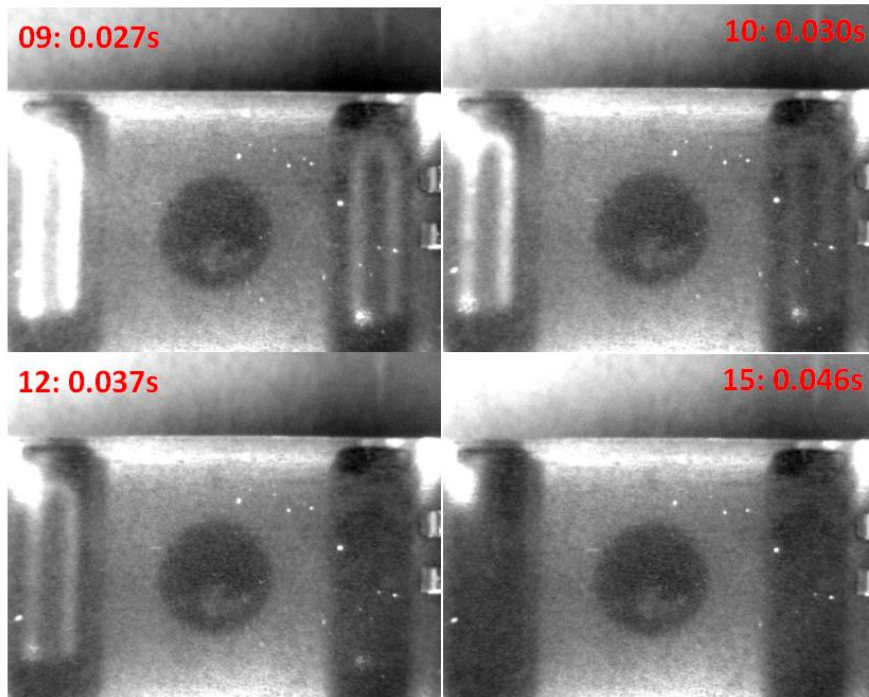
Window: 50%
Framerate: 328 Hz
Flash: 50%
Folder D:\Cranfield\Coatings Experiment\TBCTest12
File: Test12 07 001



Figure_Apx 3 – bulb pulse + afterglow pt.1 (correction: top right is frame1)



Figure_Apx 4 - bulb pulse + afterglow, pt. 2



Figure_Apx 5 - bulb pulse + afterglow, pt.3

Observations on flash bulbs 04 August 2015 (high framerate)

Flash bulbs both functional, both appear similar in temperature post flash.

Right hand bulb appears dimmer from 0.018s post flash, and appears to cool more rapidly than the other. Both bulbs appear homogenous and cooler than surroundings (from active air cooling) from ~ 0.04 s. This may indicate difference between the two bulbs.

Homogenous saturation of both bulbs until f6, ~ 0.018 s. Right bulb cools more rapidly till f12, 0.037s. Left bulb cools more slowly, equalising between f10-12, at approx. 0.040s.

Conclusions

- Both bulbs are functional
- Slight discrepancy between two bulbs has been observed
- May indicate post-flash “afterglow” emission lasts up to 0.040s (when it reaches “cool” equilibrium to surrounding casing)
- Low emissivity of reflective interior of box raises questions on previous point

- Air cooling fans rapidly cool bulb surface, truncating any thermal emissions from the heating of the bulb gas

Appendix C – Data tables

C.1 Oxidation furnace calibration

BF-13 Calibration to AMS2750D

REQUIRED TEMPERATURE [°C]	SETPOINT [°C]	ERROR [± °C]
1000	985	4
1050	1035	4
1100	1084	3
1135		
1150	1134	3
1190	1174	3
1200		

Date: 22.08.14

Next calibration due: 22.02.15

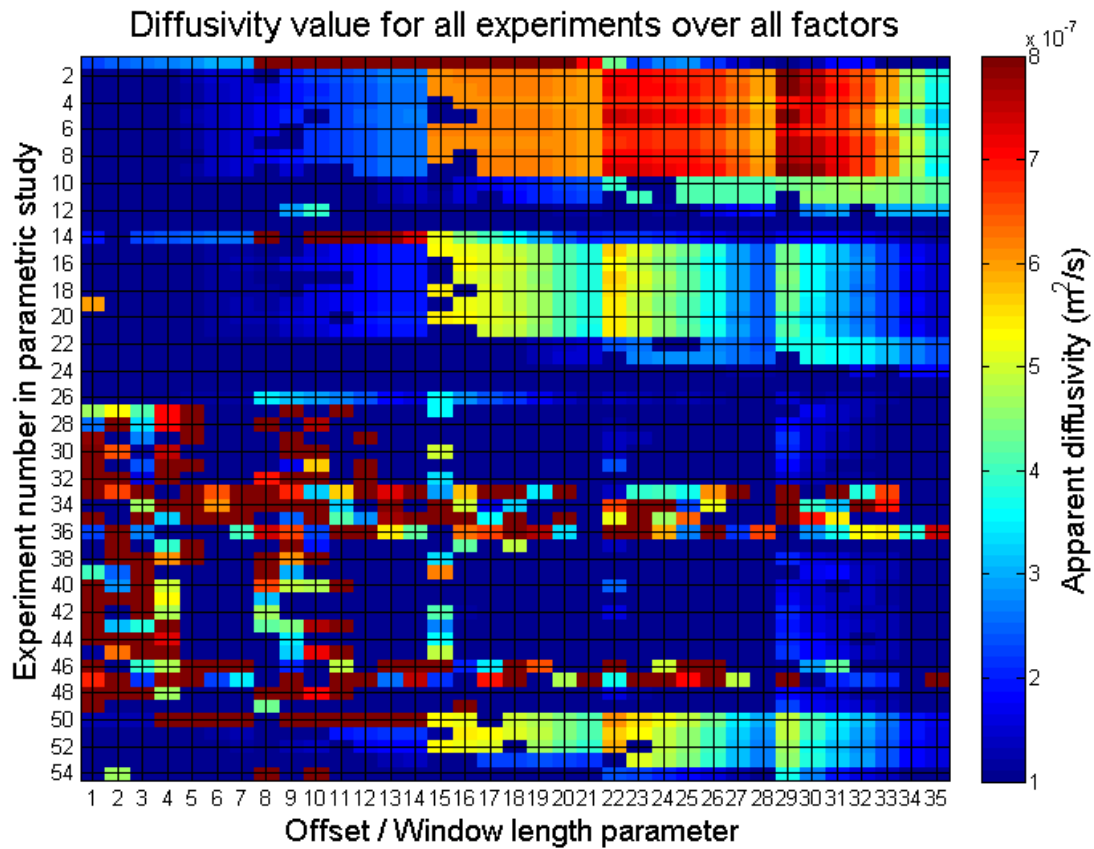
3 x new thermocouples used 21873-1A, -2A, -3A. Type N

Calibration set up procedure, 3 blades on oxidation test tray (1 back middle; 2 left front; 3 right front).

Pico logger csv files: BF13 22.08.14 (filter x 30 required for Pico-logger stability).

Data file: SAS\COATINGS\General\Equipment\Furnaces\BF13\Calibration 22.08.14

Appendix D – full range of experiments for parametric study



Figure_Apx 6 - plot of diffusivity results of a multiple data captures (y-axis) varied with analysis parameters (x-axis) taken with a combination of integration time (i.e. 2271us) and flash power (25-100%), cycling through data capture parameters in series from left to right: data offset (0), window length 10, 12, 14, 16, 20, 30, 40; data offset (1), window length (10, 12,..); (2), (10, 12..). Other parameters were included to check effect / no effect i.e. change in ambient conditions, captures on different days.